Ab initio simulations of local current densities in mesoscopic films:
Current vortices in functionalized graphene nanoribbons

Zur Erlangung des akademischen Grades eines

DOKTORS DER NATURWISSENSCHAFTEN

von der Fakultät für Physik
des Karlsruher Instituts für Technologie (KIT)

genehmigte

DISSERTATION

von

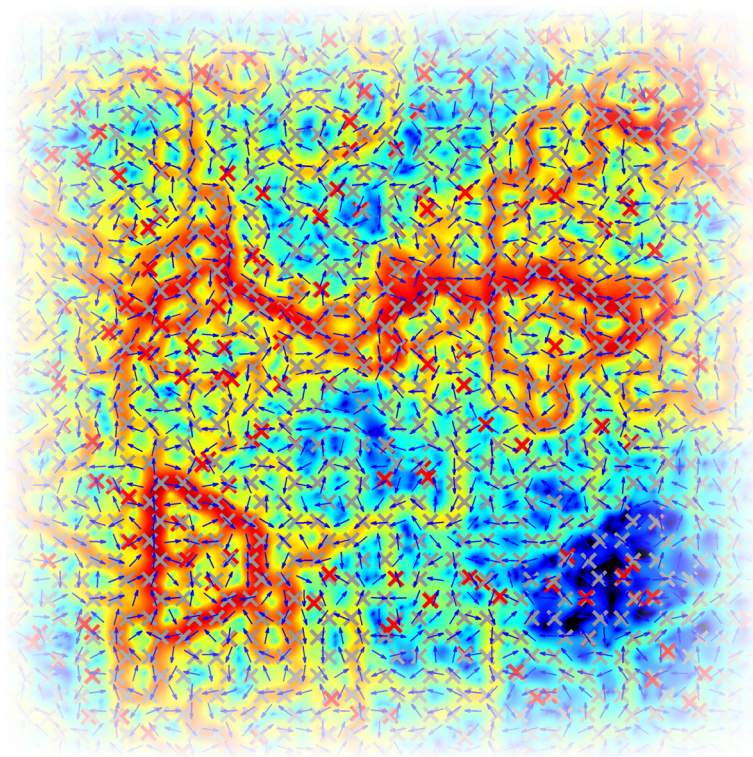Dipl.-Phys. Michael Steffen Walz
aus Tübingen

Für die numerischen Transportberechnungen wurde Code direkt in C++/Fortran geschrieben, wobei die üblichen numerischen Bibliotheken genutzt wurden. Die Dichtefunktionaltheoriedaten wurden von den Paketen FHI-aims* und Turbomole† geliefert. Die numerische und grafische Auswertung erfolgte meist in MATLAB‡ oder mit Gnuplot§/Inkscape¶. Analytische Berechnungen wurden von Hand oder mit Mathematica‖ bewältigt. Der Satz dieser Arbeit erfolgte mit dem Textsatzsystem LaTeX. Zusätzlich wurde Standardsoftware, wie sie in der Linux-Distribution Debian** vorhanden ist, genutzt.

---

* `http://www.fhi-berlin.mpg.de/aims/`

† `http://www.turbomole.com/`

‡ `http://www.mathworks.com/products/matlab/`

§ `http://www.gnuplot.info/`

¶ `https://inkscape.org/`

‖ `http://www.wolfram.com/mathematica/`

** `https://www.debian.org/`

Ab initio simulations of local current densities in mesoscopic films:

Current vortices in functionalized graphene nanoribbons

Dissertation

by

Dipl.-Phys. Michael Steffen Walz

2012–2015

To Nora Elina

"Heheheee..."

and to Kathrin, Rose & Rolf

for all their love and support

Contents

Appendices

Introduction: Quantum interference and ring currents in nanoscopic physics

In the physical nanosciences, sending a current through a device is a common way to probe the internal structure, e.g., electrical currents serve as sensors in scanning tunneling microscopes (STM)[1, 2] and mechanically controllable break junctions (MCBJ)[3, 4]. In molecular electronics[5], they operate single molecular switches[6–11] as well as molecular motors[12–16]. For such applications it is important to understand how current flows through a device: Sensing can be efficient only if the signatures of the measured current-voltage characteristics (IV) can be related reliably to their microscopic origin. Likewise, a controlled device operation and a systematic improvement of its performance also relies on a precise knowledge about the driving currents. For instance, the dissipation of heat is closely intertwined with the local current densities. To establish the required microscopic understanding, a good part of the *theoretical* nanosciences has always dealt with the question of how to interpret the experimental IV in terms of the detailed physics that governs at the nanoscale.

Current flow at the nanoscale differs qualitatively from its classical counterparts due to quantum interference. Such quantum interference effects can significantly enhance or reduce the current through quantum structures. Where the classical Kirchhoff's circuit law predicts a current increase by a factor of two for two identical paths, constructive interference allows for enhancements up to a factor four. In non-identical paths, destructive quantum interference is possible, reducing the resulting current by orders of magnitude. Indeed, quantum interference effects in transport through single molecules has been a topic intensively investigated over the last decade, both experimentally[17–28] and theoretically[29–40]. Both, constructive and destructive interference effects were recently shown to survive at room temperature: constructive interference enhancement beyond Kirchhoff's circuit law has been demonstrated in a single molecule with two parallel connected benzene rings[27, 28], whereas destructive interference was measured in, e.g., anthracene (three benzene rings) with additionally adsorbed oxygen atoms providing destructive interference paths[26, 40].

Even in a single atom ring, e.g. in benzene, quantum interference can be experimentally observed. Much lower conductance values are measured for meta-connected benzene rings (with asymmetric

current paths) as compared to para-connected rings (with symmetric current paths)[17–24]. The destructive quantum interference has been explained in terms of non-interacting tight-binding models[33–39]. Interestingly, such tight-binding studies also exhibit ("bond") currents circulating around the carbon ring[36, 38]. Even though circulating (ring) currents do not contribute to the total transport current they are important to analyze: (a) the magnitude of the ring currents can significantly exceed the total current and (b) ring currents induce local magnetic fields which may influence electron and nuclear spins as well as the electron motion itself.

In this thesis, we explicitly investigate the appearance of such ring currents and more generally current patterns in transport through mesoscopic graphene[A] ribbons. In other words, we analyze the spatial structure of the scattering states. So far, explicit investigations of the spatial dependence of the scattering states with their associated local current patterns are quite rare. The reason is, presumably, that the local current density is not easily resolved, experimentally. (However, related suggestions will be made later in this work.) This is unfortunate since current patterns turn out to exhibit a very rich substructure that originates from quantum interference. Figure 1.1 offers an illustration. The current patterns feature, e.g., small current vortices that are related to orbital magnetism.

Indeed, ring currents in ring structures have been investigated already for a long time. For instance, ring currents induced by magnetic fields applied to aromatic molecules is a field on its own in quantum chemistry[41–43]. This goes back to 1936, when Pauling[44] and Lonsdale[45] calculated the diamagnetic response in "benzene and other aromatic hydrocarbon molecules [assuming] that the p_z electrons (one per aromatic carbon atom) are free to move from carbon atom to adjacent carbon atom under the influence of the impressed fields"[44]. The induced ring currents generate a magnetic field which counteracts the external magnetic field (Lenz's law). In the late 1960s, the
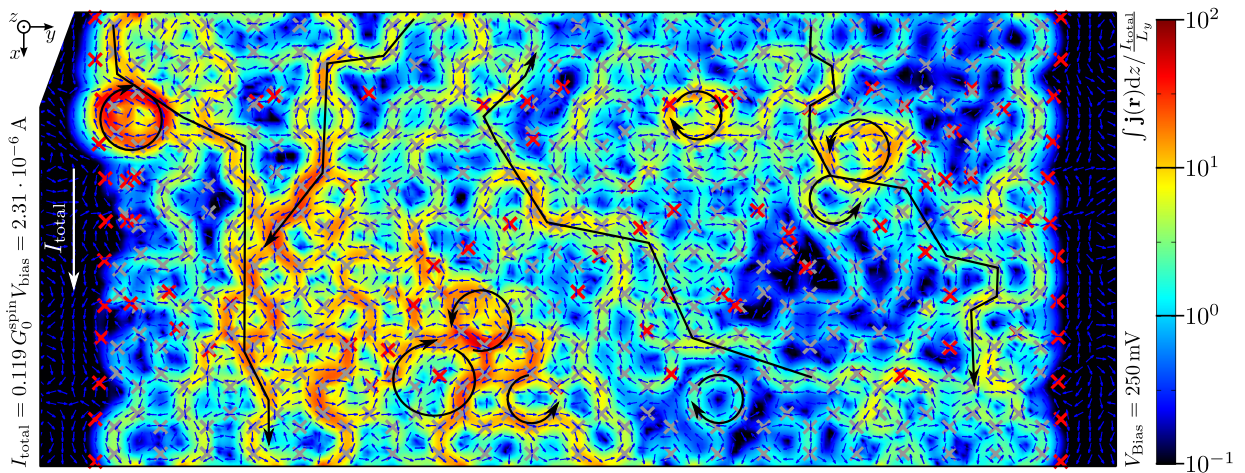
Figure 1.1: Simulated local current density (integrated over the out-of-plane direction and normalized to the spatial average current) induced by an applied bias voltage $V_{\text{bias}} = 250\,\text{mV}$ in a hydrogenated graphene ribbon. Some interesting current paths are drawn in the picture for illustration, e.g., local current vortices exceeding the spatial average current by orders of magnitude (see red regions). Plot shows current amplitude (color), current direction (arrows), carbon atoms (gray crosses) and hydrogen atoms (red crosses).

interaction of these shielding currents with the nuclear spin of hydrogen atoms has been measured by NMR experiments[46–51]. Since the 1990s, *ab initio* studies became available which showed the spatial structure of the induced current density[52–57].

Diamagnetic currents induced by magnetic fields are not restricted to small molecules; they exist in all structures with highly mobile electrons, e.g., also in graphene[58], in fullerenes[59], and also in conducting metal rings. The latter are often used to investigate the consequences of the Aharonov-Bohm (AB) effect[60]. (An electron picks up a phase when encircling a magnetic flux.) To allow for interference effects, the phase coherence length must be larger than the dimensions of the ring. Therefore, one needs either very small or clean samples or suppression of phase relaxation by other means, e.g., by superconductivity in superconducting rings. Including two Josephson junctions[61], such rings serve as superconducting quantum interference devices (SQUID)[62–64]. The induced ring currents allow for the measurement of very tiny changes in applied magnetic fields. Superconductivity is a topic on its own which we do not discuss in this thesis, but Büttiker *et al.* realized already in 1983, that also ring structures made of non-superconducting materials can be driven by external magnetic fields: "small [...] rings of normal metal, driven by an external magnetic flux, act like superconducting rings with a Josephson junction, except that $2e$ is replaced by e"[65, 66]. Soon after, in 1985, the so called AB oscillations have been observed in normal metal rings, i.e., in a gold ring of diameter $d \approx 800\,\text{nm}$ [67]. (Up to now, AB rings have been fabricated from various materials, e.g., also from graphene[68].) In the presence of an external magnetic field, non-superconducting rings can also carry persistent currents: dissipationless circulating electron currents that do not require an external voltage[69]. The electronic groundstate of the ring carries a current. Time-reversal invariance is broken by the external magnetic field. The difference to superconducting ring currents is that the ring currents vanish for zero external field. Evidence for such persistent currents have been observed for low temperatures, $T \approx 10\,\text{mK}$, in 1990/91 for a array of mesoscopic copper rings[70] as well as for an isolated gold loop[71].

In this thesis, instead of applying a magnetic field to induce ring currents, we apply an electric field, i.e., a dc-bias voltage. This produces local current vortices, which in-turn induce local magnetic fields. An established concept to calculate transport currents based on a microscopic system description is the Landauer-Büttiker formalism[72–74]. It describes charge transport as a sequence of scattering processes of (very weakly) interacting particles and applies in situations where transport can safely be assumed to be phase coherent. The charming aspect of this approach is that it reduces the transmission calculation for complicated nanostructures to the calculation of the scattering asymptotics, incarnated in (usually a small number of) transmission coefficients. As is often the case, reducing the complexity in such a way also eliminates fundamental physics; in this case the spatial structure of the electron current density $\mathbf{j}(\mathbf{r})$, which describes the pathway through the device.

To assess the local currents, the Landauer-Büttiker formalism is often reformulated in terms of non-equilibrium Green's function techniques (NEGF)[75, 76]. Indeed, tight-binding (TB) transport studies using NEGF have been widely employed to calculate the local current structure in graphene and graphene ribbons[77–85]. The resulting TB ("bond") currents show vortices, ring current contribution produced by local scattering centers like impurities and lattice defects[77–83]. Similar TB transport studies in carbon nanotubes[86] and aromatic molecules (beyond benzene)[87, 88] also show the formation of ring currents in the presence of scattering centers.

While the TB simulations reveal a exciting qualitative feature of local current flows (ring currents) their quantitative interpretation is not straight-forward. Calculations of the current density $\mathbf{j}(\mathbf{r})$ or the induced magnetic field $\mathbf{B}(\mathbf{r})$ that are valid on atomic length scales and start from the TB ("bond") currents can be performed only if the spatial structure of real-space wavefunctions is reinstalled.[B] However, usually the real-space representation (spatial basis set) of a given TB model is not given sufficiently accurately and therefore this reconstruction is not practical. This is one of the reasons, why we will avoid the use of TB models and rather advance a different approach in this thesis.

Local basis sets are given explicitly, namely, when working with conventional codes employing, e.g., the density functional theory (DFT) in order to construct an effective single-particle Hamiltonian for a given microscopic system ("device"). Making use of this, we combine DFT with non-equilibrium Green's function techniques (DFT+NEGF) to address the local transport problem. This combination has been used in the past by our group as well as by many others[89–96] for the calculation of IVs. Its validity has been a matter of an intensive debate over the years; by now, the Kohn-Sham (KS) based transport method can be considered an established tool.[C] To the best of my knowledge, an application for local current densities, as we establish it in this work, has not been realized before.

The main challenge of this thesis was the high computational cost of DFT transport for graphene flakes with up to 2500 carbon atoms. Our calculations were run on the HERMIT/HORNET supercomputer at the High Performance Computing Center (HLRS) in Stuttgart who kindly granted a budget of five million CPU-hours for this work.[D]

Although we investigate the emergence of vortices in the local current density in graphene ribbons, our results have a much wider scope. We presume that the effect applies to mesoscopic transport with broken symmetries in general, and that a tendency for ring currents in seen in generic mesoscopic systems.

We arranged our work into the following chapters: In Chap. 2 (and Appx. B), we present our new implementation of the DFT+NEGF method, focusing on local transport quantities as well as efficiency (parallelization and scalability) for large system sizes. Local transport quantities include the local current densities $\mathbf{j}(\mathbf{r})$, but also induced observables like the induced magnetic field $\mathbf{B}(\mathbf{r})$ and the total sample magnetization $\mathbf{m}$. For this thesis, I implemented the DFT+NEGF method for large two-dimensional systems on top of the existing transport code AITRANSS[97, 98]. (The latter had been developed in our group to treat transport through molecules, and was not yet suited for large transport calculations on a supercomputer.) Our implementation scales efficiently when using up 1000 CPU cores, reaching graphene sizes containing of the order of 10^3 carbon atoms. Relying on DFT, our implementation is not restricted to graphene, and may be used in the future to study dc-transport in molecular films in general.

As first application, we investigate the transport behavior of narrow armchair graphene nanoribbons in Chap. 3. We see that already pristine nanoribbons feature inhomogeneous current patterns, streamline patterns, due to the presence of confining edges which can be explained with simple zone-folding arguments. These streamline patterns also provide an intuitive explanation for the well-known strong position dependence of impurities[81, 99–102]. If the impurity is placed outside the streamlines of the pristine ribbon, no qualitative changes in the current densities are

observed. When individual scatterers are placed inside a streamline, the current patterns change significantly. In that case, we observe ring currents, prominent current density vortices that can exceed the average through current by orders of magnitude. We illustrate the fundamental origin of these ring currents by using simple two-path tight-binding (toy) models.

An interesting question is how these current vortices behave in large samples which include many scattering centers. Does one observe a rich current pattern which features many vortices? In Chap. 4, we see that this is indeed the case.

For that purpose, we investigate large hydrogenated graphene nanoribbons with a finite hydrogen coverage, i.e., many hydrogen adsorbates which act as local scattering potentials. We discover pronounced patterns in the local current density, current vortices, that go along with orbital magnetism. The induced magnetism is important for several reasons. First, random magnetic fields can induce spin relaxation which may be important for graphene spintronics[103]. Second, the random magnetic fields can be experimentally observed, thereby serve as indication for the vortex pattern. We propose a NMR-type experiment in the presence of an applied bias voltage to observe the spatial fluctuations of the induced magnetic fields. Alternatively, one may tend to measure the total induced magnetization m_z, which is effectively the average rotation sense of all current vortices. We predict a total magnetization of $\sqrt{\langle m_z^2 \rangle} \sim 1\,\mu_\mathrm{B} \cdot \sqrt{V_\mathrm{bias}/\mathrm{V}}$ that scales with the square root of the bias voltage, independent of the system size.

A quantitative analysis of the current density fluctuations reveals that they follow a lognormal distribution; in particular, the magnitude of the ring currents exceeds the average through current by orders of magnitude in large spatial regions. In other regions, the current density is significantly below the average through current. The associated magnetic fields exhibit drastic fluctuations and large field gradients.

In the second part of Chap. 4, we discuss how the observed effects depend on system size, on finite bias voltages, on different adsorbate concentrations or different adsorbate types, and on relaxation effects. In all cases, the individual current patterns change, but the general (statistical) features—strong current vortices significantly exceeding the average through current and a lognormal distribution of the current density—remain. We thus propose that the observed current vortices are generic and also relevant for experimental sample sizes, which are usually much larger than the systems reachable by DFT transport.

Next, we discuss the influence of spin polarization on the transport behavior. First, we would like to mention that we do not cover Kondo physics in this work. (For a recent review on Kondo impurities in graphene, we refer to Ref. 104.) Instead, we focus on temperatures well above the Kondo scale T_K. Indeed, there appears to be experimental evidence for a relatively small Kondo temperature in graphene induced by spin-$1/2$ point defects, $T_\mathrm{K} \lesssim 2\,\mathrm{K}$ [105]. In Chap. 5, we focus on the spin-flip transmission as well as on the influence of spin polarization on the local current density. We show that the spin-flip transmission in small hydrogenated graphene ribbons can reach the same order of magnitude as the spin-conserving one. We relate this effect to exchange-interaction rather than intrinsic spin-orbit interaction.

As the last topic covered in this thesis, we turn to self-consistency in Chap. 6. We discuss self-consistency in the magnetic field, i.e., how the induced magnetic field backfeeds into the electronic states. Since current-induced magnetic fields have not been discussed in graphene before, this is

an open question. Our results show that the magnetic feedback is indeed minor and can be ignored in most cases. The reason is simple: the current vortices mostly encircle single rings; the magnetic flux through single rings is very small, in the order of 10^{-7} times the magnetic flux quantum Φ_0. Thus, the induced phase changes in the electronic wavefunctions are also small.

We close with conclusions and outlook in Chap. 7.

Last, I feel obliged to mention that several publications[106–113] were written during the work on this thesis, see page 171 for the publication list. Therefore, also ideas of my coworkers have found their way into this thesis. A great thanks to all my coworkers! Hence, a large overlap between these publications and this thesis is expected. On the other hand, this thesis also contains material, like the current density distribution functions, that have not—except at presentations— been published yet.

Notes & Appendices

The main part of this thesis focuses on conveying the essential ideas and important results. Therefore, short technical notes—that are not intended for the first-time reader—are moved to the end of each chapter. They are marked by capital Latin characters in superscript, as [A,B,C,···]. Longer discussions are deferred to the appendices. For example, in Appx. A, we discuss the nomenclature of graphene ribbons, the employed unit system, and give a list of abbreviations used throughout this thesis.

Notes to chapter 1

The notes are for completeness, reproducibility and to help interested readers understand all the fine technical details.

[A] We have chosen graphene, a two-dimensional sheet of carbon atoms arranged in a honeycomb lattice, because it is a famous representative for two-dimensional materials. Its unique features include a linear dispersion at the Fermi energy and a high electron mobility rate[114–116]. Graphene, and two-dimensional materials in general, have been studied intensively in the last decade[117]; especially after Novoselov *et al.* had proven the stable existence of graphene in 2004[118]. Before, two-dimensional materials were believed to be unstable due to the Mermin-Wagner theorem[119, 120]. Graphene and other (effectively) two-dimensional materials are stabilized by small deformations into the third dimension. As expected, the main effort of transport investigations in graphene[114–116] focused on global observables, like the total current. The underlying spatial structure of the current density was mostly ignored. (page 2)

[B] The problem of lacking spatial information is apparent already in the simplest examples. Consider a infinitely long circular wire carrying a spatially homogeneous current I_0. The wire radius R is the unknown spatial information. According to Ampère's circuital law, the azimuthal magnetic field *inside* the wire (at distance r to the wire center) is $B_\varphi = \frac{\mu_0 I_0}{2\pi} \frac{r}{R^2}$ and therefore strongly depends on the (unknown) wire radius R. For infinitesimal thin wires, the magnetic field diverges. This dependence becomes even more pronounced when dropping the homogeneity assumption of the current density. (page 4)

[C] A disadvantage of DFT based transport is that a formal justification exists—as often—only for special cases[121–125]. For the qualitative results, that we are after, that does not pose a problem. It is sufficient to note that the exact pathways—as predicted by the simulated current densities $\mathbf{j}(\mathbf{r})$—are probably not reproducible in experiment. The qualitative features—tendencies to form current vortices and broad distribution—should be correct.

To circumvent this issue, one could in principle employ more elaborate methods like the GW approximation (GW), or coupled cluster theory (CC). In practice, these methods are computationally much too expensive to treat large graphene flakes. In other words, DFT+NEGF is a method that provides atomic resolution by employing local basis functions while, at the same time, it is computationally still feasible for graphene flakes with thousands of carbon atoms. (page 4)

[D] As mentioned, *ab initio* transport simulations of local current densities $\mathbf{j}(\mathbf{r})$ in disordered graphene nanoribbons with up too 2500 carbon atoms (equivalent to 37000 basis functions) are computationally expensive. Thus, a proposal was sent (and accepted) to the High Performance Computing Center Stuttgart (HLRS) for five million CPU-hours on the HERMIT/HORNET supercomputer. For comparison, a single workstation with 16 cores would run over 35 years for reach such a budget. Many thanks to I. Kondov, A. Bagrets, and F. Evers, who have helped writing the proposal.[113] (page 4)

2 Chapter 2

Transport method: Calculation of the local current density

This chapter presents the transport formalism based on density functional theory (DFT) as used throughout this thesis for the calculation of the spatially continuous electron current density $\mathbf{j}(\mathbf{r})$, and also for the induced quantities like the magnetic field $\mathbf{B}(\mathbf{r})$. The physical results are deferred to subsequent chapters. The basic idea of DFT based transport relies on the widespread Kohn-Sham (KS) formulation of DFT. The KS theory replaces the full many-body system by a *fictitious* non-interacting KS system. We apply single particle scattering theory to the non-interacting KS particles, i.e., we construct the KS scattering states $\psi_{\mathrm{KS}}(\mathbf{r})$ from the underlying DFT simulation and calculate the KS electron current density as

$$\mathbf{j}(\mathbf{r}) = \frac{\hbar}{2\mathrm{i}m} \lim_{\mathbf{r}' \to \mathbf{r}} (\boldsymbol{\nabla}_{\mathbf{r}} - \boldsymbol{\nabla}_{\mathbf{r}'}) \psi_{\mathrm{KS}}^*(\mathbf{r}') \psi_{\mathrm{KS}}(\mathbf{r}) \,. \tag{2.1}$$

This procedure is general and could be implemented also in other transport codes[89–96] that rely upon DFT. So far, existing codes focus on global quantities like the transmission coefficients or the current-voltage characteristics but do not calculate the local current density $\mathbf{j}(\mathbf{r})$. Examples include DFT-based tight-binding codes, like gDFTB[89] implemented on top of DFTB+[126], as well as full DFT codes, like TRANSIESTA[90], SMEAGOL[91, 92] (both based on the DFT code SIESTA[127]) or WanT[93] (based on QUANTUM ESPRESSO[128]).

We structure this chapter as follows: First, in Sec. 2.1, we summarize the basic ideas of Landauer-Büttiker transport, and present a standard formulation using non-equilibrium Green's functions (NEGF). In Sec. 2.2, we apply the transport formalism to DFT and especially discuss how a KS Hamiltonian for the bulk limit can be constructed from a DFT simulation of a finite system. The implementation of the local current density, including convergence tests for the continuity equation are presented in Sec. 2.3. The induced local magnetic fields and the influence of finite grid spacings are discussed in Sec. 2.4. After an investigation of the computational performance in Sec. 2.5, we close with a summary of recommended numerical settings (Sec. 2.6).

2.1 Landauer-Büttiker transport

In the following, we refrain from deriving the transport formulas and instead discuss the essential physical ideas of Landauer-Büttiker transport[72, 73] using the non-interacting quantum dot as toy model in Sec. 2.1.1. Then, in Sec. 2.1.2, we present how the Landauer-Büttiker formalism is usually formulated in terms of non-equilibrium Green's functions (NEGF). To deal with reservoirs, we employ a decimation technique to construct self-energies which model semi-infinite leads (Sec. 2.1.3). We conclude in Sec. 2.1.4 with a short discussion how the transport simulations are extended to systems with broken spin-rotational invariance. None of these techniques is new on its own (e.g. see book by Di Ventra[76]), but combining them with *ab initio* methods in order to investigate the local current density in film geometries has—to the best of my knowledge—never been done before.

2.1.1 A toy model: the non-interacting quantum dot

Ideally, the transport problem consists of a closed system with a battery (electron source and sink) and a junction which connects the two battery poles. In the Landauer-Büttiker approach, such a complicated system is replaced by an open junction coupled to two reservoirs with different chemical potentials μ. Next, one assumes that the transport can be described by a stationary solution, called *steady state*. In that case, the reservoirs continuously inject (or absorb) electron wave packets which move towards (or away from) the junction. Here, we move to an effective single particle description of the electrons.[A] Then, the reservoirs themselves can be modeled by closed but (semi-)infinite left and right leads. Their occupation numbers $f_{L/R}$ are given by Fermi-Dirac functions with individual chemical potentials, i.e., $f_{L/R}(E) = f(E - \mu_{L/R})$.

In the example of Fig. 2.1, the junction is represented by a single quantum dot (QD) at energy $E = \varepsilon$. When coupled to the leads, the electrons of the QD move to the left and right lead. The rate is proportional to the number of electrons N_d in the QD. The proportionality constant $\gamma/\hbar$ is called *rate* or *broadening* (see remark about broadening). At the same time, the electrons from the leads move to the QD with the same rate, but proportional to the occupation of the leads. Thus, the total particle current from the left (right) lead to the QD is

$$I_{L/R} = \frac{\gamma_{L/R}}{\hbar} \Big[f_{L/R}(\varepsilon) - N_d \Big] . \tag{2.2}$$

A stationary steady state solution requires $I_L + I_R = 0$ (no charge accumulation in the QD). The number of electrons N_d in the QD are therefore given by the weighted average of the lead occupation numbers:

$$N_d = \frac{\gamma_L f_L(\varepsilon) + \gamma_R f_R(\varepsilon)}{\gamma_L + \gamma_R} . \tag{2.3}$$

Thus, the basic ingredient for a non-equilibrium phenomenon is a difference in the occupation numbers of the leads. If the energy ε of the QD is between the chemical potentials of the leads (assume $\mu_L > \varepsilon > \mu_R$ within a few $k_B T$ for finite temperatures), the left lead continuously feeds
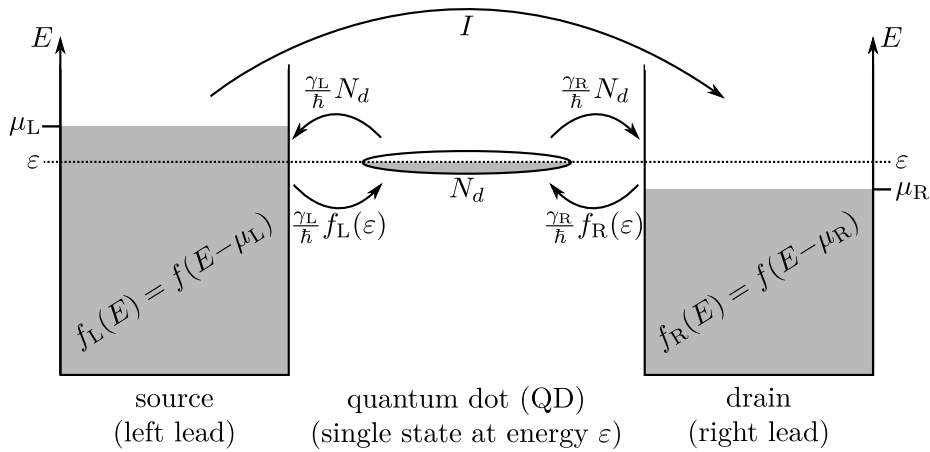
Figure 2.1: An example junction with a quantum dot (QD) coupled to two leads (source and drain). The energy ε of the QD state lies between the chemical potentials $\mu_{L/R}$ of the leads. Thus, a current I from left to right lead is generated and the occupation N_d of the QD lies between the occupation numbers $f_{L/R}$ of the left and right lead.

in electrons while the right lead continuously absorbs electrons from the junction. Thereby, they generate a current I_d through the QD:

$$I_d(\varepsilon) := I_L \overset{(2.2)}{=} \frac{\gamma_L}{\hbar}\Big(f_L(\varepsilon) - N_d\Big) \overset{(2.3)}{=} \frac{1}{\hbar}\frac{\gamma_L\gamma_R}{\gamma_L + \gamma_R}\Big(f_L(\varepsilon) - f_R(\varepsilon)\Big). \tag{2.4}$$

The dependence on the difference in the occupation numbers, $f_L(\varepsilon) - f_R(\varepsilon)$, is typical for transport phenomena.

Remark: Broadening

So far, we assumed that the density of states of the QD is sharp (i.e. a Dirac delta peak) and neglected that it is indeed broadened by the coupling to the leads. In this example, the total broadening γ of the QD state is given by the sum of the individual broadenings, i.e., $\gamma = \gamma_L + \gamma_R$. For the single QD, the broadened density of states $\rho(E)$ is a Lorentzian peaked at $E = \varepsilon$ with width γ.

In the spirit of the Landauer-Büttiker approach, we assume *independent channels*, i.e., channels with different spatial structure or at different energies do not influence each other. This also follows from linear response arguments. Thus, the total current I_{total} through the broadened state is given by integrating all contributions weighted by the density of states, i.e.,

$$I_{\text{total}} = \int_{-\infty}^{+\infty} \mathrm{d}E\, \rho(E)\, I_d(\varepsilon{=}E) = \int_{-\infty}^{+\infty} \frac{\mathrm{d}E}{2\pi\hbar}\mathcal{T}(E)\Big(f_L(E) - f_R(E)\Big) \tag{2.5}$$

with $\mathcal{T}(E) = 2\pi\rho(E)\,\gamma_L\gamma_R/(\gamma_L{+}\gamma_R)$. Here, we introduced an important quantity, the transmission function $\mathcal{T}(E)$, essentially the current per energy. It gives the probability for an electron with energy E to propagate through the junction.

2.1.2 Multichannel formulation using non-equilibrium Green's functions (NEGF)

For the general case, the main (technical) difference is that the junction—called device region in the following—contains a non-trivial inner structure. The broadenings $\gamma_{L/R}$ become broadening matrices $\mathbf{\Gamma}_{L/R}$, and the density of states and the occupation inside of the device region must be calculated incorporating the inner structure. Here, we present the Landauer-Büttiker transport through a device described by the general Hamiltonian $\mathbf{H}^{\mathrm{device}}$ (using NEGF, see Appx. B.1 for a short overview of Green's functions). Later, in Sec. 2.2, we employ DFT and use the KS Hamiltonian $\mathbf{H}^{\mathrm{KS}}$ as parametrization of the device Hamiltonian $\mathbf{H}^{\mathrm{device}}$.

Standard transmission calculation

To be more specific and to recall the basic definitions for the multichannel case, we consider an example—a thin armchair graphene nanoribbon (AGNR5)—as shown in Fig. 2.2. We partition it into a central region (device), a left and a right lead. The Green's function $\mathbf{G}_0^{\mathrm{device}}$ for the uncoupled device reads

$$\mathbf{G}_0^{\mathrm{device}}(E) = \left((E + \mathrm{i}0)\mathbb{1} - \mathbf{H}^{\mathrm{device}} \right)^{-1} . \tag{2.6}$$

To model the infinite extension of the system in the (current flow) x-direction, we compute the self-energies $\mathbf{\Sigma}_{L/R}(E)$ using absorbing boundary conditions[129] as specified in Sec. 2.1.3. The resulting Green's function

$$\mathbf{G}(E)^{-1} = \mathbf{G}_0^{\mathrm{device}}(E)^{-1} - \mathbf{\Sigma}_L(E) - \mathbf{\Sigma}_R(E) \tag{2.7}$$

describes the propagation of independent particles in the device in the presence of the leads. The transmission function $\mathcal{T}(E)$ is given by

$$\mathcal{T}(E) = \mathrm{Tr}\{\mathbf{\Gamma}_L \, \mathbf{G} \, \mathbf{\Gamma}_R \, \mathbf{G}^\dagger\} . \tag{2.8}$$

Here, $\mathbf{\Gamma}_{L/R}$ denote the anti-Hermitian parts of the self-energies, i.e., $\mathbf{\Gamma}_{L/R} = \mathrm{i}(\mathbf{\Sigma}_{L/R} - \mathbf{\Sigma}_{L/R}^\dagger)$. They are the generalization of the broadenings $\gamma_{L/R}$ (cf. Sec. 2.1.1) and account for the level broadenings in the device region due to the coupling to the leads.
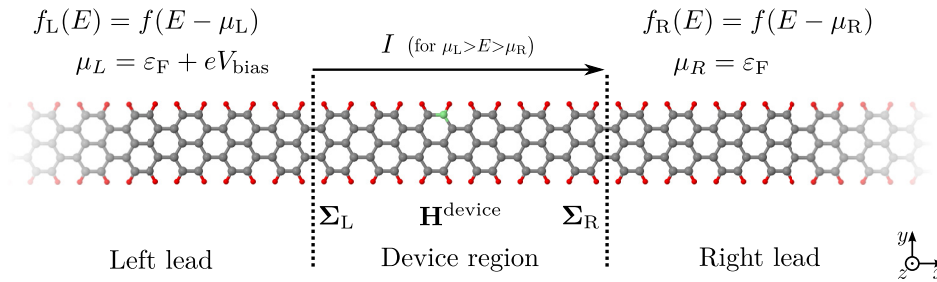
Figure 2.2: Armchair graphene nanoribbon partitioned into left lead, right lead and device region containing one nitrogen impurity (green).

When a bias-voltage is applied between the leads, $(-e)V_{\text{bias}} = \mu_{\text{R}} - \mu_{\text{L}}$, the total electric current (per spin) is given by

$$I_{\text{el}} = -eI_{\text{total}} = \frac{-e}{h} \int\limits_{-\infty}^{+\infty} \mathrm{d}E \; \mathcal{T}(E)\Big(f_{\text{L}}(E) - f_{\text{R}}(E)\Big) \tag{2.9}$$

which depends on the occupation numbers $f_{\text{L/R}}(E)$ of the left and right-travelling scattering states. For low temperatures $(T \to 0)$, the occupation numbers can be modelled by step functions $[f_{\text{L}}=\Theta(\mu_{\text{L}}-E),\ f_{\text{R}}=\Theta(\mu_{\text{R}}-E)]$. In the second step, for small bias voltages (in limit of linear response), both chemical potentials are near the Fermi energy (e.g. $\mu_{\text{L}}=\varepsilon_{\text{F}}+eV_{\text{bias}}$, $\mu_{\text{R}}=\varepsilon_{\text{F}}$) and the total current (per spin) simplifies to

$$I_{\text{el}} \xrightarrow{T\to 0} \frac{-e}{h} \int\limits_{\mu_{\text{R}}}^{\mu_{\text{L}}} \mathrm{d}E \; \mathcal{T}(E) \xrightarrow{V_{\text{bias}}\to 0} -\underbrace{\frac{e^2}{h}}_{G_0} \mathcal{T}(\varepsilon_{\text{F}})\, V_{\text{bias}}\,. \tag{2.10}$$

G_0 is the conductance quantum (per spin) and $G_0 \mathcal{T}(\varepsilon_{\text{F}})$ the zero-bias conductance. In a perfect crystal, $\mathcal{T}(E)$ equals the number of bands and the conductance—assuming spin degeneracy—is quantized in units of the conductance quantum $G_0^{\text{spin}} = 2G_0 = \frac{2e^2}{h} \approx 77.48\,\mu\text{S}$.

Local observables: current density and induced B-field

The retarded Green's function $\mathbf{G}(E)$ also allows to calculate the non-equilibrium Keldysh Green's function $\mathbf{G}^{<}(E)$:

$$\mathbf{G}^{<} = \mathrm{i}\mathbf{G}\Big[f_{\text{L}}\mathbf{\Gamma}_{\text{L}} + f_{\text{R}}\mathbf{\Gamma}_{\text{R}}\Big]\mathbf{G}^{\dagger}\,. \tag{2.11}$$

For low temperatures $(T \to 0)$, and at energies $\mu_{\text{R}} < E < \mu_{\text{L}}$, i.e. inside the voltage window, one has $f_{\text{L}}=1$, $f_{\text{R}}=0$, so that the Keldysh Green's function $\mathbf{G}^{<}$ reduces to

$$\mathbf{G}^{<}(E) = \mathrm{i}\mathbf{G}(E)\mathbf{\Gamma}_{\text{L}}(E)\mathbf{G}^{\dagger}(E)\,. \tag{2.12}$$

The Keldysh Green's function is transformed to real-space representation using the orthonormalized basis functions $\tilde{\varphi}_i(\mathbf{r})$ which are based on the underlying DFT calculation: $G^{<}(\mathbf{r}, \mathbf{r}', E) = \sum_{ij} \tilde{\varphi}_i(\mathbf{r})\mathbf{G}_{ij}^{<}(E)\tilde{\varphi}_j^*(\mathbf{r}')$ (for details, see Sec. 2.3). Using this decomposition, the particle current density (per spin and energy) is expressed as

$$\mathbf{j}(\mathbf{r}, E) = \frac{1}{2\pi}\frac{\hbar}{2m} \lim_{\mathbf{r}'\to\mathbf{r}} (\boldsymbol{\nabla}_{\mathbf{r}'} - \boldsymbol{\nabla}_{\mathbf{r}})G^{<}(\mathbf{r}, \mathbf{r}', E)\,. \tag{2.13}$$

The factor 2π reflects the Fourier transformation to energy domain. When applying a finite bias voltage V_{bias} between left and right lead, e.g. $\mu_{\text{L}}=\varepsilon_{\text{F}}+eV_{\text{bias}}$ and $\mu_{\text{R}}=\varepsilon_{\text{F}}$, current contributions within the bias window have to be integrated, i.e.,

$$\mathbf{j}(\mathbf{r}) = \int\limits_{\mu_{\text{R}}}^{\mu_{\text{L}}} \mathrm{d}E \; \mathbf{j}(\mathbf{r}, E)\,. \tag{2.14}$$

The current density response to the bias voltage (at zero bias) is given by

$$\frac{\mathrm{d}\mathbf{j}(\mathbf{r})}{\mathrm{d}(eV_{\mathrm{bias}})}\bigg|_{V_{\mathrm{bias}}=0} = \mathbf{j}(\mathbf{r}, \varepsilon_{\mathrm{F}}). \tag{2.15}$$

The Fermi energy ε_{F} can be varied experimentally, e.g., by applying a back-gate voltage V_{gate}.

Further, the electric current density $\mathbf{j}_{\mathrm{el}} = -e\mathbf{j}$ induces a magnetic field $\mathbf{B}$ and a magnetization $\mathbf{m}$ which is calculated via the Biot-Savart law as:

$$\mathbf{B}(\mathbf{r}) = \frac{\mu_0}{4\pi}\int \frac{\mathbf{j}_{\mathrm{el}}(\mathbf{r}') \times (\mathbf{r} - \mathbf{r}')}{|\mathbf{r} - \mathbf{r}'|^3}\mathrm{d}^3\mathbf{r}', \quad \mathbf{m} = \frac{1}{2}\int \mathbf{r} \times \mathbf{j}_{\mathrm{el}}(\mathbf{r})\,\mathrm{d}^3\mathbf{r}, \quad \mathbf{A}(\mathbf{r}) = \frac{\mu_0}{4\pi}\int \frac{\mathbf{j}_{\mathrm{el}}(\mathbf{r}')}{|\mathbf{r} - \mathbf{r}'|}\mathrm{d}^3\mathbf{r}'. \tag{2.16}$$

We also introduced the vector potential $\mathbf{A}$ required to calculate the magnetic feedback in Chap. 6.

Remark on finite basis sets: The current density as written in Eq. (2.13) satisfies a continuity-equation in the basis set limit: $\boldsymbol{\nabla} \cdot \mathbf{j}(\mathbf{r}) = 0$. For finite basis sets, this equation is violated. The magnitude $|\boldsymbol{\nabla} \cdot \mathbf{j}|$ decreases with increasing basis set size. At the end of all calculations, one has to ensure that the basis set was large enough, so that $\boldsymbol{\nabla} \cdot \mathbf{j} \approx 0$.

2.1.3 Modeling the reservoirs: construction of the self-energies $\Sigma_{\mathsf{L/R}}$

The Green's functions include the left and right leads (reservoirs) via the corresponding self-energies. They are readily calculated if the reservoir is quasi-onedimensional (i.e. a "long wire"), if two conditions hold true: (i) a single particle theory can be applied and (ii) the hopping along the wire is short range (i.e. only a finite number of neighbors). In that case, the lead can be represented by a Hamiltonian that exhibits a tridiagonal block-structure:

$$\mathbf{H}^{\mathrm{lead}} = \begin{pmatrix} \mathbf{H}^{\mathrm{block}}_{[0]} & \mathbf{V} & & \mathbf{0} \\ \mathbf{V}^{\dagger} & \mathbf{H}^{\mathrm{block}}_{[1]} & \ddots & \\ & \ddots & \ddots & \mathbf{V} \\ \mathbf{0} & & \mathbf{V}^{\dagger} & \mathbf{H}^{\mathrm{block}}_{[M-1]} \end{pmatrix}. \tag{2.17}$$

Each of the blocks may be thought about as a "slice" of the original wire. The Hamiltonian $\mathbf{H}^{\mathrm{lead}}$ of Eq. (2.17), therefore, corresponds to a wire consisting of M slices. Every slice is characterized by its own block-Hamiltonian, $\mathbf{H}^{\mathrm{block}}_{[j]}$. For simplicity, we assume that each slice is described by the same block matrix, $\mathbf{H}^{\mathrm{block}}_{[j]} = \mathbf{H}^{\mathrm{block}}$ and that each slice connects to the other slices via a block matrix $\mathbf{V}$ that is the same for every pair of neighboring slices (and zero otherwise). It is easy to see that due to the block-diagonal structure a self-energy is readily calculated in a recursive fashion. To motivate the recursion, we recall the familiar self-energy for coupling a quantum dot (device) to a reservoir, $\boldsymbol{\Sigma} = [\mathbf{V}^{\mathrm{lead}}]^{\dagger}\mathbf{G}^{\mathrm{lead}}\mathbf{V}^{\mathrm{lead}}$. For the quasi-onedimensional geometry, we have $[\mathbf{V}^{\mathrm{lead}}]^{\dagger} = \begin{pmatrix} \mathbf{0} & \cdots & \mathbf{0} & \mathbf{V}^{\dagger} \end{pmatrix}$ accounting for the fact, that the device couples only to the outmost

slice of the wire. Along that logic, each slice of the wire can be coupled one after another, forming the following recursion equations

$$\boldsymbol{\Sigma}^m(E) = \mathbf{V}^\dagger \mathbf{G}^{m-1}(E)\mathbf{V}\,, \qquad \boldsymbol{\Sigma}^0(E) = 0\,, \qquad (m = 0, \cdots, M{-}1) \qquad (2.18\text{a})$$

$$\mathbf{G}^m(E) = \left[(E + \mathrm{i}\eta_{\mathrm{dec}})\mathbb{1} - \mathbf{H}^{\mathrm{block}}_{[m]} - \boldsymbol{\Sigma}^m(E)\right]^{-1}. \qquad (2.18\text{b})$$

The number of blocks M it takes to converge the self-energies depends on the imaginary shift η_{dec}; typically we have $M = 50 - 400$. Therefore, it would be numerically too expensive to calculate the lead's Green's function $\mathbf{G}^{\mathrm{lead}} = [(E + \mathrm{i}\eta_{\mathrm{dec}})\mathbb{1} - \mathbf{H}^{\mathrm{lead}}]^{-1}$ by full matrix inversion. The set of recursion equation is often referred to as block decimation technique. On a mathematical level, it is effectively a Gaussian elimination scheme.

In the final step, we make use of the fact that the full Hamiltonian, including left and right lead together with the device, again has a block-structure:

$$\mathbf{H} = \begin{pmatrix} \mathbf{H}^{\mathrm{lead}} & \mathbf{V}_{\mathrm{L}} & 0 \\ \mathbf{V}_{\mathrm{L}}^\dagger & \mathbf{H}^{\mathrm{device}} & \mathbf{V}_{\mathrm{R}}^\dagger \\ 0 & \mathbf{V}_{\mathrm{R}} & \mathbf{H}^{\mathrm{lead}} \end{pmatrix}. \qquad (2.19)$$

Then, we evaluate the self-energies for the left and right lead using the same logic as before:

$$\boldsymbol{\Sigma}_{\mathrm{L}}^M = \mathbf{V}_{\mathrm{L}}^\dagger \mathbf{G}_{\mathrm{L}}^{M-1}\mathbf{V}_{\mathrm{L}}\,, \qquad \boldsymbol{\Sigma}_{\mathrm{R}}^M = \mathbf{V}_{\mathrm{R}}^\dagger \mathbf{G}_{\mathrm{R}}^{M-1}\mathbf{V}_{\mathrm{R}}\,. \qquad (2.20)$$

To determine the coupling matrices $\mathbf{V}_{\mathrm{L/R}}$, we assume that the device Hamiltonian $\mathbf{H}^{\mathrm{device}}$ also contains a left and right contact region, each of which is identical to a building block $\mathbf{H}^{\mathrm{block}}$ of the lead, i.e.,

$$\mathbf{H}^{\mathrm{device}} = \begin{pmatrix} \mathbf{H}^{\mathrm{block}} & \cdots & \cdots \\ \cdots & \cdots & \cdots \\ \cdots & \cdots & \mathbf{H}^{\mathrm{block}} \end{pmatrix}. \qquad (2.21)$$

That way, the (large) coupling matrices $\mathbf{V}_{\mathrm{L/R}}$ can be built by using the same coupling matrix $\mathbf{V}$ as in the leads:

$$\mathbf{V}_{\mathrm{L}} = \begin{pmatrix} \vdots & \vdots & \vdots \\ 0 & 0 & 0 \\ \mathbf{V} & 0 & 0 \end{pmatrix}, \qquad \mathbf{V}_{\mathrm{R}} = \begin{pmatrix} 0 & 0 & \mathbf{V} \\ 0 & 0 & 0 \\ \vdots & \vdots & \vdots \end{pmatrix}. \qquad (2.22)$$

For simplicity, we have been assuming here, that left and right leads are twins.[B]

The Green's function for an arbitrary device $\mathbf{H}^{\mathrm{device}}$ in the presence of the leads is readily found via matrix inversion:

$$\mathbf{G}(E) = \left[E\mathbb{1} - \mathbf{H}^{\mathrm{device}} - \boldsymbol{\Sigma}_{\mathrm{L}}^M(E) - \boldsymbol{\Sigma}_{\mathrm{R}}^M(E)\right]^{-1}. \qquad (2.23)$$

The Green's function $\mathbf{G}(E)$ thus found is used to compute the transmission coefficient (Eq. (2.8)) and the electron current density (Eq. (2.13), see Sec. 2.3 for details).

Technical remark: The construction of the self-energies does not make explicit reference to the device Hamiltonian $\mathbf{H}^{\text{device}}$. Therefore, as long as different devices share the same coupling matrices $\mathbf{V}_{\text{L/R}}$, they also share the same self-energies. Hence, it is computationally advantageous to store them on the hard disk. This technique was used, e.g., for treating AGNRs with different impurity configurations.

Absorbing boundary conditions

The decimation technique (DT) gives a numerically exact result for the self-energy. It is efficient with quasi-onedimensional wires and short range hopping.

In its standard implementation, DT is working with a (spatially) constant damping rate η_{dec}. In order to generate an effectively smooth lead density of states near the Fermi energy ε_{F}, its magnitude should somewhat exceed the level spacing Δ_M, i.e., $\eta_{\text{dec}} \gtrsim \Delta_M$. The level spacing decreases with the wire length, $\Delta_M \sim v_{\text{F}} 2\pi\hbar/(Ml)$, where v_{F} denotes the Fermi velocity and l the width of each slice.

For realistic modeling, the absorption should occur in the leads, i.e., sufficiently far away from the device. Therefore, a second requirement on η_{dec} is that it should be negligible near the contact to the device. Ideally, η_{dec} vanishes in the device region. Now, if the damping is taken to be spatially constant, then η_{dec} will be small everywhere, so M must be large to satisfy the inequality.

As in previous studies[97, 98, 106], we apply absorbing boundary conditions (ABC)[129] to work with a spatially varying η_{dec}. We include ABC in the DT with the replacement $\eta_{\text{dec}} \rightarrow \hat{\boldsymbol{\eta}}_{\text{ABC}}$ in Eq. (2.18), using a purely local damping

$$\hat{\boldsymbol{\eta}}_{\text{ABC}} = \eta(\mathbf{r})\,\delta(\mathbf{r} - \hat{\mathbf{r}})\,. \tag{2.24}$$

The leakage rate (or damping rate) $\eta(\mathbf{r})$ describes how electrons are adsorbed into the leads, and (as discussed) should be negligible near the device and increase smoothly in the leads. As suitable default parametrization for the leakage rate, we use

$$\eta(\mathbf{r}) = \eta_0\, \mathrm{e}^{-\kappa(L-d)}\,, \tag{2.25}$$

where κ is the damping coefficient and d denotes the distance between the device region and the absorption point $\mathbf{r}$ inside the reservoir.
(default values: $\eta_0 = 1\,\text{Ha} \approx 27.2\,\text{eV}$ and $\kappa = 16/L$ where L is total length of each lead$^{\text{C}}$)

When applying this method to DFT (cf. Sec. 2.2.1), we take advantage of the local basis set: the basis functions $|\tilde{\varphi}_i\rangle$ are centered at atoms sitting at position $\mathbf{r}_i$, and we approximate $\langle\tilde{\varphi}_j|\hat{\mathbf{r}}|\tilde{\varphi}_i\rangle \approx \mathbf{r}_i\delta_{ij}$, i.e., $\hat{\boldsymbol{\eta}}_{\text{ABC}}$ becomes a diagonal matrix.

Pictorial illustration: Fig. 2.3 shows an illustration of building the leads, applying the ABC via the damping rate $\eta_{\text{L/R}}$, and connecting the leads to the device.

Figure 2.3: Bottom: Schematic assembly of the total system for transport through an AGNR5 with one nitrogen substituent. It consists of left and right lead, and device region. For each lead, M equal building blocks $\mathbf{H}^{\text{block}}$ are connected using the coupling matrix $\mathbf{V}$. The device region already contains the beginning of each lead, represented by two contact regions (dashed blue box). Top: Schematic spatial dependence of the leakage rates $\eta(d)$ in the left and right lead as used for absorbing boundary conditions. Near and in the contact region the leakage rate is exponentially small (nearly zero).

Figure 2.4: Actual geometry in a DFT calculation of an impurity and a lead system showing the cutting procedure. The armchair graphene nanoribbons (carbon atoms in gray) are terminated with hydrogen (red). The upper system contains a single nitrogen atom (green) as impurity in the central device region.

2.1.4 Extension to systems with broken spin-rotational invariance

Most of this thesis deals with transport through systems with spin-rotational invariance. Nevertheless, including spin into the method is straightforward and we investigate the spin effects of small AGNRs in Chap. 5 (partly published in Ref. 111). For simplicity (and since it is sufficient for the following), we assume that the leads are spin-unpolarized. This is to be expected for AGNRs.[D] Formally, the block matrix $\mathbf{H}^{\text{block}}$ and therefore the self-energies $\mathbf{\Sigma}_{\text{L/R}}$ get spin-indices but are really spin-diagonal with identical spin blocks in both channels, i.e., $\mathbf{H}^{\text{block}}_{\sigma\sigma'} = \mathbf{H}^{\text{block}}\delta_{\sigma\sigma'}$, $\mathbf{\Sigma}^{\sigma\sigma'}_{\text{L/R}} = \mathbf{\Sigma}_{\text{L/R}}\delta_{\sigma\sigma'}$.

All non-trivial spin-physics is restricted to the device region. The spin-dependent device Hamiltonian $\mathbf{H}^{\text{device}}_{\sigma\sigma'}$ can contain non-diagonal elements, e.g., due to spin-orbit interaction. As a consequence, the Green's functions $\mathbf{G}_{\sigma\sigma'}$ and $\mathbf{G}^<_{\sigma\sigma'}$ also carry spin indices and contain non-diagonal spin elements.

The generalized transmission function, cf. Eq. (2.8),

$$\mathcal{T}(E) = \sum_{\substack{\sigma\sigma' \\ \tilde{\sigma}\tilde{\sigma}'}} \text{Tr}\{(\mathbf{\Gamma}_{\text{L}}\delta_{\sigma\tilde{\sigma}})\,\mathbf{G}_{\tilde{\sigma}\sigma'}\,(\mathbf{\Gamma}_{\text{R}}\delta_{\sigma'\tilde{\sigma}'})\,[\mathbf{G}^\dagger]_{\tilde{\sigma}'\sigma}\} = \sum_{\sigma\sigma'} \underbrace{\text{Tr}\{\mathbf{\Gamma}_{\text{L}}\,\mathbf{G}_{\sigma\sigma'}\,\mathbf{\Gamma}_{\text{R}}\,[\mathbf{G}^\dagger]_{\sigma'\sigma}\}}_{=:\mathcal{T}_{\sigma\sigma'}} = \sum_{\sigma\sigma'} \mathcal{T}_{\sigma\sigma'}\,,$$

(2.26)

can be dismantled into spin-conserving ($\mathcal{T}_{\uparrow\uparrow}$, $\mathcal{T}_{\downarrow\downarrow}$) and spin-flip ($\mathcal{T}_{\uparrow\downarrow}$, $\mathcal{T}_{\downarrow\uparrow}$) terms, see Chap. 5 for

the physical discussion. On the other hand, the total current density, cf. Eq. (2.13),

$$\mathbf{j}(\mathbf{r}, E) = \underset{\sigma}{\mathrm{Tr}} \underbrace{\frac{1}{2\pi} \frac{\hbar}{2m} \lim_{\substack{\mathbf{r}' \to \mathbf{r} \\ \sigma' \to \sigma}} (\boldsymbol{\nabla}_{\mathbf{r}'} - \boldsymbol{\nabla}_{\mathbf{r}}) G_{\sigma\sigma'}^{<}(\mathbf{r}, \mathbf{r}', E)}_{=:\mathbf{j}_\sigma} = \sum_{\sigma} \mathbf{j}_\sigma \,, \qquad (2.27)$$

can only be separated into spin up and spin down currents. The off-diagonal spin elements of $\lim_{\mathbf{r}' \to \mathbf{r}} (\boldsymbol{\nabla}_{\mathbf{r}'} - \boldsymbol{\nabla}_{\mathbf{r}}) G_{\sigma\sigma'}^{<}(\mathbf{r}, \mathbf{r}', E)$ do not have a (direct) physical interpretation. Please note that the spin up current $\mathbf{j}_\uparrow$ may vanish arbitrarily and reappear in the spin down current $\mathbf{j}_\downarrow$. Only the total current density $\mathbf{j} = \mathbf{j}_\uparrow + \mathbf{j}_\downarrow$ is conserved, i.e., the continuity equation holds true, $\boldsymbol{\nabla} \cdot \mathbf{j} = 0$.

Remark: Independent spin channels (collinear spin physics)

If the spin channels are effectively independent, as in case of a collinear open-shell DFT calculation, each molecular orbital is assigned to one of the two spin channels. No states with contributions from both spin channels are allowed. Thus, the spin-dependent device Hamiltonian $\mathbf{H}_{\sigma\sigma'}^{\mathrm{device}}$ contains only spin-diagonal elements which are usually different in both channels, i.e., $\mathbf{H}_{\sigma\sigma'}^{\mathrm{device}} = \mathbf{H}_\sigma^{\mathrm{device}} \delta_{\sigma\sigma'}$. All quantities then carry this single spin index. As a consequence, the whole calculation separates into two additive spin-independent calculations, one for the spin up channel ($\mathbf{H}^{\mathrm{device}} = \mathbf{H}_\uparrow^{\mathrm{device}}$) and one for spin down channel ($\mathbf{H}^{\mathrm{device}} = \mathbf{H}_\downarrow^{\mathrm{device}}$).

2.2 Density functional theory (DFT) based transport calculations

So far, the description of the method was general; the block matrices $\mathbf{H}^{\mathrm{block}}$, $\mathbf{V}$, and $\mathbf{H}^{\mathrm{device}}$ have not yet been specified. In this thesis, we base the atomistic description on density functional theory (DFT). [Please refer to Appx. B.2.1 for an overview on DFT.] Nevertheless, several other effective single particle descriptions of molecular films are compatible with this methodology, e.g., nearest-neighbor-tight-binding models and Hartree-Fock (HF).

For this thesis, I implemented the presented formalism in our transport module AITRANSS[97, 98]. It reconstructs the Kohn-Sham (KS) Hamiltonian $\mathbf{H}^{\mathrm{KS}}$ from KS orbitals which are given in terms of local basis functions. (See Appx. B.2.2 for details on the employed basis functions.) To keep the computational effort feasible, our implementation employs the massively parallelized *ab initio* package FHI-AIMS[130], whose scalability has already been demonstrated up to several thousand CPUs[130–133]. To preserve this scalability, shared-memory (via OpenMP) and distributed-memory (via MPI) parallelization approaches were implemented in our transport module (see Sec. 2.5 and Appx. B.3 for details). Our module is readily adapted to other electronic structure codes that deliverer all (occupied and virtual) eigenstates in terms of local basis functions, e.g., an interface to the TURBOMOLE package[134] has also been implemented and—whenever possible—we use TURBOMOLE to cross-check our results.

It should be noted that the KS-based Landauer-Büttiker formalism has been established to reproduce the exact (physical) conductance only in two model situations: for non-interacting particles and also in the presence of strong correlations, namely in the framework of the single impurity

Anderson model (SIAM)[121–125]. Our implementation aims at intermediate situations, with interaction effects that can be modelled qualitatively by effective local potentials and corresponding excitations with a single-particle nature. With this caveat, we expect the general *qualitative* features of our simulation results to be representative of the real physical system, in particular the tendencies to form ring currents or streamline patterns—while the actual flow pattern for a given atomic arrangement of device might somewhat deviate from our simulations. Nevertheless, one must be aware that there are special examples where KS transport fails, even qualitatively (e.g., see Ref. 135).

2.2.1 Construction of the (bulk) Kohn-Sham Hamiltonian

With DFT (as well as HF) a minor complication arises because the matrices $\mathbf{H}^{\text{block}}$, $\mathbf{V}$, and $\mathbf{H}^{\text{device}}$ refer to the electronic structure of a subsystem embedded in the infinite bulk. For systems with translational invariance, such as clean wires, the block matrices can be extracted from DFT calculations employing plane waves and periodic boundary conditions. In this way, $\mathbf{H}^{\text{block}}$ and $\mathbf{V}$ could be found.

In contrast, the device block $\mathbf{H}^{\text{device}}$ is not periodic and here a different procedure should be applied. We extract it from a DFT calculation performed for a finite sized system using local basis functions $|\varphi_i\rangle$. (For basis function details, see Appx. B.2.2.)

A schematic representation of the partitioning is depicted in Fig. 2.4 (top). In the spirit of Eq. (2.21), a part of the leads is also included in the device block $\mathbf{H}^{\text{device}}$ ("extended device block"). As said, in this way, the coupling matrices $\mathbf{V}_{\text{L/R}}$, which couple the surface of the extended device region to the electrodes, contain the same matrix elements as $\mathbf{V}$.

Due to our choice of a local basis set, the KS Hamiltonian of the whole finite sized system, which contains the extended device, exhibits a block-structure. The inner part resembles $\mathbf{H}^{\text{device}}$. The extensions have to be chosen long enough to ensure the convergence of $\mathbf{H}^{\text{device}}$. On a technical level, the procedure is as follows. The KS orbitals $|\psi_i^{\text{KS}}\rangle$ (with KS energies $\varepsilon_i^{\text{KS}}$) are represented by expansion coefficients $\tilde{c}_{ji}$ with respect to the orthogonal basis set $|\tilde{\varphi}_j\rangle$, i.e., $|\psi_i^{\text{KS}}\rangle = \sum_j |\tilde{\varphi}_j\rangle \tilde{c}_{ji}$. The number of molecular orbitals $|\psi_i^{\text{KS}}\rangle$ equals the number of basis functions, so that the expansion coefficients $\tilde{c}_{ji}$ form a square matrix. The orthogonal basis set $|\tilde{\varphi}_j\rangle$ is constructed from the non-orthogonal basis set $|\varphi_j\rangle$ of the underlying DFT calculation using Löwdin orthogonalization[136]: $|\tilde{\varphi}_i\rangle = \sum_j |\varphi_j\rangle [S^{-1/2}]_{ji}$ where S is the (symmetric) overlap matrix $S_{ij} = \langle \varphi_i | \varphi_j \rangle$, see Appx. B.4.1 for details.

The device region is associated with the subset of all basis functions $|\tilde{\varphi}_i\rangle$ that are localized on the atoms belonging to the device region. The device block Hamiltonian $\mathbf{H}^{\text{device}}$ is given by the matrix elements of the KS Hamiltonian

$$\hat{\mathcal{H}}_0^{\text{KS}} = \sum_n |\psi_n^{\text{KS}}\rangle \varepsilon_n^{\text{KS}} \langle \psi_n^{\text{KS}}| = \sum_{ij} |\tilde{\varphi}_i\rangle \mathbf{H}_{0,ij}^{\text{KS}} \langle \tilde{\varphi}_j| , \qquad (2.28)$$

with $\mathbf{H}_{0,ij}^{\text{KS}} = \sum_n \tilde{c}_{in} \, \varepsilon_n^{\text{KS}} \left[\tilde{c}^T \right]_{nj}$, restricted to the basis functions of the device region subset.

By following the same line of ideas, one can also extract the block Hamiltonians for the lead slices, $\mathbf{H}^{\text{block}}$ and $\mathbf{V}$, so that there is actually no need to employ a different set of computations with periodic boundary conditions. Specifically, one considers a piece of a homogeneous wire, see Fig. 2.4 (bottom), with left and right center slice and extensions to both sides. The corresponding KS Hamiltonian will again represent this situation in its block structure when expressed in the localized basis set $|\tilde{\varphi}_i\rangle$:

$$
\mathbf{H}^{\text{KS}} = \begin{pmatrix} \mathbf{H}^{\text{ext}} & \mathbf{V}^{\text{ext}} & 0 & 0 \\ \mathbf{V}^{\text{ext}\dagger} & \mathbf{H}^{\text{block}} & \mathbf{V} & 0 \\ 0 & \mathbf{V}^{\dagger} & \mathbf{H}^{\text{block}} & \mathbf{V}'^{\text{ext}} \\ 0 & 0 & \mathbf{V}'^{\text{ext}\dagger} & \mathbf{H}'^{\text{ext}} \end{pmatrix} . \tag{2.29}
$$

Once again, the blocks $\mathbf{V}$ and $\mathbf{H}^{\text{block}}$ of interest to us are given by the matrix elements of $\mathbf{H}^{\text{KS}}$ that are associated with the corresponding left and right subblocks (slices). Again, care has to be taken with the size of the extensions in order to ensure convergence of the center subblocks.[E]

2.2.2 Convergence tests: Kohn-Sham Hamiltonian & transmission coefficients

Kohn-Sham Hamiltonian

We present convergence tests that illustrate, how the KS blocks $\mathbf{H}^{\text{block}}$ and $\mathbf{V}$ converge with increasing length of the extension, i.e., with a growing distance of the center slices to the (left/right) system boundaries. To this end, we perform a single DFT run for a long piece of the lead electrode. The wire can be cut into slices and for each slice the diagonal block $\mathbf{H}^{\text{block}}_{[n]}$ (together with the coupling $\mathbf{V}_{[n]}$ to the neighboring blocks) can be extracted. The index n is a measure for the distance of the respective slice to the boundary. Slices sufficiently far away from the boundary ($n \to \infty$) exhibit the same block-elements. These blocks enter the decimation procedure.

As a specific example to illustrate the convergence behavior, we examine a pristine AGNR5 in a (spin-unpolarized) DFT calculation. For $n = 0, \ldots, 9$, we construct several block Hamiltonians $\mathbf{H}^{\text{block}}_{[n]}$ for slices which are n carbon rings away from the boundaries, see Fig. 2.5a. To quantify the deviation $\Delta\mathbf{H}$ between block Hamiltonians, we use two norms: the maximum norm $\|\Delta\mathbf{H}\|_{\text{max}}$ (referring to the maximal deviation in the corresponding matrix elements) and the Euclidean norm $\|\Delta\mathbf{H}\|_2$. As is seen in Fig. 2.5b, either norm rapidly converges to the bulk limit. In fact, we find that, e.g., $n = 9$ can be taken as a faithful approximation for the bulk block Hamiltonian, i.e. of one slice in the infinite 1D system ($n \to \infty$) and therefore we take it as our reference in Fig. 2.5b. We checked that the absolute convergence behavior for $\mathbf{V}$ is the same as for $\mathbf{H}^{\text{block}}$. (Data is not shown.)

Transmission coefficients

The matrix norms give an unbiased measure for the convergence of the block Hamiltonian. In the physical context, however, one is more interested in the convergence of observables, which may

(a) Extraction of $\mathbf{H}_{[n]}$

(b) Dependence of $\mathbf{H}_{[n]}$ on n
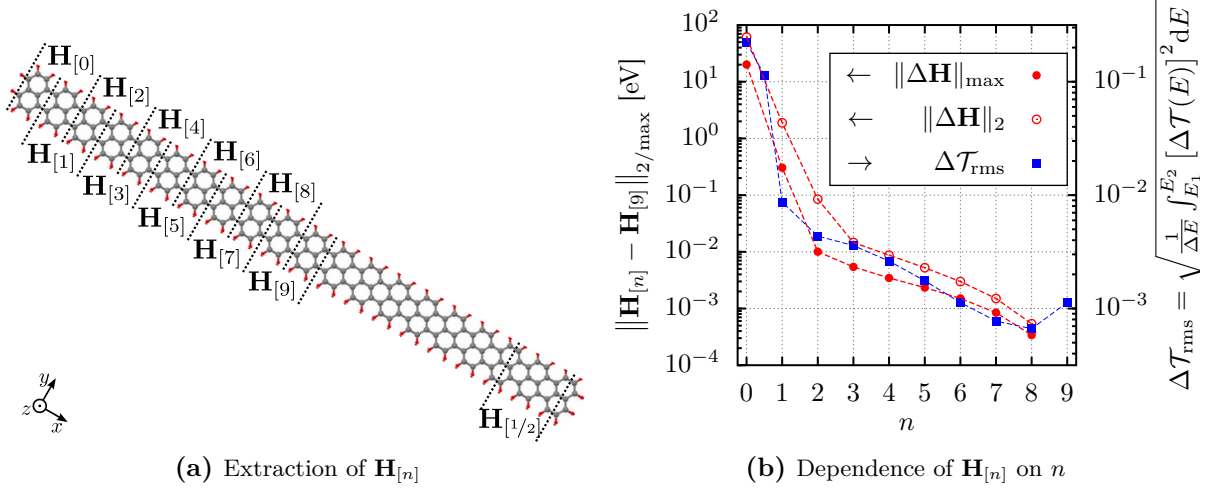
Figure 2.5: (a): Schematic extraction of the (pairwise overlapping) Hamiltonians $\mathbf{H}_{[n]}$ from an AGNR5 with a total length of 20 carbon rings. Each Hamiltonian $\mathbf{H}_{[n]}$ covers 2×2 carbon rings (28 atoms [20 C, 8 H] and 320 basis functions). n denotes the distance of the extracted subsystem to the border of the finite DFT system measured in carbon rings. [DFT details: FHI-AIMS, basis set `tier1`, closed-shell, 284 atoms [200 C, 84 H], 3220 basis functions]

(b): Dependence of the subsystem Hamiltonian $\mathbf{H}_{[n]}$ on its position in an pristine AGNR5 with 20 carbon rings in length. As matrix norms (left y-axis), we use the maximum norm $\|\Delta\mathbf{H}\|_{\max} = \max_{ij}(|\Delta\mathbf{H}_{ij}|)$ and the Euclidean norm $\|\Delta\mathbf{H}\|_2 = \sigma_{\max}$ where $\sigma_{\max}$ is the largest singular value of $\Delta\mathbf{H}$. The root mean square deviation $\Delta\mathcal{T}_{\mathrm{rms}}$ (right y-axis) is plotted to show differences in the transmission calculation, see Appx. B.5.1 for further details.

or may not be well represented by the unbiased measures that we have considered. Therefore, an independent check of the convergence of the transmission is indicated, as well.

To this end, we perform a series of transport simulations using the set $\mathbf{H}_{[n]}^{\mathrm{block}}$ to construct the corresponding sequence of self-energies. At the same time, $\mathbf{H}_{[n]}^{\mathrm{block}}$ is used as device Hamiltonian, i.e., $\mathbf{H}^{\mathrm{device}} = \mathbf{H}_{[n]}^{\mathrm{block}}$, $\mathbf{V}_{\mathrm{L}} = \mathbf{V}_{\mathrm{R}} = \mathbf{V}$. We calculate the deviation $\Delta\mathcal{T}(E)$ between the calculated transmission $\mathcal{T}(E)$ and its exact value, which is given by the number of bands of the infinite pristine AGNR5 at energy E (for bandstructure, cf. Fig. 2.6a). In Fig. 2.5b, we display the root mean square deviation $\Delta\mathcal{T}_{\mathrm{rms}}$, obtained by averaging $\Delta\mathcal{T}(E)$ over an energy interval $E_1 = \varepsilon_{\mathrm{F}} - 3\,\mathrm{eV}$ to $E_2 = \varepsilon_{\mathrm{F}} + 3\,\mathrm{eV}$ (for details on $\Delta\mathcal{T}_{\mathrm{rms}}$, cf. Appx. B.5.1).

Already at $n \geq 1$, the deviation in the transmission $\Delta\mathcal{T}_{\mathrm{rms}}$ drops below 10^{-2} and we see a regular convergence pattern. Hence, we conclude that very short extensions, actually only a single carbon ring wide, are sufficient in order to obtain quantitative transport coefficients in graphene ribbons.

To further illustrate the validity of our method, we also display the energy-resolved convergence behavior in Fig. 2.6b. Only near steps, small deviations (up to 0.05 eV) are discernible (see inset of Fig. 2.6b). The exact positions of steps are recovered with minimally larger blocks (2 and 3 rings). We thus confirm our previous results.

(a) Bandstructure

(b) Transmission function
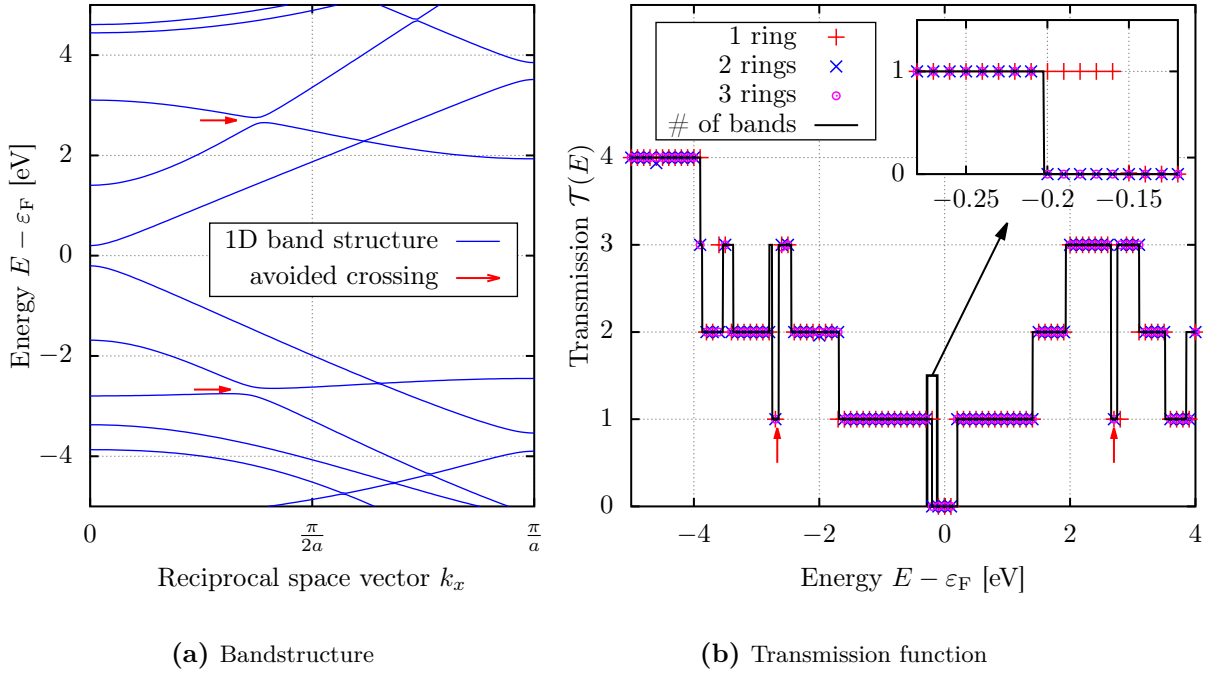
Figure 2.6: (a): Bandstructure of infinite one-dimensional pristine AGNR5 calculated with FHI-AIMS `tier1`. (b): Transmission function and number of bands for different sizes of $\mathbf{H}^{\text{block}}$ (using blocks with 1, 2, and 3 carbon rings in transport direction). Please note that the transmission calculation is even able to resolve the marked avoided crossings in the bandstructure. As required, the transmission functions drops by 2 in a small energy range at each avoided crossing.

Summarizing, we conclude that to achieve the numerical accuracy in the transport coefficients that we are after in this work, it is sufficient for us to work with blocks $\mathbf{H}^{\text{block}}$ and $\mathbf{V}$ containing only one carbon ring; further coupling matrix elements can be neglected.[F]

Remark on damping coefficients in $\hat{\eta}_{\text{ABC}}$: For the test calculations presented in Fig. 2.5b and Fig. 2.6b, the default parametrization for the leakage rate $\eta(\mathbf{r})$ (summarized after Eq. (2.25)) has been used. We have ensured that our conclusions do not change under a moderate variation of the damping rate and its spatial arrangement (cf. Appx. B.5.1). Specifically, when the leakage rate is sufficiently large ($\eta_0 \approx 0.1 - 1\,\text{Ha}$) and smoothly approaches zero near the device region ($\kappa L \approx 8 - 64$), the step-like transmission function is reproduced as long as the leads are long enough ($M \approx 50 - 200$). This is consistent with earlier works[129] for tight-binding models.

We mention that the number of building blocks M needs to be adjusted manually because it depends on the width of the graphene ribbon. As a rule of thumb, the total length of each lead should exceed its width at least by a factor of $L/W \approx 10 - 25$.[G]

2.3 Spatially resolved current density $\mathbf{j}(\mathbf{r})$

So far, we focused on global observables, like the transmission function $\mathcal{T}(E)$, that involve spatial averages, see Eq. (2.8). In this section, we discuss how to calculate spatially resolved observables, like the current density $\mathbf{j}(\mathbf{r})$.

2.3.1 Representation of the continuous current density using a finite basis set

As described in Eq. (2.13), the current density $\mathbf{j}(\mathbf{r}, E)$ is calculated as a spatial derivative of the Keldysh Green's function $G^<(\mathbf{r}, \mathbf{r}', E)$. Here, we explicitly evaluate $\mathbf{j}(\mathbf{r}, E)$ in terms of the local basis functions $\tilde{\varphi}_i(\mathbf{r})$, i.e.,

$$
\begin{aligned}
\mathbf{j}(\mathbf{r}, E) &= \frac{1}{2\pi} \frac{\hbar}{2m} \lim_{\mathbf{r}' \to \mathbf{r}} (\boldsymbol{\nabla}_{\mathbf{r}'} - \boldsymbol{\nabla}_{\mathbf{r}}) G^<(\mathbf{r}, \mathbf{r}', E) \\
&= \frac{1}{2\pi} \frac{\hbar}{2m} \lim_{\mathbf{r}' \to \mathbf{r}} (\boldsymbol{\nabla}_{\mathbf{r}'} - \boldsymbol{\nabla}_{\mathbf{r}}) \sum_{ij} \tilde{\varphi}_i(\mathbf{r}) \mathbf{G}^<_{ij} \tilde{\varphi}_j(\mathbf{r}') \\
&= \frac{1}{2\pi} \frac{\hbar}{m} \sum_{ij} \left[\tilde{\varphi}_i(\mathbf{r}) \underbrace{\frac{1}{2}\left(\mathbf{G}^<_{ij} - \mathbf{G}^<_{ji}\right)}_{=:\overset{\text{as}}{\mathbf{G}}{}^<_{ij}} \left(\boldsymbol{\nabla}\tilde{\varphi}_j(\mathbf{r})\right) \right] \\
&= \frac{1}{2\pi} \frac{\hbar}{m} \sum_{ij} \tilde{\varphi}_i(\mathbf{r}) \overset{\text{as}}{\mathbf{G}}{}^<_{ij} \left(\boldsymbol{\nabla}\tilde{\varphi}_j(\mathbf{r})\right),
\end{aligned}
\tag{2.30}
$$

where $\overset{\text{as}}{\mathbf{G}}{}^< := \frac{1}{2}(\mathbf{G}^< - [\mathbf{G}^<]^T)$ is an abbreviation for the anti-symmetric elements of the Keldysh Green's function. We employed that the basis functions $\tilde{\varphi}_i(\mathbf{r})$ are always real by construction (cf. Appx. B.2.2 for basis function details).

Other local quantities, like the non-equilibrium density $n(\mathbf{r}, E)$ or the local density of states $\rho(\mathbf{r}, E)$, are calculated in a similar fashion (see end of Appx. B.4.1).

Remarks on discretization errors due to finite basis set sizes: The physical current density must fulfill the continuity equation: $\boldsymbol{\nabla} \cdot \mathbf{j}(\mathbf{r}) = 0$ at all points $\mathbf{r}$. The basis sets we use (either numerical orbitals or Gaussian orbitals) are finite and thereby incomplete. Hence, the orthodox continuity equation is satisfied approximately and will be recovered only in the basis set limit.[H] Therefore, we monitor in our calculations the divergence

$$
\begin{aligned}
\boldsymbol{\nabla} \cdot \mathbf{j}(\mathbf{r}, E) =& \frac{1}{2\pi} \frac{\hbar}{m} \sum_{ij} \tilde{\varphi}_i(\mathbf{r}) \overset{\text{as}}{\mathbf{G}}{}^<_{ij} \left(\Delta\tilde{\varphi}_j(\mathbf{r})\right) \\
&+ \frac{1}{2\pi} \frac{\hbar}{m} \underbrace{\sum_{ij} \left(\boldsymbol{\nabla}\tilde{\varphi}_i(\mathbf{r})\right) \overset{\text{as}}{\mathbf{G}}{}^<_{ij} \left(\boldsymbol{\nabla}\tilde{\varphi}_j(\mathbf{r})\right)}_{=0 \text{ (due to symmetry)}},
\end{aligned}
\tag{2.31}
$$

and ensure that our observables are converged with respect to the size of the basis set.

Finite differences: The necessary derivatives of the basis functions $\varphi_i(\mathbf{r})$ are calculated numerically using a symmetric two-point rule ($\mathbf{e}_j$ are the canonical basis vectors):

$$\boldsymbol{\nabla}_j\varphi_i(\mathbf{r}) = (2\Delta)^{-1}\left[\varphi_i(\mathbf{r}+\Delta\mathbf{e}_j) - \varphi_i(\mathbf{r}-\Delta\mathbf{e}_j)\right], \tag{2.32}$$

$$\boldsymbol{\nabla}_j^2\varphi_i(\mathbf{r}) = \Delta^{-2}\left[\varphi_i(\mathbf{r}+\Delta\mathbf{e}_j) - 2\varphi_i(\mathbf{r}) + \varphi_i(\mathbf{r}-\Delta\mathbf{e}_j)\right].$$

We chose $\Delta = \sqrt[3]{\varepsilon}$, ($\varepsilon \approx 2.2\cdot10^{-16}$ being the double floating point machine precision), leading to accuracies in the order of 10^{-10} and 10^{-5} for first and second derivative, respectively.[I]

2.3.2 Convergence tests: basis size dependence of the current density

As a test, we investigate the local electron current density in pristine and functionalized AGNR5. For the physical discussion of the results, please refer to Chap. 3. We raster the current and divergence formulas, Eq. (2.30) and Eq. (2.31), on a Cartesian grid with a grid spacing of 0.1 Å. The eight grid corners of the grid cuboid are $(x, y, z) = (x_{\mathrm{max/min}}\pm1\,\text{Å}, y_{\mathrm{max/min}}\pm1\,\text{Å}, \pm4\,\text{Å})$, where $x_{\mathrm{max/min}}$ denote the maximal/minimal x-coordinate of any atom in the structure. All atoms are located in the $z = 0$ plane.

Pristine AGNR5

In Fig. 2.7, we show an electron current density map at $z = 0.4\,\text{Å}$. A perfect streamline pattern arises as a consequence of quantum confinement in the transverse direction (see Sec. 3.1 for the physical discussion). The plot illustrates the partitioning and how the current flow is generated in the NEGF approach. Within the left and right contact region (blue boxes), the self-energy $\boldsymbol{\Sigma}_{\mathrm{L/R}}$ is non-zero. Its anti-Hermitian piece generates the current flow, left source and right drain. Outside source and drain, the divergence of the current is seen to be very small and can be controlled by the size of the basis set, see Appx. B.5.2.

(a) $|\mathbf{j}_{xy}(\mathbf{r}, E)|$ (b) $\boldsymbol{\nabla}\cdot\mathbf{j}(\mathbf{r}, E)$
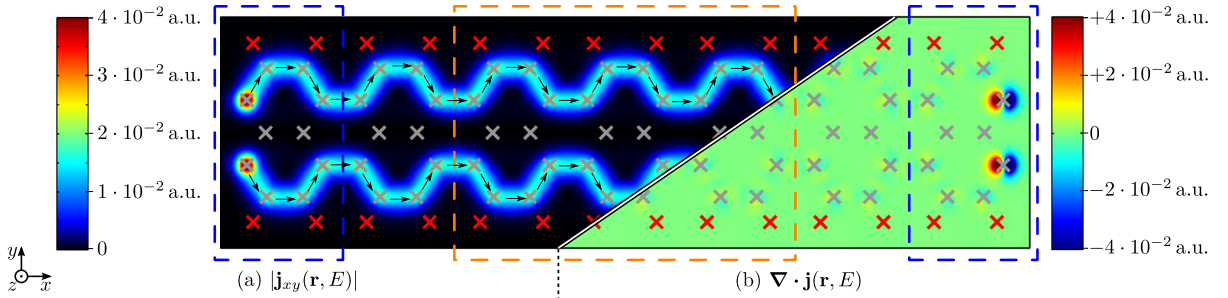
Figure 2.7: Inplane current density $\mathbf{j}_{xy}(\mathbf{r}, E)$ (left) and current divergence $\boldsymbol{\nabla}\cdot\mathbf{j}(\mathbf{r}, E)$ (right) for a pristine AGNR5 at $E = \varepsilon_{\mathrm{F}} + 1\,\text{eV}$, at a plane $z = 0.4\,\text{Å}$ above the carbon and hydrogen atoms (gray and red crosses, respectively). The current density carries one conductance quantum, $\mathcal{T}(E) = 1$; its direction is indicated by black arrows. The contact regions, where the self-energies representing the leads are added, are marked in dashed blue. In these areas, numerical artifacts are seen in the current density and in the divergence because the current appears from/disappears into the leads. The dashed orange box is used for further convergence tests, see Fig. 2.10 and Fig. 2.11. The arrows give the direction of the current density. [DFT details: FHI-AIMS, basis set `tier1`, closed-shell]

AGNR5 with a single nitrogen substituent

As next test, one carbon atom near the border of the AGNR5 is substituted by nitrogen, cf. Fig. 2.2. The latter then acts as a strong scatterer. The atomistic equilibrium structure of the graphene lattice is hardly distorted and in particular stable against out of plan perturbation (see Sec. 3.2 for the physical discussion).

First, we note that the dependence of the transmission function on the basis set size is weak, see Fig. 2.8. We compare closed-shell calculations (with fractional occupation numbers using FHI-AIMS) with the majority spin channel (α) of collinear open-shell calculations (with integer occupation numbers using TURBOMOLE). Indeed, we observed a good collapse of all data curves.[J] The main differences are small shifts in energy. As example, the energy points with $\mathcal{T}(E) = 0.5$ are marked with colored arrows.

In Fig. 2.9, we investigate the dependence of the current density on the basis set size. For a proper comparison, we need to account for the small energy shifts of the KS Hamiltonian due to the variation in the basis set size. Accordingly, we compare the current pattern based on the principle that we fix the transmission (rather than the energy) when going from a current pattern obtained for one basis set to the next one.

We observe a very rapid convergence of the current pattern. Only the divergence of the current exhibits a significant quantitative flow. For increasing basis set size (`tier1` to `tier2`), the divergence decreases rapidly. Note, that the basis sets SVP and `tier1` are of equal size but differently constructed, and therefore their divergence pattern also differ slightly.

An additional check is to calculate the current density integrated over a cross section at fixed x in the yz-plane, $I_x(x) = \iint j_x(\mathbf{r}, E)\, \mathrm{d}y\, \mathrm{d}z$, and compare it to the total current $\frac{e^2}{h}\,\mathcal{T}(E)$ (per energy
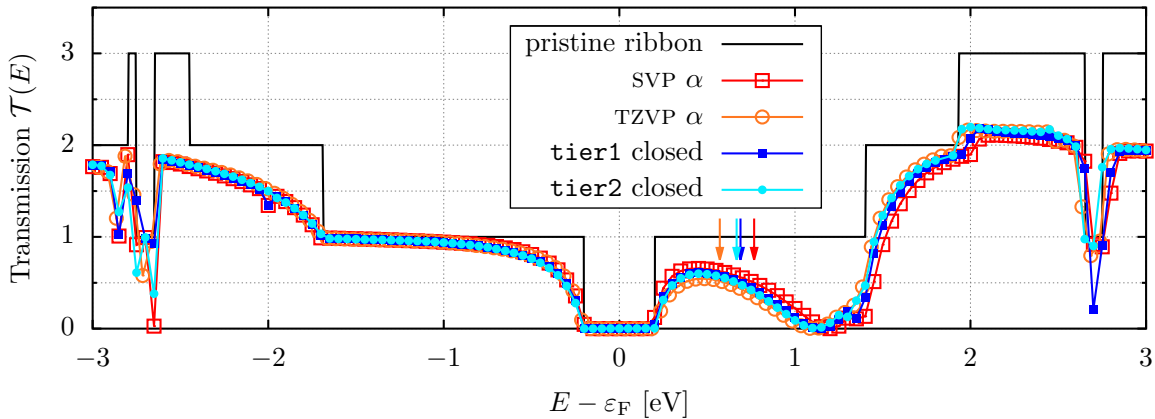
Figure 2.8: Transmission function depending on basis set size and on spin treatment (open-shell vs. closed-shell calculation). The main differences are small shifts in energy. As example, the energy points with $\mathcal{T}(E) = 0.5$ are marked with colored arrows. TURBOMOLE: only α-channel of an open-shell calculation in SVP and TZVP basis set; FHI-AIMS: closed-shell calculation in `tier1` and `tier2` basis set.

(a) $|\mathbf{j}_{xy}(\mathbf{r}, E)|$ – TURBOMOLE SVP α

(b) $|\mathbf{j}_{xy}(\mathbf{r}, E)|$ – FHI-AIMS `tier1`

(c) $|\mathbf{j}_{xy}(\mathbf{r}, E)|$ – FHI-AIMS `tier2`

(d) $\boldsymbol{\nabla} \cdot \mathbf{j}(\mathbf{r}, E)$ – TURBOMOLE SVP α

(e) $\boldsymbol{\nabla} \cdot \mathbf{j}(\mathbf{r}, E)$ – FHI-AIMS `tier1`

(f) $\boldsymbol{\nabla} \cdot \mathbf{j}(\mathbf{r}, E)$ – FHI-AIMS `tier2`
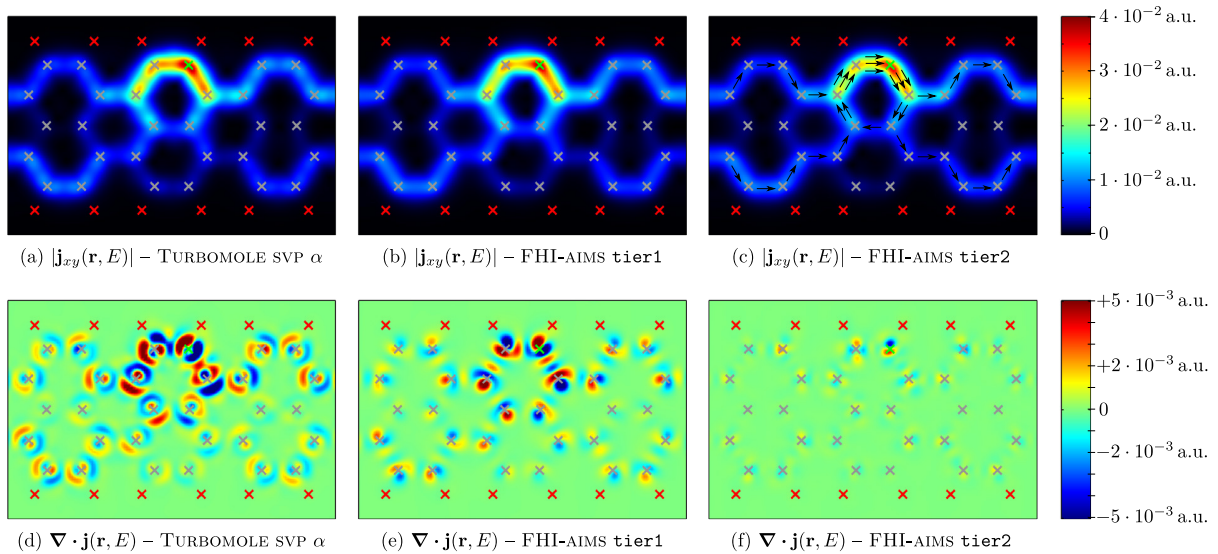
Figure 2.9: (a)-(c): Variation of the in-plane current density $\mathbf{j}_{xy}(\mathbf{r}, E)$ with increasing size of the basis set for an AGNR5 with one nitrogen substituent (green cross) at a plane $z = 0.4\,\text{Å}$ above the carbon atoms restricted in x-direction to the central region near the nitrogen impurity (dashed orange box in Fig. 2.7). The current density carries half a conductance quantum, $\mathcal{T}(E) = 0.5$, in all cases; the energy E is varied such that all plots share the same transmission value, see colored arrows in Fig. 2.8 for exact position. The current direction is indicated by black arrows for the largest basis set. (d)-(f): The divergence $\boldsymbol{\nabla} \cdot \mathbf{j}(\mathbf{r}, E)$ belonging to the respective current pattern in (a)-(c). The divergence converges very rapidly with increasing size of the basis set. Divergence errors have a very small impact on the current pattern.
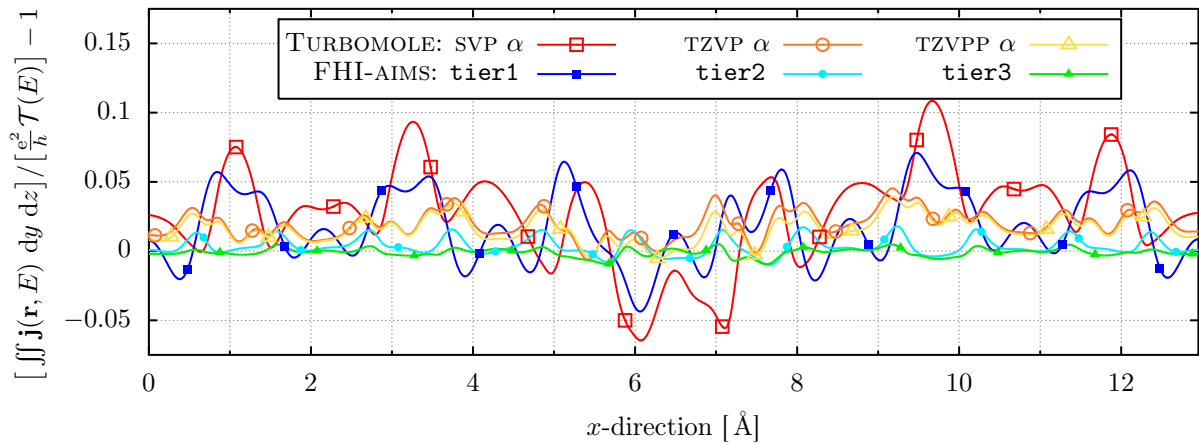
Figure 2.10: Relative deviation between the local current density integrated over a yz-plane and the total current given by the transmission function. The x-position of the integration plane is measured from the left side of the dashed orange box shown in Fig. 2.7, coinciding with the plot range of Fig. 2.9. Also, as in Fig. 2.9, the transmission is fixed at $\mathcal{T} = 0.5$. For clarity, only the markers of every 12th sampling point are shown.

and spin). The latter we have fixed by our choice to select the energy. The ratio of both, $I_x/[\frac{e^2}{h}\mathcal{T}]$, should be unity and its deviation is reproduced in Fig. 2.10 as function of x. The deviation from unity is small, with an amplitude that reduces rapidly with increasing basis set size.

Convergence tests for the current density: In Fig. 2.11, we show the current pattern deviation ($\Delta_{\mathbf{j}}$), the current divergence ($\Delta_{\boldsymbol{\nabla}\cdot\mathbf{j}}$), and the comparison to transmission ($\Delta_{\mathcal{T}}$). All three are formulated as root mean square errors:

$$\Delta_{\mathbf{j}} = \sqrt{\frac{1}{V}\int \mathrm{d}^3\mathbf{r}\left|\mathbf{j}(\mathbf{r},E) - \mathbf{j}_{\mathrm{largestBasis}}(\mathbf{r},E)\right|^2}\,, \tag{2.33}$$

$$\Delta_{\boldsymbol{\nabla}\cdot\mathbf{j}} = \sqrt{\frac{1}{V}\int \mathrm{d}^3\mathbf{r}\left(\boldsymbol{\nabla}\cdot\mathbf{j}(\mathbf{r},E)\right)^2}\,, \tag{2.34}$$

$$\Delta_{\mathcal{T}} = \sqrt{\int \frac{\mathrm{d}x}{L_x}\left(I_x/\left[\frac{e^2}{h}\mathcal{T}(E)\right] - 1\right)^2}\,, \tag{2.35}$$

with $I_x = \iint j_x(\mathbf{r},E)\,\mathrm{d}y\,\mathrm{d}z$. In case of the current pattern, an exact reference solution is not available, so we have to resort to the current pattern calculated using the largest basis set (`tier3` using FHI-AIMS) for comparison. The spatial integrals are done by summing over the same grid points which have been used for calculating the local currents, as described in the beginning of Sec. 2.3.2, restricting the x-integration further to the (dashed orange) central part of the device region, cf. Fig. 2.7.[K]
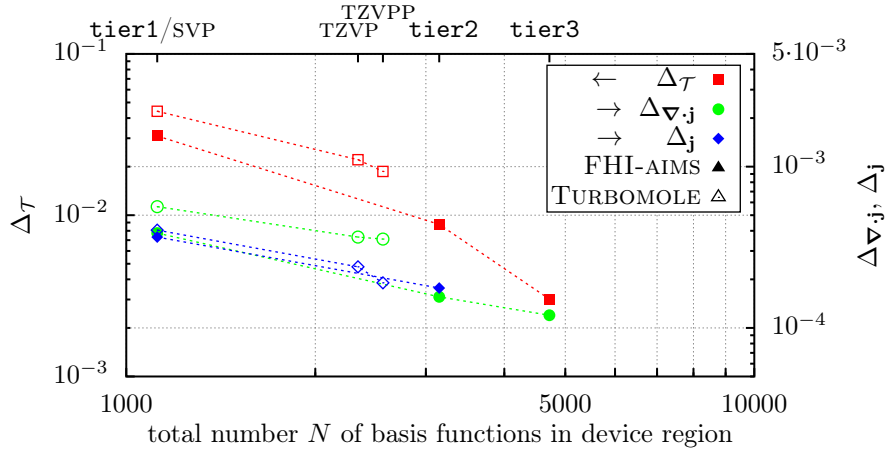
Figure 2.11: Convergence analyses of the local currents shown in Fig. 2.9 with respect to the basis set using FHI-AIMS (closed markers) and TURBOMOLE (open markers). The root mean square deviations Δ_X are plotted over the number of basis functions per carbon atom ($\Delta_{\mathcal{T}}$ on left y-axis; $\Delta_{\mathbf{j}}$ and $\Delta_{\boldsymbol{\nabla}\cdot\mathbf{j}}$ on right y-axis). All error measures decrease when increasing the basis set size. The different basis set contains different number of basis functions per hydrogen/carbon/nitrogen atom: `tier1`/SVP: 5/14/14; TZVP: 6/31/31; TZVPP: 14/31/31; `tier2`: 15/39/39: `tier3`: 31/55/55.

All three error measures decrease when increasing the basis set size, irrespective of the underlying DFT code. Interestingly, the error measures for the transmission ($\Delta_{\mathcal{T}}$) and for the divergence ($\Delta_{\nabla \cdot \mathbf{j}}$) are, for the same basis set size, always smaller using FHI-AIMS basis sets compared to TURBOMOLE basis sets.

The results of this section are encouraging, because they suggest that the local current density is an observable that rapidly converges with the size of the basis set. Already the smallest sets, SVP/`tier1`, allow for quantitative results.

AGNR41 with 20% hydrogen adsorbates

We now apply the presented method to larger systems, namely the AGNR41 shown in Fig. 2.12 functionalized with 20% hydrogen. For the physical discussion of the current vortices seen there, please refer to Chap. 4. Here, we cover important technical details, e.g., the convergence behavior with the basis set size.

Current patterns: Fig. 2.13 displays the current pattern of the large, mesoscopic sample for two different basis sets, `tier1` and `tier2`. The visible deviations are located near the left/right boundaries with values at the lower end of the logarithmic colorscale (dark blue). In the upper three orders of magnitude, the current density is virtually identical.

Transmission function: In Fig. 2.14, also the transmission functions corresponding to the current patterns are shown. At the energy chosen for Fig. 2.13, $E=\varepsilon_{\mathrm{F}}-635\,\mathrm{meV}$ (orange arrow),
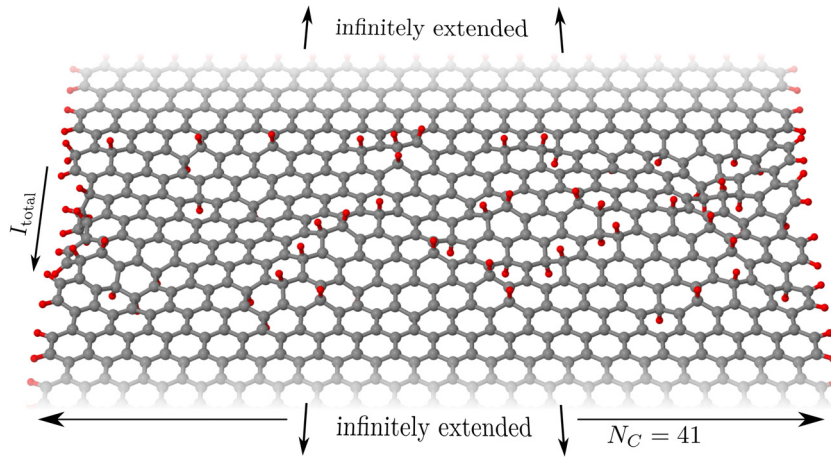
Figure 2.12: Atomic structure of a wide hydrogen-terminated armchair graphene nanoribbon (8×41) with $N_C = 41$ carbon atoms in transverse direction (AGNR41). The nanoribbon has been functionalized with additional 20% hydrogen atoms (additional 66 hydrogen atoms). Imagine a bias voltage being applied between the (infinitely extended) upper and lower leads so that a current flows across the device.

(a) basis set: `tier1`

(b) basis set: `tier2`
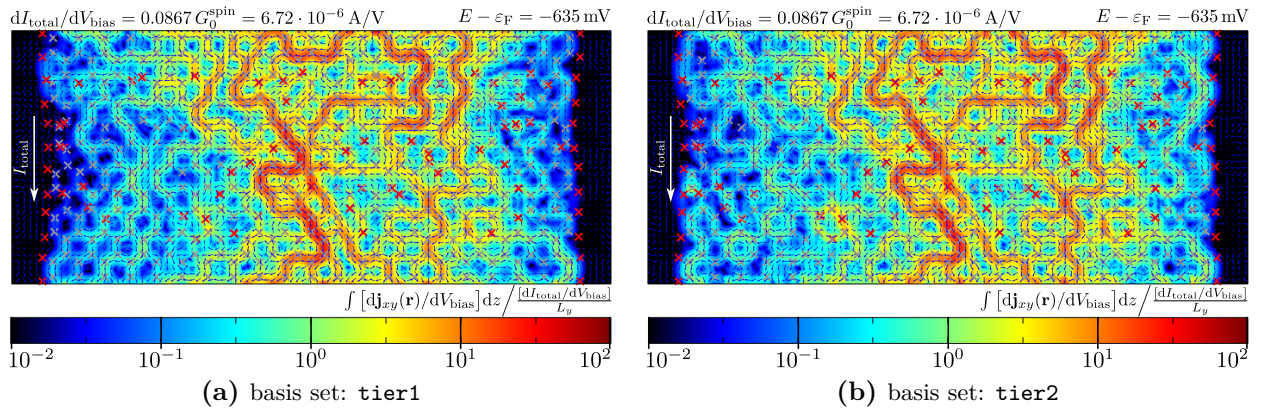
Figure 2.13: Basis set comparison of the local current density response (integrated over the out-of-plane direction) in the AGNR41 of Fig. 2.12 at energy $E=\varepsilon_F-635\,\text{meV}$ (orange arrow in Fig. 2.14). The current exhibits very strong mesoscopic fluctuations which exceed the average current by two orders of magnitude in the logarithmic color scale. The current density is plotted relative to average current density I/L_y, with width $L_y = 5.19\,\text{nm}$. Plot shows current amplitude (color), current direction (arrows), carbon atoms (gray crosses) and hydrogen atoms (red crosses).
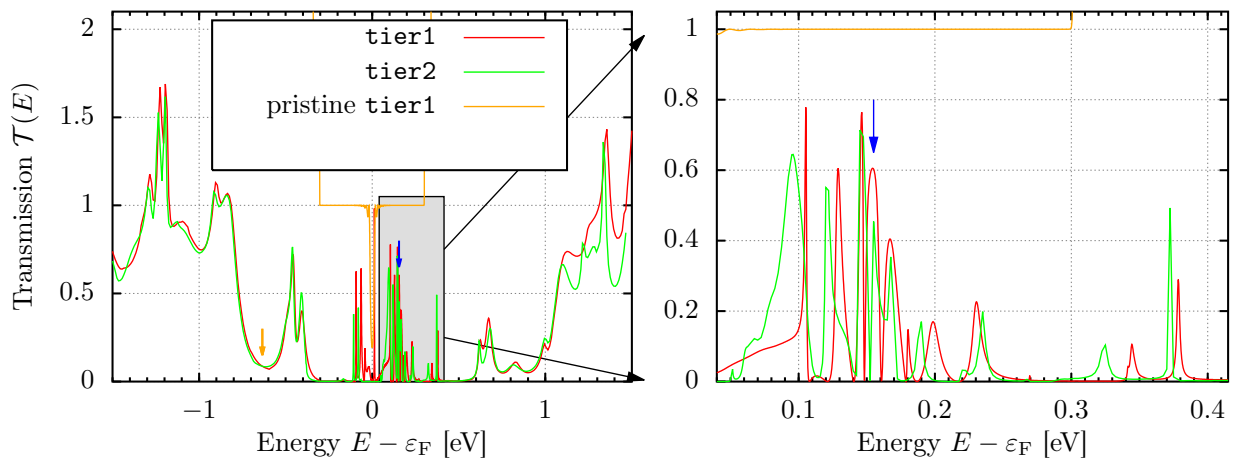
Figure 2.14: Transmission of the AGNR41 shown in Fig. 2.12 comparing the basis set convergence (`tier1` vs. `tier2`) of the relaxed structure with the deviation to the distorted (unrelaxed) structure with a `tier1` basis set. Additionally, the number of channels of the pristine AGNR41 is shown (orange).

the transmission is well converged, as was to be expected. For different energies slightly larger deviations can be seen, that are mostly to be interpreted as small shifts of the resonance energies. Only in the relatively dense region of the spectrum, these shifts can become comparable to the level spacing, so that larger deviations occur. In these regions, differences in the current patterns can occur (see Appx. B.5.4 for current pattern at $E = \varepsilon_F + 155\,\text{meV}$, blue arrow in Fig. 2.14).

We conclude, that a `tier1` basis set already gives a qualitatively reliable transmission function, but for resolving the fine structure of the transmission a larger basis set is required.

2.4 Magnetic field $\mathrm{B(r)}$ induced by the local current density

Additionally to the local current density (which is not easy to measure in actual experiments), we can calculate the induced magnetic field $\mathbf{B}(\mathbf{r})$ and the vector potential $\mathbf{A}(\mathbf{r})$ that accompanies the dc-current flow. The magnetic fields can feed back into the current flow itself (see Chap. 6). But also, the magnetic fields could potentially be detected in experimental setups that allow to perform a measurement of the nuclear magnetic resonance (NMR) in the presence of the current flowing (see Sec. 4.1.4).

2.4.1 Implementation of the law of Biot-Savart

The integrals in Eq. (2.16) for the magnetic field $\mathbf{B}$, the vector potential $\mathbf{A}$ and the magnetic moment $\mathbf{m}$ are readily evaluated on a properly chosen Cartesian grid with grid spacing δ, which was already used to raster the current density $\mathbf{j}(\mathbf{r})$ in the device region:

$$\mathbf{m} = \frac{\delta^3}{2} \sum_{\mathbf{r}} (\mathbf{r} - \mathbf{O}) \times [-\mathbf{j}(\mathbf{r})] \,, \tag{2.36}$$

$$\mathbf{B}(\mathbf{r}) = \alpha^2 \delta^3 \sum_{\substack{\mathbf{r}' \\ \mathbf{r}' \neq \mathbf{r}}} \frac{[-\mathbf{j}(\mathbf{r}')] \times (\mathbf{r} - \mathbf{r}')}{|\mathbf{r} - \mathbf{r}'|^3} \,, \tag{2.37}$$

$$\mathbf{A}(\mathbf{r}) = \alpha^2 \delta^3 \left[\sum_{\substack{\mathbf{r}' \\ \mathbf{r}' \neq \mathbf{r}}} \frac{[-\mathbf{j}(\mathbf{r}')]}{|\mathbf{r} - \mathbf{r}'|} + \frac{\zeta\,[-\mathbf{j}(\mathbf{r})]}{\delta} \right] \,, \tag{2.38}$$

where we replaced $\frac{\mu_0}{4\pi}$ by the squared fine-structure constant α^2, reflecting the atomic units used in the calculations. (The minus sign reflects the negative electron charge). As usual, the definition of the dipole moment makes explicit reference to the origin of the coordinate system, $\mathbf{O}$. In order to eliminate spurious contributions to $\mathbf{m}$ originating from the leads, we chose for $\mathbf{O}$ the center of the integration box. For the magnetic field integral, the sum over $\mathbf{r}'$ explicitly omits the singular point $\mathbf{r} = \mathbf{r}'$. It does not contribute, because the angle integration of $\mathbf{j}(\mathbf{r}') \times (\mathbf{r} - \mathbf{r}')$ vanishes in the cubic volume element with center $\mathbf{r}$.

For the vector potential, we treat the cube with center $\mathbf{r}$ analytically, the singularity can be integrated to

$$\int\limits_{-\delta/2}^{+\delta/2} \int\limits_{-\delta/2}^{+\delta/2} \int\limits_{-\delta/2}^{+\delta/2} \frac{\mathrm{d}x\,\mathrm{d}y\,\mathrm{d}z}{\sqrt{x^2+y^2+z^2}} = \delta^2 \underbrace{\int\limits_{-1/2}^{+1/2} \int\limits_{-1/2}^{+1/2} \int\limits_{-1/2}^{+1/2} \frac{\mathrm{d}x\,\mathrm{d}y\,\mathrm{d}z}{\sqrt{x^2+y^2+z^2}}}_{=:\zeta} = \delta^3 \frac{\zeta}{\delta} \tag{2.39}$$

where ζ is the grid-spacing independent integral, $\zeta = \frac{1}{2}[3\ln(7 + 4\sqrt{3}) - \pi] \approx 2.380$.
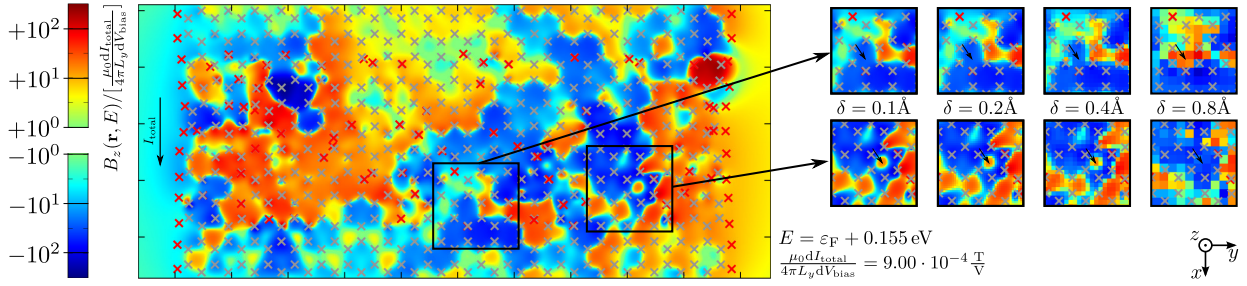
Figure 2.15: Convergence of the magnetic field distribution (in out-of-plane direction at z=0) induced by the current distribution at energy E=ε_F+155 meV (blue arrow in Fig. 2.14; cf. Appx. B.5.4, Fig. B.10). The magnetic field strongly varies and changes sign from region to region. On the right side, the convergence of the magnetic field with respect to the grid spacing δ is shown. Note how some features (marked by black arrow) simply vanish when employing a too coarse grid, e.g. $\delta = 0.8\,\text{Å}$.
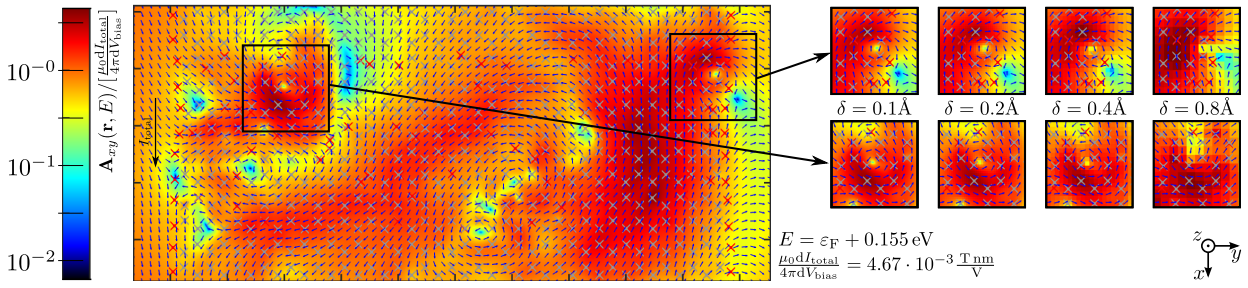
Figure 2.16: Convergence of the vector potential (in-plane components at z=0) induced by the current distribution at energy E=ε_F+155 meV (blue arrow in Fig. 2.14; cf. Appx. B.5.4, Fig. B.10). On the right side, the convergence of the vector potential with respect to the grid spacing δ is shown. The spatial average was removed before plotting, i.e., $\mathbf{A} - \langle \mathbf{A} \rangle$ is plotted.

2.4.2 Convergence tests: grid spacing dependence of the magnetic field

As with any discretization, the magnetic field $\mathbf{B}(\mathbf{r})$, the vector potential $\mathbf{A}(\mathbf{r})$ and the magnetic moment $\mathbf{m}$ carry a residual dependence on the grid spacing δ, that vanishes in the continuum limit $\delta \to 0$.

Magnetic field & vector potential pattern

In Fig. 2.15 and Fig. 2.16, the grid dependence of the spatial pattern of the magnetic field and the vector potential is displayed: $\mathbf{B}(\mathbf{r}, E$=ε_F+155 meV) and $\mathbf{A}(\mathbf{r}, E$=ε_F+155 meV), cf. blue arrow in Fig. 2.14. One convinces oneself that at grid spacings $\delta \lesssim 0.2\,\text{Å}$), both, the magnetic field and the vector potential are converged. For coarser grids, features (arbitrarily) vanish from the calculated fields.

Global deviations

In order to obtain more quantitative information, we also consider the discretization error for quantities that average over the entire sample.

The magnetic moment, associated with the magnetic field shown in Fig. 2.15, is $\mathbf{m}_{\delta=0}(E) = (0.03, -0.01, -1.51)\,\mu_{\mathrm{B}}/\mathrm{V}$ (extrapolated for $\delta \to 0$). In Fig. 2.17, we show the relative root mean square deviation of the magnetic moment and how it converges when taking the continuum limit.

$$\Delta_{\mathbf{m},\mathrm{rel}}(\delta) = \frac{\sqrt{\left|\mathbf{m}_\delta(E) - \mathbf{m}_{\delta=0}(E)\right|^2}}{\sqrt{\left|\mathbf{m}_{\delta=0}(E)\right|^2}} \,. \tag{2.40}$$

As is seen there, the magnetization rapidly converges reaching accuracies better than 1% at $\delta \lesssim 0.2\,\text{Å}$. Data for a similar convergence test for the magnetic field $\mathbf{B}(\mathbf{r})$ with

$$\Delta_{\mathbf{B},\mathrm{rel}}(\delta) = \frac{\sqrt{\frac{1}{V}\int_\delta \mathrm{d}^3\mathbf{r}\left|\mathbf{B}_\delta(\mathbf{r}, E) - \mathbf{B}^{\mathrm{finestGrid}}(\mathbf{r}, E)\right|^2}}{\sqrt{\frac{1}{V}\int_\delta \mathrm{d}^3\mathbf{r}\left|\mathbf{B}^{\mathrm{finestGrid}}(\mathbf{r}, E)\right|^2}} \,, \tag{2.41}$$

are also displayed in Fig. 2.17. In order to reduce the numerical effort, here the reference point is taken to be the calculation with the finest computational feasible grid, being $\delta^{\mathrm{finestGrid}}{=}0.1\,\text{Å}$ for $\mathbf{B}(\mathbf{r})$. The symbol $\int_\delta$ indicates a summation over the grid with spacing δ. At $\delta \lesssim 0.2\,\text{Å}$, the relative discretization error drops below 10% which we feel is acceptable given that the raw data spread over four orders of magnitude.
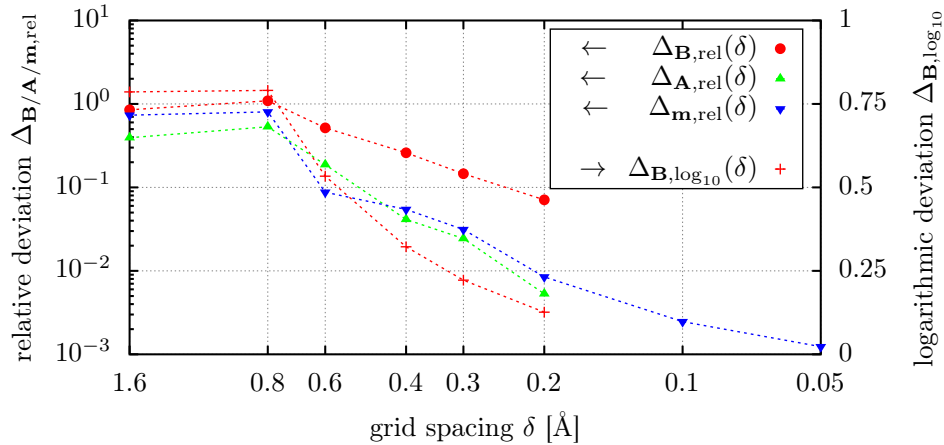
Figure 2.17: The relative mean root square (left y-axis) of the magnetic field $\mathbf{B}(\mathbf{r}, E{=}\varepsilon_{\mathrm{F}}{+}155\,\mathrm{meV})$, the vector potential $\mathbf{A}(\mathbf{r}, E{=}\varepsilon_{\mathrm{F}}{+}155\,\mathrm{meV})$, and the magnetic moment $\mathbf{m}(E{=}\varepsilon_{\mathrm{F}}{+}155\,\mathrm{meV})$ depending on the grid spacing δ. The grid spacing is used for both, rastering the current, and integrating over space. Additionally, the logarithmic deviation (right y-axis) of the magnetic field is shown.

An analogous relative error measure for the vector potential, $\Delta_{\mathbf{A},\text{rel}}(\delta)$, shows that the vector potential converges even faster, dropping below 1% for $\delta \lesssim 0.2\,\text{Å}$.

In order to better account for the logarithmically broad distribution in magnetic field strengths, we introduce a logarithmic measure for the discretization error,

$$\Delta_{\mathbf{B},\log_{10}}(\delta) = \sqrt{\frac{1}{V}\int_{\delta}\mathrm{d}^3\mathbf{r}\sum_{i=1}^{3}\left|\log_{10}\left[\mathbf{B}_i(\mathbf{r},E)/\mathbf{B}_i^{\text{finestGrid}}(\mathbf{r},E)\right]\right|^2}, \qquad (2.42)$$

effectively a root mean square error for the exponents. Again, there is a clear convergence behavior, see Fig. 2.17. Already at $\delta \lesssim 0.3\,\text{Å}$, the logarithmic deviation falls below a quarter decade, so that deviations are hardly visible in logarithmic plots like Fig. 2.15.

2.5 Performance measurements: scaling and parallelizability

In our DFT calculations of larger systems exceeding thousand carbon atoms, we rely on FHI-AIMS. It uses the ELPA[133] package tuned for petaflop-applications to solve the Kohn-Sham eigenvalue problem on massive parallel computer clusters. The scalability of FHI-AIMS has been shown by the maintainers[130]. Therefore, we restrict ourselves to the discussion of the performances of our new transport module; the KS states of the DFT reference calculation and the eigenvector representation of the corresponding overlap matrix S are assumed to be given and stored on the hard disk in a HDF5-file[137].

The observables we consider for benchmarking are the transmission $\mathcal{T}$, and the current density $\mathbf{j}(\mathbf{r})$; our test systems are hydrogen saturated AGNRs of 4 different sizes, see Fig. 2.18. Further parameters: `tier1` basis set (14 basis functions per C; 5 per H), self-energy is iterated $M = 200$ times and the resolution of the real space grid was δ=0.2 Å, with 31 lattice points in z-direction. Performance checks were carried out at the High Performance Computing Center Stuttgart (HLRS)
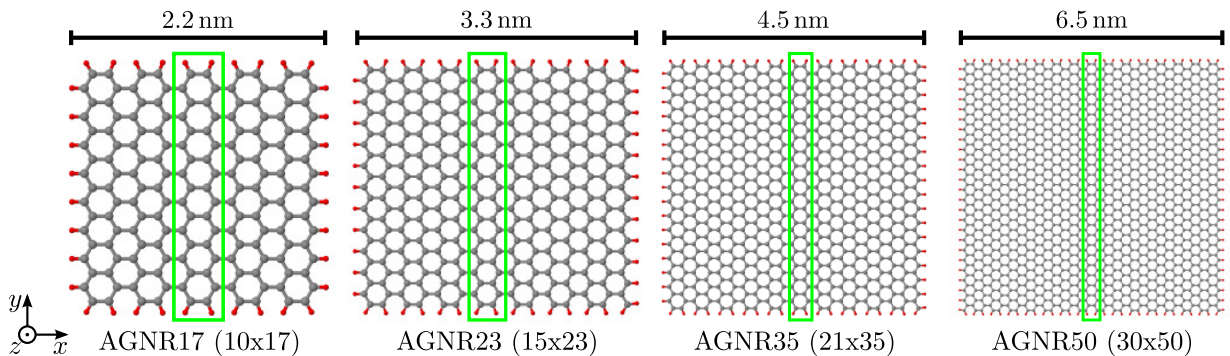
Figure 2.18: AGNRs used for benchmarking from left to right: 170 carbon atoms (10×17), 345 (15×23), 735 (21×35) and 1500 (30×50). The size of the block $\mathbf{H}^{\text{block}}$ used to build the lead is marked in green (one carbon ring in transport direction); the whole system (including hydrogen termination) is used as device $\mathbf{H}^{\text{device}}$.

on the CRAY XE6 (Hermit) cluster. Each node is equipped with $2 \cdot 16 = 32$ cores (Dual Socket AMD Interlagos @ 2.3GHz 16 cores) with 1–2 GiB RAM per core. The nodes are connected by a fast interconnect, the CRAY Gemini interconnect technology.

Scaling of computational time and memory: Fig. 2.19a displays how the memory ($\mathcal{M}$) and CPU-time (T) requirements scale with the system size parametrized by the number of basis functions, N. As is seen from the fits,[L] the memory requirement scales with N^2 (number of elements in the Green's functions). The computational time for the current calculation also scales like a second order polynomial in N (and not third order) because the overlap of basis functions at different atoms is negligible beyond a distance that exceeds several bond lengths.

Parallelizability: The data presented in Fig. 2.19a has been obtained with a single MPI process ($N_{\mathrm{MPI}} = 1$) parallelized using threads on $p = 32$ CPU cores. We now report about the speedup that we achieve using MPI to run several processes (each combining $p = 8$ CPU cores) on different computational nodes. Then, the wall time (total real world calculation time) $T_{N_{\mathrm{MPI}}}$ decreases with the number of processes N_{MPI}; ideally, it is inversely proportional to it.

(a) Computational cost

(b) Scaling behaviour
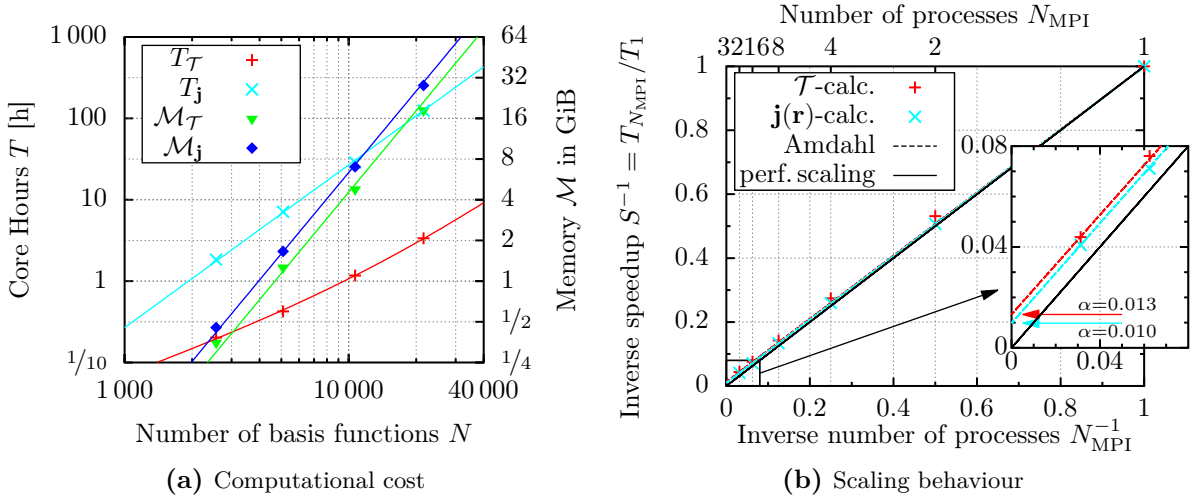
Figure 2.19: (a): Left axis: Core hours (wall time times number of CPU cores) $T_{\mathcal{T}}$ and $T_{\mathbf{j}}$ for calculating transmission $\mathcal{T}$ and current density $\mathbf{j}$ per energy point (average value for 128 energy points), respectively. Right axis: The corresponding memory requirements $\mathcal{M}_{\mathcal{T}}$ and $\mathcal{M}_{\mathbf{j}}$. The solid lines are the following fits (with $n = N/10\,000$): $T_{\mathcal{T}} = (0.660n + 0.409n^2)\,$h, $T_{\mathbf{j}} = 26.8n^2\,$h, $\mathcal{M}_{\mathcal{T}} = 4.55n^2\,$GiB, $\mathcal{M}_{\mathbf{j}} = 6.37n^2\,$GiB.

(b): Scaling behavior when using N_{MPI} processes, each using $p = 8$ cores, which communicate via MPI with each other. For an AGNR35 (21×35) containing $N = 10675$ basis functions, $n_E = 128$ transmission values and $n_E = 32$ current densities have been calculated, ensuring that every process can calculate on a separate energy point. The (theoretical) perfect scaling $S(P) = P$ is shown in solid black. This benchmark employs up to 256 CPU cores.

In Fig. 2.19b, we plot the reduction factor (inverse speedup) $S^{-1} = T_{N_{\mathrm{MPI}}}/T_1$ over the inverse number of MPI processes, N_{MPI}^{-1}. According to Amdahl's law $S^{-1} = [\alpha + (1-\alpha)/N_{\mathrm{MPI}}]$ the "serial fraction" of the code, i.e., the saturation α, can be estimated (α is the remaining value in the inset of Fig. 2.19b for $N_{\mathrm{MPI}}^{-1} \to 0$). It turns out to be 1% for 10675 basis functions. In other words, the present parallelization will cease to be efficient at $\alpha N_{\mathrm{MPI}} \approx 1$, i.e., at ~ 1000 cores.

2.6 Summary: recommended numerical parameters

In this chapter, we have presented a formalism to calculate the electron current density $\mathbf{j}(\mathbf{r})$ and the induced magnetic field $\mathbf{B}(\mathbf{r})$. It is based on the non-equilibrium Green's function technique and density functional theory formulated in an atom-centered basis sets. The implementation of the formalism is especially constructed towards quasi-onedimensional wires. Then, the leads can be dealt with employing a standard recursive Green's function method (decimation technique). Extensive test of the numerical parameters have been performed to establish the reproducibility of the results. In particular, we ensured that despite of the finite basis set the continuity equation is fulfilled in the basis set limit.

For the important application to the case of armchair graphene nanoribbons (see the following chapters), we have summarized the numerical parameters for quantitative correct results in Tab. 2.1, as they are used throughout this thesis. In particular, we use a moderate basis set (14 basis function per carbon atom; double-ζ quality) to calculate quantitatively correct current patterns. Larger basis sets are needed if small energy shifts in the transmission function are unacceptable.

Additionally, Tab. 2.1 also lists settings for strict convergence tests. All calculations which show new physical effects must be checked using at least these stricter settings. For this thesis, we have always picked test systems which were checked for convergence using these settings.

	recommended settings for		reference
	quantitative results	convergence checks	
basis set size (basis functions per carbon atom)	tier1 / SVP (14/14)	tier2 / TZVPP (39/31)	Figs. 2.9, 2.10, 2.11, 2.13, 2.14
grid spacing δ	$\delta = 0.2$Å	$\delta \leq 0.1$Å	Figs. 2.15, 2.16, 2.17
length-width-ratio of each lead	$L/W \approx 10 - 25$	$L/W \geq 50$	Sec. 2.2.2, Tab. B.3
length of each slice $\mathbf{H}^{\mathrm{block}}$	1 carbon ring	≥ 2 carbon rings	Fig. 2.5b, Eq. (2.29)
length of extensions $\mathbf{H}^{\mathrm{ext}}$	1 carbon ring	≥ 3 carbon rings	Fig. 2.6b

Table 2.1: Recommended numerical parameters for quantitative correct results and for additional (more strict) convergence checks. The last column lists references to the data on which the recommendations are based.

---

[1]This is the end of the method chapter.[M]

Notes to chapter 2

The notes are for completeness, reproducibility and to help interested readers understand all the fine technical details.

[A] The effective single particle treatment is—in the Landauer-Büttiker framework—necessary for electrons in the leads because otherwise, even injecting electrons moving towards the junction requires solving a full many-body problem. In this thesis, we also restrict ourselves to effective single particle treatment for the electrons in the junction, although this is not required by the Landauer-Büttiker viewpoint. One exception is given in Sec. 3.3.3 where explicit interaction effects are shortly discussed on the basis of a small tight-binding model. (page 10)

[B] Please note, that the left and right leads are assembled from opposite directions, but are otherwise identical. The resulting self-energies are thereby related by a symmetry transformation. In practice, it is much easier to calculate two self-energies. For the left lead, Eq. (2.18) are iterated as written. For the right lead, one replaces $\mathbf{V} \to \mathbf{V}^\dagger$. (page 15)

[C] The total length of the lead is given by the number M of slices $\mathbf{H}^{\mathrm{block}}$ in the lead plus one (for the contact region) times the length l of a single slices, i.e., $L = (M+1)l$. (page 16)

[D] Since we examine transport in armchair ribbons, the left and right border is of zig-zag type. These zig-zag borders facilitate spin-separation, especially for ribbons which are not much longer than wide[138]. These spin-separations do not describe the infinitely extended system, which we intend to investigate. Therefore, we suppress the spin-separation using spin-unpolarized DFT simulations. In the following, the remaining finite-size effects (caused by the difference between hydrogen termination and carbon continuation) are dealt with by choosing a large enough system. (page 17)

[E] Ideally, both matrix blocks $\mathbf{H}^{\mathrm{block}}$ in Eq. (2.29) are identical. In practice, they slightly deviate from each other for finite sized extensions. These deviations are usually small and not important for the transport phenomena; we minimize them by taking the arithmetic average of both matrix blocks (per element with respect to the orthogonal basis set $|\tilde{\varphi}_i\rangle$). (page 20)

[F] A single carbon ring contains 4 carbon atoms in transport direction (i.e. armchair direction). Thus, the matrix $\mathbf{V}$ describing only one carbon ring includes all carbon-carbon couplings up to fourth-nearest-neighbors. (page 22)

[G] For the AGNR5, containing 2 carbon rings in width, the rule of thumb means that values $M = 2 \cdot L/W \approx 20 - 50$ are reasonable. For wider ribbons, larger values are needed, i.e. for AGNR41, containing 20 carbon rings in width, values of $M = 20 \cdot L/W \approx 200 - 450$ are necessary for converged leads. Please, compare this with Fig. 2.14 (left) where the bandgap, calculated with $M = 200$, of the pristine AGNR41 is not yet fully developed. The (theoretical sharp) step near $E = \varepsilon_{\mathrm{F}}$ is still slightly smoothed. (page 22)

[H] The continuity equation can only be fulfilled exactly at all spatial points using a finite basis set if the basis functions themselves are tuned to fulfill the continuity equation, i.e. by forcing that they comply with the Laplace equation: $\boldsymbol{\nabla} \cdot \boldsymbol{\nabla} \varphi_j(\mathbf{r}) = \Delta \varphi_j(\mathbf{r}) = 0$. Liouville's theorem forces such (harmonic) basis functions to be constant everywhere in space (since basis functions are bounded to represent molecular orbitals), perishing any usefulness of this approach. (page 23)

[I] The functional error of the symmetric two-point rule for first and second derivative with spacing Δ scales with $\mathcal{O}(\Delta^2)$. Therefore a small Δ should be chosen. On the other hand, calculating differences is numerically unfavorable because of a finite machine precision ε (double precision: $\varepsilon = 2.2 \cdot 10^{-16}$). The finite precision error scales with $\mathcal{O}(\varepsilon \Delta^{-1})$ and $\mathcal{O}(\varepsilon \Delta^{-2})$ for first and second derivative calculation, respectively. Since we only need the second derivative for the divergence which is not a physical quantity but a convergence measure, we sacrifice its accuracy in favor of a uniform Δ, and choose an optimal $\Delta = \sqrt[3]{\varepsilon}$ for the first derivative, leading to accuracies in the order of 10^{-10} and 10^{-5} for first and second derivative, respectively. The units used in the code are atomic units, i.e., Bohr radius for the length scale, which is the correct length scale on which the basis function vary. (page 24)

[J] The minority channel (β) looks slightly different due to different occupation induced by an overall odd number of electrons in combination with integer occupation number. Allowing for fractional occupation numbers as in FHI-AIMS, a collinear open-shell calculation converges to the closed-shell calculation. (page 25)

[K] In x-direction, we exclude one carbon ring additionally to the (dashed blue) contact regions since the basis functions cannot be strictly separated in space and therefore the contact regions do not have the strict borders implied by the dashed blue box. In fact, parts of the self-energies $\boldsymbol{\Sigma}_{\mathrm{L/R}}$, representing the leads, also contribute to regions next to the blue dashed region, cf. Appx. B.5.2. Please also note, that the absolute value of the error measures $\Delta_{\mathbf{j}}$ and $\Delta_{\boldsymbol{\nabla} \cdot \mathbf{j}}$ depend (arbitrarily) on the upper and lower integration borders in y and z-direction. Away from the AGNR5, the local currents and the divergence are exactly zero, giving no measurable error. Because of the averaging procedure, the error measures $\Delta_{\mathbf{j}}$ and $\Delta_{\boldsymbol{\nabla} \cdot \mathbf{j}}$ can become arbitrarily small by integrating over sufficiently space. To compare the error measures, it is important to perform the integration always on the same grid. (page 27)

[L] For comparison, we also fitted a single exponent (valid only in the plotted regime): $T_{\mathcal{T}} = 10^{-5.24} N^{1.32}$ h, $T_{\mathbf{j}} = 10^{-6.46} N^{1.97}$ h, $\mathcal{M}_{\mathcal{T}} = 10^{-6.77} N^{1.85}$ GiB, $\mathcal{M}_{\mathbf{j}} = 10^{-6.95} N^{1.94}$ GiB. (page 34)

[M] I dedicate this extremely useful footnote to Sir "Terry" Pratchett (*28 April 1948; †12 March 2015), e.g., see Ref. 139. (page 35)

3 Chapter 3

Application I:
Narrow armchair graphene nanoribbons

We investigate the transport behavior of narrow armchair graphene nanoribbons. We start with pristine ribbons in Sec. 3.1, and observe perfect streamline patterns in the current density. These streamline patterns arise as a consequence of quantum confinement in the transverse direction, as can be explained with simple zone-folding arguments. Next, in Sec. 3.2, we investigate the transport properties of ribbons with nitrogen substituents, and observe a strong dependence on the position of the nitrogen substituent. This dependence is intuitively explained by the streamline patterns. If the nitrogen is placed outside the streamlines of the pristine ribbon, hardly any effect on the transport is observed. Placing the nitrogen inside a streamline, the current pattern changes significantly and shows prominent vortices, ring currents, which induce orbital magnetism. The fundamental origin of these ring currents is then explored in Sec. 3.3 using simple two-path tight-binding toy models.

3.1 Pristine ribbons

As first application, we investigate the current flow through pristine AGNRN_C, armchair graphene nanoribbons with N_C carbon atoms in the transverse direction (y-direction), see Appx. A.1 for detailed nomenclature. We find perfect streamline patterns (Sec. 3.1.1) which are a consequence of quantum confinement in the transverse direction (Sec. 3.1.2). We observe and explain a threefold periodicity in N_C. The periodicity remains valid in the bulk limit (Sec. 3.1.3), i.e., for very wide ribbons.

Pristine armchair graphene nanoribbons are spin-unpolarized, in contrast to ribbons with zigzag borders, which facilitate spin-separation[138]. Thus, no spin-effects are considered in this section, and we apply closed-shell DFT transport calculations using TURBOMOLE and FHI-AIMS as described in Chap. 2.

3.1.1 Streamline patterns in the current density

The simulated current pattern for a single channel ($\mathcal{T} = 1$) in an AGNR5 is shown in Fig. 3.1. We make the following observations, which remain true for wider AGNRs discussed later in Sec. 3.1.2.

A perfect streamline pattern arises (see Fig. 3.1a). The current flows along carbon-carbon bonds but there are carbon atoms in the center of the AGNR5 which are not even touched by the current flow. Thus, the overall current pattern is strongly inhomogeneous already in this simple pristine case. Two cuts perpendicular to the current direction are shown in Figs. 3.1b and 3.1c. The current is divided into flows above and below the carbon plane. This is expected because the current follows the shape of the π-orbitals of the electrons near the Fermi energy. These π-orbitals are hybridizations of p_z-orbitals of single carbon atoms. Therefore, they have a node in the carbon plane, suppressing any current contribution there. Because of the perfect z-mirror symmetry of the current density and the trivial structure in z-direction, we restrict ourselves to xy-cuts at z=0.5 Å (as shown in Fig. 3.1a) in the following. The value z=0.5 Å is chosen since it corresponds to the maximum current density (see Figs. 3.1b and 3.1c).

The transmission function $\mathcal{T}(E)$ of pristine AGNR5—shown in Fig. 3.2a—is quantized in integer values due to the perfect periodicity of the ribbon in transport direction. Effectively, $\mathcal{T}(E)$ counts the number of bands available for transport at energy E. So far, we discussed the single channel case ($\mathcal{T} = 1$, black arrow in Fig. 3.2a). Now, we shortly turn to the two channel case ($\mathcal{T} = 2$, gray arrow). The current pattern shown in Fig. 3.2b shows the superposition[A] of two channels, the already discussed streamline channel and an additional second channel. Due to the latter, the

(a) xy-cut at z=0.5 Å   **(b)** yz-cut at x=x_0 **(c)** yz-cut at x=x_1
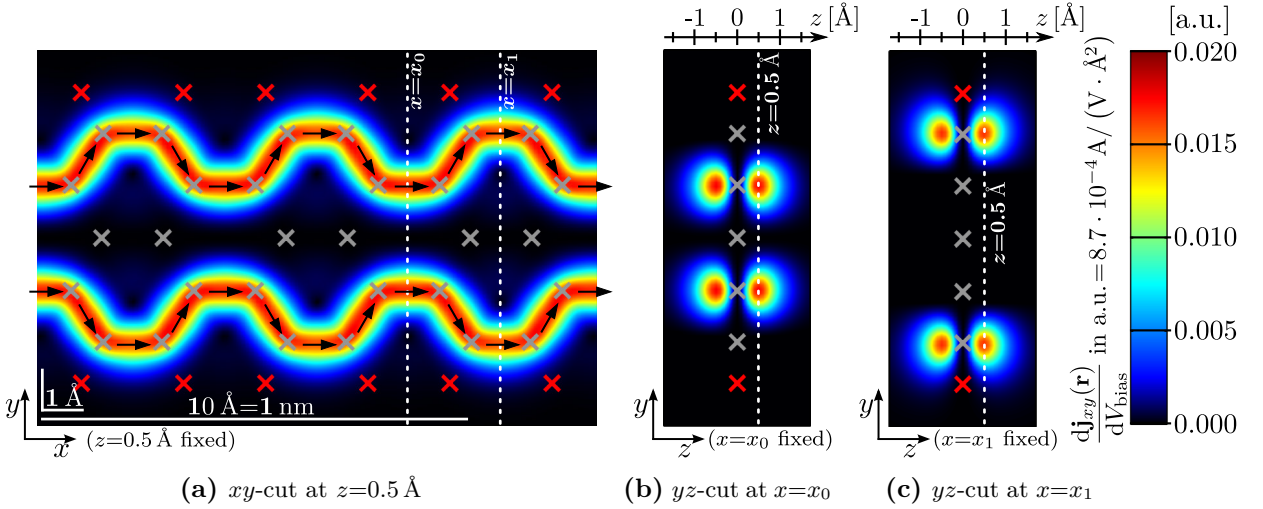
Figure 3.1: Local current density response (per spin) for perfect single channel transmission $\mathcal{T}$=1 in a pristine narrow hydrogen-terminated armchair graphene nanoribbon (AGNR5) for different cuts: (a) a cut along the xy-plane at z=0.5 Å, and (b/c) cuts along yz-planes at x=x_0 and x=x_1 in, respectively. The current pattern shows two prominent streamlines, see (a), which are split into flows below and above the ribbon plane, see (b/c). The z=0.5 Å-plane, and the x_0/x_1-planes are shown in dashed white. Plot shows current amplitude (color), current direction (arrows), carbon atoms (gray crosses), and hydrogen atoms (red crosses). [DFT details: Turbomole, basis set tzvpp, closed-shell]

(a) Transmission of pristine AGNR5

(b) Current pattern at $\mathcal{T} = 2$
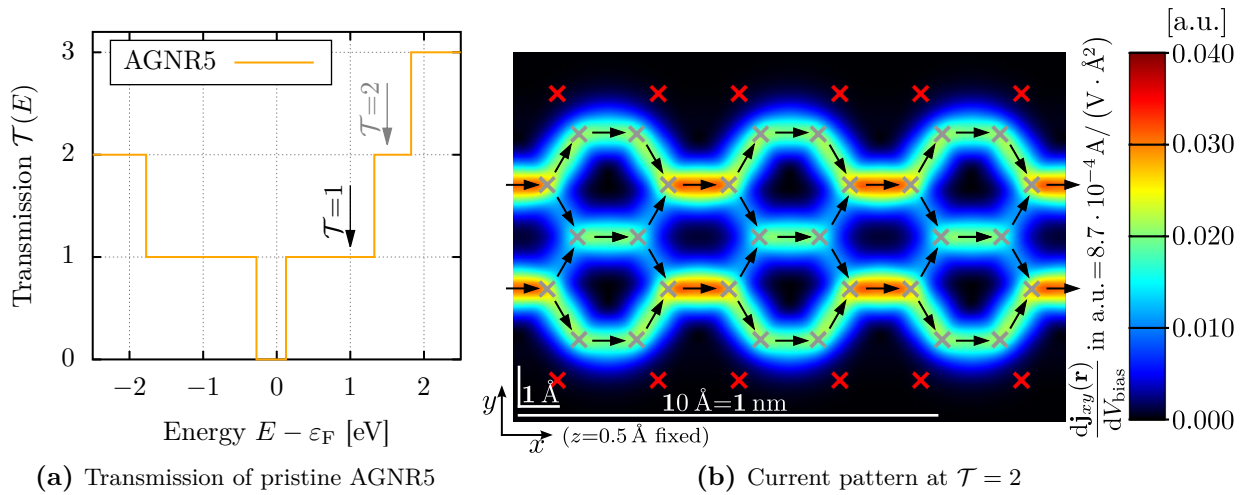
Figure 3.2: (a) Transmission function of pristine AGNR5. The single channel ($\mathcal{T}=1$) case and double channel case ($\mathcal{T}=2$) are marked. The corresponding current patterns are shown in Fig. 3.1 and Fig. 3.2b, respectively. (b) Local current density response (per spin) for two channels ($\mathcal{T}=2$) in pristine AGNR5. The streamline pattern mixes with an additional channel, so that all carbon atoms are touched by the current flow. Plot shows current amplitude (color), current direction (arrows), carbon and hydrogen atoms (gray and red crosses). [DFT details: TURBOMOLE, basis set TZVPP, closed-shell]

current touches all carbon atoms resulting in a more homogeneous flow. To focus on fundamental properties of single scattering states, we will restrict the investigations to the single channel case in the remainder of this thesis, meaning $\mathcal{T}=1$ (or $\mathcal{T}<1$ when including impurities).

3.1.2 Influence of transverse confinement & selection rules

After discussing the current flow in pristine AGNR5, we will now generalize the results to broader ribbons and investigate the dependence of the current flow on the number of transverse carbon atoms N_C. This work has been done in close collaboration with J. Wilhelm and has also been published in his master thesis[140] and in our joined publication[109].

Transmission function of AGNRs

To discuss the dependence of transport properties on N_C, we explicitly investigate four ribbons: AGNR11–14. The transmission function, shown in Fig. 3.3, already shows three classes: AGNR($3m$), AGNR($3m-1$), and AGNR($3m-2$) [$m \in \mathbb{N}$]. AGNR11 and AGNR14, belonging to class AGNR($3m-1$), feature a small bandgap ($\approx 0.1\,\text{eV}$) and a wide energy region with exactly one channel ($\mathcal{T}=1$). AGNR12 [AGNR($3m$)] shows a larger bandgap ($\approx 0.6\,\text{eV}$) and still a moderate region with exactly one channel. AGNR13 [AGNR($3m-2$)] also has a larger bandgap ($\approx 0.8\,\text{eV}$) but it features a significantly smaller single channel region. These three classes are consistent with earlier DFT bandgap calculations[141–143]. The three-fold periodicity remains true for larger AGNRs, but the bandgaps decrease as $1/N_C$ with a class dependent prefactor.
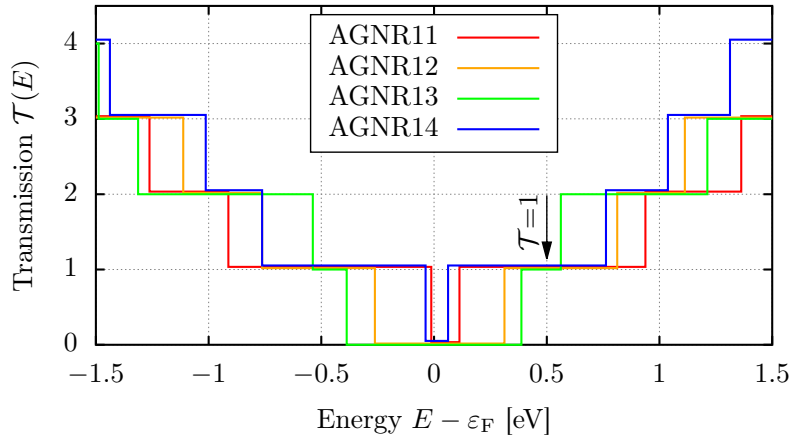
Figure 3.3: Transmission function of several consecutive pristine AGNRs. The single channel ($\mathcal{T}$=1) case is marked by an arrow. The corresponding current patterns (for the single channel) are shown in Fig. 3.4. For plotting reasons, the transmission functions are slightly shifted on the y-axis; the correct values are always exact integer multiples. My thanks to J. Wilhelm who performed the numerical calculations[140]. [DFT details: TURBOMOLE, basis set SVP, closed-shell]

Current patterns in AGNRs

Next, we tend to the current patterns of AGNR11–14, shown in Fig. 3.4. For N_{C}=3m−1, Figs. 3.4a and 3.4d, we still see the perfect streamline pattern. Please note, that all streamlines together form a single channel. Therefore, the current per streamline decreases with the number of streamlines, as can be seen by comparing AGNR11 and AGNR14.

The other two classes, N_{C}=3m (Fig. 3.4b) and N_{C}=3m−2 (Fig. 3.4c) , still show strongly textured current patterns but no perfect streamlines. Only at the border, the streamlines survive. In the interior, the current is more complicated but its amplitude still shows a node structure in transverse direction, e.g., the current pattern in AGNR12 has three nodes in y-direction: one in the center and two next to the surviving streamlines at the borders. This already hints at transverse quantum confinement as origin for these effects. Also, the number of nodes, and equivalent the number of maxima, grows with increasing ribbon width. In fact, the integer m is the number of maxima in transverse direction. Also, m equals to the number of streamlines for N_{C}=3m−1.

This periodicity in the ribbon width continues to wider ribbons. In every third ribbon, for N_{C}=3m−1, a perfect streamline pattern exists. For $N_{\mathrm{C}}\neq$3m−1, the current density shows streamlines only at the boundaries, but more complicated patterns in the ribbon center. We thus also find a periodicity on N_{C} for the current patterns, but only two qualitatively different cases: N_{C}=3m−1 (with streamlines) and $N_{\mathrm{C}}\neq$3m−1 (without perfect streamlines).

As a final remark, please note that pristine AGNR12 and AGNR13 even show backflowing currents, local current contributions that flow (at least partially) against the total current direction.

$\dfrac{\mathrm{d}\mathbf{j}_{xy}(\mathbf{r})}{\mathrm{d}V_{\text{bias}}}$ in a.u. $= 8.7 \cdot 10^{-4}\,\mathrm{A}/\left(\mathrm{V}\cdot\mathrm{\AA}^2\right)$

0.000 0.002 0.004 0.006 0.008 0.010

y $(z{=}0.5\,\mathrm{\AA}\ \text{fixed})$ x

|			
$N_{\mathrm{C}}{=}3m{-}1$	$N_{\mathrm{C}}{=}3m$	$N_{\mathrm{C}}{=}3m{-}2$	$N_{\mathrm{C}}{=}3m{-}1$
(a) AGNR11	**(b)** AGNR12	**(c)** AGNR13	**(d)** AGNR14
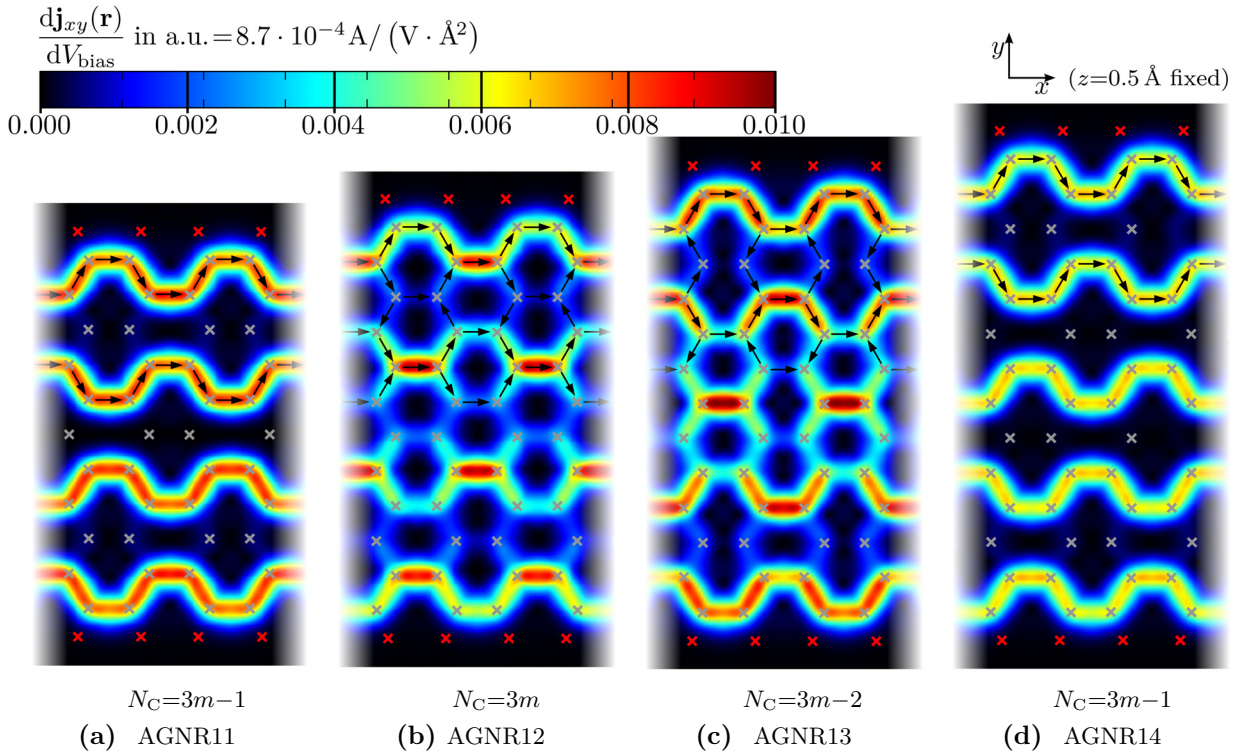
Figure 3.4: Local current density response (per spin) for perfect single channel transmission ($\mathcal{T}{=}1$) in pristine AGNR11–14. AGNR11 and AGNR14 show perfect streamline patterns, while for AGNR12 and AGNR13 the streamline pattern survive only at the border. Plots show current amplitude (color), current direction in the upper part (black arrows), carbon atoms (gray crosses), and hydrogen atoms (red crosses). My thanks to J. Wilhelm who performed the numerical calculations[140].
[DFT details: Turbomole, basis set svp, closed-shell]

Selection rules

The transverse structure of the current patterns can be explained by standard zone-folding arguments, which are well-known in carbon nanotubes[144, Sec. 3.2], and have also already been applied to AGNRs[143]. First, we look at the spatial structure of the wavefunction ψ in transverse direction and assume that hardcore boundary conditions apply, i.e.,

$$\psi(y{=}0) = 0\,, \qquad \text{and} \qquad \psi(y{=}L_y) = 0\,, \tag{3.1}$$

with L_y being the ribbon width. The only k-points respecting these conditions are

$$k_{y,m} = \frac{\pi}{L_y} \cdot m\,, \qquad \text{for } m \in \mathbb{Z}\,. \tag{3.2}$$

The width of an AGNRN_{C} is approximately[B] given by $L_y = (N_{\mathrm{C}} + 1)a_y$. Here, $a_y = a\sqrt{3}/2$ is the carbon-carbon bond length projected to the y-axis. [The carbon-carbon bond length is a and a

(a) Brillouin zone of graphene

(b) Transversal dependence of the wavefunction in AGNRs
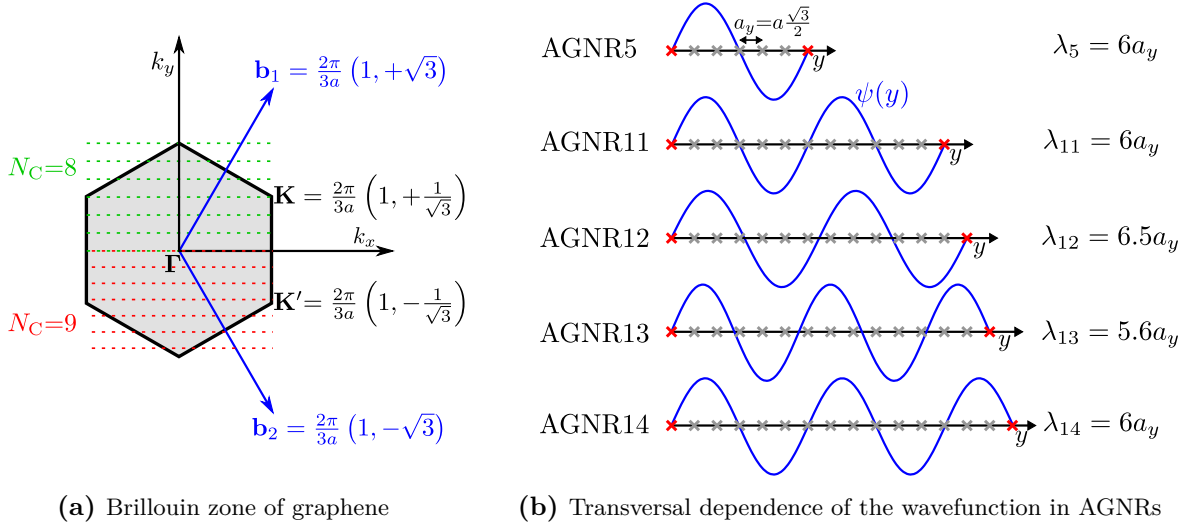
Figure 3.5: (a) First Brillouin zone of graphene showing both Dirac points, $\mathbf{K}$ and $\mathbf{K'}$, and reciprocal lattice vectors, $\mathbf{b}_1$ and $\mathbf{b}_2$. The zone-folding procedure is indicated for AGNR8 and AGNR9, exemplarily. (b) Schematic visualisation of the wavefunctions for states near the Fermi energy, showing their dependence on the transverse direction. Hardcore boundary conditions are applied at the hydrogen atoms (red crosses). In the case of AGNR5/11/14 (AGNR($3m-1$) in general), the nodes of the wavefunction exactly matches carbon atoms (gray crosses), explaining the perfect streamline pattern. In the other case, the nodes are slightly shifted away from carbon positions, so that all carbon atoms carry contributions near the Fermi energy.

link between neighboring atoms is given by, e.g., $\mathbf{a} = a(1/2, \sqrt{3}/2)$.] In Fig. 3.5a, the first Brillouin zone of graphene with the two Dirac cones $\mathbf{K}$ and $\mathbf{K'}$ is "sliced" at the valid k-points

$$k_{y,m} = K_y \frac{3m}{N_{\mathrm{C}}+1}, \qquad \left[K_y = \tfrac{2\pi}{3\sqrt{3}a} = \tfrac{\pi}{3a_y}\right] \tag{3.3}$$

exemplary shown for $N_{\mathrm{C}} = 8$ and $N_{\mathrm{C}} = 9$. For $N_{\mathrm{C}} = 8$, as for any $N_{\mathrm{C}} = 3m-1$, the Dirac cone is directly hit: $k_{y,m} = K_y$. Thus, the spatial structure of electronic states near the Fermi energy in an AGNR($3m-1$) is expected to be governed by K_y (at least in y-direction). Together with the contribution of the other Dirac cone, $K'_y = -K_y$, a standing wave with wavelength $\lambda = 2\pi/K_y = 6a_y$ emerges. Being an even integer multiple of the transverse bond-distance a_y (and because of symmetry), the nodes of such a standing wave coincide with carbon atoms. This is sketched in Fig. 3.5b for AGNR5/11/14 and explains the formation of perfect streamline patterns in the current density of AGNRs($3m-1$).

For AGNRs with $N_{\mathrm{C}} \neq 3m-1$, no allowed wavevector $k_{y,m}$ coincides with the Dirac cones. The nearest allowed wavevector $\tilde{K}_y = k_{y,m}$—choosing $m \in \mathbb{Z}$ so that $|\tilde{K}_y - K_y|$ is minimal—is slightly off. Therefore, the wavelength

$$\lambda_{N_{\mathrm{C}}} = 2\pi/\tilde{K}_y = 6a_y \cdot \begin{cases} 1 + \frac{1}{N_{\mathrm{C}}} & \text{for } N_{\mathrm{C}} = 3m \\ 1 & \text{for } N_{\mathrm{C}} = 3m - 1 \\ 1 - \frac{1}{N_{\mathrm{C}}+2} & \text{for } N_{\mathrm{C}} = 3m - 2 \end{cases} \tag{3.4}$$

is no integer multiple of a_y (for $N_C \neq 3m-1$) and the nodes of the standing wave pattern do not match the carbon rows, see Fig. 3.5b. Instead the nodes are "between" the carbon atoms which is the reason for the node structures seen in AGNR12 and AGNR13.

Remark: The above arguments apply equally well to the local density of states (LDOS) in equilibrium. Indeed, the LDOS shows the same node structure in the transverse direction as the current density (see for example our publication[109, Fig. 10]). But the LDOS does not obey a continuity equation, and therefore shows additional structure along the ribbon direction (x-direction). Therefore, the LDOS forms at most pseudo-streamlines. On the other hand, the LDOS can be accessed by a scanning tunneling microscope (STM), see Tersoff-Hamann theory[145]. Nevertheless, to the best of my knowledge, no experiment has so far observed the pseudo-streamlines (or current streamlines) in AGNRs($3m-1$), probably because edge irregularities destroy the streamlines and the fabrication of perfect pristine AGNRs remains challenging.

3.1.3 Streamline patterns in the bulk limit

We now explain how the bulk limit of the current density is reached. In the bulk limit, the streamline pattern should vanish because the boundaries should no longer play a significant role. But when investigating the current density response for wider ribbons (up to AGNR41, see Fig. 3.6), we see no indication that the streamline patterns vanish, except that the total current is distributed into m streamlines whose amplitudes are therefore reduced by m (cf. Appx. C.1 for further details).

The streamlines vanish in the bulk limit in another fashion. The energy range $\Delta E_{\mathcal{T}=1}$ in which only a single channel exists decreases for increasing ribbon width. As discussed on the basis of Fig. 3.2b, the streamlines only exist at $\mathcal{T} = 1$. One expects a $1/N_C$ decay for this energy range in wide ribbons. Our DFT simulations support such a decay (cf. Appx. C.1) and give as numerical value

$$\Delta E_{\mathcal{T}=1} \approx \frac{25\,\text{eV}}{N_C} \qquad \text{for } N_C \gg 1\,. \tag{3.5}$$

For bias voltages larger than this energy window, $eV_{\text{bias}} > \Delta E_{\mathcal{T}=1}$, the streamline pattern mixes with other channels, thereby vanishing. Thus, for fixed bias voltage, the streamline pattern becomes less and less important for increasing ribbon width. Nevertheless, for sufficiently small bias voltages, we predict the appearance of streamlines in all AGNRs($3m-1$), regardless of their width.
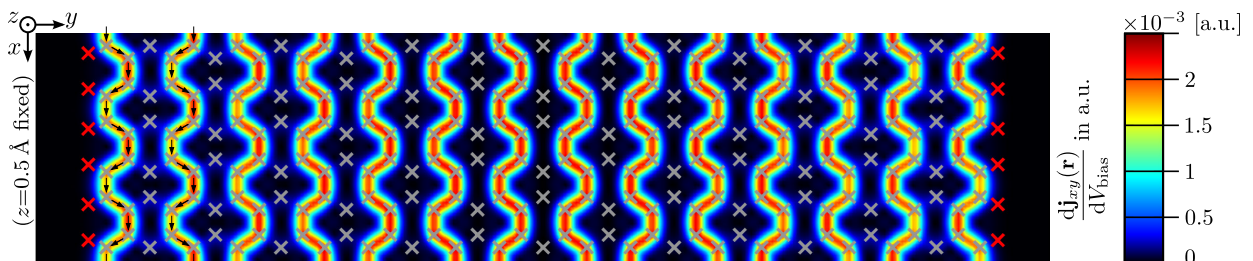
Figure 3.6: Local current density response (per spin) in pristine AGNR41 (single channel, $\mathcal{T}=1$). No deviations from the perfect streamline pattern are visible. Note, that the plot has been rotated compared to previously shown current density plots. [DFT details: FHI-AIMS, basis set `tier1`, closed-shell]

3.2 Ribbons with a single nitrogen substituent

After discussing current patterns in pristine AGNRs, we now consider ribbons with a single nitro-gen substituent as scattering center. There are three different (not symmetry-equivalent) positions in an AGNR5 for a nitrogen substituent, see Fig. 3.7a. In Sec. 3.2.1, we examine the influence of the nitrogen position on the transport properties. Placed inside a pristine streamline, the current pattern changes significantly and shows prominent vortices. These ring currents induce orbital magnetism which we discuss in Sec. 3.2.2 using the example of nitrogen substituted to position 3. Finally, in Sec. 3.2.3, we summarize simulations with other impurity types, and conclude that the discussed effects (strong position dependence and ring currents) are generic and independent of the impurity type.

Remark: We checked that all three structures (AGNR5 with a single nitrogen substituent as shown in Fig. 3.7a) remain planar. For this purpose, we placed the nitrogen atom $0.2\,\text{Å}$ above the in-plane position of the substituted carbon atom. After a geometry relaxation using DFT, the nitrogen returns into the planar position with an accuracy better than $10^{-4}\,\text{Å}$.

(a) AGNR5 with nitrogen atom

(b) Transmission of AGNR5 with nitrogen substituents
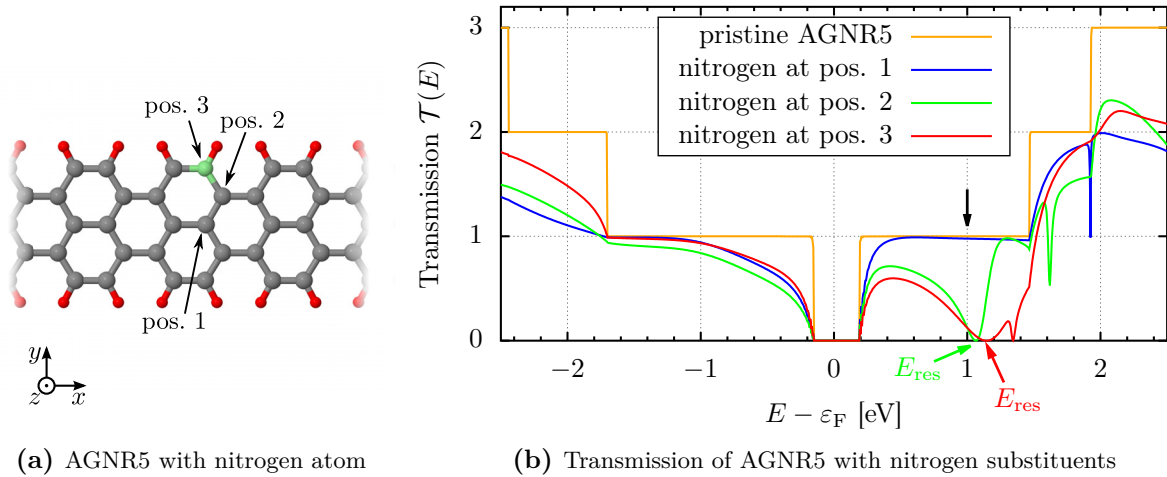
Figure 3.7: (a) Atomic structure of an AGNR5 with one nitrogen substituent (in green at position 3). All three symmetry-inequivalent positions for a nitrogen substituent are marked.
(b) Transmission function for AGNR5 containing a single nitrogen substituent. The black arrow marks the energy ($E=\varepsilon_\text{F}+1\,\text{eV}$) for which the current density responses are shown in Fig. 3.8a–c. The transmission of AGNR5 with nitrogen at position 2 or 3 shows a prominent dip, an antiresonance at energy $E = E_\text{res}$. [DFT details: FHI-AIMS, basis set `tier1`, closed-shell]

3.2.1 Position of impurities: placement inside or outside the streamlines

In Fig. 3.7b, we show the transmission of all three systems together with the pristine case. Most interestingly, the transmission function for position 1 (blue) does not show any qualitative changes near the Fermi energy when compared to the pristine case. Only the steps are smeared out which is expected as soon as the perfect periodicity is perturbed. Also, the current density response at $E=\varepsilon_F+1\,\mathrm{eV}$—shown in Fig. 3.8a—does not show any visible deviations from the streamline pattern. We conclude that placing a nitrogen substituent outside of the pristine streamlines hardly influences the transport near the Fermi energy.
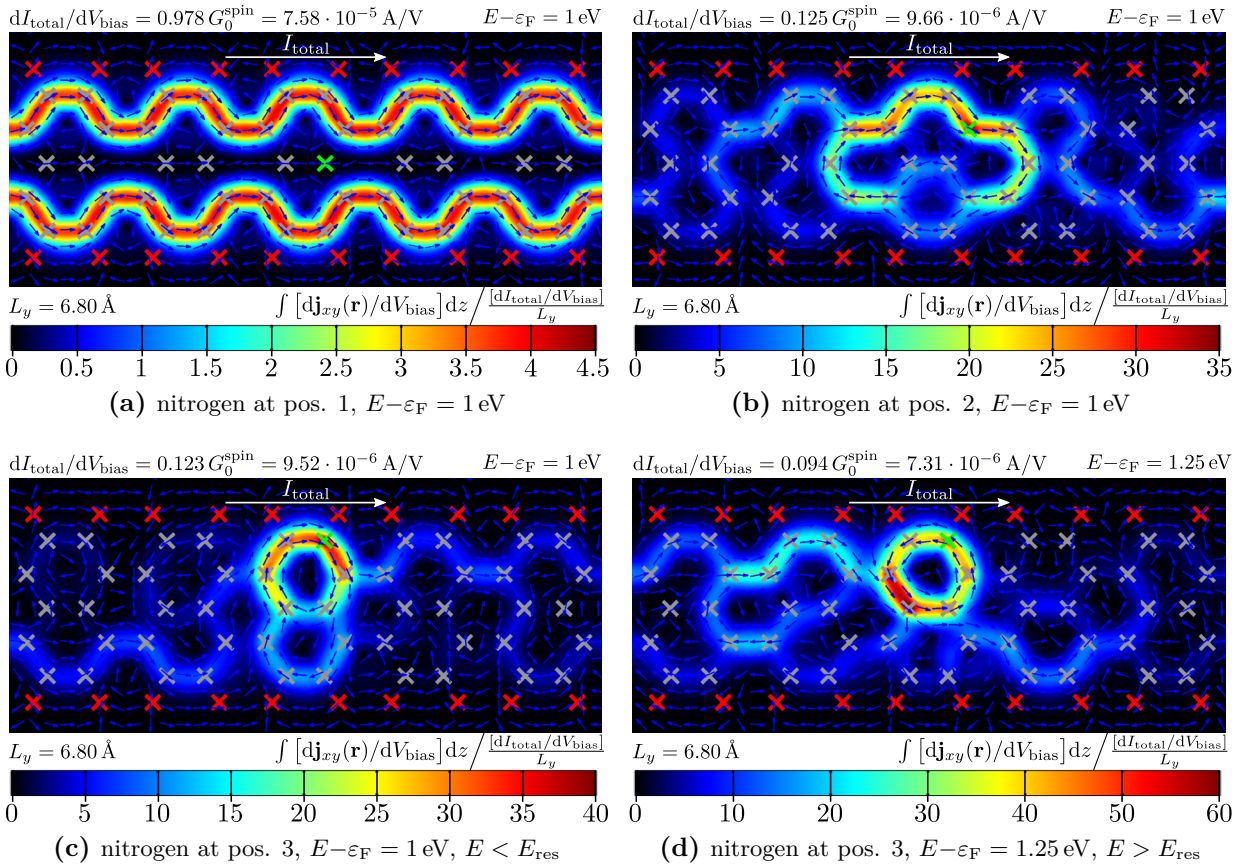
Figure 3.8: (a–c) Local current density response (integrated over the out-of-plane direction) normalized to the average through current of AGNR5 with a single nitrogen substituent (green cross) at position 1–3, respectively. The corresponding energy ($E=\varepsilon_F+1\,\mathrm{eV}$) is marked in Fig. 3.7b by a black arrow. The current pattern in (a) shows a hardly perturbed streamline pattern, while (b/c) show prominent ring currents whose amplitudes exceed the average through current by a factor of about 30 (see color scale).
(d) Current density response corresponding to (c), but above the antiresonance ($E > E_\mathrm{res}$), whereas (c) shows the current pattern below the antiresonance ($E < E_\mathrm{res}$). Note how the ring current direction changes between (c) and (d). [DFT details: FHI-AIMS, basis set `tier1`, closed-shell]

Quite the opposite happens when the nitrogen substituent is placed inside a streamline. The transmission function for position 2 and 3 shows an additional feature, a dip (antiresonance) at $E = E_{\text{res}}$ which is due to interference effects. The current density response near the antiresonance is shown in Fig. 3.8b and Fig. 3.8c. Both current patterns differ qualitatively from the streamline pattern, showing a prominent ring current near the nitrogen substituent.

We will discuss these ring currents in Sec. 3.2.2, but for the moment let us summarize that we can analyze the dependence on the position of the impurities in AGNRs($3m-1$) in terms of streamlines and we find a simple, intuitive explanation for the position dependence. If the impurity is placed inside a streamline, the transmission is suppressed over a large energy window. On the other hand, the transmission function and the current pattern is hardly affected when placing an impurity outside a streamline. This explanation seems to be general, see Sec. 3.2.3 for an example with OH-adsorbates on AGNR11.

Remark on spin magnetism: The nitrogen feeds in an extra electron into the conduction band of the ribbons. Having an odd number of electrons, one may think about spin-polarization and Kondo effect. Concerning the Kondo effect, we recall that the flat geometric structure of the ribbons suggests that the unpaired electron is not localized but completely immersed in the ribbon's π-band. We therefore do not expect a Kondo effect/Coulomb-blockade type situation. For all three nitrogen positions, we checked this expectation by an open-shell calculation that produces two (identical) half-occupied states at the Fermi energy suggesting the absence of a (nearby) magnetic instability. Hence, Kondo-physics is probably not relevant in these systems.[C]

3.2.2 Ring currents & orbital magnetism

We now investigate the antiresonance in the transmission function at $E = E_{\text{res}}$ (cf. Fig. 3.7b). We restrict ourselves to the nitrogen at position 3 (red curve). In Fig. 3.8c and Fig. 3.8d, the current density response is plotted below and above the antiresonance, respectively. At first glance, both patterns look similar: they feature a prominent ring current around the 6-atom ring with the nitrogen substituent. The magnitude of the ring currents is not restricted by the total current. Instead, we observe that the ring currents are larger than the average through current by a factor 30–50 (see color scale).

Nevertheless, there is an essential difference between the two current patterns: the ring current direction. It changes from clock-wise (below E_{res}, Fig. 3.8c) to anti-clockwise (above E_{res}, Fig. 3.8d). This becomes even more interesting, if we recall that ring currents are related to orbital magnetism. The induced magnetic field, shown in Fig. 3.9, also changes the direction when transversing the antiresonance. The magnetic field strength reaches $\mathrm{d}B_z/\mathrm{d}V_{\text{bias}} = 150\,\text{mT/V}$ with a large gradient reaching $1\,\text{T}/(\text{V nm})$. The observations are especially important in the context of nanoelectronics. Such a ribbon may work as a current-field converter: a nanoscopic coil. The sign of a macroscopically applied voltage fixes the sign of a microscopic induced field.

$dI_{total}/dV_{bias} = 0.123\,G_0^{spin} = 9.52 \cdot 10^{-6}\,\mathrm{A/V}$ $E - \varepsilon_F = 1\,\mathrm{eV}$

$\frac{\mu_0 dI_{total}}{4\pi L_y dV_{bias}} = 1.40\,\mathrm{mT/V}$ $\left[dB_z(\mathbf{r})/dV_{bias} \right] / \frac{\mu_0 dI_{total}}{4\pi L_y dV_{bias}}$

$-100 \qquad -50 \qquad 0 \qquad +50 \qquad +100$

(a) nitrogen at pos. 3, $E - \varepsilon_F = 1\,\mathrm{eV}$, $E < E_{res}$

$dI_{total}/dV_{bias} = 0.094\,G_0^{spin} = 7.31 \cdot 10^{-6}\,\mathrm{A/V}$ $E - \varepsilon_F = 1.25\,\mathrm{eV}$

$\frac{\mu_0 dI_{total}}{4\pi L_y dV_{bias}} = 1.07\,\mathrm{mT/V}$ $\left[dB_z(\mathbf{r})/dV_{bias} \right] / \frac{\mu_0 dI_{total}}{4\pi L_y dV_{bias}}$

$-150 \quad -100 \quad -50 \qquad 0 \qquad +50 \quad +100 \quad +150$

(b) nitrogen at pos. 3, $E - \varepsilon_F = 1.25\,\mathrm{eV}$, $E > E_{res}$
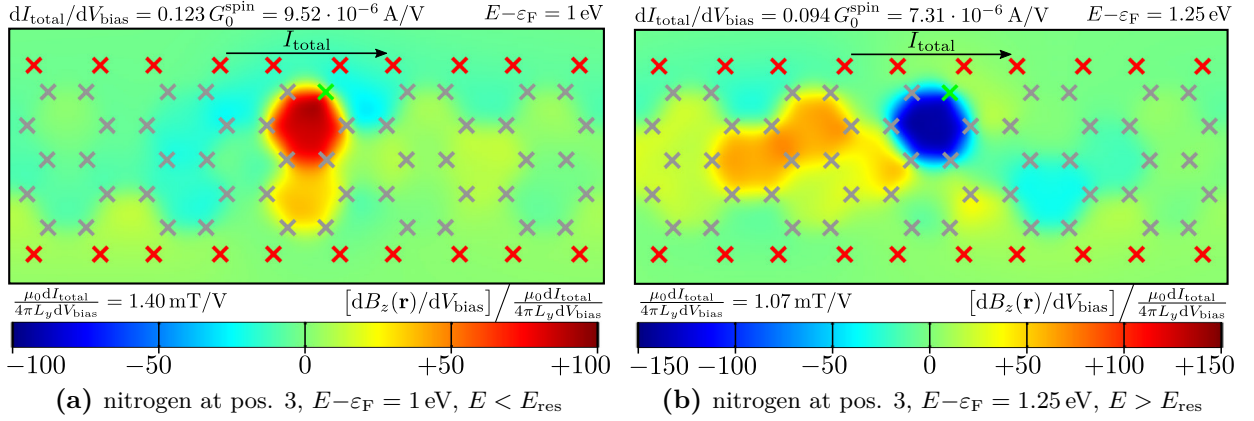
Figure 3.9: Magnetic field response (in out-of-plane direction) induced by the current patterns shown in Figs. 3.8c and 3.8d, respectively. The field is plotted in the carbon plane ($z=0$), but being divergence free, it hardly changes with z (checked for $z = \pm 1$ Å). [DFT details: FHI-AIMS, basis set `tier1`, closed-shell]
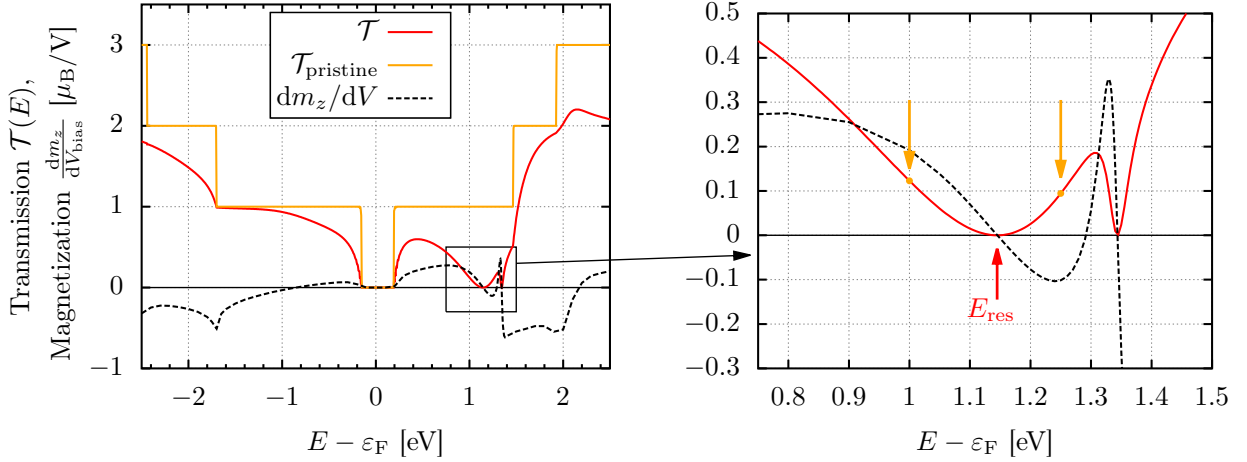
Figure 3.10: Transmission function (solid red) and magnetization per bias dm_z/dV_{bias} (perpendicular to the graphene plane, dashed black) for the AGNR5 with nitrogen at position 3 (transmission as in Fig. 3.7b). The magnetization shows a sign change directly at the antiresonance $E = E_{res}$. The orange arrows mark the energy for which the current response is plotted in Figs. 3.8c and 3.8d, respectively. [DFT details: FHI-AIMS, basis set `tier1`, closed-shell]

Magnetization

To investigate the ring currents in the complete energy range, we calculate the magnetic response dm_z/dV_{bias} induced by the current patterns and show it in Fig. 3.10. [total magnetization: $\mathbf{m} = \frac{1}{2} \int \mathbf{r} \times \mathbf{j}_{el}(\mathbf{r})\, d\mathbf{r}$, cf. Eq. (2.16)] First, note that the magnetic response changes its sign exactly at the antiresonance (see magnification), reflecting the change of the ring current direction. Second, the magnetic moment (and also the inducing ring currents) is linear in the detuning $E - E_{res}$ whereas the transmission shows a quadratic dependence. That means that near the antiresonance,

the ring currents dominate. They become arbitrarily large compared to the total through current. For all energies, the amplitude of the magnetic response is in the order of 0.1–0.5 μ_B/V (per spin). An experimental observation should be feasible.

Remark 1: Although interesting from a theoretical point of view, comparing the ring currents to near-vanishing through currents may be of less importance from a practical point of view. As a compromise, we only plot current density responses with finite transmission $\mathcal{T} \gtrsim 0.1$ in the main part of this thesis, so that an experimental observation is—in principle—possible (see Appx. C.2 for an example with near-vanishing transmission).

Remark 2: There is an additional much-sharper antiresonance at $E = \varepsilon_F + 1.345\,\text{eV}$, see magnification of Fig. 3.10. The same effects can be observed: the transmission vanishes quadratically but the magnetic moment vanishes only linearly, see Appx. C.2 for further details.

Finite bias voltage

So far, we discussed only the current density response to an infinitesimal bias voltage. From the magnetization response dm_z/dV_{bias} in Fig. 3.10, one already expects finite ring currents also for finite bias voltages because there are large regions with dm_z/dV_{bias} having a constant sign. In Fig. 3.11, the current density and the induced magnetic field is calculated for a bias voltage $eV_{\text{bias}} = E_{\text{res}} - \varepsilon_F = 1.145\,\text{eV}$ which covers the range between Fermi energy and antiresonance. In that range, the magnetic response dm_z/dV_{bias} does not change its sign.

Thus, Fig. 3.11 suggest that the ring currents should be observable for finite bias voltages. In that case, we expect a ring current exceeding the average through current by about a factor of 10. The magnetic field reaches 130 mT which might be detectable experimentally, e.g., by a magnetic STM.

(a) Current density (finite bias voltage) **(b)** Induced magnetic field (finite bias voltage)
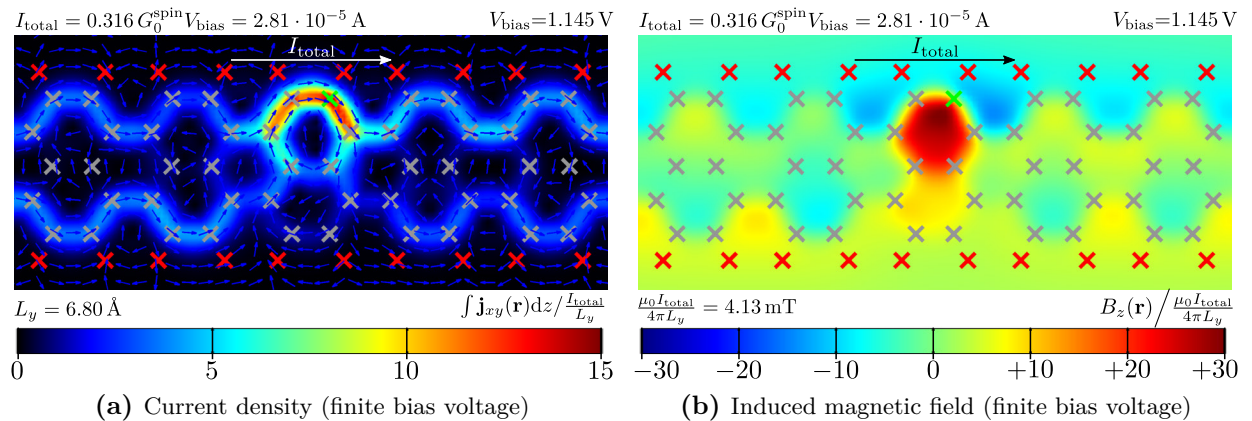
Figure 3.11: (a) Current density and (b) induced magnetic field for a finite bias voltage V_{bias}=1.145 V. All previously discussed features remain. The magnetic moment of the current density is m_z=0.44 μ_B for both spin channels (m_z=0.22 μ_B per spin channel). [DFT details: FHI-AIMS, basis set `tier1`, closed-shell]

The associated total magnetic moment $m_z=0.44\,\mu_B$ (for both spin channels) lies also in an observable order of magnitude. For our system, it significantly exceeds previously reported values of orbital magnetism, e.g., by Im *et al.* [146] who report orbital magnetism in carbon nanotubes due to structural (Stone-Wales) defects with a maximum magnitude of $m=0.08\,\mu_B$.

Remark on m_x, m_y, B_x, B_y: In this section, we have restricted ourselves to the magnetic field $B_z(z=0)$ and magnetic moment m_z perpendicular to the graphene ribbon. Since both, **B** and **m** are pseudovectors (axial vectors), their in-plane components are exactly zero due to the z-mirror symmetry of the transport setup. In the case of disorder, like hydrogen adatoms in Chap. 4, some carbon atoms are moved out of the ribbon plane, and the symmetry is broken. Then, the in-plane components m_x, m_y, B_x, B_y are finite. Nevertheless, they are still suppressed by an approximate z-mirror symmetry, and we will focus on m_z/B_z also in these cases.

3.2.3 Summary & generalization to other impurity types

So far, we discussed a nitrogen substituent as an example and found two main effects: (i) a strong position dependence explainable by the streamlines and (ii) a tendency to form ring currents. We presume that these results are general since they also appear with many different types of impurities as well. In this section, we summarize and refer to such other examples.

The first effect, the position dependence, is also shown in Fig. 3.12 for OH adsorbates on AGNR11. If the OH group is adsorbed on a carbon atom inside a streamline, the transmission is suppressed over a large energy window (cf. Fig. 3.12b). Otherwise the transmission and the current pattern is hardly affected (cf. Fig. 3.12a). The antiresonance for OH at position 4 ($E\approx\varepsilon_F-0.45\,\text{eV}$)

(a) OH placed outside streamline

(b) OH placed inside streamline
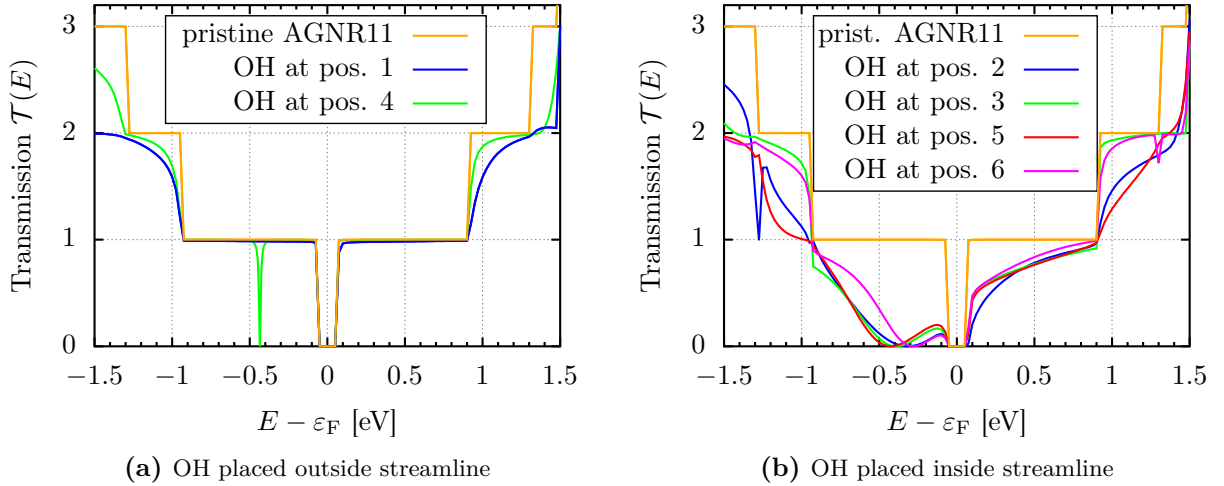
Figure 3.12: Transmission function of AGNR11 with one OH-adsorbate at different positions. The positions are counted from the center of the AGNR11, corresponding to the nomenclature used in AGNR5, see Fig. 3.7a. My thanks to J. Wilhelm who performed the numerical calculations[140].
[DFT details: TURBOMOLE, basis set SVP, closed-shell]

is very sharp with minor contributions to transport with finite bias voltages. The general features, that the transmission is strongly dependent on the position of the OH group, was already observed[81, 99–102], and the streamline patterns of the underlying pristine ribbons provide an intuitive explanation.

Second, also the tendency to form ring currents is general. In close collaboration with J. Wilhelm, we have observed ring currents for adsorbates (OH and H), as well as for substituents (nitrogen and boron) for several different AGNRs[111, 140]. Our results are supported by other groups which have applied TB models to disordered graphene ribbons; the resulting TB bond currents also show ring currents[77–83]. Ring currents have also been reported in carbon nanotubes due to structural defects[146]. In all these cases, the ring currents are related to a quadratically vanishing transmission at an antiresonance. The ring currents vanish linearly and change their direction at the antiresonance.

3.3 Tight-binding (toy) models explaining the ring current formation

In this section, we investigate tight-binding (TB) toy models to explain the formation of ring currents. We can explain all qualitative features of the *ab initio* treatment, but of course no quantitative features, like numbers and local spatial structures.

The transport method for TB systems follows the DFT method—as described in Chap. 2—but with one crucial difference. Local current densities are not available due to missing spatial information. Instead, we need to work with "bond currents", current contributions flowing from one TB site to another. Such bond currents are defined to fulfil at least a continuity equation in the TB lattice, but not in real space (see Appx. C.3 for details). The bond current $j_{l \to i}$ flowing directly from site l site i is defined as

$$j_{l \to i} := \frac{2}{\hbar} \operatorname{Im} t_{li} \langle \psi | l \rangle \langle i | \psi \rangle \,, \tag{3.6}$$

where $|\psi\rangle$ is the scattering state and t_{li} the hopping element between site l and i.

We first discuss a non-interacting TB two-path model in detail (Sec. 3.3.1). Then, in Sec. 3.3.2, we discuss the role of broken path symmetry using a selection of different non-interacting TB tow-path models. Last, we shortly comment on multi-particle interaction effects (Sec. 3.3.3).

3.3.1 A non-interacting two-path model

Our two-path (toy) model, defined in Fig. 3.13a, features two paths—a top and bottom path—that connect to the same reservoirs, given by semi-infinite TB chains. Importantly, the symmetry between the two paths is broken by adding (different) on-site potentials $\varepsilon_{\mathrm{T/B}}$ to each path. The results of a simple analytic calculation (which we postpone to the end of this section) are displayed in Fig. 3.13b. First, it reproduces the well known fact[147] that antiresonances (destructive interference) are generic encounter in this model: the transmission function $\mathcal{T}$ vanishes at the antiresonance $E_{\mathrm{res}} = \frac{1}{2}(\varepsilon_{\mathrm{T}} + \varepsilon_{\mathrm{B}})$.

(a) TB-model

(b) Bond currents & magnetization
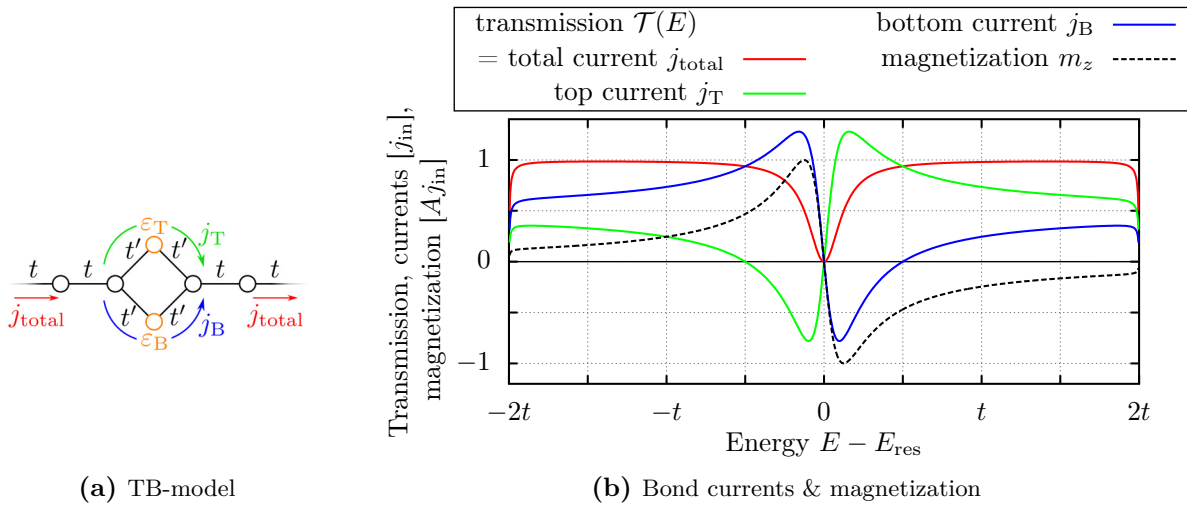
Figure 3.13: (a) Tight-binding (TB) two-path model featuring a ring (hoppings t') with (different) on-site potential $\varepsilon_{T/B}$ in both arms. The ring is attached to semi-infinite TB chains with hopping t. (b) The total current, proportional to the transmission, and current in both arms as calculated for the two-path model of (a). The currents are proportional to the incoming current j_{in}. The magnetization $m_z = (j_B - j_T)A/2$ (proportional to the orbital current) depends on the unspecified area A of the ring. ($t' = t/\sqrt{2}$; $\varepsilon_T = -\varepsilon_B = \frac{1}{2}t$)

As novel results, we also calculate the currents in the separate arms, j_T and j_B. Near the antiresonance, they have opposite sign, thereby generating a loop current. The orbital magnetization $m_z = (j_B - j_T)A/2$ is given in terms of the (unspecified) area A of the ring. Both, the currents in the ring and the orbital magnetization vanish linearly near the antiresonance while the through current (transmission) vanishes quadratically. Thus, the model recovers the qualitative aspects of the AGNR5 with a nitrogen substituent, as discussed in the previous section. Again, the ratio of the ring currents and the through current becomes arbitrarily large near the antiresonance E_{res}, and the ring current changes its direction emphasizing the close relation of the effect to quantum interference.

Qualitative explanation of the antiresonance

To qualitatively explain the interference effect, we first regard a single path (TB chain) with an on-site potential ε_0 on one site. The scattering phase φ,

$$\tan \varphi = -\frac{\varepsilon_0}{2t \sin k} \,, \tag{3.7}$$

accumulated by a plane wave (wavevector k) depends on the absolute value and the sign of ε_0 (cf. Appx. C.4). This is expected, since a positive (negative) on-site potential locally decreases (increases) the kinetic energy and therefore increases (decreases) the wavelength. In two-path models, containing two equidistant paths with different on-site potentials, the different wavelengths lead to a phase difference, which is the origin of the destructive interference effect at the antiresonance.

Analytic solution

To get additional insight, like access to the (complex) transmission amplitude $\phi(E)$, we now solve the two-path (toy) model analytically. The Hamiltonian

$$
\hat{\mathcal{H}} = \left(-t \sum_{n=1}^{\infty} \Big[|-(n+1)\rangle\langle -n| + |n+1\rangle\langle n| \Big] - t' \Big[|T\rangle\langle -1| + |T\rangle\langle 1| \Big] - t' \Big[|B\rangle\langle -1| + |B\rangle\langle 1| \Big] + \text{h.c.} \right)
$$
$$
+ \varepsilon_{\mathrm{T}} |T\rangle\langle T| + \varepsilon_{\mathrm{B}} |B\rangle\langle B| \tag{3.8}
$$

describes the ring and two semi-infinite TB chains, as shown in Fig. 3.13a. We are interested in the scattering solution, i.e., we search for eigenstates of $\hat{\mathcal{H}}$ which include an incoming wave $|\psi_{\mathrm{in}}\rangle = \sum_{n=1}^{\infty} \mathrm{e}^{+ik(-n)} |-n\rangle$ with wavevector k. We thereby effectively restrict the energy $E = -2t \cos k$ to the band of the TB chain, i.e., $E \in [-2t, 2t]$. For the scattering state, we make the ansatz

$$
|\psi\rangle = \sum_{n=1}^{\infty} \left[\left(\mathrm{e}^{+ik(-n)} + r\mathrm{e}^{-ik(-n)} \right) |-n\rangle + \phi \mathrm{e}^{+ikn} |n\rangle \right] + T|T\rangle + B|B\rangle \tag{3.9}
$$

which includes 4 free parameters: a reflexion amplitude r as prefactor of the reflected wave, a transmission amplitude ϕ as prefactor of the transmitted wave, and the wavefunction weights T and B for the sites $|T\rangle$ and $|B\rangle$, respectively. Enforcing the state to be an eigenstate of the Hamiltonian with energy $E = -2t \cos k$, we get four conditions:

$$
\phi \overset{!}{=} \frac{t'}{t} (T + B) \overset{!}{=} 1 + r, \tag{3.10a}
$$

$$
-t'(\mathrm{e}^{-ik} + r\mathrm{e}^{+ik} + \phi \mathrm{e}^{+ik}) + X\varepsilon_{\mathrm{X}} \overset{!}{=} EX \qquad \text{for } X \in \{T, B\}. \tag{3.10b}
$$

Solving this linear set of equations and introducing the abbreviation $E_{\mathrm{res}} = \frac{1}{2}(\varepsilon_{\mathrm{T}} + \varepsilon_{\mathrm{B}})$, we get

$$
T = \frac{2itt' \sin k}{D} (E - \varepsilon_{\mathrm{B}}), \qquad\qquad B = \frac{2itt' \sin k}{D} (E - \varepsilon_{\mathrm{T}}), \tag{3.11a}
$$

$$
\phi = \frac{4it'^2 \sin k}{D} (E - E_{\mathrm{res}}), \qquad\qquad r = \frac{2t'^2 E(E - E_{\mathrm{res}}) - t^2(E - \varepsilon_{\mathrm{B}})(E - \varepsilon_{\mathrm{T}})}{tD}, \tag{3.11b}
$$

which all share a common denominator $D := t(E - \varepsilon_{\mathrm{B}})(E - \varepsilon_{\mathrm{T}}) + 4t'^2 \mathrm{e}^{ik}(E - E_{\mathrm{res}})$.

The transmission function is given by the absolute square of the transmission amplitude, i.e.,

$$
\mathcal{T}(E) = |\phi|^2 = \frac{1}{1 + \left[\dfrac{2t'^2 E(E - E_{\mathrm{res}}) - t^2(E - \varepsilon_{\mathrm{B}})(E - \varepsilon_{\mathrm{T}})}{4tt'^2(E - E_{\mathrm{res}}) \sin k} \right]^2}. \tag{3.12}
$$

For $\varepsilon_{\mathrm{T}} \neq \varepsilon_{\mathrm{B}}$, the transmission vanishes at $E = E_{\mathrm{res}}$ due to destructive interference (antiresonance). Please note that there is no antiresonance (and therefore also no ring currents) without the on-site energies. In particular, $\mathcal{T}(E) = 1 \; \forall E$ if $\varepsilon_{\mathrm{T}} = \varepsilon_{\mathrm{B}} = 0, t' = t/\sqrt{2}$.

We calculate the bond currents in the ring as well as the incoming and total current as

$$j_{\text{in}} := j_{-2 \to -1}\Big|_{\psi = \psi_{\text{in}}} = \frac{2}{\hbar} t \sin k \,, \tag{3.13a}$$

$$j_{\text{total}} := j_{-2 \to -1} = j_{1 \to 2} = \frac{2}{\hbar} t \sin k \, \mathcal{T} \,, \tag{3.13b}$$

$$j_{\text{T}} := j_{T \to 1} = \frac{2}{\hbar} t \sin k \, \mathcal{T} \frac{E - \varepsilon_{\text{B}}}{2(E - E_{\text{res}})} \,, \tag{3.13c}$$

$$j_{\text{B}} := j_{B \to 1} = \frac{2}{\hbar} t \sin k \, \mathcal{T} \frac{E - \varepsilon_{\text{T}}}{2(E - E_{\text{res}})} \,. \tag{3.13d}$$

As expected, the ratio between the total current j_{total} and the incoming current j_{in} is given by the transmission $\mathcal{T}$. The current formulas for the top and both path can be combined to

$$j_{\text{T/B}} = \mathcal{T} \frac{E - \varepsilon_{\text{B/T}}}{2(E - E_{\text{res}})} j_{\text{in}} \,. \tag{3.14}$$

Because of the denominator $(E - E_{\text{res}})$, the local currents $j_{\text{T/B}}$ become arbitrarily large compared to the transmission $\mathcal{T}$ near the antiresonance at E_{res}.

Expansion near the antiresonance E_{res}

Next, we expand the solution in the vicinity of the antiresonance E_{res} keeping only the leading order (assuming $\varepsilon_{\text{T}} \neq \varepsilon_{\text{B}}$). The sine of the wavevector k_{res} near the antiresonance stays positive as long as k_{res} stays away from the band edges, i.e., $\sin k_{\text{res}} > 0$ for $-2t < E_{\text{res}} < 2t$. The auxiliary denominator D used in Eq. (3.11) is given by a (real and negative) constant,

$$D_{\text{res}}(E) = \underbrace{-\frac{t}{4}(\varepsilon_{\text{T}} - \varepsilon_{\text{B}})^2}_{D_{\text{res}}^0} + \mathcal{O}(E - E_{\text{res}}) \,, \qquad D_{\text{res}}^0 \in \mathbb{R}^- \,, \tag{3.15}$$

at the antiresonance. Thus, the transmission amplitude

$$\phi_{\text{res}}(E) \overset{(3.11b)}{=} \underbrace{\frac{4it'^2 \sin k_{\text{res}}}{D_{\text{res}}^0}}_{\phi_{\text{res}}^1} (E - E_{\text{res}}) + \mathcal{O}\Big([E - E_{\text{res}}]^2\Big) \qquad \phi_{\text{res}}^1 \in i\mathbb{R}^- \tag{3.16}$$

vanishes linearly at E_{res} and changes its sign. This is important for two reasons. First, it means that the transmission

$$\mathcal{T}_{\text{res}}(E) = |\phi_{\text{res}}|^2 = |\phi_{\text{res}}^1|^2 (E - E_{\text{res}})^2 + \mathcal{O}\Big([E - E_{\text{res}}]^3\Big) \tag{3.17}$$

vanishes quadratically at the antiresonance. And second, it means that the ring current vanishes linearly, changing its sign and sense of rotation. This is evident from Eq. (3.14), whose expansion

$$j_{\text{T/B}_{\text{res}}}(E) \overset{(3.14)}{=} \mathcal{T}_{\text{res}} \frac{E - \varepsilon_{\text{B/T}}}{2(E - E_{\text{res}})} j_{\text{in}} = \pm \frac{j_{\text{in}}}{4} |\phi_{\text{res}}^1|^2 (\varepsilon_{\text{T}} - \varepsilon_{\text{B}}) (E - E_{\text{res}}) + \mathcal{O}\Big([E - E_{\text{res}}]^2\Big) \tag{3.18}$$

vanishes linearly at the antiresonance. The different signs arise from the term $E - \varepsilon_{\text{B/T}}$; with positive sign for j_{T}, negative sign for j_{B}.

Interference effects

To understand the importance of the sign change in the transmission amplitude for the ring current reversal, we take one step back and consider the total scattering state $|\psi(E)\rangle$,

$$|\psi(E)\rangle = \underbrace{|\psi_{\mathrm{in}}\rangle}_{\sum\limits_{n=-\infty}^{-1} e^{+ikn}|n\rangle} + r(E)\overbrace{|\psi_{\mathrm{r}}\rangle}^{\sum\limits_{n=-\infty}^{-1} e^{-ikn}|n\rangle} + \phi(E)\underbrace{|\psi_{\mathrm{t}}\rangle}_{\sum\limits_{n=1}^{\infty} e^{+ikn}|n\rangle + \frac{t}{2t'}(|T\rangle+|B\rangle)} + \chi(E)\overbrace{|\psi_{\mathrm{imp}}\rangle}^{|T\rangle - |B\rangle}, \tag{3.19}$$

as a superposition of an incoming wave $|\psi_{\mathrm{in}}\rangle$, a reflected wave $|\psi_{\mathrm{r}}\rangle$, a transmitted wave $|\psi_{\mathrm{t}}\rangle$ and a local non-degenerate impurity state $|\psi_{\mathrm{imp}}\rangle$ (with prefactor $\chi(E) = \frac{itt'\sin k}{D}(\varepsilon_{\mathrm{T}}-\varepsilon_{\mathrm{B}})$). The first three terms are just plane waves, with e^{ikn} being the only energy-dependence. Further, we include the term $\frac{t}{2t'}(|T\rangle+|B\rangle)$ in the transmitted wave $|\psi_{\mathrm{t}}\rangle$, so that $|\psi_{\mathrm{in}}\rangle + r|\psi_{\mathrm{r}}\rangle + \phi|\psi_{\mathrm{t}}\rangle$ already satisfies the continuity equation.[D]

To study the interference effects, we investigate the transmitting region where only two terms are relevant, e.g., only $|\psi\rangle = \phi|\psi_{\mathrm{t}}\rangle + \chi|\psi_{\mathrm{imp}}\rangle$ contributes. The bond current from site i to site j is then given by

$$j_{i\to j} = \frac{2}{\hbar}\,\mathrm{Im}\,t_{ij}\langle\psi|i\rangle\langle j|\psi\rangle \tag{3.20}$$

$$= \frac{2}{\hbar}\,\mathrm{Im}\,t_{ij}\Big\{ \underbrace{|\phi|^2\langle\psi_{\mathrm{t}}|i\rangle\langle j|\psi_{\mathrm{t}}\rangle}_{\text{normal current for }|\psi_{\mathrm{t}}\rangle} + \underbrace{|\chi|^2\langle\psi_{\mathrm{imp}}|i\rangle\langle j|\psi_{\mathrm{imp}}\rangle}_{\to\,0\text{ since real}} + \underbrace{\Big[\phi\chi^*\langle\psi_{\mathrm{imp}}|i\rangle\langle j|\psi_{\mathrm{t}}\rangle + \phi^*\chi\langle\psi_{\mathrm{t}}|i\rangle\langle j|\psi_{\mathrm{imp}}\rangle\Big]}_{\text{interference term linear in }\phi} \Big\}$$

where the first term, proportional to the transmission $\mathcal{T} = |\phi|^2$, gives the normal through current for the transmitted state. The second term vanishes since, assuming time-reversal invariance, $|\psi_{\mathrm{imp}}\rangle$ does not carry a current on its own. The interesting term is the third one, where interference effects occur between the local impurity state $|\psi_{\mathrm{imp}}\rangle$ and the transmitted wave. Explicit calculations show that this term carries the ring currents.[E] Near an antiresonance, the transmission amplitude ϕ changes its sign, but χ remains finite. $[\chi_{\mathrm{res}}(E) = \frac{t}{4t'}\,\phi^1_{\mathrm{res}}\,(\varepsilon_{\mathrm{T}}-\varepsilon_{\mathrm{B}}) + \mathcal{O}(E-E_{\mathrm{res}})]$ Therefore, the total sign of the interference term changes simply due to the sign change in the transmission amplitude. This explains the ring current reversal near such antiresonances.

A similar (much shorter) analysis for the interference effects in carbon nanotubes due to structural (Stone-Wales) defects has also been reported by Im et al. *[146].*

3.3.2 The role of broken path symmetry in two-path models

In Fig. 3.14, we show several TB two-path models with and without ring currents. This serves two purposes. First, we show that the physics described by our model is general, and not restricted to exactly one two-path model. Second, we discuss how exact symmetries can suppress the emergence of ring currents.
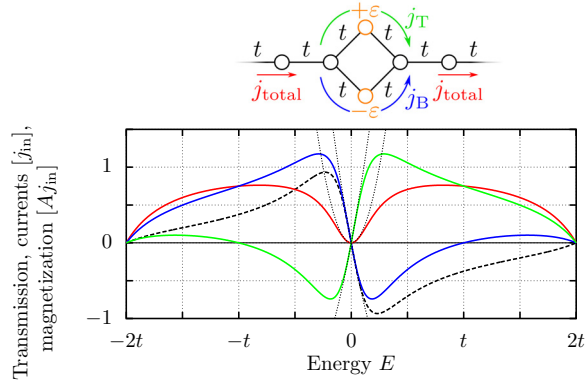
(a) 4-site ring model with symmetry-breaking on-site potentials $\pm\varepsilon$ in the paths. This leads to current backflows running opposite the total current direction. [$\varepsilon=t$; $m_z=(j_B-j_T)A/2$; the dotted curves are $\pm 8(E/t)^1+8(E/t)^2$ and $+16(E/t)^2$]
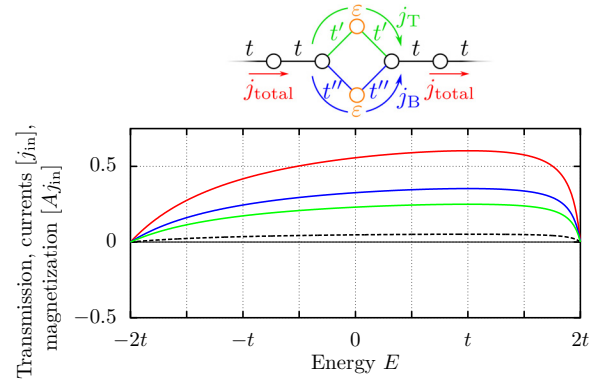
(b) 4-site ring model with different hoppings t', t'' in the paths which is not sufficient to generate backflow currents, i.e., all currents remain positive: $j_{T/B}(E)\geq 0 \quad \forall E$. [$t'=t/2$; $t''=t/\sqrt{2}$; $\varepsilon=t$; $m_z=(j_B-j_T)A/2$]
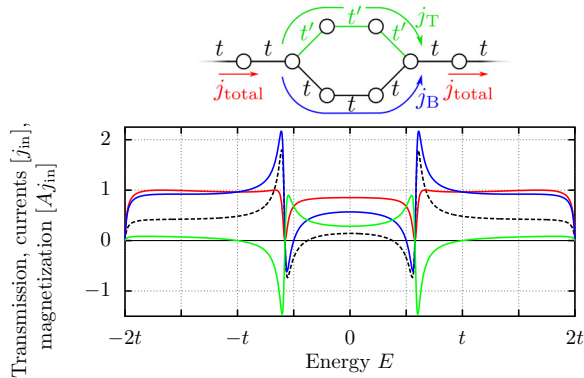
(c) 6-site ring model where the symmetry of the two paths is broken by different hoppings t and t'. [$t'=t/2$; $m_z=(j_B-j_T)A/2$]
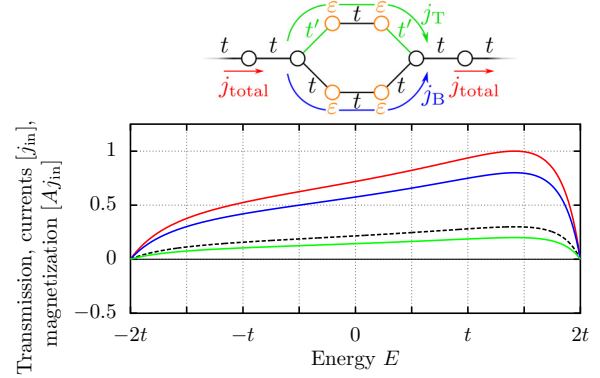
(d) 6-site ring model with the same hopping t *inside* the two paths. The difference in hoppings of the paths to the leads is not sufficient to generate backflow currents. [$t'=t/2$; $\varepsilon=t$; $m_z=(j_B-j_T)A/2$]

Legend

transmission $\mathcal{T}(E)$	
= total current j_{total}	———
top current j_T	———
bottom current j_B	———
magnetization m_z	- - - - -
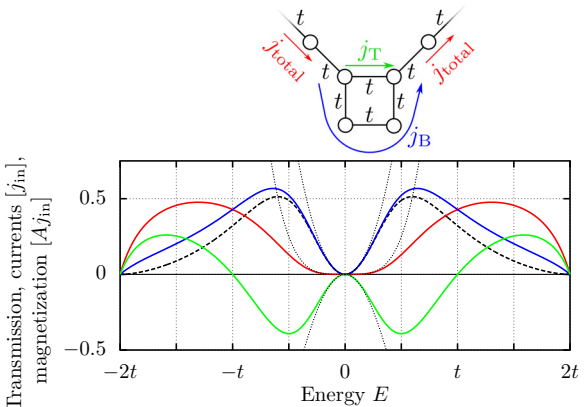
(e) 4-site ring model where the leads are connected asymmetrically, forming different path lengths. In such a model, no further symmetry-breaking terms (in hopping elements or on-site energies) are needed to allow for current backflows. [$m_z=(3j_B-j_T)A/4$; dotted curves are $\pm 4(E/t)^2+2(E/t)^4$ and $+4(E/t)^4$]

Figure 3.14: A selection of tight-binding (toy) models with (left column) and without (right column) ring currents. Ring currents include current backflow, i.e., the current through (at least) one path becomes negative at some energies: $j_T < 0$ or $j_B < 0$.

The first model, Fig. 3.14a, is the already discussed two-path model but with a restricted parameter set ($t'=t$, $\varepsilon_{\mathrm{T}}=-\varepsilon_{\mathrm{B}}$). As discussed, it shows ring currents with sign changes near the antiresonance. The asymmetry in the on-site potentials is important for this model. Without this asymmetry, no antiresonances and ring currents are observed, cf. Fig. 3.14b. Here, the symmetry $t'|T\rangle \leftrightarrow t''|B\rangle$ prohibits ring currents, i.e., the top current j_{T} must flow in the same direction as the bottom current j_{B}.

On-site potentials are not a necessary ingredient for the emergence of rings currents. In larger rings, e.g. a 6-site ring as in Fig. 3.14c, different internal hoppings are sufficient. Since the graph is bipartite (and without on-site potentials), the model is particle-hole symmetric, resulting in a mirror-symmetry for the transport quantities around zero energy. Thus, the two antiresonances are symmetric to zero energy. Both feature a quadratically vanishing through current and a linearly vanishing magnetization. The different inner hoppings are important in this model. Without that difference, no ring current emerge, cf. Fig. 3.14d. We conclude, that exact symmetries relating the inner structure of two paths are sufficient to suppress ring currents; see Appx. C.5 for a detailed (formal) proof.

The last model, Fig. 3.14e, shows the emergence of ring currents due to asymmetric path lengths. Again, such a model is particle-hole symmetric, forbidding a sign change in the transmission amplitude at $E_{\mathrm{res}} = 0$. Instead, the transmission amplitude goes as $\phi_{\mathrm{res}} \propto (E - E_{\mathrm{res}})^2$. This behavior causes quadratically vanishing ring currents (proportional to ϕ_{res}) and a quartic dependence of the transmission, $\mathcal{T}_{\mathrm{res}} = |\phi_{\mathrm{res}}|^2 \propto (E - E_{\mathrm{res}})^4$.

We conclude that the investigated physics is general. Ring currents are proportional to the transmission amplitude ϕ near antiresonances, and therefore, they always exceed the through current which is quadratic in ϕ. Only exact symmetries are able to suppress the phenomenon. Since such exact symmetries are (nearly) always broken in experiment, we expect local ring currents in all geometries that include rings.

3.3.3 Multi-particle interaction effects: a DMRG study

So far, we worked with (effective) one particle theory. In our TB (toy) models, interaction effects were ignored, and on the DFT transport level, interaction is effectively treated at a mean-field level. Therefore, the question whether ring currents survive explicit interaction effects was never touched. For that, we cite the master thesis of B. Schönauer[148]. Although there are many studies of explicit interaction effects in TB models, the work of Schönauer is of special importance to our work since he studied the interaction effects on the bond currents using the same TB two-path model as used in this thesis, cf. Fig. 3.13a for the TB model.[F]

In his work, density matrix renormalization group (DMRG[149, 150]) was used to study the influence of interactions on the time-dependence of bond currents. The interaction was given by a nearest-neighbor density-density interaction,

$$\Delta\hat{\mathcal{H}} = U\left[\hat{n}_{\mathrm{T}}\,\hat{n}_{+1} + \hat{n}_{+1}\,\hat{n}_{\mathrm{B}} + \hat{n}_{\mathrm{B}}\,\hat{n}_{-1} + \hat{n}_{-1}\,\hat{n}_{\mathrm{T}}\right], \tag{3.21}$$

where $U > 0$ is the repulsive interaction and $\hat{n}_x$ is the density operator of site x. The interaction was restricted to the 4-site ring structure. The leads were assumed non-interacting, but correlation effects in the leads were kept.

An example of his investigations is shown in Fig. 3.15. There are two main effects. First, the upper and lower link currents exceed the transmitted current significantly, and most of the time, one of them flows against the total current direction. Thus, explicit interaction effects do not destroy ring currents, at least not in principle. This is the most important result of Schönauer's work in the context of this thesis.

Second, his work shows that there are even more open questions related to ring currents. As shown in Fig. 3.15, the bond currents oscillate in time. Schönauer was able to relate the frequency ω of the current oscillations to the energy difference between the many-body groundstate of the uncoupled ring structure and its first excited state. So far, an estimate for the time-scale on which (if at all) the oscillations decay to a steady state is not available and remains an open question.

Please refer to Schönauer's thesis[148] as we are neglecting many (numerical and physical) details.
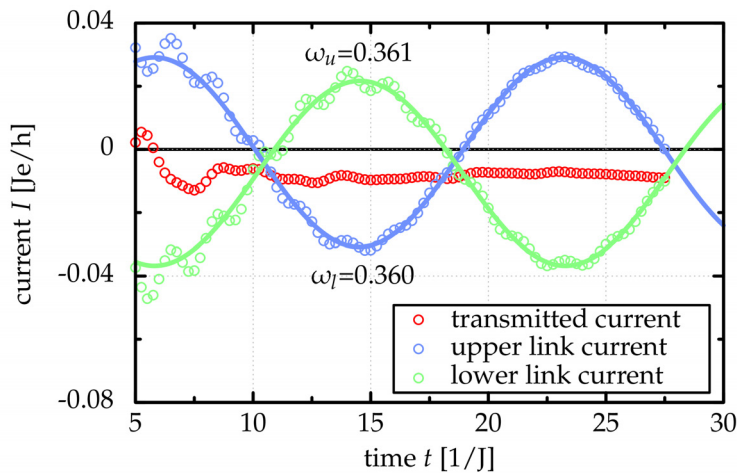
Figure 3.15: Time-dependence of bond currents in a two-path TB model which includes a nearest-neighbor density-density interaction. At time $t < 0$, the system is prepared in the groundstate with an applied bias voltage V_{bias}. At time $t = 0$, the bias voltage is instantaneously switched off and the system evolves according to the Schrödinger equation. Cosine functions with frequency ω (solid lines) are fitted to the numerical data (circles). Numerical parameters: $t=t'=J$, $\varepsilon_{\mathrm{T}}=0.5J$, $\varepsilon_{\mathrm{B}}=0$, $U=2J$, $t''=0.5J$, $eV_{\mathrm{bias}}=0.4J$. Plot reproduced with permission of B. Schönauer[148, Fig. 4.9].

Notes to chapter 3

The notes are for completeness, reproducibility and to help interested readers understand all the fine technical details.

^{A} The superposition of several current channels in pristine AGNRs is a simple summation of all channels. No interference effects occur between the channels. The interference effects are already included in the band-structure determining the spatial shape of the individual bands/channels. (page 38)

^{B} We write that the width of an AGNRN_C is only *approximately* equal to $L_y = (N_C + 1)a_y$ because it is unclear where the exact border is; how much "space" do the hydrogen atoms "occupy"? The choice $L_y = (N_C + 1)a_y$ is a simple choice consistent with TB considerations. Implementing hardcore boundary conditions as in Eq. (3.1) in a TB model could be done by adding one additional site (the hydrogen site) at each border with an infinite on-site potential. In that case, the width L_y is proportional to N_C+1. (page 41)

^{C} There is evidence that an AGNR5 with a nitrogen substituent (placed on position 3) does not feature spin-polarization. In FHI-AIMS, a spin-polarized DFT calculation with an initial spin density of unity at the nitrogen atom converges to a nearly spin-unpolarized solution. The states at the Fermi energy of the finite cluster are split by $3.5\,\mathrm{meV}$ in the different spin channels whereas the average level splitting (of ten states near the Fermi energy) is about $200\,\mathrm{meV}$. For states away from the Fermi energy, the spin splitting is even smaller. This remaining spin-polarization is probably due to the need to stop the SCF iteration at some point. (Basis set: `tier1`, convergence settings: `sc_accuracy_rho/eev/etot 7E-5/1E-3/1E-6`)

Furthermore, open-shell and closed-shell calculations yield the same transport behavior. In Fig. 2.8, we compared closed-shell calculations (with fractional occupation numbers using FHI-AIMS) with the majority spin channel (α) of collinear open-shell calculations (with integer occupation numbers using TURBOMOLE). Indeed, we observed a good collapse of all data curves. The minority channel (β) looks slightly different due to different occupation induced by an overall odd number of electrons in combination with integer occupation number. Allowing for fractional occupation numbers as in FHI-AIMS, a collinear open-shell calculation converges to the closed-shell calculation. (page 46)

^{D} An alternative explanation for the partitioning used in Eq. (3.19) is to move all terms directly proportional to the scattering amplitude ϕ to the transmitted wave. On the technical level, the partitioning separates the contribution of the two paths, in a symmetric and anti-symmetric part:

$$T|T\rangle + B|B\rangle = \hspace{3cm} (3.22)$$

$$= \underbrace{\frac{T + B}{2}}_{\text{symmetric}}\left(|T\rangle + |B\rangle\right) + \underbrace{\frac{T - B}{2}}_{\text{anti-symmetric}}\left(|T\rangle - |B\rangle\right).$$

where $\overset{(3.10a)}{=} \frac{t}{2t'}\phi$ and $\overset{(3.11a)}{=} \frac{itt'\sin k}{D}$.

The symmetric parts contribute to the total through current and are therefore included in $|\psi_\mathrm{t}\rangle$. The asymmetric terms remain in $|\psi_\mathrm{imp}\rangle$. (page 54)

^{E} Here, we explicitly evaluate the interference term

$$j_{i\to j}^{\mathrm{interf.}} = \frac{2}{\hbar}\,\mathrm{Im}\,t_{ij}\left[\phi\chi^*\langle\psi_\mathrm{imp}|i\rangle\langle j|\psi_\mathrm{t}\rangle + \phi^*\chi\langle\psi_\mathrm{t}|i\rangle\langle j|\psi_\mathrm{imp}\rangle\right] \quad (3.23)$$

near the antiresonance $E = E_\mathrm{res}$. [The interference term was originally defined in Eq. (3.20).] We restrict ourselves to the top path, i.e., to $j_\mathrm{T} := j_{T\to 1}$, meaning $i = T$, $j = 1$. The second part of the interference term vanishes because $\langle 1|\psi_\mathrm{imp}\rangle = 0$. We are left with the first part,

$$j_{\mathrm{T\,res}}^{\mathrm{interf.}} = \frac{2}{\hbar}\,\mathrm{Im}\,t'\left[\underbrace{\phi_\mathrm{res}}_{\phi_\mathrm{res}^1\,(E - E_\mathrm{res})} \cdot \overbrace{\chi_\mathrm{res}^*}^{\frac{t}{4t'}[\phi_\mathrm{res}^1]^*(\varepsilon_\mathrm{T} - \varepsilon_\mathrm{B})} \cdot \underbrace{\langle\psi_\mathrm{imp}|T\rangle}_{1} \cdot \overbrace{\langle 1|\psi_\mathrm{t}\rangle}^{\mathrm{e}^{ik_\mathrm{res}}}\right] + \ldots$$

$$= \underbrace{\frac{t\sin k_\mathrm{res}}{2\hbar}}_{j_\mathrm{in}/4}|\phi_\mathrm{res}^1|^2\,(\varepsilon_\mathrm{T} - \varepsilon_\mathrm{B})\,(E - E_\mathrm{res}) + \ldots, \quad (3.24)$$

which exactly reproduces the top current $j_{\mathrm{T\,res}}$ near the antiresonance, cf. Eq. (3.18). (page 54)

^{F} In addition to the TB (toy) model shown in Fig. 3.13a, B. Schönauer[148] replaced the link t directly between the 4-site ring and the two semi-infinite TB chains by a weak link $t'' < t$. (page 56)

4 Chapter 4
Application II:
Graphene with hydrogen adsorbates

We investigate the current density $\mathbf{j}(\mathbf{r})$ in hydrogenated armchair graphene nanoribbons (AGNRs) with finite hydrogen coverage with about 10^3 carbon atoms. We start, in Sec. 4.1, by studying the linear current response of a rectangular graphene flake (16×83) for a fixed hydrogen concentration. We discover pronounced patterns in the local current density, namely current vortices, that induce orbital magnetism. The current density follows a lognormal distribution, that reflects in broad (spatial) fluctuations. This indicates that the magnitude of the ring currents in several spatial regions exceeds the average (through) current by orders of magnitude. The associated magnetic fields exhibit strong fluctuations and large field gradients. To observe the spatial fluctuations of the induced magnetic fields, we propose a NMR-type experiment in the presence of an applied bias voltage.

In Sec. 4.2, we discuss the dependence of our results on the system size. Our predictions aim at the bulk limit, i.e., for experimental sample sizes, which are typically larger than the systems accessible to DFT transport. Additionally, we cover the effects of finite bias voltages, different adsorbate concentrations, and different adsorbate types. In all cases, the general features—large current vortices and a lognormal distribution of the current density—remain.

In Sec. 4.3, we analyze the magnetization m_z, effectively the average sense of rotation of all current vortices. We predict a total magnetization of $\sqrt{\langle m_z^2 \rangle} \sim 1\,\mu_\mathrm{B} \cdot \sqrt{V_\mathrm{bias}/\,\mathrm{V}}$ which scales with the square root of the bias voltage, and is independent of the system size.

Effects of lattice relaxation, especially crosstalk between several adsorbates via their interaction in terms of lattice strain, can play an important role for the optimal lattice geometry. In Sec. 4.4, we study the relaxation effects in hydrogenated AGNR41. We find that the crosstalk indeed feeds back into the electronic structure, the transmission function and the local current density. However, the qualitative (statistical) features of the current density remain unaffected.

(a) AGNR16×83

(b) AGNR8×41
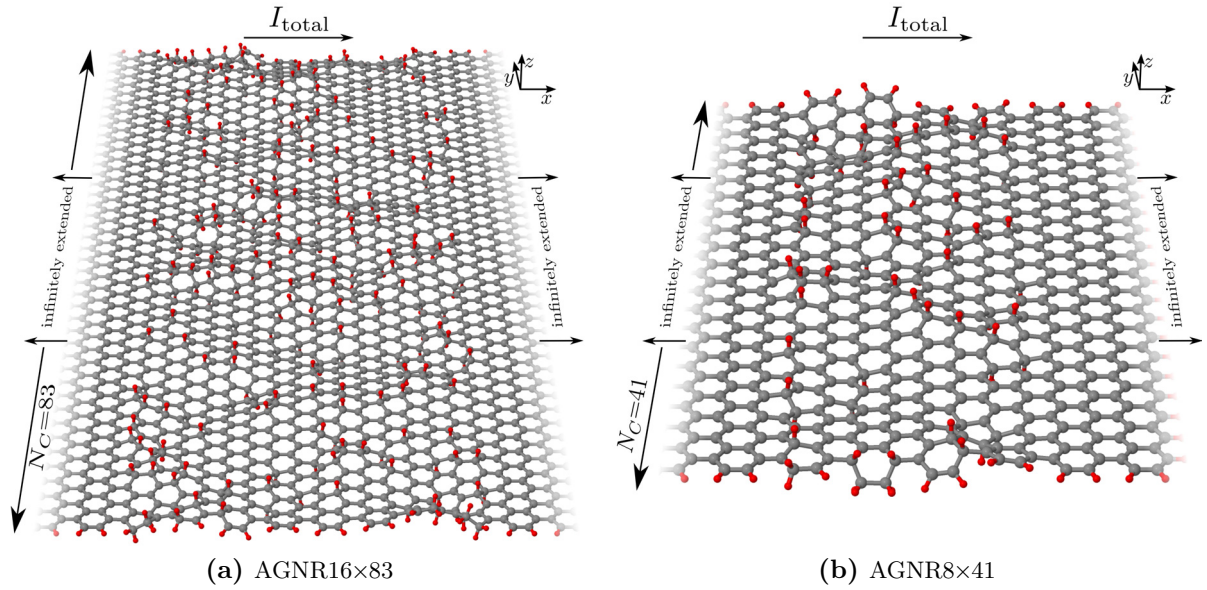
Figure 4.1: (a) A wide hydrogen-terminated armchair graphene nanoribbon (AGNR16×83) that has been functionalized with 20% hydrogen atoms. The functionalized area (16×83 carbon atoms including hydrogen termination and additional 266 adsorbed hydrogen atoms) has been geometrically relaxed using DFT. The ribbon is extended (infinitely) in x-direction by pristine AGNR83 employing an infinite lattice algorithm. (b) A smaller sample (AGNR8×41) with 20% hydrogen adsorbates (i.e., additional 66 adsorbed hydrogen atoms). [Plot shows carbon atoms in gray, hydrogen atoms in red. Transport is in x-direction.]

4.1 Transport through wide hydrogenated AGNRs

We start our investigations by considering a wide armchair graphene nanoribbon: an AGNR16×83 which is functionalized with 20% hydrogen, see Fig. 4.1a. This is one of the largest AGNRs available to our DFT transport method. For comparison against finite size effects, we also employ a smaller sample (AGNR8×41), also functionalized with 20% hydrogen, as shown in Fig. 4.1b. The hydrogen adatoms are randomly positioned above and below the carbon atoms. (For construction details, see Appx. A.1.) The AGNRs are geometrically relaxed using DFT until all remaining forces drop below 10^{-2} eV/Å. For our simulations, we use closed-shell DFT with `tier1` basis functions using the Perdew-Burke-Ernzerhof functional (PBE)[151] as implemented in FHI-AIMS[130].

We chose hydrogen because hydrogen is one of the common adsorbates on graphene seen in experiment. The concentration of 20% is selected due to two reasons: (i) experiments are usually performed with a (quite large) finite concentration, (ii) the concentration should be below the percolation threshold of 30.3% site defects.[A]

In this section, we focus on transport effects in the linear response limit of AGNR16×83/AGNR8×41 with a fixed hydrogen concentration of $n = 20\%$. We defer investigation of the detailed size dependence, effects of a finite bias voltage, different adsorbate concentrations, and different adsorbate types to Sec. 4.2. The effects of spin polarization on the current density are deferred to the following chapter, especially to Sec. 5.2.4.

(a) AGNR16×83   **(b)** AGNR8×41
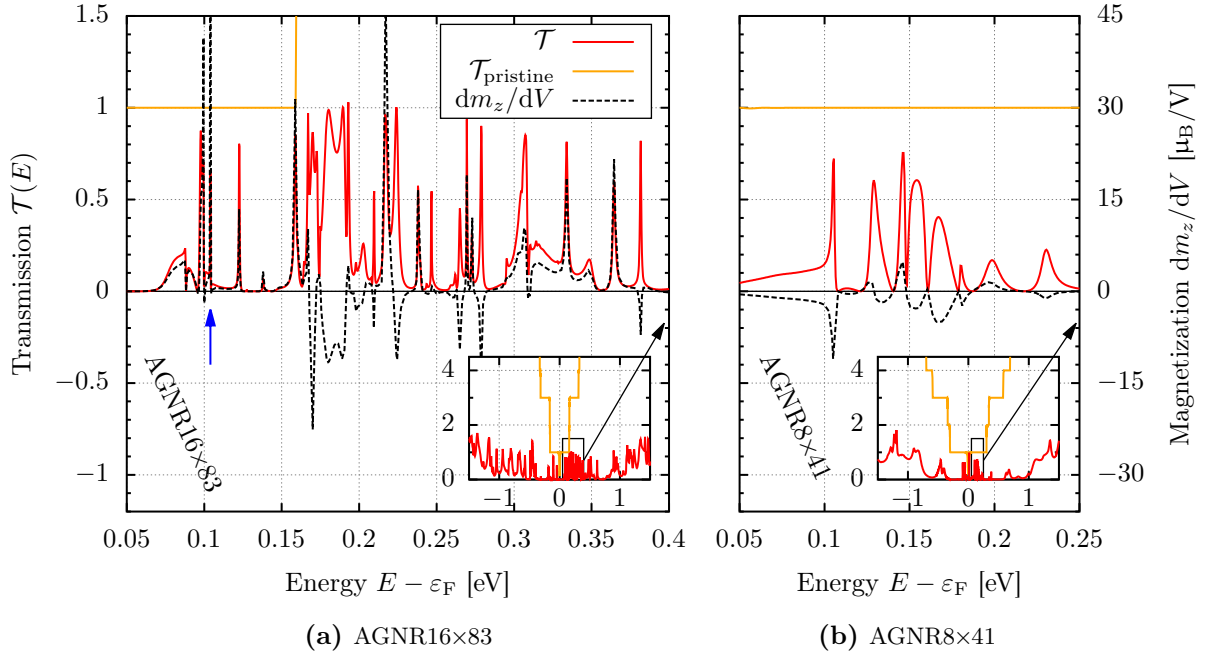
Figure 4.2: Transmission functions $\mathcal{T}$ (red, left y-axis) and sample magnetization per bias $\mathrm{d}m_z/\mathrm{d}V_{\mathrm{bias}}$ (perpendicular to the graphene plane, dashed black, right y-axis) belonging to the ribbons shown in Fig. 4.1. The transmission features many antiresonances; in the vicinity of the antiresonances, the sample magnetization $\mathrm{d}m_z/\mathrm{d}V_{\mathrm{bias}}$ shows sign changes. The transmission functions $\mathcal{T}_{\mathrm{pristine}}$ (orange, left y-axis) of pristine ribbons exhibit sharp steps and a small band gap at $E = \varepsilon_{\mathrm{F}}$ with $\mathcal{T} = 0$. The blue arrow marks the energy for which the current density and magnetic field response are plotted in Fig. 4.3. [DFT details: FHI-AIMS, basis set tier1, closed-shell. For the AGNR16×83, there are two clipped peaks in the magnetization at $E - \varepsilon_{\mathrm{F}} = 0.102\,\mathrm{eV}$ (and $0.217\,\mathrm{eV}$), reaching up to $\mathrm{d}m_z/\mathrm{d}V = 67.8\,\mu_{\mathrm{B}}/\mathrm{V}$ (and $50.1\,\mu_{\mathrm{B}}/\mathrm{V}$), respectively.]

4.1.1 Transmission and magnetization

As a first evidence that sizable ring currents, as discussed in Chap. 3, also exist in larger samples, we plot the transmission and the total magnetization (per bias) in Fig. 4.2 for both AGNRs. The ring currents reflect in a non-zero total magnetization $\mathrm{d}m_z/\mathrm{d}V_{\mathrm{bias}}$. [Total magnetization: $\mathbf{m} = \frac{1}{2}\int \mathbf{r} \times \mathbf{j}_{\mathrm{el}}(\mathbf{r})\,\mathrm{d}\mathbf{r}$, cf. Eq. (2.16).] The transmission function, $\mathcal{T}(E)$, is strongly peaked; each peak reflects an individual current carrying sample states. The many maxima are separated by very sharp antiresonances.

A suppressed transmission ($\mathcal{T} \approx 0$) in this setup should be understood as a consequence of quantum interference. The adsorbates split off resonant levels from the conduction band continuum. In the present case, the hydrogen adsorbates force the underlying carbon atom into an sp^3-hybridization. Thus, the former π-electron of the carbon atom is removed from the π-band. The associated quasi-localized state contributes a separate transport channel that can interfere with the original ones. At the antiresonances, the interference is destructive and the transmission vanishes. The magnetization $\mathrm{d}m_z/\mathrm{d}V_{\mathrm{bias}}$ follows the peak structure of the transmission; at most antiresonances, it also changes its sign. Such physics is described by the same mechanism as in Sec. 3.3: sign changes in the transmission amplitude are induced by quantum interference effects, and reflect in a quadratically vanishing transmission function, but in linearly vanishing local ring currents.
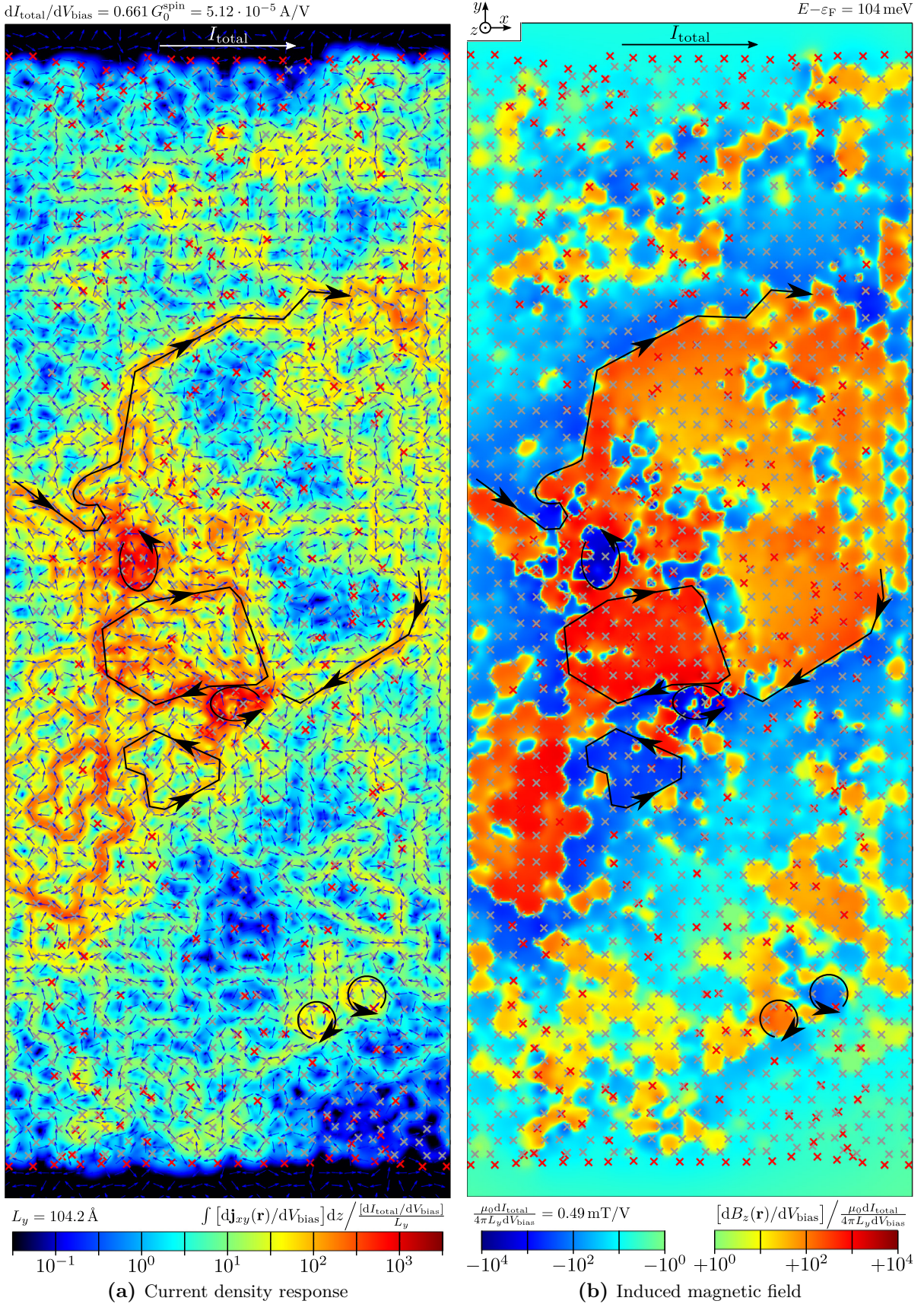
Figure 4.3: (a) Local current density response (integrated over the out-of-plane direction) for the hydrogenated AGNR16×83 shown in Fig. 4.1a. The current exhibits very strong mesoscopic fluctuations that reflect in a logarithmic color scale covering five decades. Some interesting current paths are drawn in the picture for illustration. Plot shows current amplitude (color), current direction (arrows), carbon atoms (gray crosses), and hydrogen atoms (red crosses). (b) Induced magnetic field (in out-of-plane direction). The magnetic field strongly varies and changes sign from region to region. The field is plotted in the (averaged) carbon plane ($z{=}0$), but being divergence free, it hardly changes with z.

4.1.2 Current density response and induced magnetic field

Current density

Figure 4.3a shows the current density response in AGNR16×83 at the energy corresponding to the transmission peak marked by a blue arrow in Fig. 4.2a. The current flow follows indeed a complicated filamentary pattern, and more importantly, the flow has a pronounced tendency to form ring structures (eddies) with a local current strength that exceeds the (average) through current by orders of magnitude (see dark red regions). Also, local backflow channels where the current runs against the average current exist. Such local backflow channels are evidence of ring currents of a larger spatial extend. In general, large current fluctuations—the current density in Fig. 4.3a covers five decades (see logarithmic color scale)—are characteristic for mesoscopic fluctuations of wavefunctions in disordered media[152]. The latter manifest as reproducible fluctuations of the transmission (cf. Fig. 4.2) with an amplitude corresponding to the order of one conductance quantum when control parameters like the energy are varied, e.g., by gating.

We checked that the current density response at other transmission peaks is qualitatively the same: local ring currents exceed the average through current by orders of magnitude, and the current magnitude strongly varies from region to region. This is to be expected also from the magnetization response plotted in Fig. 4.2 since the latter shows the same features over a broad energy range.

Magnetic fields

The strong fluctuations in the current density induce a highly inhomogeneous magnetic field, see Fig. 4.3b. The sign of the out-of-plane component B_z changes from region to region. The resulting magnetic islands strongly vary in size, ranging from subatomic distances up to several nanometers. This is an additional evidence for current eddies of different size since each magnetic island correspond to a ring current which encloses the corresponding region.

Remark on m_x, m_y, B_x, B_y: We have restricted ourselves to the magnetization m_z and magnetic field $B_z(z{=}0)$ perpendicular to the graphene ribbon. The other components of the magnetization are suppressed by an approximate z-mirror symmetry. For example, the magnetization (per spin) induced by the current density of Fig. 4.3a is calculated as $\mathbf{m} = (-0.7, 0.5, 67.8)\,\mu_B/V$. It perfectly aligns in z-direction. [The finite grid error for each component is in the order of $\Delta\mathbf{m}^{\mathrm{grid}}_{x/y/z} = 2\,\mu_B/V$ so that m_x, m_y vanish within our systematic error bounds.] The in-plane-components of the magnetic field, B_x and B_y, also follow an approximate z-mirror symmetry, i.e., every contribution above the carbon plane is canceled by an opposite contribution from below. Additionally, the divergence condition $\partial_z B_z + \cdots = 0$ reduces the z-dependence of B_z while the features of B_x, B_y wash out quite fast when moving away from the carbon plane (see Appx. D.2.2 for an example).

4.1.3 Distribution functions of the current density and the induced magnetic field

Current density

We already discussed that the current density has a broad distribution since its magnitude covers five decades as shown in Fig. 4.3a. In this section, we quantify the current density distribution, and see that it is logarithmically broad, i.e., described by a lognormal distribution.

Figure 4.4 shows the distribution

$$\mathcal{P}(\ln x) = \frac{1}{N_{\text{Points}}} \sum_{\mathbf{r}} \delta\left(\ln x - \ln \frac{\left| \int \mathrm{d}z\, j_i^\diamond(\mathbf{r}) \right|}{j_{\text{avg;y}}^\diamond} \right) \qquad \left[j_{\text{avg;y}}^\diamond = \frac{\mathrm{d}I_{\text{total}}}{L_y \mathrm{d}V_{\text{bias}}} = \frac{e\mathcal{T}}{hL_y} \right] (4.1)$$

of the current density response $j_i^\diamond = \mathrm{d}j_i/\mathrm{d}V_{\text{bias}}$, integrated over the z-direction. To form a dimensionless quantity, the integrated current density is normalized to the average through current per width $j_{\text{avg;y}}^\diamond$, and the logarithm of the ratio is investigated. (To avoid overcrowded distribution plots, we use a diamond $\diamond$ to mark linear response quantities, i.e., $X^\diamond = \mathrm{d}X/\mathrm{d}V_{\text{bias}}$.)

We first note that the distribution of the current magnitude follows (nearly perfectly) a lognormal distribution

$$\mathcal{P}_{\text{lognormal}}(\ln x) = \frac{1}{\sqrt{2\pi}\sigma} \exp\left[- \frac{(\ln x - \mu)^2}{2\sigma^2} \right], \qquad \left[x = \left| \int \mathrm{d}z\, \mathbf{j}^\diamond \right| \Big/ j_{\text{avg;y}}^\diamond \right] (4.2)$$

which has been parameterized by the mean value μ and the standard deviation σ of the simulated
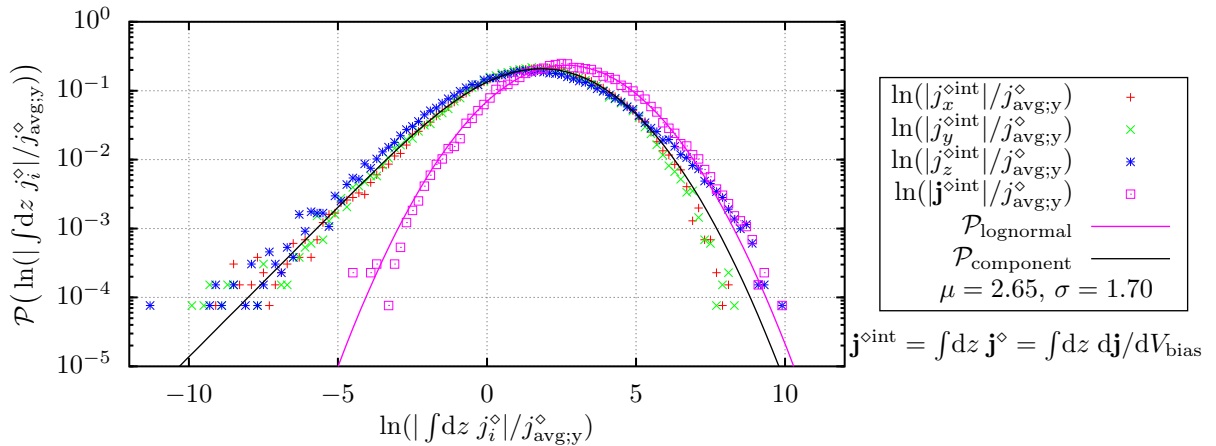
Figure 4.4: Distribution function for the current density response $\mathbf{j}^{\diamond\text{int}} = \int \mathrm{d}z\, \mathrm{d}\mathbf{j}/\mathrm{d}V_{\text{bias}}$ (integrated over the out-of-plane direction and normalized to the average through current) of an AGNR16×83 at $E-\varepsilon_{\text{F}}=0.104\,\text{eV}$ (as shown in Fig. 4.3a). The lognormal distribution $\mathcal{P}_{\text{lognormal}}$ has been parameterized by the calculated mean μ and standard deviation σ of the distribution $\mathcal{P}[\ln(|\mathbf{j}^{\diamond\text{int}}|/j_{\text{avg;y}}^\diamond)]$. It appears as a (downward opening) parabola in the double-logarithmic plot. The values μ and σ also determine $\mathcal{P}_{\text{component}}$ which is the expected distribution function for a single component of a vector whose magnitude is lognormal distributed, assuming that all components are equivalent (see text and Appx. D.5.2).

current magnitude.[B] Most surprisingly, the mean value—the most frequent value—is significantly larger than zero, $\mu > 0$. The mean value μ refers to the current density normalized to the average through current. Therefore, already the most probable (i.e. typical) current density value (maxima of the $\mathcal{P}_{\mathrm{lognormal}}$ in Fig. 4.4) exceeds the average through current by a factor of $\mathrm{e}^{\mu} \approx 14$. Due to the continuity equation, this must imply the presence of strong ring currents, as seen in Fig. 4.3a.

Next, we turn to the distributions of the individual current components $j_{x/y/z}$, cf. Fig. 4.4. These distributions are asymmetric with long tails for smaller values. The asymmetry and the long tails are expected and coincide well with the analytical expectation $\mathcal{P}_{\mathrm{component}}$. The distribution $\mathcal{P}_{\mathrm{component}}$,

$$
\mathcal{P}_{\mathrm{component}}(\ln |x_i|) = \int\limits_0^{2\pi} \mathrm{d}\varphi \underbrace{\mathcal{P}(\varphi)}_{1/2\pi} \int\limits_{-1}^{+1} \mathrm{d}\cos\theta \underbrace{\mathcal{P}(\cos\theta)}_{1/2} \times
$$

$$
\times \int\limits_{-\infty}^{+\infty} \mathrm{d}\ln x \; \mathcal{P}_{\mathrm{lognormal}}(\ln x)\, \delta\big(\ln |x_i| - \ln(|x\cos\theta|)\big) \qquad (4.3)
$$

$$
= \frac{\mathrm{e}^{\frac{\sigma^2}{2}}}{2} \frac{|x_i|}{\tilde{x}} \operatorname{erfc}\Big(\frac{\sigma}{\sqrt{2}} + \frac{1}{\sqrt{2}\sigma} \ln\frac{|x_i|}{\tilde{x}}\Big), \qquad \text{with } \tilde{x} := \mathrm{e}^{\mu},
$$

describes individual components x_i of a vector whose magnitude $x = |\mathbf{x}|$ follows a lognormal distribution with mean μ and width σ. An additional assumption in the calculation of $\mathcal{P}_{\mathrm{component}}$ is that all three vector components are equivalent, i.e., the spherical angles φ and $\cos\theta$ are uniformly distributed: $\mathcal{P}(\varphi) = 1/2\pi$ and $\mathcal{P}(\cos\theta) = 1/2$ (see Appx. D.5.2 for the analytical calculation of $\mathcal{P}_{\mathrm{component}}$).

Surprisingly, the assumption of equivalent vector components seems to hold true for the current density distributions shown in Fig. 4.4, i.e., the distribution for the out-of-plane current component (j_z) coincides with the distributions for the in-plane current component (j_x/j_y). This happens only for a large impurity concentration (cf. Sec. 4.2.2) where the graphene sheet is no longer locally flat but strongly distorted since many carbon atoms are moved out of the average carbon plane due to sp³-hybridization. Therefore, we relate isotropic current density distribution functions to lattice deformation in the out-of-plane direction.

The assumption of uniformly distributed angles can also be checked directly by calculating the distribution functions of the angles, see Fig. 4.5. The in-plane angle φ is indeed (nearly) uniformly distributed, while the distribution for the out-of-plane angle $\cos\theta$ is only approximately uniform. The remaining features are an enhancement of $\cos\theta = 0$ ($\mathbf{j} \perp \mathbf{e}_z$) and $\cos\theta = \pm 1$ ($\mathbf{j} \| \mathbf{e}_z$).

The first peak ($\cos\theta{=}0$)—describing a preferred current flow *in* the carbon plane—is expected. The second peak ($\cos\theta{=}\pm 1$), however, is unexpected since it describes currents perpendicular to the graphene plane. In that case, some of the electronic orbitals that form the hydrogen-carbon bonds participate in the transport. (See Appx. D.2 for additional cuts through the three-dimensional current density.)

In summary, we found that the magnitude of the current density follows a lognormal distribution, centered at a current value which exceeds the average through current. This is important since
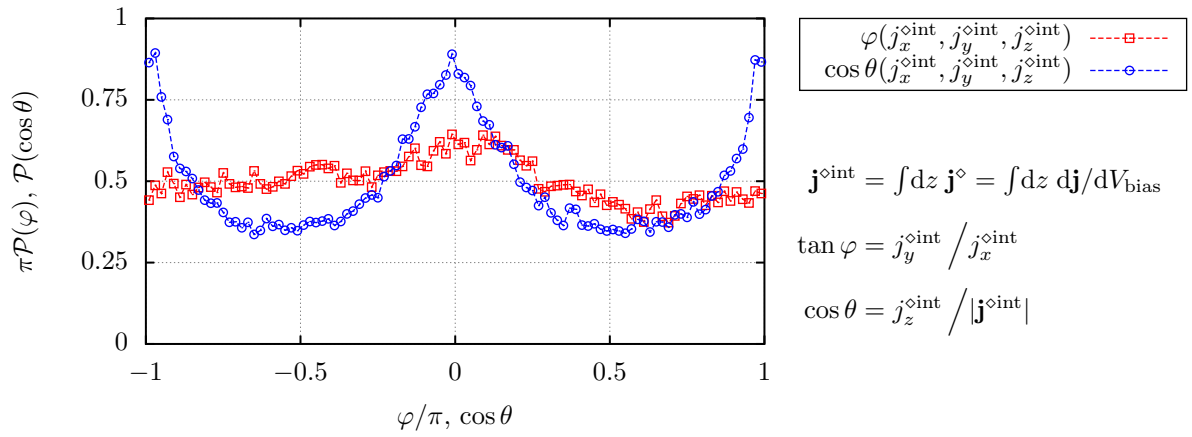
Figure 4.5: Distribution functions for the azimuthal angle φ and the polar angle θ of the current density response $\mathbf{j}^{\diamond\mathrm{int}} = \int \mathrm{d}z\,\mathrm{d}\mathbf{j}/\mathrm{d}V_{\mathrm{bias}}$ (integrated over the out-of-plane direction and normalized to the average through current) of an AGNR16×83 at $E - \varepsilon_{\mathrm{F}} = 0.104\,\mathrm{eV}$ (as shown in Fig. 4.3a). [$j_x^{\diamond\mathrm{int}} = |\mathbf{j}^{\diamond\mathrm{int}}|\sin\theta\cos\varphi$, $\ j_y^{\diamond\mathrm{int}} = |\mathbf{j}^{\diamond\mathrm{int}}|\sin\theta\sin\varphi$, $\ j_z^{\diamond\mathrm{int}} = |\mathbf{j}^{\diamond\mathrm{int}}|\cos\theta$]

(a) Distribution of induced magnetic field

(b) Distribution of magnetic field angles
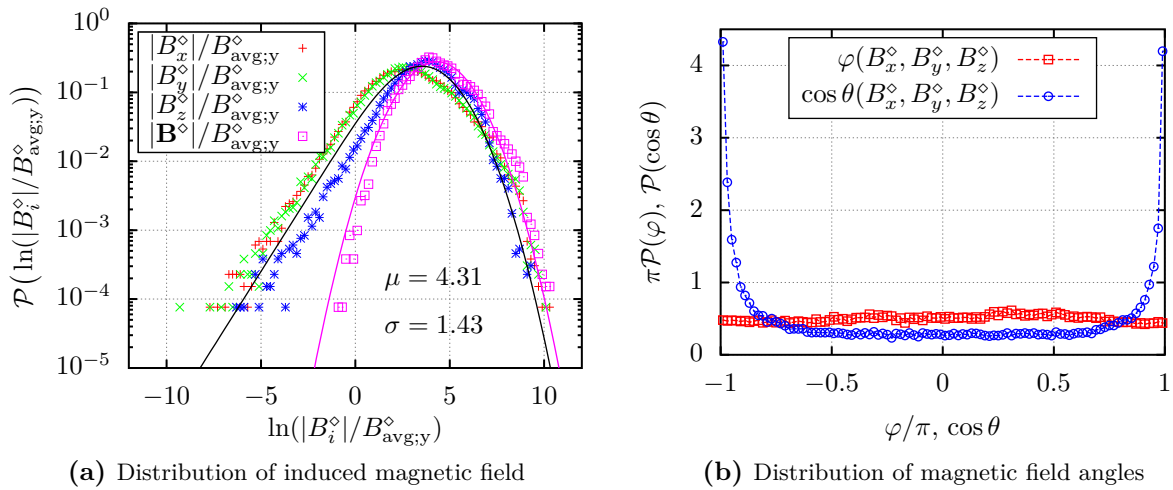
Figure 4.6: (a) Distribution functions for the magnetic field response $\mathbf{B}^{\diamond} = \mathrm{d}\mathbf{B}/\mathrm{d}V_{\mathrm{bias}}$ (in the carbon plane, $z=0$) of an AGNR16×83 at $E - \varepsilon_{\mathrm{F}} = 0.104\,\mathrm{eV}$ (as shown in Fig. 4.3b). (b) Distribution functions of the angles of the induced magnetic field.

$\left[\mathbf{B}_x^{\diamond} = |\mathbf{B}^{\diamond}|\sin\theta\cos\varphi, \ \ \mathbf{B}_y^{\diamond} = |\mathbf{B}^{\diamond}|\sin\theta\sin\varphi, \ \ \mathbf{B}_z^{\diamond} = |\mathbf{B}^{\diamond}|\cos\theta, \ \ B_{\mathrm{avg;y}}^{\diamond} = (\mu_0\mathrm{d}I_{\mathrm{total}})/(4\pi L_y\mathrm{d}V_{\mathrm{bias}}) = (\mu_0 e\mathcal{T})/(4\pi L_y h)\right]$

these current contributions must refer to ring currents due to the continuity equation. (Since the current density integrated over any cross section yields the through current, any local enhancement must result in backflow somewhere else.)

Magnetic field

The distribution functions for the magnetic field component are shown in Fig. 4.6. They may be relevant for NMR-type experiments since they determine the distribution of the NMR-shifts (cf. Sec. 4.1.4). Since the magnetic field is induced by the current density, one expects a similar distribution for both. Indeed, the absolute value of the magnetic field also follows a lognormal distribution. On the other hand, the magnetic field has a preferred direction: the z-direction. The angles $\cos\theta = \pm 1$ ($\mathbf{B}\|\mathbf{e}_z$) are more likely than angles with in-plane contributions, see Fig. 4.6b.

Remark: The current density decays exponentially at the transition from the graphene flake to the vacuum. We are not interested in these border effects. They start to emerge in the vicinity of the hydrogen termination. Therefore, only current contributions at least one carbon ring away from the border are included in the distribution functions. Similarly for the magnetic field. Please refer to Appx. D.5.3 for details.

4.1.4 Observable consequences of nanoscale ring currents

Detailed mappings of the current flow have been attempted relatively recently. In 2000, Topinka *et al.*[153, 154] investigated the current flow through quantum dots (QD) embedded in a two-dimensional electron gas, and measured the change of the conductance $\delta G(\mathbf{r})$ induced by placing a charged AFM-tip in the current flow at position $\mathbf{r}$. A large change in $\delta G(\mathbf{r})$ was related to a large current density at point $\mathbf{r}$ (before disturbing with the tip). They observed a rich filamentary structure. However, the original interpretation of the pattern in terms of current flows has been questioned, later. Indeed, the conductance change $\delta G(\mathbf{r})$ is not necessarily directly proportional to $|\mathbf{j}(\mathbf{r})|$. Instead, in the course of the analysis[155], it was emphasized that, strictly speaking, $\delta G(\mathbf{r})$ reflects the sensitivity of the scattering states to local perturbations at position $\mathbf{r}$. The dependence of the scattering states on the (perturbed) scattering potential $V(\mathbf{r})$ is nonlocal due to the quantum-mechanical origin. Placing a tip somewhere, may influence the current pattern far away since it changes the local phases, and thereby influences quantum-interference effects directly.

Since the local current density is not easily measured directly, it is important to look for indirect evidence. The induced magnetic field provides such indirect evidence. A manifestation of current eddies are strong fluctuations in the local magnetic field. Such magnetic fields could feed back into the current flow itself and induce spin-relaxation. Furthermore, they could potentially be detected in experimental setups that allow to perform a measurement of the nuclear magnetic resonance (NMR) in the presence of a current. Also, one can think of a direct mapping of the induced magnetic field, instead of a mapping of the current density.

Spin-relaxation due to the induced (inhomogeneous) magnetic field

In leading order perturbation theory, the spin-relaxation rate is $\tau_{\mathrm{s}}^{-1} \sim (\mu_{\mathrm{B}} B_0)^2 \tau$, where B_0 is the typical strength of the random magnetic field and τ denotes the time it takes the electron to move from one current loop to the next[156]. For the magnetic field depicted in Fig. 4.3b, we expect $\mu_{\mathrm{B}} B_0/\hbar \sim 100\,\mathrm{MHz}$ at $V_{\mathrm{bias}} = 1\,\mathrm{mV}$.[C] This value is in the range typical of hyperfine-

interactions. When other sources of spin-relaxation are missing, e.g. spin-relaxation induced by spin-orbit interaction is weak, the current-induced spin-relaxation might become the relevant source of spin-relaxation. In particular, for strongly disordered films, the relaxation rate τ_s formally diverges due to multiple scattering events, i.e., the electron is "trapped" in current loops around scattering centers[157]. On the other hand, recent works indicate that spin-orbit interaction may be significant in hydrogenated graphene, enhanced by lattice distortion[158–160], and therefore it is momentarily not clear if current-induced spin-relaxation is a relevant mechanism in graphene.

NMR-type experiment

Second, we discuss a potential NMR-type experiment. The important part is to measure the NMR-resonances in the presence of a current. In the case of hydrogenated graphene, one would focus on the spin of the hydrogen cores, i.e., spins of individual protons. In addition to the NMR-shift due to the chemical environment, the observed NMR-shifts depend on the induced local magnetic field, and therefore depend on the applied bias voltage. If one is able to reconstruct the atomic structure (via NMR or otherwise), and is able to follow individual NMR-resonances, one might "see" the ring currents emerge when slowly increasing the bias voltage. Since the NMR-shifts measure the local magnetic field, one can in principle measure the orbital current flow with atomic precision in a global experiment. Admittedly, such an NMR-type experiment would likely be challenging because it needs to be performed under an applied bias voltage.

Direct mapping of the magnetic field

A direct measurement of the induced magnetic field pattern could be possible using Lorentz transmission electron microscopy (LTEM)[161, 162]. A high energy electron beam is shot through the sample. The beam is deflected by the magnetic field in and near the sample. Measuring the angle of deflection, the magnetic field can be reconstructed. The advantage of this method is that it directly gives the spatial dependence (in contrast to NMR and spin-relaxation which first average over the sample). Resolving larger magnetic islands, in the order of nanometers, would be sufficient to show the existence of the current eddies. When increasing the bias voltage, current eddies at different positions would dominate, and one would see the creation and destruction of magnetic islands.

4.2 Influence of system details and bias voltage on the local current density

We presented the linear current density response and the induced magnetic field for a large flake (AGNR16×83) in Sec. 4.1, and discussed the physical implications. In this section, we investigate if the picture of local current vortices must be altered when details in the transport setup are varied. First, in Sec. 4.2.1, we analyze how the statistics of the individual scattering states evolve for different sized AGNRs as well as for different hydrogen concentration (Sec. 4.2.2). Next, in
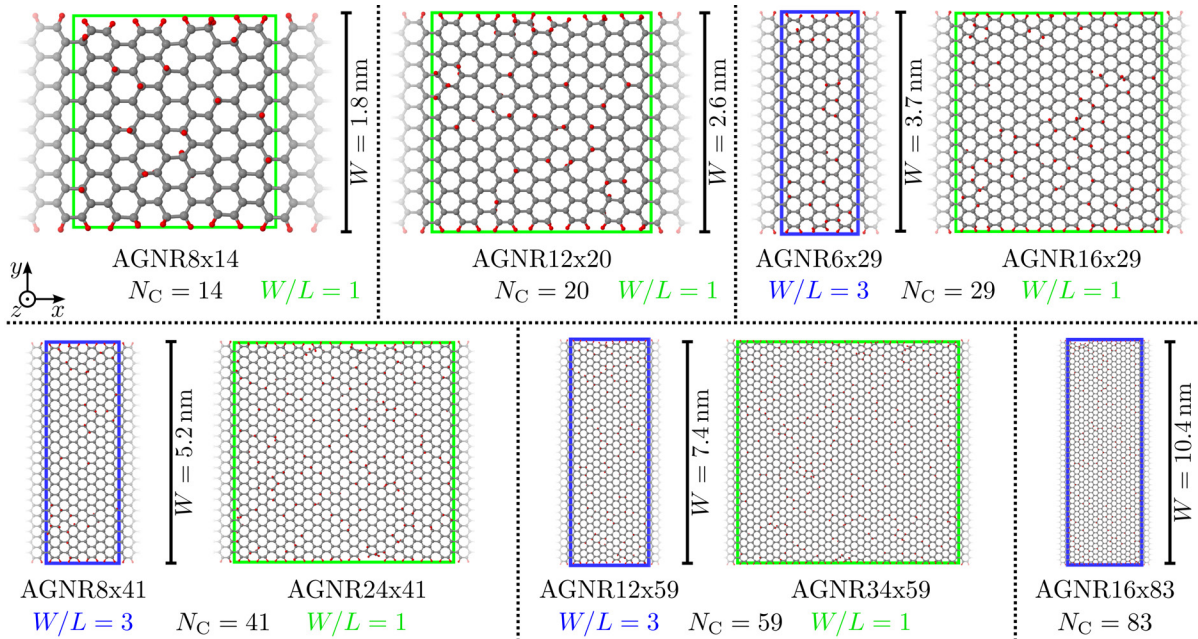
Figure 4.7: Overview over all hydrogen-terminated AGNRs used to study the size dependence. The colored boxes mark the region that is functionalized with 20% hydrogen atoms. Two different aspect ratios are investigated: square ($W/L = 1$, green boxes) and wide ($W/L = 3$, blue boxes) AGNRs. The self-energies, representing the semi-infinite leads, only depend on the width of the AGNR, i.e., on the number of transverse carbon atoms N_C. The self-energies were therefore stored on hard disk and recycled (cf. remark at end of Sec. 2.1.3). [Plot shows carbon atoms in gray, hydrogen atoms in red. Transport is in x-direction.]

Sec. 4.2.3, we discuss the effect of a finite bias voltage, i.e., how several transport states add up. The effects of a different adsorbate, hydroxyl groups, is discussed in Sec. 4.2.4. In all cases, we find the qualitative picture of current vortices remaining unchanged.

4.2.1 System size dependence

System selection: wide and square AGNRs

In this section, we investigate the dependence of the observed phenomena on the system size. For this purpose, we employ differently sized AGNRs as shown in Fig. 4.7. We employ two different width-to-length ratios: square AGNRs with $W/L = 1$ and wide AGNRs with $W/L = 3$. Both sets of AGNRs are functionalized by 20% hydrogen which were randomly positioned above and below the carbon atoms. Then, the structures were geometrically relaxed until all remaining forces drop below 10^{-2} eV/Å. For further construction details, please refer to Appx. A.1.

$dI_{total}/dV_{bias} = 0.651 \, G_0^{spin} = 5.04 \cdot 10^{-5}$ A/V

$E - \varepsilon_F = -366$ meV

I_{total}

$L_y = 74.3$ Å

$\int \left[d\mathbf{j}_{xy}(\mathbf{r})/dV_{bias} \right] dz \bigg/ \frac{[dI_{total}/dV_{bias}]}{L_y}$

10^{-1} 10^0 10^1 10^2
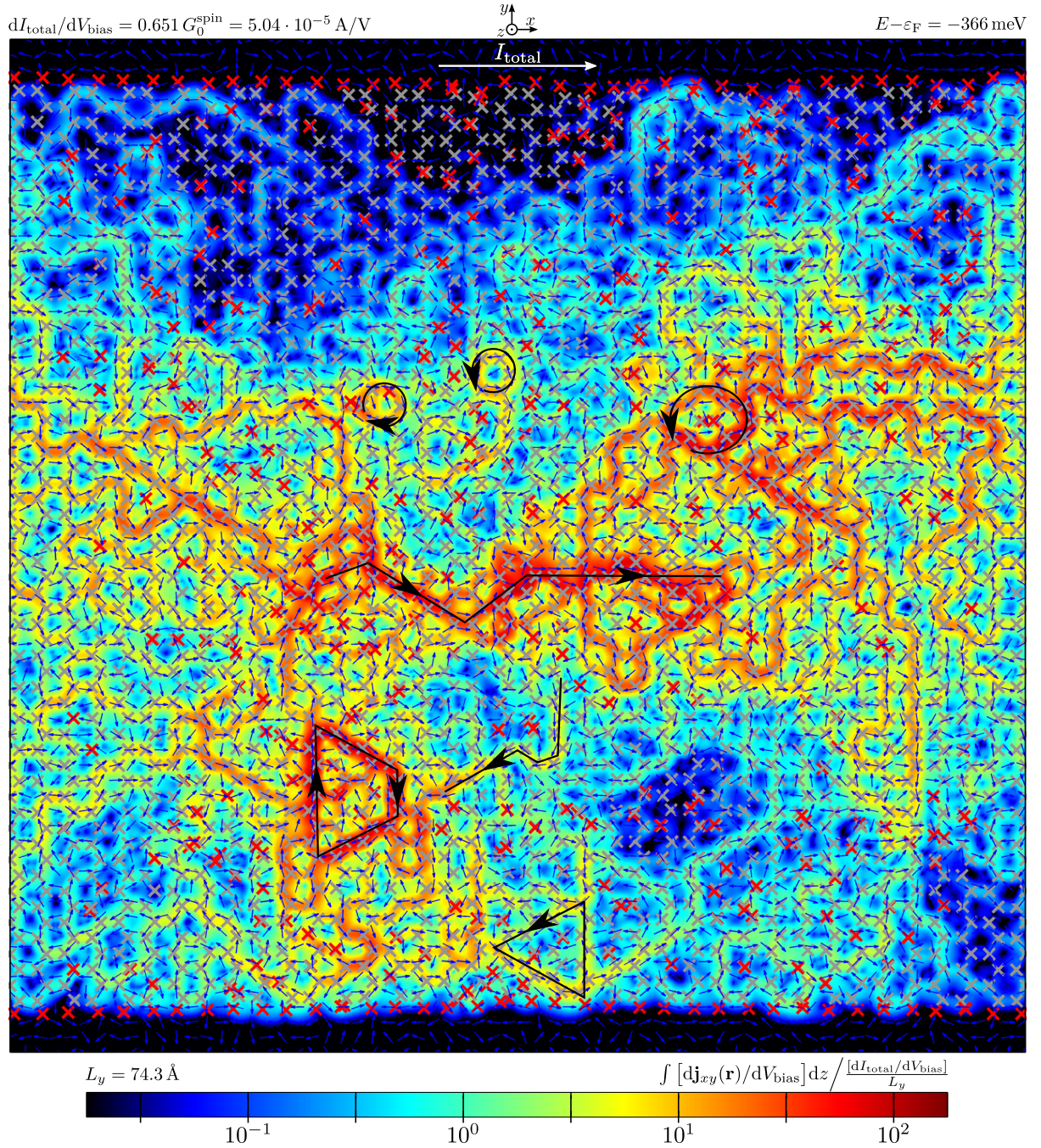
Figure 4.8: Local current density response (integrated over the out-of-plane direction) for the hydrogenated AGNR34×59 shown in Fig. 4.7. The current exhibits very strong mesoscopic fluctuations that reflect in a logarithmic color scale covering four decades. Some interesting current paths are drawn in the picture for illustration. Plot shows current amplitude (color), current direction (arrows), carbon atoms (gray crosses), and hydrogen atoms (red crosses).
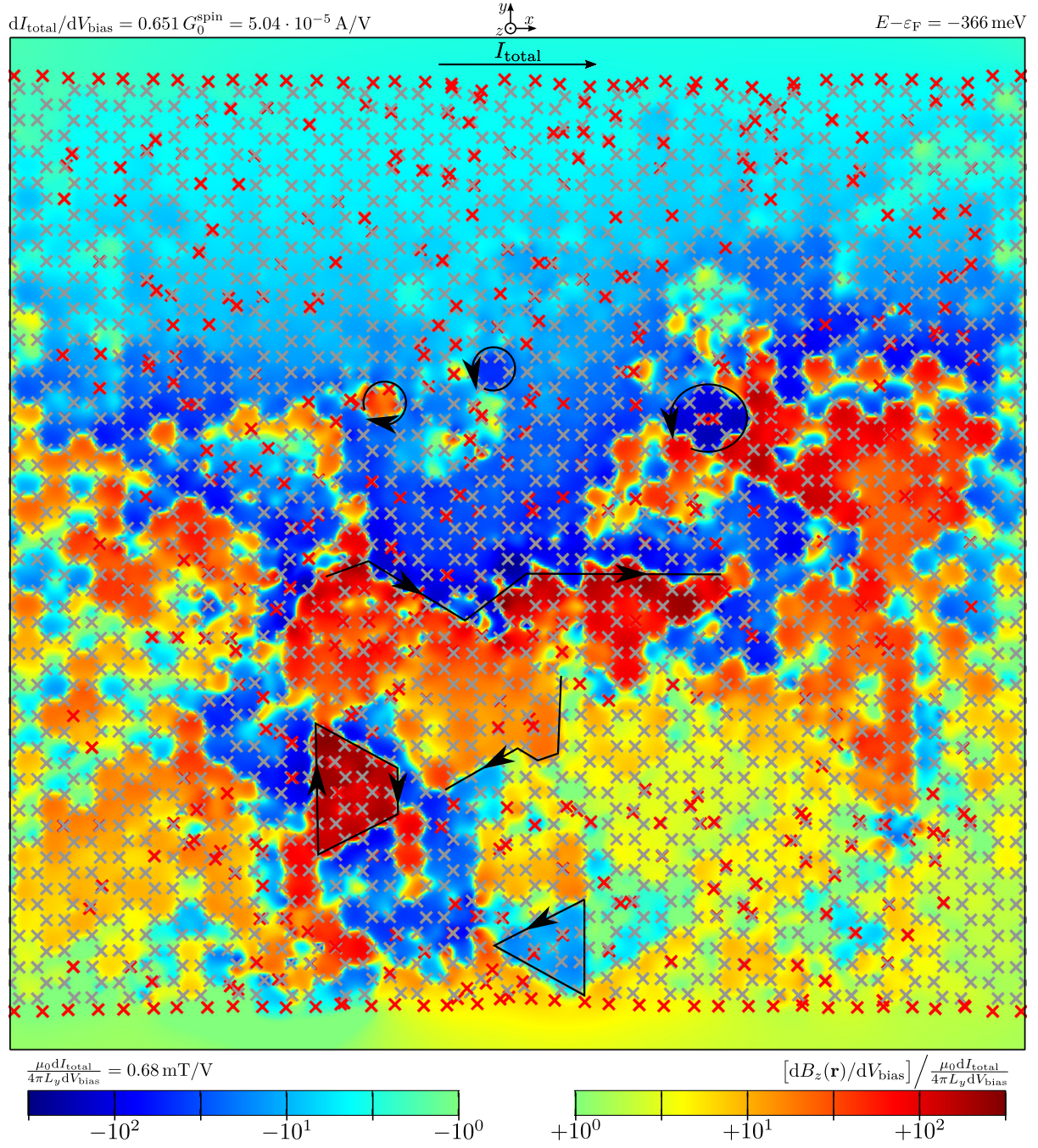
Figure 4.9: Magnetic field response (in out-of-plane direction) induced by the current density response shown in Fig. 4.8. The magnetic field strongly varies and changes sign from region to region. The field is plotted in the (averaged) carbon plane ($z=0$), but being divergence free, it hardly changes with z.

AGNR34×59

A candidate for wide AGNRs was already discussed in the previous section. As candidate for square AGNRs, we shortly discuss the emergence of ring currents in AGNR34×59. The transmission function $\mathcal{T}(E)$ of AGNR34×59 is also dominated by individual sharp peaks (only shown in Appx. D.7.1, Fig. D.13e). We checked that the magnetic response dm_z/dV_{bias} also shows the known sign changes at most antiresonances (not shown). We thus presume that the aspect ratio of the AGNR has a minor influence on the discussed qualitative physics.

We check this conjecture in Fig. 4.8 and Fig. 4.9, which show the current density response and the induced magnetic field for an energy corresponding to a transmission peak. Again, we see the usual pattern: ring currents exceeding the average through current by orders of magnitude and large spatial fluctuations resulting in a color scale covering four decades. The induced magnetic field shows again magnetic islands of strongly varying size. We note that the ratio of the maximal current density normalized to the average through current is in the order of 10^2 whereas for the wide AGNR16×83 it was larger, in the order of 10^3. An similar tendency can be observed in the magnetic field response. We, thus, presume that the effect of current vortices is more pronounced in wide AGNRs. This is supported by the magnetization m_z which features larger values for wide AGNRs, see Sec. 4.3.

The distribution functions shown in Fig. 4.10 show that the current magnitude still follows a lognormal distribution, and the angles are still approximately uniformly distributed. The distributions are smoother due to the larger number N_{Points} of spatial points used in the calculation. The very small difference between $\varphi = 0$ ($j_x > 0$) and $\varphi = \pm\pi$ ($j_x < 0$) results in the small average through current. All together, this supports the previously discussed results of Sec. 4.1.

(a) Distribution of the current density

(b) Distribution of the current density angles
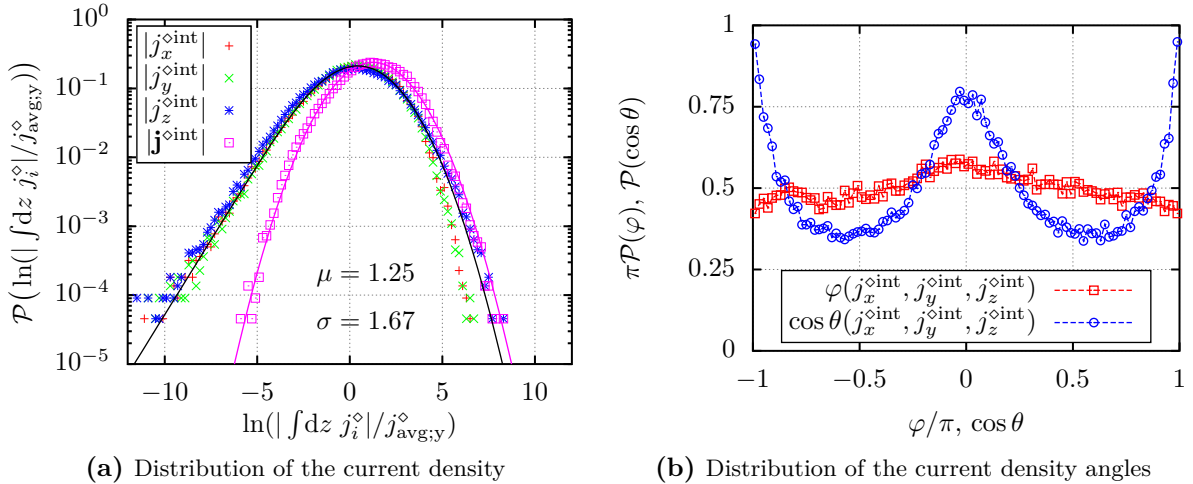
Figure 4.10: (a) Distribution function for the current density response $\mathbf{j}^{\diamond\mathrm{int}} = \int dz\, d\mathbf{j}/dV_{\mathrm{bias}}$ (integrated over the out-of-plane direction and normalized to the average through current) of an AGNR34×59 at $E - \varepsilon_{\mathrm{F}} = -366\,\mathrm{meV}$ (as shown in Fig. 4.8). (b) Corresponding distribution functions for the azimuthal angle φ and the polar angle θ.

Characterization of distribution function via mean μ and width σ

To further quantify the statistics of individual scattering states—especially their size dependence—we apply the following procedure: For all systems shown in Fig. 4.7, we calculate the transmission function which always features a peak structure near the Fermi energy. Then, we choose transmission peaks near the Fermi energy and calculate the current density response, the induced magnetic field, and the corresponding distribution functions. We do not present the raw data explicitly (all data is given in Appx. D.7), but instead, we focus on the distribution functions of the current density, and characterize them by their mean μ and standard deviation σ. These moments refer to the logarithm of the integrated current density normalized to the average through current, as employed in Figs. 4.4 and 4.10a.

Figure 4.11 shows the size dependence of the mean μ and standard deviation σ averaged over all selected energies. We see a weak dependence on the AGNR size. If anything, the mean μ decreases slightly for larger systems whereas the width σ increases. For all systems, $\mu + \sigma > 2$, meaning that a significant portion of the current density exceeds the average through current by two orders of magnitude. [Remember that μ and σ are the moments of the *lognormal* distribution.] Because of the continuity equation, this can only result in significant ring currents.

Simply calculating the moments μ and σ does not ensure that the current distributions follow a lognormal distribution. We manually checked the current distributions, see Appx. D.7, and
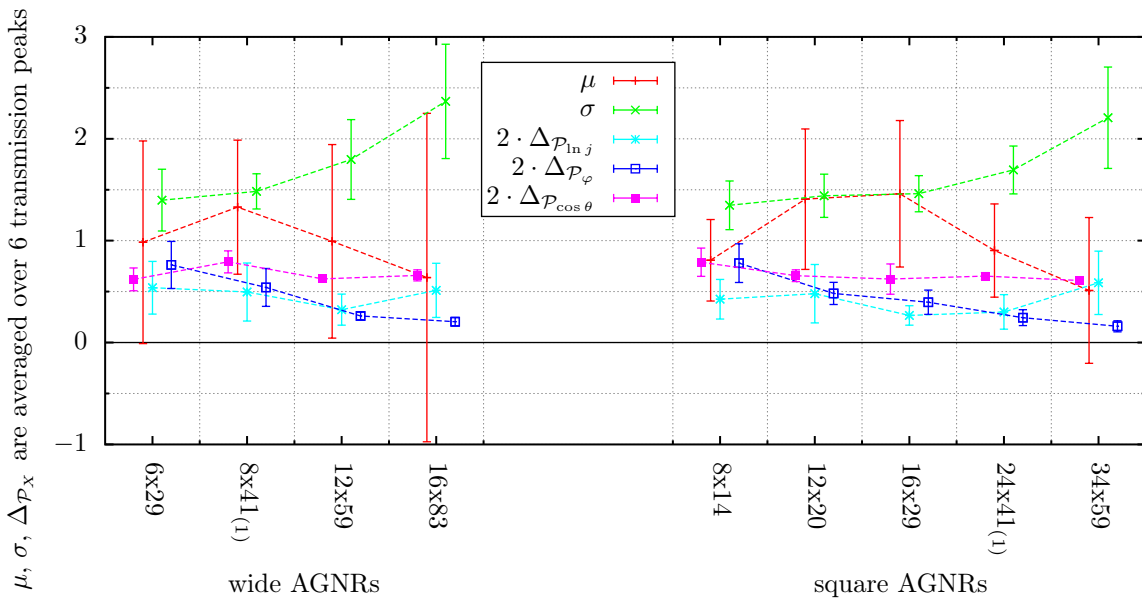
Figure 4.11: Flow of the mean μ and width σ of the lognormal distribution of the magnitude of the current density response in different AGNRs with 20% hydrogen adsorbates. For each AGNR, the current density response is calculated at several energies (each with peaks in the transmission). The mean μ and width σ of the corresponding distribution function is averaged over all considered energies. The analogue is performed for the three deviation measures $\Delta\mathcal{P}_X$. (Note that the deviation measures $\Delta\mathcal{P}_X$ are multiplied by a factor of two, c.f. plot legend. For geometries, see Fig. 4.7.)

indeed, the magnitude of the current density always follows a lognormal distribution. To visualize this verification in the flow diagram, Fig. 4.11, we define a deviation measure $\Delta_{\mathcal{P}_{\ln j}}$,

$$\Delta_{\mathcal{P}_{\ln j}} \propto \sqrt{\int \mathrm{d} \ln x \left| \ln \mathcal{P}(\ln x) - \ln \mathcal{P}_{\text{lognormal}}(\ln x) \right|^2}, \qquad (4.4)$$

that measures the deviation of the distribution function $\mathcal{P}(\ln x)$ from a lognormal distribution (parameterized with correct center and width), i.e., it measures the deviation from the (downward opening) magenta parabola plotted in Figs. 4.4 and 4.10a (see Appx. D.5.1 for the full definition of $\Delta_{\mathcal{P}_{\ln j}}$ including integration cut-off). Similarly, we define the measures $\Delta_{\mathcal{P}_{\varphi}}$ and $\Delta_{\mathcal{P}_{\cos \theta}}$ that quantify the deviation of the current density angles from a uniform distribution (again, see Appx. D.5.1 for a formal definition). For our purpose, deviation measures below unity are evidence that the current magnitude and the angles of the current density approximately follow a lognormal and uniform distribution, respectively. Please note that $\Delta_{\mathcal{P}_{\varphi}}$ decreases monotonously for increasing system size. Thus, in the limit of large system sizes, the in-plane angle φ seems to be perfectly uniformly distributed. That means that local current fluctuations, i.e. ring currents, are isotropic and completely mask the through current. In such a case, one might expect a power law behavior, e.g., an inverse linear dependence on the system size, $\Delta_{\mathcal{P}_{\varphi}} \propto N_{\text{carbon}}^{-1}$. Our data is compatible with an exponent of -1 (but also with many others due to a small statistics).

We thus conclude that the magnitude of the current density response follows a lognormal distribution, irrespective of the size of the AGNR. A significant portion of the current distribution exceeds the average through current by orders of magnitude leading to strong current vortices.

Remark: Here, we based our investigations on AGNRsN_{C} with $N_{\text{C}}=3m-1$ ($m \in \mathbb{N}$), in which streamlines emerge in the pristine case (cf. Chap. 3.1). In Appx. D.7.3, we investigate hydrogenated AGNR42 and AGNR43, and find no qualitative differences for the other classes, $N_{\text{C}}=3m$ and $N_{\text{C}}=3m-2$.

4.2.2 Impurity concentration

Until now, we worked with a fixed hydrogen concentration of $n = 20\%$. In this section, we vary the hydrogen concentration from 0% to 40% at fixed system size. We already discussed the limiting case of pristine AGNRs with zero concentration $n = 0\%$ in Sec. 3.1. [The distributions of pristine ribbons are shown in Appx. D.5.4, Fig. D.12.] Now, we simulate transport through AGNR41 with varying hydrogen concentration. In all cases, the leads are given by pristine AGNR41. Thus, the self-energies are identical, and stored on hard disk for recycling. To study the current density statistics, we repeat our procedure: From the calculated transmission function, transmission peaks are selected, and the associated current density responses and distribution functions are calculated. In Fig. 4.12, we plot the flow of the mean μ and width σ of the distribution function averaged over the selected energies. For finite concentration, i.e., $n \geq 1\%$, the mean μ is above zero so that significant portions of the current density exceed the average through current. The width σ hardly depends on the concentration. The deviation measures $\Delta_{\mathcal{P}}$ are more interestingly. They all increase for small impurity concentrations, $\Delta_{\mathcal{P}_{\ln j}}$ and $\Delta_{\mathcal{P}_{\cos \theta}}$ even diverge. The magnitude of the
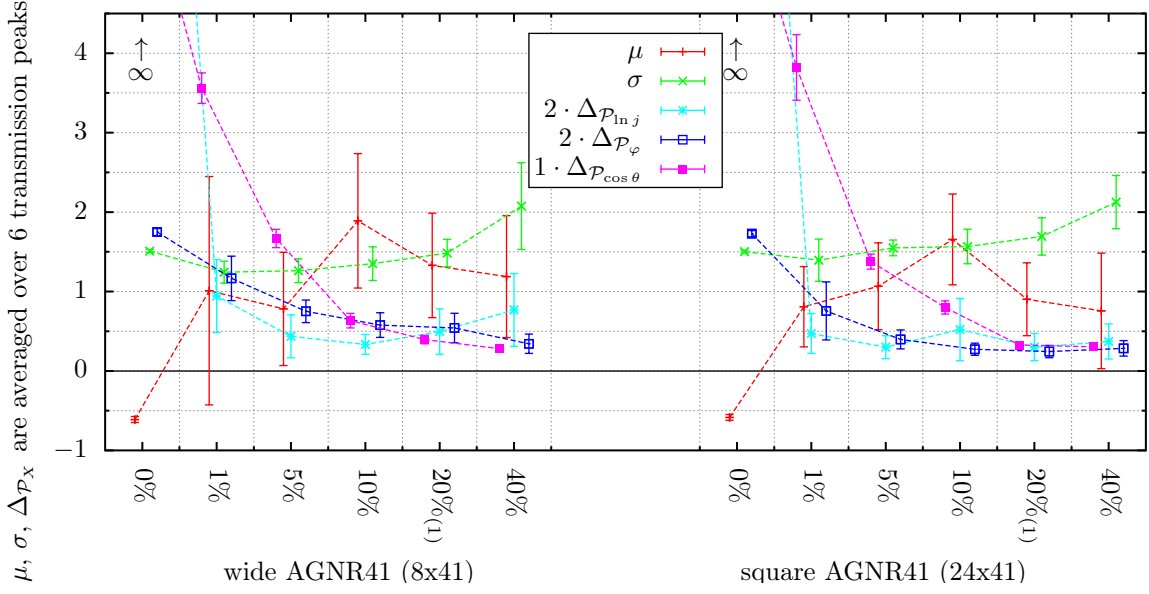
Figure 4.12: Flow of the mean μ and width σ of the lognormal distribution of the magnitude of the current density response for an AGNR41 with varying concentration of hydrogen adsorbates. For each concentration, the current density response is calculated at several energies (each with peaks in the transmission). The mean μ and width σ of the corresponding distribution functions are averaged over all selected energies. The analogue is performed for the three deviation measures $\Delta \mathcal{P}_X$. In pristine AGNRs, $n = 0\%$, there are no transmission peaks. The averaging was performed over six energies with $\mathcal{T} = 1$; all showing identical streamline patterns. (Note that the deviation measures $\Delta \mathcal{P}_{\ln j}$ and $\Delta \mathcal{P}_\varphi$ are multiplied by a factor of two, c.f. plot legend.)

(a) AGNR24×41 with 1% H
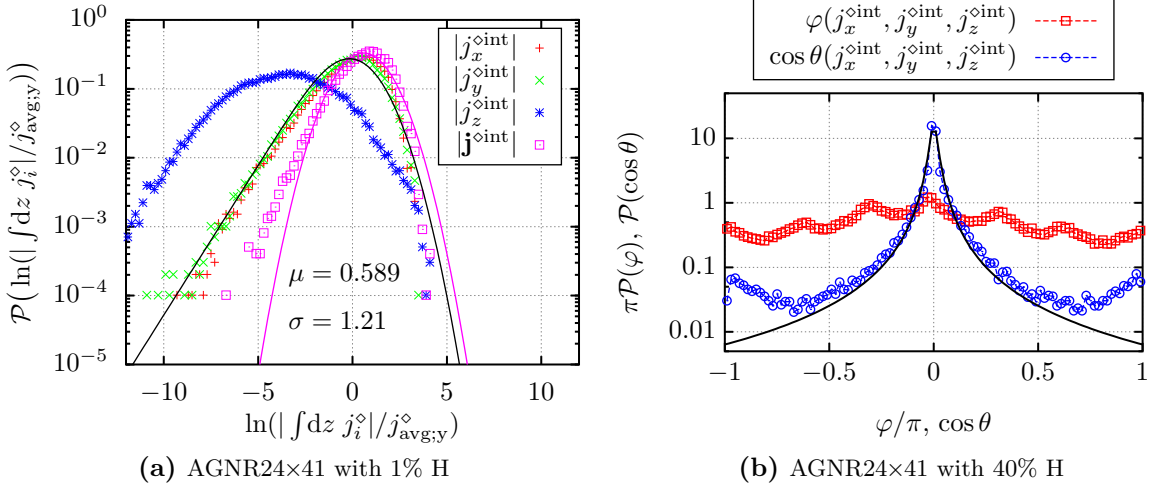
(b) AGNR24×41 with 40% H

Figure 4.13: (a) Distribution functions for the current density response in AGNR24×41 with 1% hydrogen adsorbates. The out-off-plane current component j_z shows a qualitatively different distribution function when compared to the in-plane current component j_x and j_y. (b) Corresponding distribution functions for the azimuthal angle φ and the polar angle θ. The azimuthal angle φ is approximately uniformly distributed. In contrast, the distribution of polar angle $\cos\theta$ shows as significant peak at $\cos\theta = 0$ which favors the in-plane current component ($\mathbf{j} \perp \mathbf{e}_z$). A Lorentzian $\frac{1}{\pi} \frac{\gamma/2}{(\cos\theta)^2 + (\gamma/2)^2}$ ($\gamma = 0.04$) is shown for comparison.

current density is no longer lognormal in pristine ribbons and $\cos\theta$ is not uniformly distributed for small concentrations. Thus, there are two questions: (i) how is the current density distributed for small but finite concentrations, e.g. for $n = 1\%$, and (ii) how are the angles then distributed?

To answer this type of questions, we tend to the current distribution for $n = 1\%$ as shown in Fig. 4.13a. The magnitude of the current distribution still follows a lognormal distribution and the in-plane current components also follow the expected behavior given by $\mathcal{P}_{\text{component}}$. The distribution for the out-of-plane current component (j_z) is however shifted to smaller values, i.e., in-plane current components dominate. This is consistent with the angle distribution shown in Fig. 4.13b. The polar angle $\cos\theta$ is no longer near a uniform distribution but shows a pronounced peak at $\cos\theta = 0$. Please note the logarithmic scale. Thus, for smaller hydrogen concentrations, we find that the current density flows mainly along the graphene plane. Only minor current contributions from the bottom to top side exist. This is what one expects in pristine AGNR, the current near the Fermi energy is solely carried by π-orbitals. The π-orbitals have a node in the graphene plane and cannot mediate a current contribution from one side to the other. For higher concentrations, more and more π-electrons form bonds to the adsorbed hydrogen atoms. The remaining σ-orbitals (z-mirror symmetric) start to contribute. That way, current paths connecting both graphene sides exist.

4.2.3 Finite bias voltage

Current density for $eV_{\text{bias}} \gg \Delta$ [bias voltage $\gg$ level spacing]

So far, we discussed the current density response $d\mathbf{j}/dV_{\text{bias}}$ induced by an infinitesimal bias voltage dV_{bias}, i.e., the limit in which the applied bias voltage V_{bias} is much smaller than the level spacing Δ. In this section, we investigate the opposite limit, a large bias voltage $eV_{\text{bias}} \gg \Delta$.

Applying a finite bias voltage involves the integration of current contributions over an energy range of width eV_{bias}. This is computationally demanding and therefore we restrict the investigation to 20% hydrogen on the medium sized AGNR8×41 whose atomic structure and transmission function have already been presented in Fig. 4.1b and Fig. 4.2b, respectively. The level spacing of the AGNR8×41 near the Fermi energy is approximately $\Delta \approx 50\,\text{meV}$ (cf. Appx. D.1). We use a bias voltage of $V_{\text{bias}} = 1\,\text{V}$, summing over about $\mathcal{N} = eV_{\text{bias}}/\Delta \approx 20$ states.

The current density induced by $V_{\text{bias}} = 1\,\text{V}$ is shown in Fig. 4.14a. The current density exhibits a streamline-type pattern carrying the total current (from top to bottom) that is overlaid by strong fluctuations that reflect in a logarithmic color scale covering three decades. Local current vortices (eddies) still exist, but mostly encircle only single carbon rings. Although they still exceed the average current by about one order of magnitude, they are not as prominent as for infinitesimal bias voltage.

We explain this behavior in the following way: Inside the bias window, individual transport states exist which all show current vortices of varying sizes. These vortices are differently positioned, and by summing over the states, the vortices encircling several carbon rings are washed out. Only the smallest vortices (encircling one carbon ring) survive. On the other hand, contributions to the average through current cannot cancel each other. Therefore, the average through current
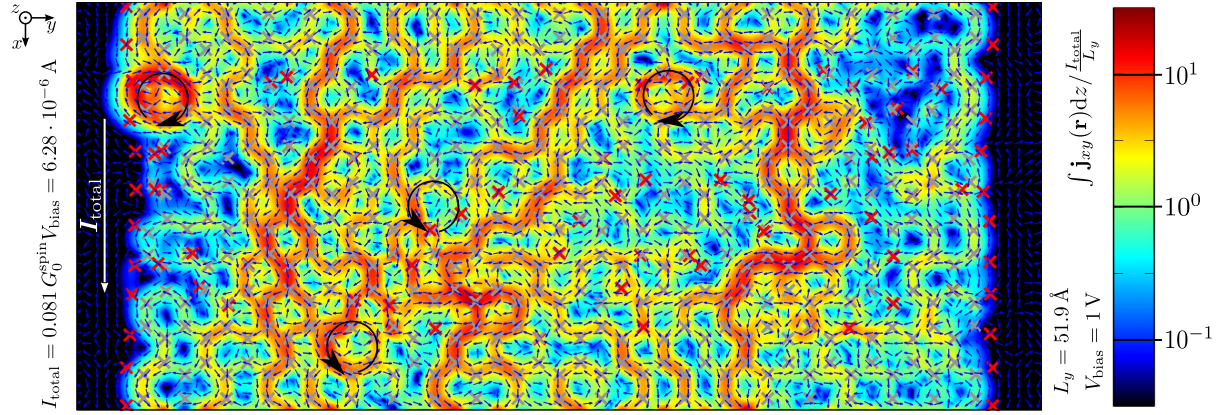
(a) Current density at finite bias $V_{\text{bias}} = 1\,\text{V}$
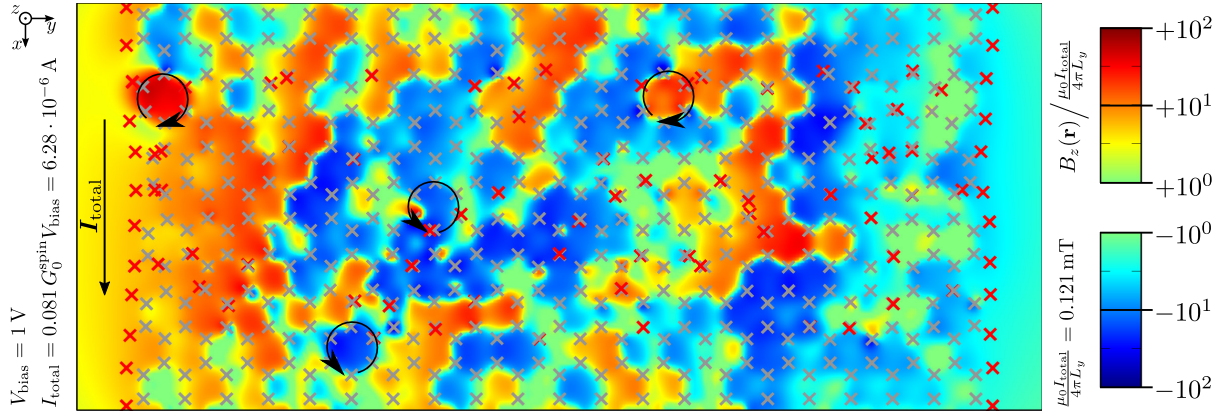
(b) Induced magnetic field
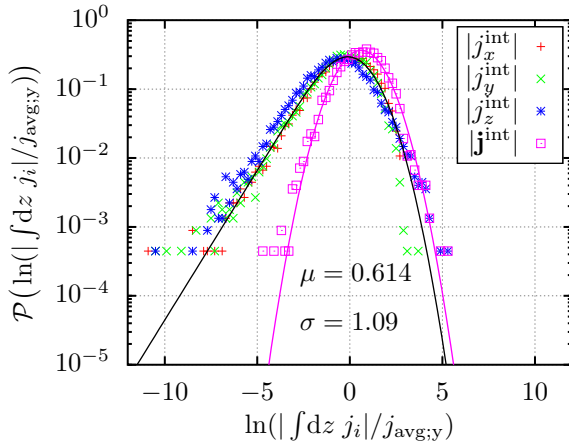
(c) Distribution function of the current density
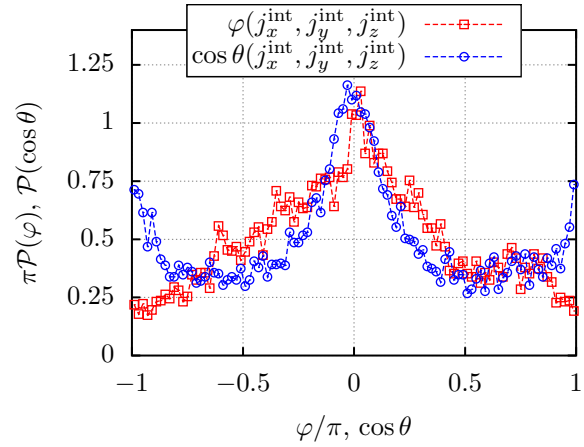
(d) Distribution function of the current angles

Figure 4.14: (a) Local current density for the hydrogenated AGNR8×41 (shown in Fig. 4.1b) at a finite bias voltage $V_{\text{bias}} = 1\,\text{V}$. The current density integrated over the out-of-plane direction normalized to the average through current $j_{\text{avg};y} = I_{\text{total}}/L_y$. The current density exhibits a streamline-type current pattern carrying the total current (from top to bottom) that is overlaid by strong fluctuations that reflect in a logarithmic color scale covering three decades. Local current vortices encircle mostly only single carbon rings. (b) Magnetic field (in out-of-plane direction) induced by the current distribution shown in panel (a). Induced magnetic field (in out-of-plane direction). The field is plotted in the (averaged) carbon plane ($z=0$). (c) Distribution function for the current density $\mathbf{j}^{\text{int}}/j_{\text{avg};y} = \int \mathrm{d}z\, \mathbf{j}/j_{\text{avg};y}$ shown in panel (a). (d) Corresponding distribution functions for the azimuthal angle φ and the polar angle θ.

becomes larger compared to the current vortices. On a quantitative level, the analysis is as follows: Adding up current vortices scales like adding up random numbers, i.e., increasing like $\sqrt{\mathcal{N}}$. On the other hand, the through current increases linearly, $I_{\text{total}} \propto \mathcal{N}$. Therefore, the current fluctuations normalized to the average through current are expected to decrease as $1/\sqrt{\mathcal{N}}$.

The induced magnetic field still shows random magnetic islands, see Fig. 4.14b. The amplitude B_0 of the field fluctuations is about $B_0 \sim 10\,\text{mT}$. This is larger than our earlier estimate, $B_0 \sim 1\,\text{mT}$ (cf. Sec. 4.1.4), for a single transport state. Here, we integrate over about $\mathcal{N} \approx 20$ states, so that a larger field of about $\sqrt{\mathcal{N}} \approx 4.5$ is expected if the transport states add up randomly. [Since the through current increases linearly with the number of transport states, this means that the magnetic field per through current decreases as $1/\sqrt{\mathcal{N}}$.]

The distribution functions of the finite current density normalized to the through current are shown in Figs. 4.14c and 4.14d. They show the same features as before: the magnitude of the current density follows a lognormal distribution, all three individual current component are equivalent. The mean $\mu = 0.61$ of the lognormal distribution is however shifted to smaller values reflecting in the reduced dominance of the current vortices observed in Fig. 4.14a. [For comparison, $\mu \gtrsim 2$ for an infinitesimal bias voltage.]

The distributions of the angles are still similar to the infinitesimal bias voltage case, but the small bump at $\varphi = 0$ evolved to a significant peak in $\mathcal{P}(\varphi)$. This peak accounts for a significant net current through the ribbon. [$\varphi = 0$ refers to a forward flow, while $\varphi = \pm\pi$ refers to backflow.]

Thus, for $eV_{\text{bias}}/\Delta = 20$, we see the same qualitative features—current vortices and a broad lognormal current distribution—as for an infinitesimal bias voltage ($eV_{\text{bias}}/\Delta \to 0$). On a quantitative level, however, we observe that the magnitude of the current vortices (normalized to the through current) is reduced and we expect that for large bias voltages or larger samples ($eV_{\text{bias}}/\Delta \gg 100$) streamline patterns of the through current dominate, current vortices are further reduced and vanish in the limit $eV_{\text{bias}}/\Delta \to \infty$.

Current density evolution for continuously increasing V_{bias}

Instead of looking at a single bias voltage, one is also interested in the evolution of the current density and its associated distribution functions for continuously increasing the bias voltage. We focus on the evolution of the current distribution function which is characterized by the moments μ and σ. (A selection of current density plots for varying bias voltage is given in Appx. D.3, Fig. D.4.)

As a preparation, we consider the transmission $\mathcal{T}$ and the density of states (DOS) ρ plotted over the integrated number $\mathcal{N}$ of transport states, as shown in Fig. 4.15 (bottom). This choice of the x-axis has the advantage that the individual transport resonances (peaks in $\mathcal{T}$ and ρ for $\mathcal{N} < 15$) are equidistant; of course, the area below the curves no longer correspond to the energy integral. [The transmission function as function of the energy E is shown in Fig. 4.2b.] From the individual equidistant peaks, we conclude that each peak in the transmission refers to a separate state in the sample.
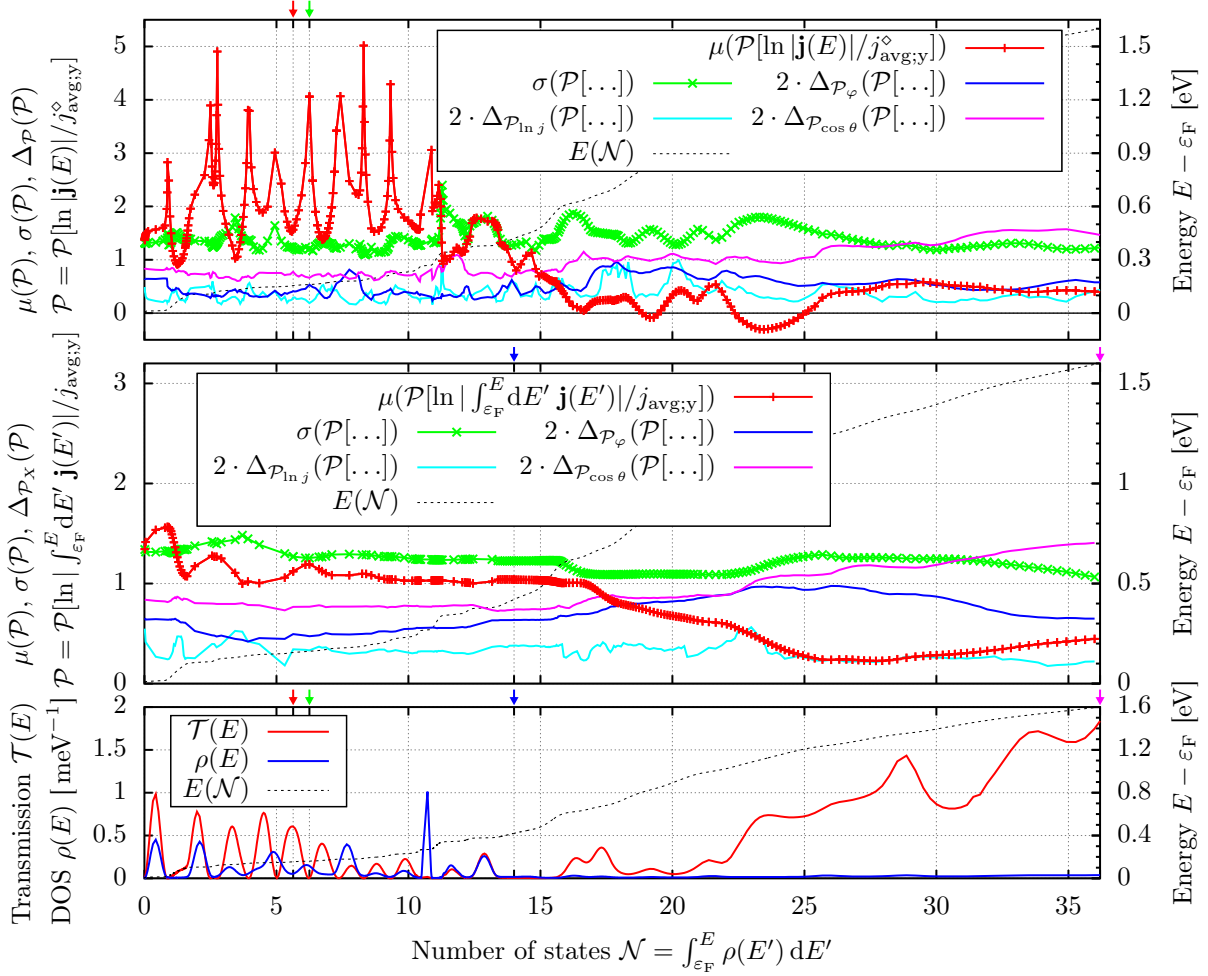
Figure 4.15: (top/center): Flow of the mean μ (red) and width σ (green) of the lognormal distribution of the current density magnitude in hydrogenated AGNR8×41 (shown in Fig. 4.1b). Additionally, several deviation measures $\Delta \mathcal{P}_X$ are shown. In the top panel, the current density response is taken at a specific energy, $\mathbf{j}(E) = \mathrm{d}\mathbf{j}/\mathrm{d}(eV_{\mathrm{bias}})|_E$, whereas the current density is integrated from the Fermi energy to the chosen energy in the center panel, $\mathbf{j} = \int_{\varepsilon_{\mathrm{F}}}^{E} \mathrm{d}E' \, \mathbf{j}(E')$. (Note that the deviation measures $\Delta \mathcal{P}_X$ are multiplied by a factor of two, c.f. plot legend.)
(bottom): Transmission function $\mathcal{T}(E)$ and DOS $\rho(E)$ taken at energy $E(\mathcal{N})$. The x-axis (of all panels) is not the energy E but given by the number of states $\mathcal{N}$ (integrated DOS from Fermi energy to energy E); that way, the transmission peaks (for $\mathcal{N} < 15$) are equidistant. They are evidence that the current is carried by individual sample states. For convenience, the energy $E(\mathcal{N})$ is given on the right y-axis (dashed black). [The small current arrows (red, green, blue, magenta) on top of each panel mark the energies for which explicit distribution function are shown in Appx. D.5.4, Fig. D.10 and Fig. D.11.]

In Fig. 4.15 (center), the moments of the current density distribution for a finite bias voltage V_{bias} are shown. The bias voltage is related to the number of states $\mathcal{N}$ by $\mathcal{N} = \int_{\varepsilon_{\mathrm{F}}}^{E} \rho(E')\mathrm{d}E'$ with $E = \varepsilon_{\mathrm{F}} + eV_{\mathrm{bias}}$, i.e., $\mathcal{N} = 0$ refers to $V_{\mathrm{bias}} = 0$. We checked that the distribution for the current magnitude remains lognormal for all bias voltages, cf. the deviation measure $\Delta \mathcal{P}_{\ln j}$ (see also Appx. D.5.4, Fig. D.11 for example distributions). The center μ of the lognormal distribution moves to smaller values but stays above zero, $\mu > 0$. Hence, the lognormal distribution is always

centered at current values above the average through current. Its width $\sigma \gtrsim 1$ is virtually constant, i.e., it does not depend on the bias voltage V_{bias}. At first glance, this is somewhat surprising: averaging $\mathcal{N}$ uncorrelated distributions, one would expect the width of the average distribution to decay as $1/\sqrt{\mathcal{N}}$. One has to keep in mind that we do not average the distribution functions but the spatially resolved current density. Spatial fluctuations in the current density are correlated across different transport states belonging to nearby energy, i.e., regions with small (or large) local current density feature a small (or large) current density for a broad energy window. [The results fit the discussion for $V_{\text{bias}} = 1\,\text{V}$ showing a lognormal distribution for the current density magnitude for $V_{\text{bias}} = 1\,\text{V}$, cf. Fig. 4.14c.]

Last, in Fig. 4.15 (top), the moments of the distribution of the current density response for infinitesimal bias voltages are shown. The number of states $\mathcal{N}$ refer to the energy E at which the current density responses are calculated. Again, the distributions remain lognormal for all energies, cf. the deviation measure $\Delta_{\mathcal{P}_{\ln j}}$ (see also Appx. D.5.4, Fig. D.10 for example distributions). Note that the peaks of the moment μ are shifted with respect to the peaks in the transmission $\mathcal{T}$. This behavior is due to the normalization of the current density to the average through current, i.e., to the transmission. At antiresonances, the transmission vanishes faster (usually quadratically) than the induced current vortices (usually linearly). At zero transmission, the mean μ of the ratio between current density and transmission then diverges. In the plot, the peaks are not fully resolved. The actual sample points are therefore marked.

Remark: A finite bias voltage involves an energy integration, which is performed numerically by rastering the energy landscape and using a simple trapezoidal integration rule. A common energy spacing, as used for the discussed AGNR41 near transmission peaks, is $\delta = 1\,\text{meV}$. This might feel unnecessarily small (much smaller than the average level spacing $\Delta \approx 50\,\text{meV}$), but the peaks are not uniformly distributed, and some peaks are only of width $\Delta \sim 10\,\text{meV}$. We still need several energy points to resolve them properly. To ensure converged energy integrals, we always check that quantitatively same results are obtained if only every other integration point is used.

4.2.4 Adsorbate chemistry: hydroxyl groups

So far, we mostly discussed hydrogen adsorbates. In this section, we demonstrate that the effects do not qualitatively depend on hydrogen to be used as adatoms. We observe the same effects for hydroxyl groups.

Structure

We use an AGNR24×41 functionalized with 5% hydroxyl groups[D] (OH-groups) as shown in Fig. 4.16. The hydroxyl groups are randomly positioned above or below carbon atoms and the whole structure is geometrically relaxed. The procedure is identical to the procedure used for hydrogen adsorbates (cf. Sec. A.1) with the addition that the hydroxyl groups are randomly oriented before relaxation, i.e., the hydrogen atoms point in random direction (but with fixed C-O-H angle).
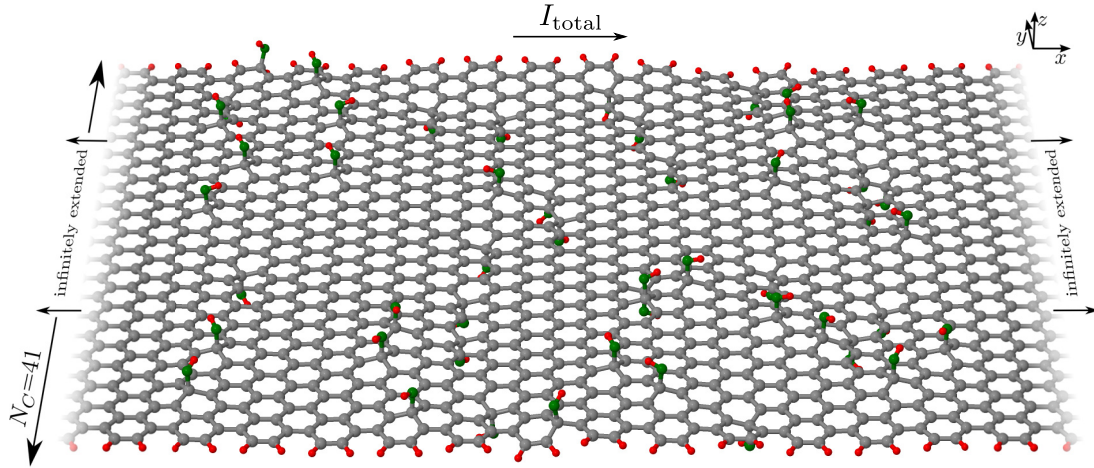
Figure 4.16: A hydrogen-terminated armchair graphene nanoribbon (AGNR24×41) that has been functionalized with additional 5% hydroxyl groups (49 OH-groups). The functionalized area (24×41 carbon atoms including hydrogen termination and hydroxyl groups) has been geometrically relaxed using DFT. The ribbon is infinitely extended in x-direction by pristine ribbon AGNR41. [Plot shows carbon atoms in gray, hydrogen atoms in red, oxygen atoms in dark green. Transport is in x-direction.]

(a) Transmission

(b) Distribution function of the current density
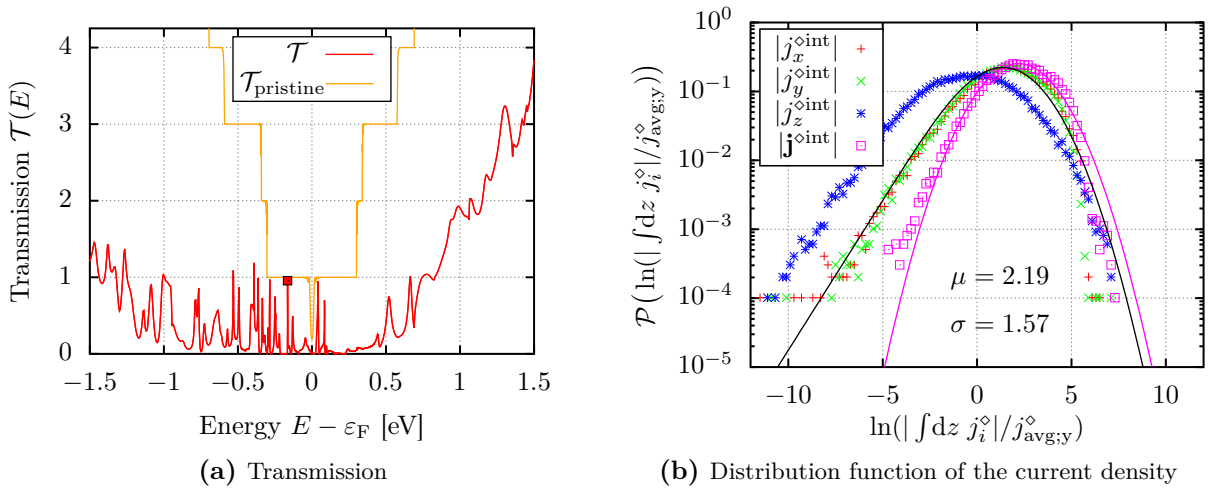
Figure 4.17: (a) Transmission function for the AGNR24×41 functionalized with 5% hydroxyl groups shown in Fig. 4.16. The transmission shows the usual peak structure near the Fermi energy. At the marked peak ($E=\varepsilon_\mathrm{F}-164.5\,\mathrm{meV}$, red box), the current density response is calculated (shown in Fig. 4.18). (b) Distribution function for the current density response $\mathbf{j}^{\diamond\mathrm{int}} = \int \mathrm{d}z\, \mathrm{d}\mathbf{j}/\mathrm{d}V_\mathrm{bias}$ (integrated over the out-of-plane direction and normalized to the average through current) calculated for the transmission peak marked by a red box in panel (a). As before, a lognormal distribution $\mathcal{P}_\mathrm{lognormal}$ and the distribution $\mathcal{P}_\mathrm{component}$ expected for equivalent vector components are shown for comparison. They have been parameterized only by the calculated mean μ and standard deviation σ of the distribution $\mathcal{P}[\ln(|\mathbf{j}^{\diamond\mathrm{int}}|/j_\mathrm{avg;y}^\diamond)]$.
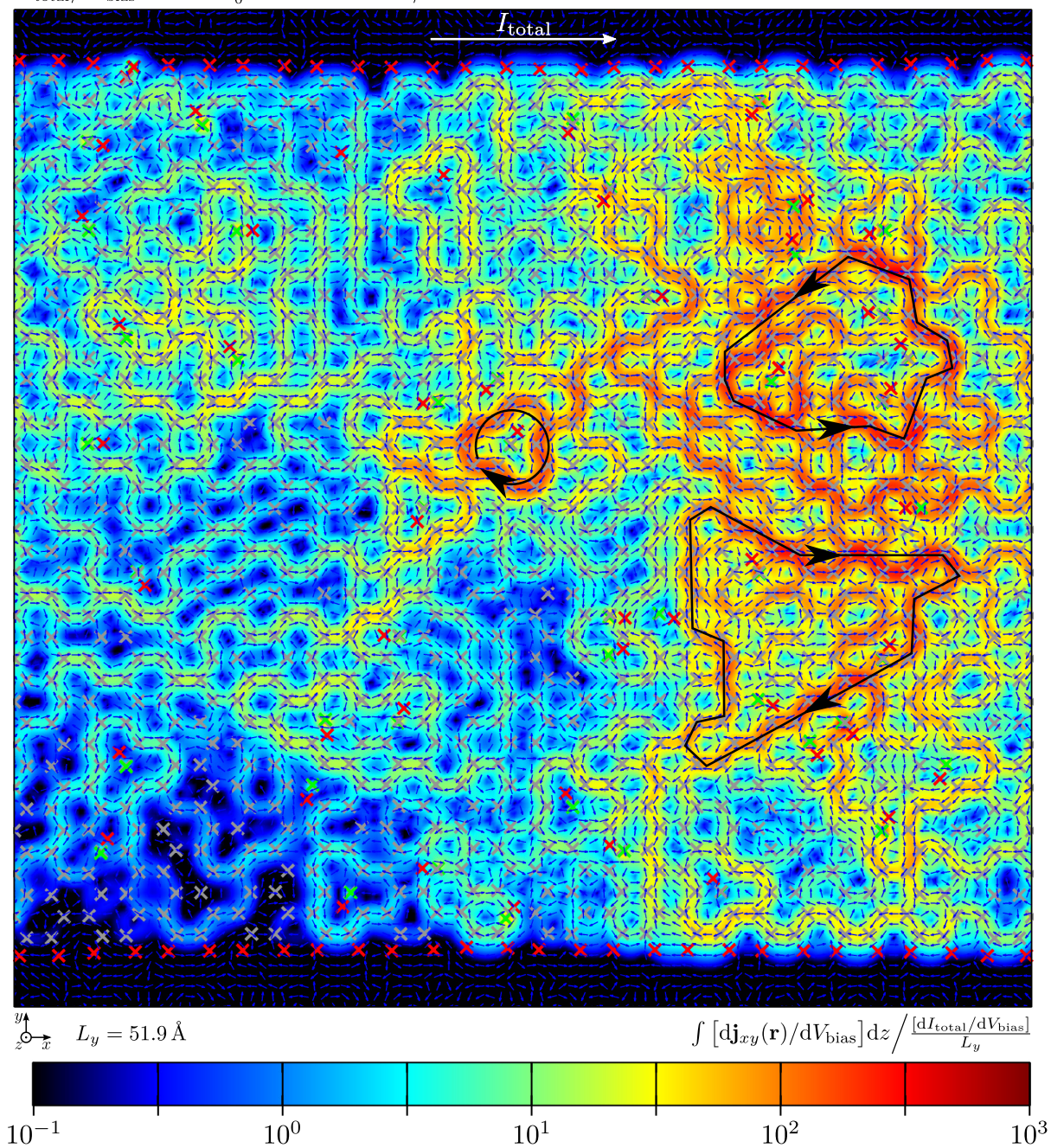
Figure 4.18: Local current density response (integrated over the out-of-plane direction) for the AGNR24×41 functionalized with 5% hydroxyl groups (shown in Fig. 4.16). The current exhibits very strong mesoscopic fluctuations that reflect in a logarithmic color scale covering four decades. Some interesting current paths are drawn in the picture for illustration. Plot shows current amplitude (color), current direction (arrows), carbon atoms (gray crosses), hydrogen atoms (red crosses), and oxygen atoms (green crosses).

Transmission and current density response

The transmission $\mathcal{T}(E)$ through the ribbon is shown in Fig. 4.17a. $\mathcal{T}(E)$ exhibits the expected peak structure near the Fermi energy. The current density response calculated at the marked transmission peak is shown in Fig. 4.18. We see the familiar picture: current vortices exceeding the average through current by orders of magnitude. The associated distribution functions are presented in Fig. 4.17b. The magnitude of the current density follows a lognormal distribution. The in-plane components j_x/j_y follow the expectation for equivalent vector components (cf. Appx. D.5.2). The out-of-place component j_z follows a shifted distribution, as it is also the case for hydrogen adsorbates at small concentrations. The shift is comparable to a hydrogen concentration of 5% (cf. Fig. D.15i in Appx. D.7.2). This suggests that—from the point of view of the statistics of the current pattern—there is no significant difference between H and OH-adsorbates. We thus expect that the distribution for j_z coincides again with the ones of j_x/j_y for larger hydroxyl concentrations.

4.3 Magnetization m_z modeled by independent magnetic moments

So far, we focused on local quantities: the current density, the induced magnetic field, and the associated distribution functions. Since spatially averaged quantities are experimentally easier to access, we here analyze the total magnetization m_z which is a measure for the average sense of rotation of the current vortices. [Total magnetization: $\mathbf{m} = \frac{1}{2} \int \mathbf{r} \times \mathbf{j}_{\text{el}}(\mathbf{r}) \, d\mathbf{r}$, cf. Eq. (2.16).] In fact there are two types of averaging procedures involved: (i) a spatial averaging over sample area, and (ii) an energy average over different states in the bias window.

4.3.1 System size dependence: $\langle (\mathrm{d}m_z/\mathrm{d}V_{\text{bias}})^2 \rangle \propto N_{\text{carbon}}$

We first focus on the spatial averaging procedure. For that purpose, we analyze the magnetization $\mathrm{d}m_z/\mathrm{d}V_{\text{bias}}$ for the hydrogenated AGNRs already used before, see Sec. 4.2.1. For the size dependence, we already calculated the current density response for several energies (all selected energies feature transmission peaks). The magnetizations induced by these current density responses—together with their mean and standard deviations—are shown in Fig. 4.19a and Fig. 4.19b, separately for the two different system ratios. The mean value is close to zero whereas the standard deviation increases with increasing system size. One might expect a power law behavior with exponent 1/2, i.e., an increase like $\sqrt{N}$, where N is the number of carbon atoms in the functionalized area. [Our data is compatible with an exponent 1/2. But our low statistics—typical for *ab initio* studies—would also allow other exponents.]

A square root behavior can be motivated by a simple model that considers m_z as a sum of $N/2$ uncorrelated magnetic moments with magnitude μ_{ring} and random signs. [There are $N/2$ carbon rings in an AGNR with N carbon atoms.] In other words, we assume that each carbon ring carries
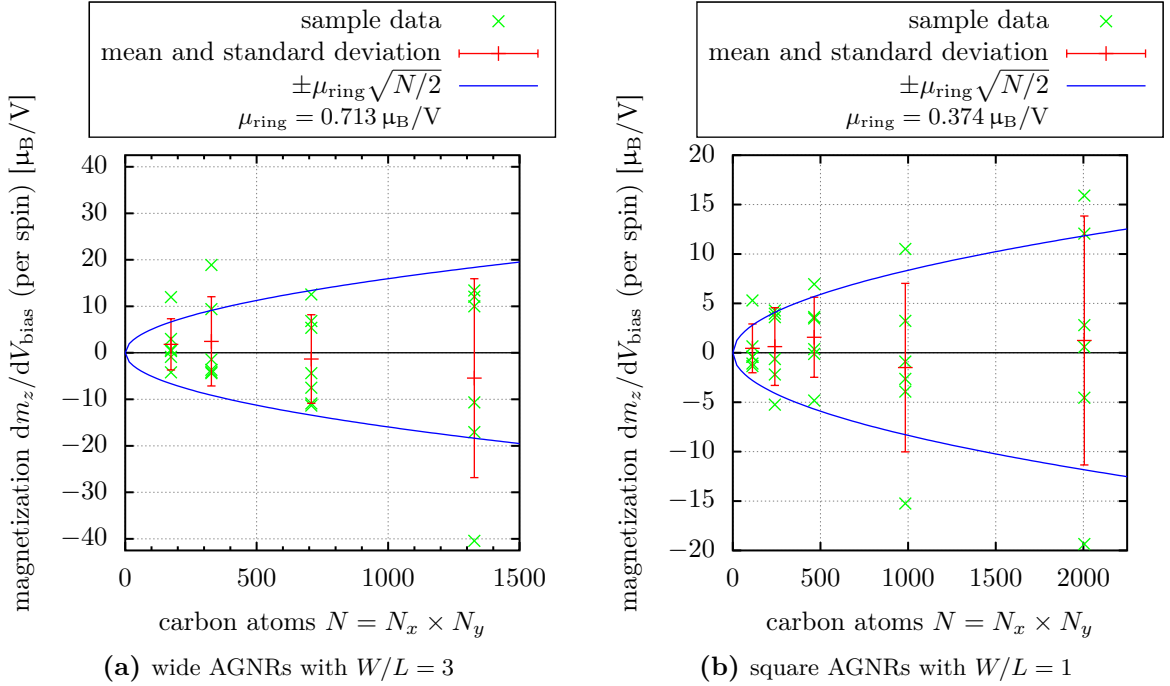
Figure 4.19: Dependence of the magnetization dm_z/dV_{bias} (per bias) on the system size. For each AGNR, the current density response is calculated at several energies (each with peaks in the transmission). The corresponding induced magnetizations dm_z/dV_{bias} (green crosses) are averaged. The mean (red cross) is near zero while the standard deviation (red bar) increases with system size. Independent magnetic moments μ_{ring} located at each carbon ring—randomly oriented in either up or down direction—predict a width of $\mu_{\text{ring}}\sqrt{N/2}$ (blue line). The values of μ_{ring} are determined by fits to the calculated standard deviation of the sample data. (The raw data is listed in Appx. D.6. For geometries, see Fig. 4.7.)

a magnetic moment μ_{ring} which randomly points in the up or down direction.[E] We thus expect a Gaussian distribution with zero mean,

$$\left\langle \frac{dm_z}{dV} \right\rangle^{\text{peak}} = 0 \,, \tag{4.5}$$

and width

$$\sigma^{\text{peak}}_{dm_z/dV} = \mu_{\text{ring}}\sqrt{N/2} \,, \tag{4.6}$$

which increases with the square root of the number of independent magnetic moments. The magnitude of the magnetic moment μ_{ring} per carbon ring is estimated by fits in Fig. 4.19a and Fig. 4.19b. The value for wide systems ($W/L{=}3$) exceeds the value for square systems ($W/L{=}1$) considerably, by almost a factor of two.

A dependence on the system ratio W/L is not unexpected; the most trivial dependence is probably a linear W/L dependence, which already manifests itself in the conductance G of clean graphene,

$G \propto W/L$ (for $W \gg L$).[F] Here, we are neither in the correct limit nor do we have enough data to estimate the dependence on the system ratio, except by noting the increase for wider ribbons. Thus, we estimate $\mu_{\text{ring}} \approx 0.5\,\mu_{\text{B}}/\text{V}$ (per spin) for $W/L \approx 1$–3, keeping in mind that μ_{ring} probably increases for increasing W/L.

4.3.2 Finite bias voltage: $\langle m_z^2 \rangle \propto V_{\text{bias}}$

We now analyze the effect of a finite bias voltage on the total magnetization. In Fig. 4.20, the voltage dependence of the magnetization (per spin) is shown for several wide and square AGNRs. The absolute value of the magnetization tends to grow with increasing bias voltage. No clear dependence on the system size is observable.

This behavior can be explained along the same lines as in the previous section. Instead of summing only over space, we now also sum over energy domain. In the previous section, we estimated the magnetic moment $\mu_{\text{ring}} \approx 0.5\,\mu_{\text{B}}/\text{V}$ of individual transport states using only peak values of the transmission function. [Recall that the transmission function shows a peak structure, one peak per transport state.] We roughly estimate the energy integrated magnetic moment $\mu_{\text{ring}}^{\text{peak}}$ (for a complete peak in the transmission) as half of the peak value μ_{ring} times the level spacing Δ (i.e. using the area of a triangle), i.e.,

$$\mu_{\text{ring}}^{\text{peak}} = \frac{1}{2}\,\mu_{\text{ring}}\,\frac{\Delta}{e}\,. \tag{4.7}$$

Using this value, we follow again the logic of summing up randomly oriented moments. There
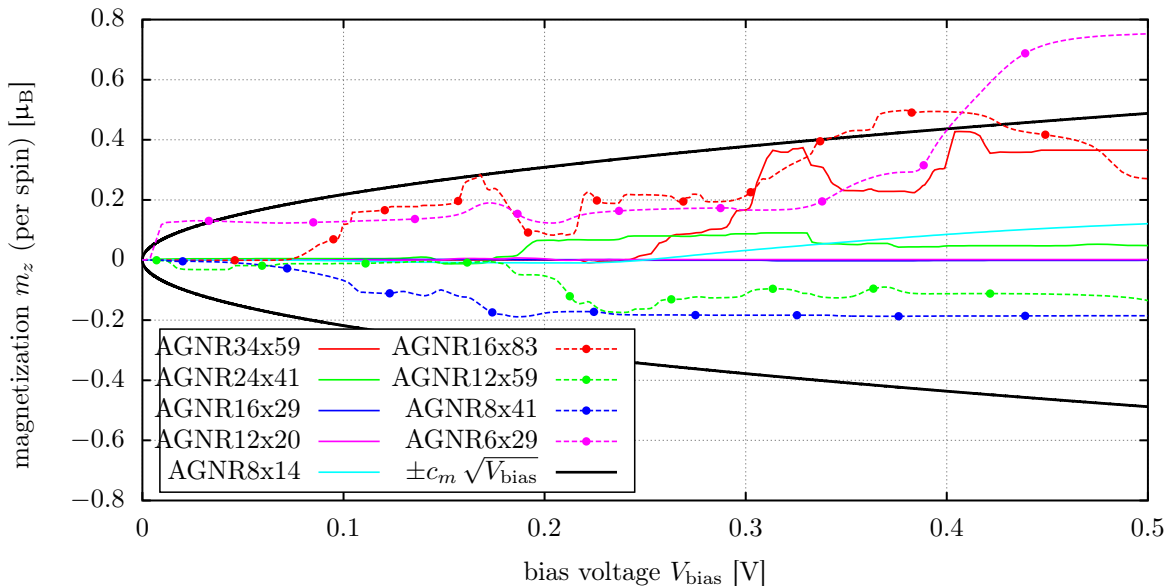
Figure 4.20: Dependence of the magnetization m_z (per spin) on the applied bias voltage V_{bias} in several AGNRs with 20% hydrogen adatoms. A simple model of magnetic moments μ_{ring} which are independently placed at each carbon ring (in space) and at each transmission peak (in energy domain) predicts a Gaussian distribution of the magnetic moment centered at zero (because of symmetry) with a width of $c_m\,\mu_{\text{B}}\,\sqrt{V_{\text{bias}}/\text{V}}$ (see text). (For geometries, see Fig. 4.7.)

are still $N/2$ carbon rings in space. Additionally, there are eV_{bias}/Δ transport states in energy domain. The total number of moments is estimated by the product,

$$\mathcal{N} = \frac{N}{2} \frac{eV_{\text{bias}}}{\Delta}\,. \tag{4.8}$$

Assuming that all these moments are independent, the sum again follows a Gaussian distribution with an average magnetization $\langle m_z \rangle = 0$. The width of the distribution,

$$\sigma_{m_z} = \mu_{\text{ring}}^{\text{peak}} \sqrt{\mathcal{N}} =: c_m\, \mu_{\text{B}}\, \sqrt{V_{\text{bias}}/\text{V}}\,, \tag{4.9}$$

increases with the square root of the bias voltage. The prefactor c_m is given by

$$c_m = 2^{-3/2}\,[\mu_{\text{ring}}\,(\mu_{\text{B}}/\text{V})^{-1}]\,\sqrt{N\Delta\,(\text{eV})^{-1}} \approx 0.69\,, \tag{4.10}$$

using the estimation $\Delta \approx 15.1\,\text{eV}/N$ for the level spacing (see Appx. D.1).

In summary, we expect a finite magnetization perpendicular to the graphene plane which scales with the square root of the applied bias voltage and is independent of the system size. The sign of the magnetization is random but its absolute value is estimated (including a spin degeneracy factor of 2) as[G]

$$\sqrt{\langle m_z^2 \rangle} \sim 1\,\mu_{\text{B}} \cdot \sqrt{V_{\text{bias}}/\,\text{V}}\,. \tag{4.11}$$

This estimation is still subject to the overall DFT uncertainty. The estimated number may deviate by a factor of order unity [i.e. give or take a factor of two]. In addition, the estimation is valid for aspect ratios of $W/L \approx 1 - 3$; we expect an increase of the magnetization for larger values of W/L.

4.4 Lattice relaxation: influence on the transmission and local current density

Lattice relaxation

An important question relates to the effect of lattice relaxation on the transport characteristics. To what extend are the transmission function and the current density sensitive to whether or not the atomistic geometry is fully relaxed into its equilibrium state? To address this question, we analyze the transport characteristics of an AGNR41 that has not been geometrically relaxed. [All AGNRs employed so far have been geometrically relaxed.]

Clearly, there is a certain arbitrariness in the selection of the unrelaxed reference state. We try to mimic at least the sp³-hybridization of the anchor carbon atoms. Therefore, we adopt the following procedure: We start with an unrelaxed structure consisting of a regular hexagonal carbon lattice (bond length $d_{\text{CC}} = 1.439\,\text{Å}$) with hydrogen termination. The adsorbed hydrogen atoms are then placed vertically above or below the carbon atoms with a bond distance of $d_{\text{CH}} = 1.095\,\text{Å}$ (see Appx. A.1 for further details). The carbon atoms (with the adsorbed hydrogen atoms) are moved

	unrelaxed	relaxed (AGNR8×41)	relaxed (AGNR34×59)
$d_{\mathrm{HC_H}}$	1.095 Å	$1.119 \pm 0.008(^{+0.017}_{-0.013})$ Å	$1.119 \pm 0.007(^{+0.020}_{-0.015})$ Å
d_{HH}	1.439 Å	$2.100 \pm 0.024(^{+0.031}_{-0.039})$ Å	$2.124 \pm 0.043(^{+0.167}_{-0.057})$ Å
$d_{\mathrm{C_0 C_0}}$	1.439 Å	$1.428 \pm 0.024(^{+0.055}_{-0.072})$ Å	$1.426 \pm 0.026(^{+0.142}_{-0.078})$ Å
$d_{\mathrm{C_0 C_H}}$	1.523 Å	$1.513 \pm 0.010(^{+0.024}_{-0.030})$ Å	$1.512 \pm 0.011(^{+0.078}_{-0.036})$ Å
$d_{\mathrm{C_H C_H}}$	1.439 Å	$1.566 \pm 0.016(^{+0.028}_{-0.014})$ Å	$1.560 \pm 0.010(^{+0.023}_{-0.022})$ Å

Table 4.1: Effect of lattice relaxation on the bond lengths d_{XY} (measured between atom type X and type Y). To reduce boundary effects, we take only atoms into account which (a) were fully relaxed and (b) are at least 3 carbon atoms away from the ribbon boundary (in y-direction). Atom types: hydrogen atom (H) adsorbed on a carbon atom ($\mathrm{C_H}$), and carbon atoms ($\mathrm{C_0}$) without any hydrogen adsorbates. In case of two hydrogen atoms (d_{HH} or $d_{\mathrm{C_H C_H}}$), both hydrogen atoms are located on the same side of the graphene flake. For the relaxed AGNR41, the distances are given as $m \pm \sigma(^{\Delta_{\max}}_{\Delta_{\min}})$ where m is the average value, σ is the standard deviation and $m + \Delta_{\max/\min}$ is the maximal/minimal value. In the unrelaxed AGNR41, all distances are exact in the sense that no spatial variations exist.

(a) unrelaxed structure

(b) relaxed structure
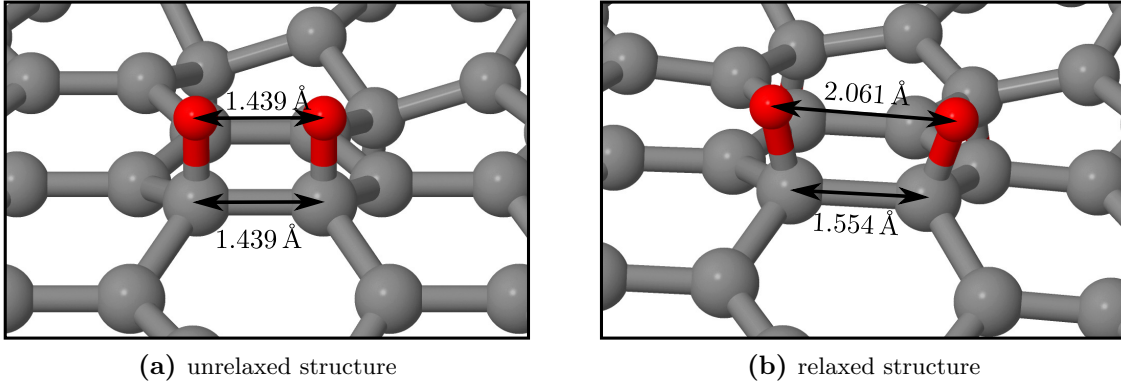
Figure 4.21: Example of lattice relaxation when two hydrogen adsorbates sit on neighboring carbon atoms. (a): Unrelaxed structure with hydrogen adsorbates placed directly above the carbon atoms (see text). (b): DFT-relaxed structure (see text). The hydrogen atoms (red spheres) repel each other to make room for their electron cloud. This also pushes the anchor carbon atoms (gray spheres) apart.

out of the graphene plane by 0.5 Å to represent the sp^3-hybridization. This geometry serves as unrelaxed reference state. For the relaxed structure, we additionally structurally relax all atoms of functionalized area (device region excluding contact region) until all atomic forces drop below 10^{-2} eV/ Å. The relaxed AGNR41 was shown in Fig. 4.1b.

We illustrate the change of the lattice constants due to relaxation in Tab. 4.1. The most important effect is that hydrogen adsorbates sitting on adjacent carbon atoms repel each other (d_{HH} grows) and also pull their anchor carbon atoms apart ($d_{\mathrm{C_H C_H}}$ grows). This effect is also shown in Fig. 4.21. Additionally, the bond-lengths are no longer the same everywhere in the ribbon but depend on the local impurity configuration, e.g. the carbon-carbon bond length $d_{\mathrm{C_0 C_0}}$ (for carbon atoms without hydrogen adsorbates) deviates up to 5% from its average value.
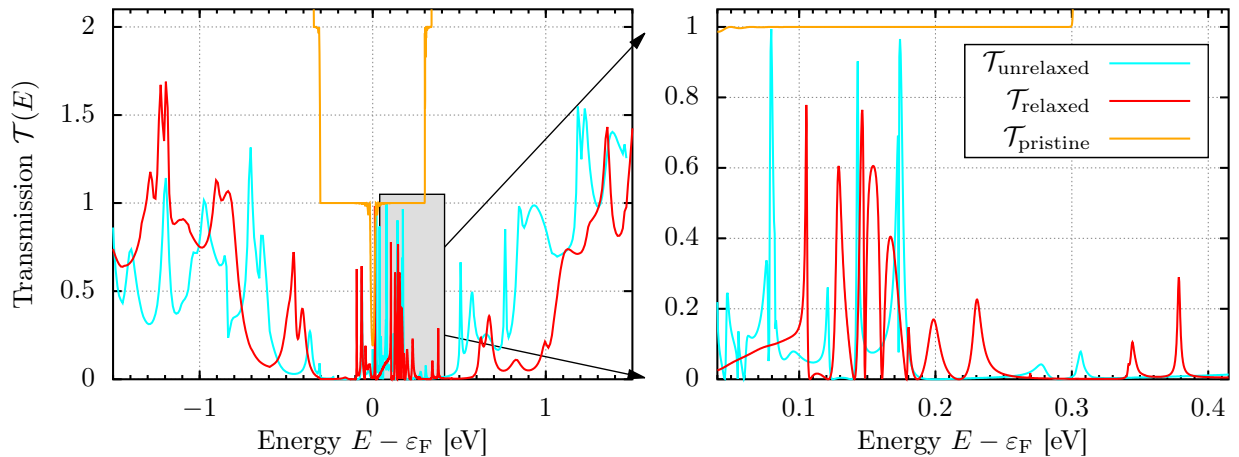
Figure 4.22: Comparison of the transmission through the relaxed and the unrelaxed version of the hydrogenated AGNR8×41 shown in Fig. 4.1b. Additionally, the number of channels of the pristine AGNR41 is shown (orange). [DFT details: FHI-AIMS, basis set `tier1`, closed-shell]

Relaxation effects on the transmission function

The transmission functions of the relaxed and unrelaxed AGNR41 are displayed in Fig. 4.22. Major modifications can be seen: neither the peak structure near the Fermi energy (see zoom-in) nor the transmission for higher energies can be reproduced. Therefore, we conclude that the details of the transmission function, especially the peak positions, are not only sensitive to where the adsorbates are placed, but also to the induced lattice distortion.

Relaxation effects on the current density

Next, we check the local current density. Since already the transmission function (total current per bias) differs, it does not make sense to expect the current density responses taken at specific energies to coincide: they certainly differ. Since the transmission of the unrelaxed AGNR41 shows a familiar peak structure near the Fermi energy, one might hope that the current density contributions are just slightly shifted but that a integrated current density is still correctly reproduced. To check this, we apply a finite bias voltage of $V_{\text{bias}} = 1\,\text{V}$. The current density and the related distribution functions of the unrelaxed AGNR41 are shown in Fig. 4.23. The current density of the relaxed lattice has already been shown in Fig. 4.14. Already at first glance, one detects significant differences between the current patterns. Thus, the lattice relaxation is also affecting the local current paths.

On the other hand, we see that the qualitative features—current vortices and broad distributions—are reproduced with the unrelaxed lattice as well. This is not surprising since we know that these general features are reproduced for several different impurity types (cf. Sec. 4.2.4). In the unrelaxed lattice, the hydrogen adatoms exert a different influence on the electronic structure, e.g., no crosstalk. They effectively behave as impurities of a different type.

(a) Current density at finite bias $V_{bias} = 1\,V$

(b) Distribution function of the current density

(c) Distribution function of the current angles
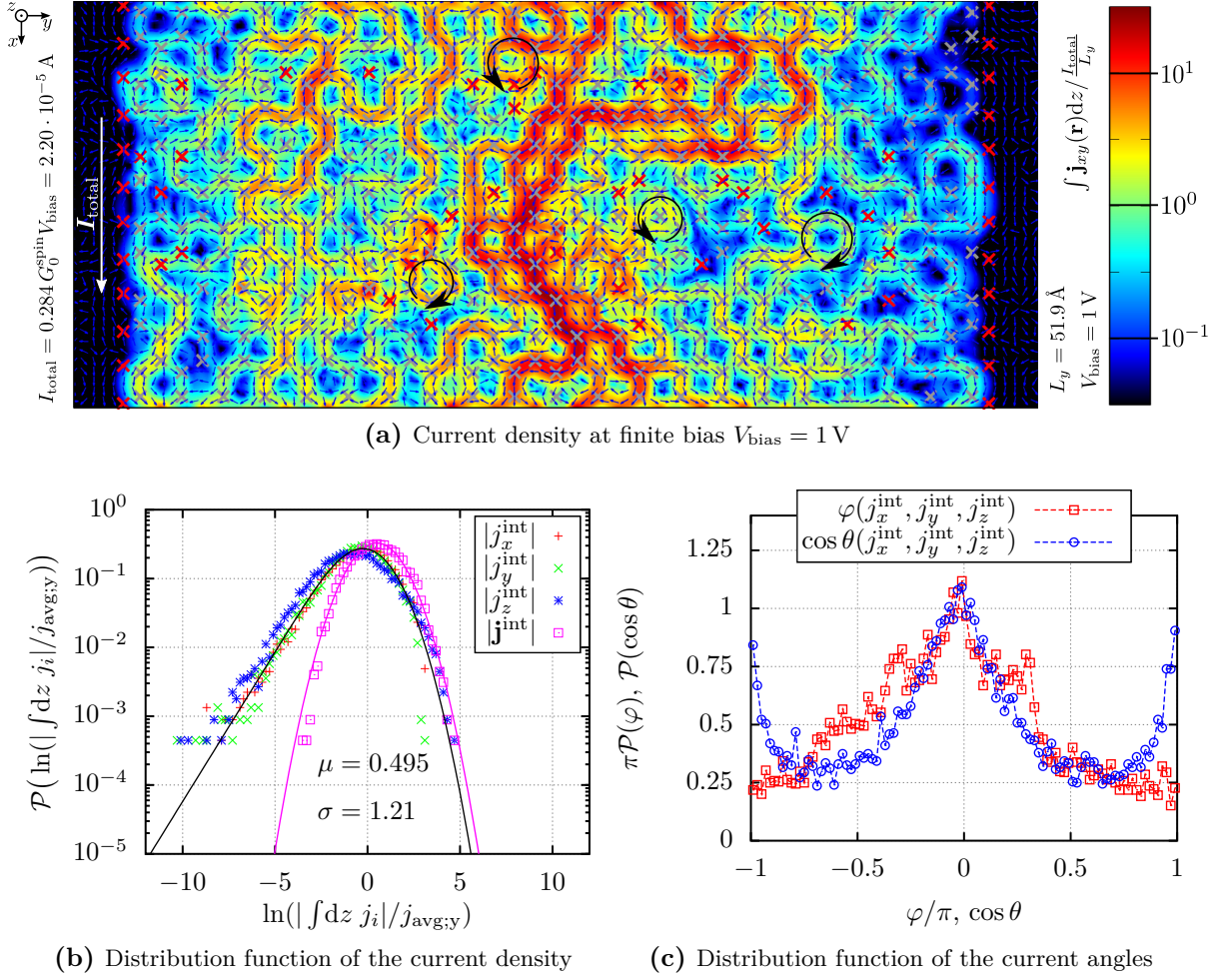
Figure 4.23: Local current density and corresponding distribution functions for the *unrelaxed* version of the hydrogenated AGNR8×41 shown in Fig. 4.1b at a finite bias voltage $V_{bias} = 1\,V$. This is the analogue figure to Fig. 4.14 which shows the local current density and corresponding distribution functions for the *relaxed* version of the hydrogenated AGNR8×41.

Our result bears a relevance for tight-binding simulations of disordered graphene flakes in the limit of large defect concentrations. Generic tight-binding studies ignore the crosstalk that two (or more) adsorbates can have via their interaction in terms of lattice strain. We expect that this crosstalk plays an important role, at higher concentrations, for the optimal lattice geometry. As our study shows, the crosstalk feeds back also into the electronic structure, the transmission function and the local current density.

Notes to chapter 4

The notes are for completeness, reproducibility and to help interested readers understand all the fine technical details.

[A] Percolation theory analyzes how many sites of a regular (infinite) lattice (where only neighboring sites are connected) can be removed before the lattice disintegrates, i.e., before the spanning cluster vanishes. Spanning clusters are connected clusters of the same order as the system size. The spanning clusters are important for transport effects since only they provide connected paths between far away regions.

In a hexagonal lattice (as graphene), $n \lesssim 30.3\%$ random sites can be removed before the spanning cluster vanishes. For the exact percolation threshold see, e.g., Ref. 163.

Therefore, we focus on hydrogenated graphene with hydrogen concentration below 30.3% so that paths exist that only involve carbon atoms which do not carry adsorbed hydrogen atoms. (page 60)

[B] Throughout this thesis, the mean μ refers to the spatial average of the logarithm of the current density normalized to the total through current, i.e.,

$$\left\langle \ln\left[\frac{\left| \int \mathrm{d}z\, \mathbf{j}(\mathbf{r}) \right|}{I_{\mathrm{total}}/L_y} \right] \right\rangle_{x,y} = \mu\,. \qquad (4.12)$$

On a linear (non-logarithmic) scale, the average of the local current density is

$$\left\langle \frac{\left| \int \mathrm{d}z\, \mathbf{j}(\mathbf{r}) \right|}{I_{\mathrm{total}}/L_y} \right\rangle_{x,y} = \mathrm{e}^{\mu + \sigma^2/2}\,, \qquad (4.13)$$

which also includes the width σ of the lognormal distribution. (page 65)

[C] The magnetic field response in Fig. 4.3b is in the order of $\mathrm{d}B/\mathrm{d}V_{\mathrm{bias}} = 1\,\mathrm{T/V}$. The width of the transmission peak (see Fig. 4.2a) is in the order of $\delta E = 1\,\mathrm{meV}$. Thus, applying a finite bias voltage of $V_{\mathrm{bias}} = 1\,\mathrm{mV}$, we expect a magnetic field of $B_0 = 1\,\mathrm{mT}$, or equivalent $\mu_{\mathrm{B}} B_0/\hbar \approx 100\,\mathrm{MHz}$. (page 67)

[D] The reader might wonder, why we use a concentration of 5% hydroxyl groups rather than our standard choice of 20%. Since the hydroxyl groups are larger than single hydrogen adatoms, randomly placing a large concentration on graphene leads to collisions, i.e. hydrogen

atoms of hydroxyl groups anchored on neighboring carbon atoms are too close. A geometric relaxation of such a system would take enormous computational resources. Instead, we tried placing 20% hydroxyl groups in one sublattice (although this significantly differs from a random configuration). Even then, the hydrogen atoms can get close, and in some positions, H_2O separates in the geometric relaxation, leaving a single oxygen radical. Chemically, we expect the oxygen to be highly reactive and to bind to nearly everything in the environment. In our simulations, the geometric relaxations are performed without an environment, and the oxygen stays without additional bonding partners leading to local charging effects. Nevertheless, we analyzed the system. It also features current vortices compatible with our results. (page 80)

[E] Summing up such random contributions is equivalent to a one-dimensional random walk[164, 165] taking $N/2$ steps with step size μ_{ring}. (page 84)

[F] In pristine graphene, the zero bias conductance G is given by

$$G = G_0^{\mathrm{spin}}\, \mathcal{T}(\varepsilon_{\mathrm{F}}) = \frac{4e^2}{\pi h} \frac{W}{L}\,, \qquad (4.14)$$

valid in the wide system limit, $W \gg L$ [115, 166, 167]. The W/L-dependence is due to the number of bands growing linearly when increasing the system width. (page 85)

[G] For a Gaussian distribution, the root mean square expectation value is equal to the width of the distribution, i.e., for the magnetization (per spin), we expect

$$\sqrt{\langle m_z^2 \rangle} = \sigma_{m_z} \approx 0.69\,\mu_{\mathrm{B}} \cdot \sqrt{V_{\mathrm{bias}}/\mathrm{V}}\,, \qquad (4.15)$$

whereas the expectation of the absolute value

$$\begin{aligned} \langle |m_z| \rangle &= \sqrt{\frac{2}{\pi}}\,\sqrt{\langle m_z^2 \rangle} = \sqrt{\frac{2}{\pi}}\,\sigma_{m_z} \\ &\approx 0.55\,\mu_{\mathrm{B}} \cdot \sqrt{V_{\mathrm{bias}}/\mathrm{V}} \end{aligned} \qquad (4.16)$$

is reduced by a constant prefactor $\sqrt{2/\pi}$. (page 86)

5 Chapter 5
Spin effects

In this chapter, we investigate the effects of spin polarization on the transport behavior, which has not been considered so far in this thesis. After a short introduction into spin DFT with an emphasis on spin-orbit interaction (Sec. 5.1), we focus on spin-flip effects in transport through hydrogenated graphene ribbons in Sec. 5.2. We find that the spin-flip transmission can reach the same order of magnitude as the spin-conserving one. We relate this effect to exchange-interaction rather than intrinsic spin-orbit interaction. We also investigate the spin effects on the unpolarized current density and find current patterns featuring broad fluctuations and strong ring currents, exactly as in the spin-independent case. The exact current patterns and transmission functions depend on the exact ground configuration but the generic features—broad fluctuations and ring currents—are always the same. Thus, we presume that these qualitative features do not depend on the exact groundstate and are also correctly reproduced in spin-restricted closed-shell simulations. In Sec. 5.3, we explicitly check this conjecture for one of the systems previously discussed in Chap. 4: a medium sized AGNR8x41 with 20% hydrogen. The qualitative results are indeed independent of the employed level of spin treatment.

5.1 DFT transport for systems with broken spin-rotational invariance

5.1.1 Spin effects in DFT

In the previous chapters, spin effects played a minor role: a spin degeneracy of two was included in all calculations but no further spin effects were covered. In these cases, the transport spin is preserved. In principle, there are several reasons, why the transport spin may not be preserved. The three most prominent ones are: (i) exchange-interaction with local spins, (ii) spin-orbit interaction (SOI), and (iii) interaction with a magnetic field. In this chapter, we study the effects of type (i) and (ii). Effects of type (iii) are partly discussed in Chap. 6.

There are two well-established procedures to include spin into KS-DFT. The first and much more common one is collinear spin DFT. Instead of working only with the total groundstate density $n(\mathbf{r})$, collinear spin DFT employs spin-resolved groundstate densities, $n_\uparrow(\mathbf{r})$ and $n_\downarrow(\mathbf{r})$, or equivalently the total density n and the spin density $s=n_\uparrow-n_\downarrow$. The spin resolved densities $n_\sigma(\mathbf{r})$ are separately represented by a sum of orthonormal KS states $\psi_{\sigma,l}^{\mathrm{KS}}(\mathbf{r})$. The reconstructed KS Hamiltonian is spin-diagonal, all KS spins point along (or against) the chosen quantization axis. For further details on collinear spin DFT please refer to the literature, e.g. Ref. 168 and references therein.

An advantage of collinear spin DFT is that it is computationally much cheaper than spinor DFT, which is an alternative way to include spin effects to DFT. In spinor DFT, the basic idea is to extend the KS states to two-component KS spinors

$$\psi^{\mathrm{KS}}(\mathbf{r}) = \begin{pmatrix} \psi_\uparrow^{\mathrm{KS}}(\mathbf{r}) \\ \psi_\downarrow^{\mathrm{KS}}(\mathbf{r}) \end{pmatrix} . \tag{5.1}$$

They represent the groundstate density

$$n(\mathbf{r}) = \sum_l \left[\psi_l^{\mathrm{KS}}(\mathbf{r}) \right]^\dagger \psi_l^{\mathrm{KS}}(\mathbf{r}) , \tag{5.2}$$

and the spin density

$$\mathbf{s}(\mathbf{r}) = \sum_l \left[\psi_l^{\mathrm{KS}}(\mathbf{r}) \right]^\dagger \frac{\hbar}{2}\boldsymbol{\sigma}\, \psi_l^{\mathrm{KS}}(\mathbf{r}) , \tag{5.3}$$

with $\boldsymbol{\sigma}$ being a vector of Pauli matrices. That way, the local spin density can point in any direction, not only parallel or antiparallel to the quantization axis. The reconstructed KS Hamiltonian can feature spin-off-diagonal elements

$$\mathbf{H}^{\mathrm{KS}} = \begin{pmatrix} \mathbf{H}_{\uparrow\uparrow}^{\mathrm{KS}} & \mathbf{H}_{\uparrow\downarrow}^{\mathrm{KS}} \\ \mathbf{H}_{\downarrow\uparrow}^{\mathrm{KS}} & \mathbf{H}_{\downarrow\downarrow}^{\mathrm{KS}} \end{pmatrix} , \tag{5.4}$$

which, in KS transport, can allow for spin-flip transmission terms $\mathcal{T}_{\uparrow\downarrow}$ and $\mathcal{T}_{\downarrow\uparrow}$. Such terms describe electrons whose spins flip when traversing the system (cf. Sec. 2.1.4). In the following, we use the spinor DFT approach as implemented in TURBOMOLE [134], which, conveniently, also features an all-electron spin-orbit interaction (SOI) module[169]. Since SOI included in spinor DFT is a less known topic, we outline the basic idea in Sec. 5.1.2.

Remark: By default, the spin quantization axis used in TURBOMOLE is the z-axis. For an arbitrary quantization axis $\mathbf{n} = (\sin\theta\cos\varphi, \sin\theta\sin\varphi, \cos\theta)$, we use an unitary transformation

$$U = \begin{pmatrix} \cos\frac{\theta}{2} & -\mathrm{e}^{-\mathrm{i}\varphi}\sin\frac{\theta}{2} \\ \mathrm{e}^{\mathrm{i}\varphi}\sin\frac{\theta}{2} & \cos\frac{\theta}{2} \end{pmatrix} , \qquad \mathbf{H}^{\mathrm{KS}} \to U\,\mathbf{H}^{\mathrm{KS}}\,U^\dagger , \tag{5.5}$$

to rotate the KS Hamiltonian in spin space. For additional details, please refer to the master thesis of J. Wilhelm[140, Ch. 6] who implemented the spin rotation in our transport module.

5.1.2 Spin-orbit interaction (SOI)

Origin of SOI

Spin-orbit interactions (SOI) originate as relativistic effects for single electrons from the Dirac equation[170]. The Dirac wavefunctions are described by four-component spinors; half of the components describe positron like contributions. In the low energy limit, the four-component spinors can be decoupled into two-component spinors

$$\psi(\mathbf{r}) = \begin{pmatrix} \psi_\uparrow(\mathbf{r}) \\ \psi_\downarrow(\mathbf{r}) \end{pmatrix} \tag{5.6}$$

with a spin up and a spin down component. These two-component spinors obey a low-energy Dirac equation:

$$\left(\hat{\mathcal{H}}_0 + \delta\hat{\mathcal{H}}_{\text{rel-scalar}} + \delta\hat{\mathcal{H}}_{\text{SOI}}\right)\psi = E\psi\,. \tag{5.7}$$

Here, $\hat{\mathcal{H}}_0$ is the unperturbed non-relativistic single particle Hamiltonian including the standard kinetic term $\mathbf{p}^2/(2m)$. The relativistic-scalar corrections $\delta\hat{\mathcal{H}}_{\text{rel-scalar}}$ include kinetic corrections $\mathbf{p}^4/(8m^3c^2)$ as well as the Darwin term $\Delta v_{\text{ex}}(\mathbf{r})\hbar^2/(8m^2c^2)$. Conceptually, they are easy to treat because they are spin-diagonal. The interesting term, is the SOI

$$\delta\hat{\mathcal{H}}_{\text{SOI}} = \frac{\hbar}{4m^2c^2}\,\boldsymbol{\sigma}\cdot\left[\left(\boldsymbol{\nabla}v_{\text{ex}}(\mathbf{r})\right)\times\mathbf{p}\right]\,, \tag{5.8}$$

because it couples the electron spin $\frac{\hbar}{2}\boldsymbol{\sigma}$ with the orbital properties $(\boldsymbol{\nabla}v_{\text{ex}})\times\mathbf{p}$. This breaks spin-rotational invariance. The SOI is proportional to the gradient of the external potential $v_{\text{ex}}(\mathbf{r})$ generated by the atom cores. Therefore, one expects a large SOI for heavy atoms but not for graphene which consists of carbon atoms. However, recent studies show that the SOI in hydrogenated graphene is massively enhanced by lattice distortion[158–160].

Incorporating SOI in spinor DFT

See Appx. B.2 for an overview of DFT nomenclature.

To include SOI in spinor DFT one must—at least in principle—express the relativistic energy corrections $\delta\hat{\mathcal{H}}_{\text{rel-scalar}}$ and $\delta\hat{\mathcal{H}}_{\text{SOI}}$ in terms of the densities $n(\mathbf{r})$ and $\mathbf{s}(\mathbf{r})$. Since this seems hopeless, one employs the KS formulation for the relativistic corrections in the same way as it has already been applied to the kinetic single particle term $\hat{t}_{\text{kin}}$: the relativistic corrections are calculated for the (non-interacting) KS states, and all further corrections are absorbed into the exchange-correlation functional E_{xc}. The full energy functional

$$\begin{aligned} E[n,\mathbf{s}] = &\sum_l \langle\psi_l^{\text{KS}}|\hat{t}_{\text{kin}} + \delta\hat{\mathcal{H}}_{\text{rel-scalar}} + \delta\hat{\mathcal{H}}_{\text{SOI}}|\psi_l^{\text{KS}}\rangle \\ &+ \frac{1}{2}\int d\mathbf{r}\, v_{\text{H}}(\mathbf{r})\,n(\mathbf{r}) + \int d\mathbf{r}\, v_{\text{ex}}(\mathbf{r})\,n(\mathbf{r}) + E_{\text{xc}}[n,\mathbf{s}]\,, \end{aligned} \tag{5.9}$$

then contains the relativistic corrections and an exchange-correlation potential $E_{xc}[n, \mathbf{s}]$ which depends on the spin density. The other terms, the (non-relativistic) kinetic energy $\hat{t}_{kin}$, the Hartree-potential $v_H(\mathbf{r})$, and the external potential $v_{ex}(\mathbf{r})$ remain unchanged. In principle, the energy functional $E[n, \mathbf{s}]$ is exact since it only defines the exchange-correlation functional E_{xc}. In practice, $E_{xc}[n, \mathbf{s}]$ is usually approximated by a non-relativistic functional, e.g. by well-established GGA- or LDA-functionals.

We have outlined only the basic idea of SOI in DFT and omitted many technical and conceptual subtleties. For these details, please refer to the TURBOMOLE *package[169, 171].*

5.2 Application: narrow hydrogenated graphene ribbons including spin-orbit interaction (SOI) & spin magnetism

We now investigate the spin-flip transmission in hydrogenated AGNR11, following closely our own publication[111]. Here, I greatly thank J. Wilhelm who performed the spinor DFT calculations. We consider two AGNR11 with different impurity configurations: (a) with a single hydrogen adatom and (b) with a finite concentration of randomly distributed hydrogen adatoms, see Fig. 5.1. The hydrogen adatoms form chemical bonds to the anchor carbon atoms which results in sp^3 hybridizations of the anchor atoms. Both systems were structurally relaxed[A] to include the strong enhancement of SOI due to local lattice distortion[158–160].

5.2.1 Single hydrogen adsorbate

We start with the AGNR11 including a single hydrogen adatom. The simulated spin-dependent transmission functions $\mathcal{T}_{\sigma\sigma'}$ are shown in Fig. 5.2. First, we focus on the situation where the total

(a) 1H on AGNR11 $\mathbf{S} = (-0.12, 0.01, 0.99)\hbar$ **(b)** 12H on AGNR4x11 $\mathbf{S} = (-0.16, 0.04, 0.86)\hbar$
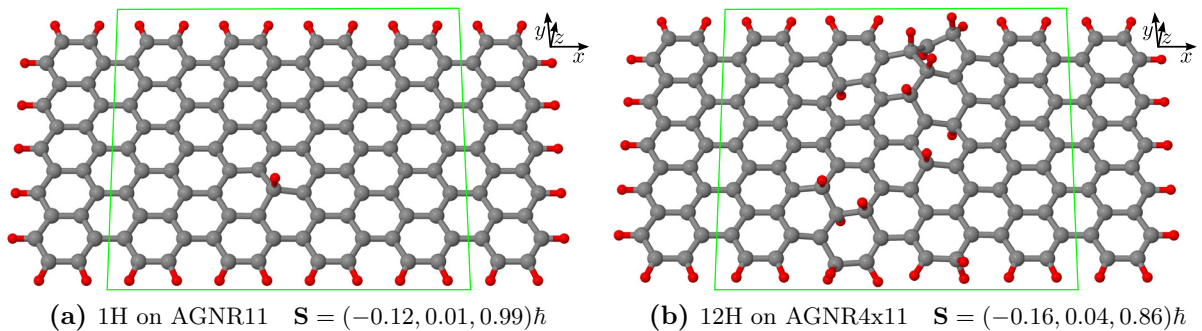
Figure 5.1: Finite sized hydrogen-terminated armchair graphene nanoribbons (carbon atoms in gray) with hydrogen adatoms (red) as used in the DFT calculation: (a) one hydrogen atom on a clean AGNR11, (b) 12 hydrogen atoms on AGNR4x11 (corresponds to 27% hydrogen coverage). For both ribbons, the total spin moment $\mathbf{S} = \int \mathbf{s}(\mathbf{r}) \, d^3\mathbf{r}$ for the finite sized ribbon, predicted by a spinor DFT simulation including SOI, nearly aligns with the z-axis, $\mathbf{S} \approx |\mathbf{S}| \, \mathbf{e}_z$. For transport simulations, the device region (green box) is extended by (semi-infinite) leads in x-direction. The leads are represented by closed-shell DFT calculations without SOI. Therefore, SOI is effectively restricted to the device region (green box).

(a) QA: $\mathbf{e}_z \parallel \mathbf{S}$ (SOI)

(b) QA: $\mathbf{e}_x \perp \mathbf{S}$ (SOI)

(c) QA: $\mathbf{e}_z \parallel \mathbf{S}$ (no SOI)

(d) QA: $\mathbf{e}_x \perp \mathbf{S}$ (no SOI)
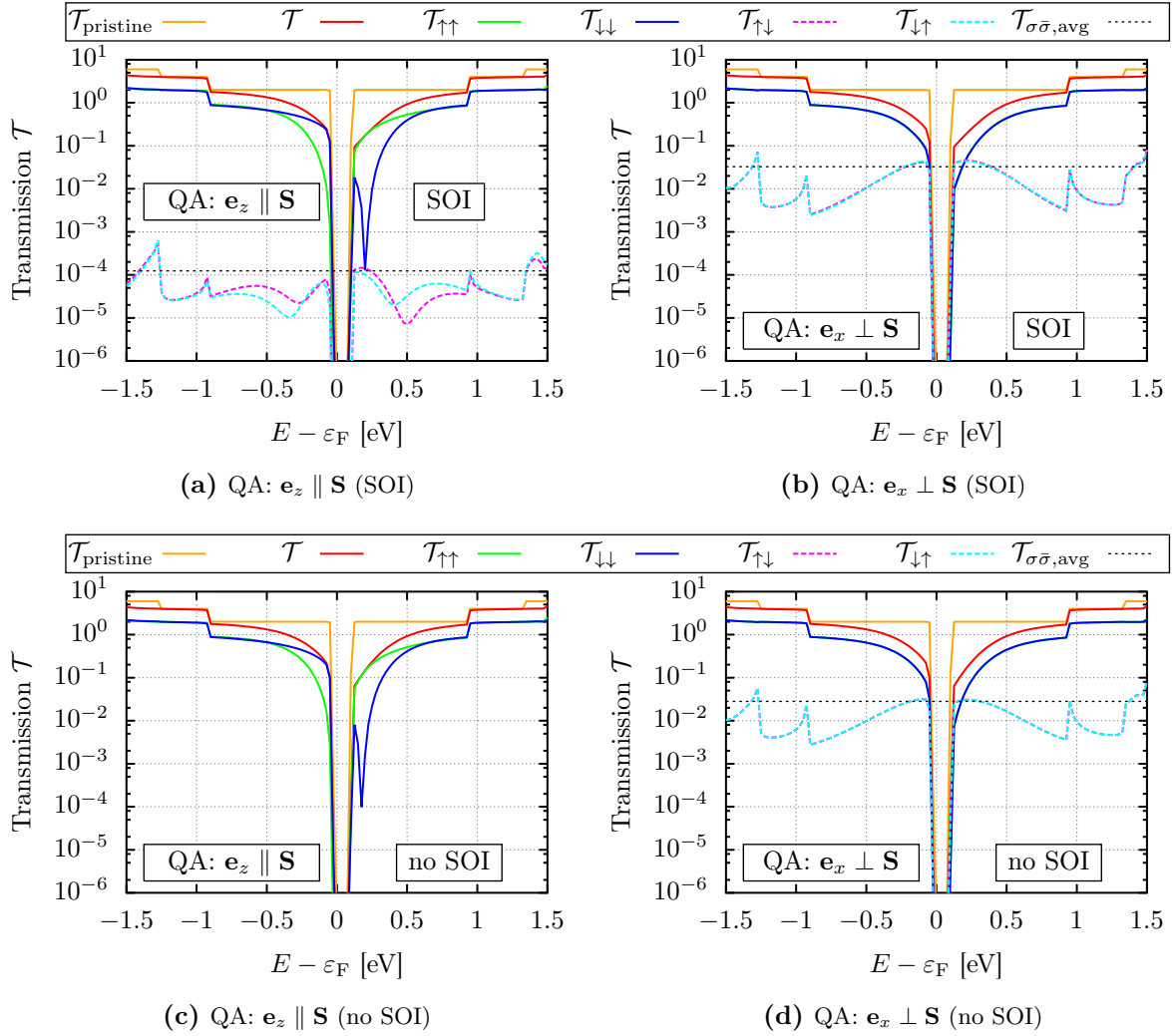
Figure 5.2: Spin-dependent transmission of transport through an AGNR11 with one hydrogen adatom with SOI (a,b) and without SOI (c,d); see Fig. 5.1a for the atomic structure. The quantization axis (QA) of the incoming electrons is either (a,c) aligned with or (b,d) perpendicular to the total spin $\mathbf{S} \approx |\mathbf{S}| \mathbf{e}_z$ of the finite sized sample. The average spin-flip transmission $\mathcal{T}_{\sigma\bar{\sigma},\mathrm{avg}}$ is calculated as the average of both spin-flip transmissions, $\mathcal{T}_{\sigma\bar{\sigma},\mathrm{avg}} = (E_2 - E_1)^{-1} \int_{E_1}^{E_2} (\mathcal{T}_{\uparrow\downarrow} + T_{\downarrow\uparrow}) \, \mathrm{d}E$, $E_{1/2} = \varepsilon_\mathrm{F} \pm 1.5\,\mathrm{eV}$. $\mathcal{T}_{\mathrm{pristine}}$ is given by the number of bands in pristine AGNR11. Please note that $\mathcal{T}_{\uparrow\uparrow}$ and $\mathcal{T}_{\uparrow\downarrow}$ are sometimes hidden behind $\mathcal{T}_{\downarrow\downarrow}$ and $\mathcal{T}_{\downarrow\uparrow}$, respectively. $\mathcal{T}_{\downarrow\uparrow}$ and $\mathcal{T}_{\uparrow\downarrow}$ are exactly zero in panel (c). My thanks to J. Wilhelm who performed the numerical calculations[140]. [DFT details: TURBOMOLE, basis set SVP, spinor DFT with and without SOI]

spin of the sample and the spin of incoming electrons are (very nearly) aligned. The former points in (near) z-direction, $\mathbf{S} = (-0.12, 0.01, 0.99)\hbar$; so we choose z as spin quantization axis for the conduction electrons. The corresponding transmission functions are shown in Figs. 5.2a and 5.2c with and without SOI, respectively. We first note, that the spin-conserving transmissions $\mathcal{T}_{\sigma\sigma}$ are virtually identical, and we conclude that SOI hardly influences $\mathcal{T}_{\sigma\sigma}$. The most prominent feature is a broad antiresonance in $\mathcal{T}_{\downarrow\downarrow}$ which refers to the quasilocalized state induced by the hydrogen adatom. Such antiresonances are well-known in literature and we already discussed

them in Secs. 3.2 and 3.3. In Fig. 5.2a, the spin-flip transmission $\mathcal{T}_{\sigma\bar{\sigma}}$ ($\mathcal{T}_{\uparrow\downarrow}$ and $\mathcal{T}_{\downarrow\uparrow}$) is very small, in the order of 10^{-4}. And it completely vanishes in Fig. 5.2c due to the absence of SOI.

Next, we consider the case where the spin of the incoming electrons is not aligned with the sample spin. In Fig. 5.2b (with SOI), the spin-flip transmission is strongly enhanced, in the order of $5 \cdot 10^{-2}$. Slightly above the bandgap, it does significantly exceed the spin-conserving transmission. We claim, that this enhancement is not related to SOI, but due to exchange interaction. As evidence, we repeat the the transmission calculation without SOI, see Fig. 5.2d. The result is indeed indistinguishable from Fig. 5.2b.

In a nutshell, the exchange-driven spin-flip can be understood as follows: assuming the sample spin $\mathbf{S}$ points into a fixed direction, say the z-direction, the exchange interaction $\mathbf{S} \cdot \mathbf{S}_{\text{cond}}$ turns into $S_z S_{z,\text{cond}} \sim \hat{\sigma}_{z,\text{cond}}$ where the Pauli matrix $\hat{\sigma}_{z,\text{cond}}$ acts on the incoming conduction electrons. Thus, an incoming spin is conserved if fully polarized in the $\pm z$-direction. In contrast, a spin is no longer conserved if it exhibits a component perpendicular to the sample spin, e.g., in x-direction. Then, spin-flips become possible. In the case of a single hydrogen adatom (as presented in Fig. 5.2), the spin-flip probability $(\mathcal{T}_{\uparrow\downarrow} + \mathcal{T}_{\downarrow\uparrow})/\sum_{\sigma\sigma'} \mathcal{T}_{\sigma\sigma'}$ reaches values near unity, for energies near the bandgap.

Remark: Additional examples which support our analysis can be found in Ref. 111 (two hydrogen adatoms on AGNR11) and Ref. 140 (OH groups on AGNR11).

5.2.2 Finite hydrogen concentration

To make a connection to Chap. 4, we also investigate a ribbon with a finite hydrogen concentration, as shown in Fig. 5.1b. The corresponding transmission functions are shown in Fig. 5.3 for two different quantization axes. First, the transmission functions show many antiresonances, leading to strong transmission fluctuations. They are due to several quasilocalized states near the Fermi energy induced by the hydrogen adatoms. Second, the spin-flip transmission reaches the same order of magnitude as the spin-conserving one in a large energy window.

Notice, for both quantization axes, the spin-flip transmission is in the order of $5 \cdot 10^{-2}$. In contrast to a single hydrogen adatom, the spin-flip transmission is not strongly suppressed if the spins of the incoming electron are aligned with the total sample spin $\mathbf{S}$. In fact, we could not find a quantization axis where the spin-flip transmission is suppressed to $\sim 10^{-4}$ similar to Fig. 5.2a. From that, we conclude, that the local spin density is strongly fluctuating in space, and that only the average is pointing in z-direction.

5.2.3 Local current density for finite hydrogen concentration

In Fig. 5.4, we show the (spin-unpolarized) local current density response for the hydrogenated AGNR11 of Sec. 5.2.2 based on spinor DFT calculations including SOI. The current exhibits strong mesoscopic fluctuations covering three decades. They are related to vortices which exceed the average current by over one order of magnitude. We compare this result with Chap. 4, in

(a) QA: $\mathbf{e}_z \parallel \mathbf{S}$ (SOI) **(b)** QA: $\mathbf{e}_x \perp \mathbf{S}$ (SOI)
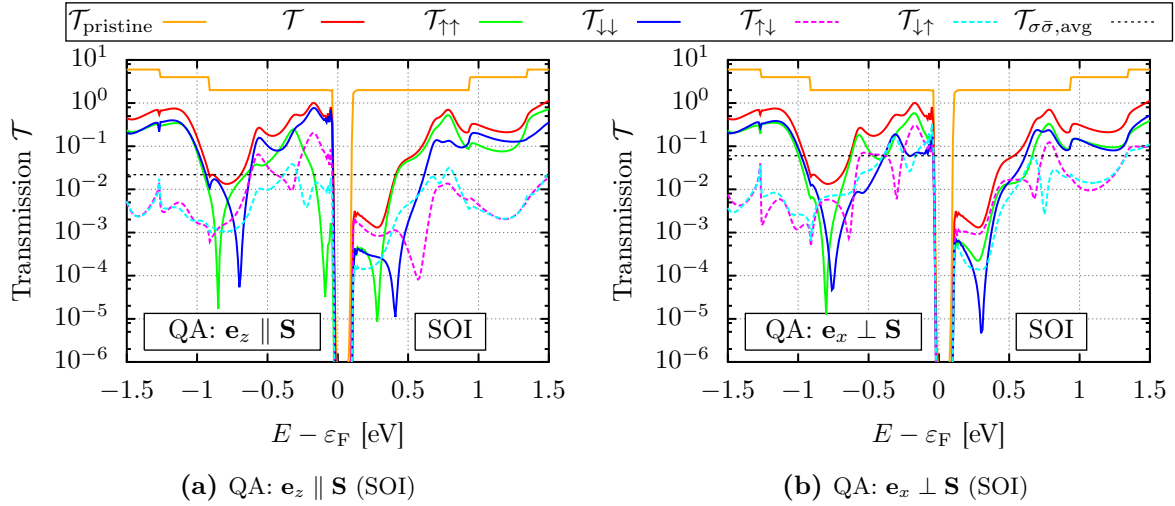
Figure 5.3: Spin-dependent transmission of transport through an AGNR11 with 12 hydrogen adatoms with SOI; see Fig. 5.1b for the atomic structure. The quantization axis (QA) of the incoming electrons is either (a) aligned with or (b) perpendicular to the total spin $\mathbf{S} \approx |\mathbf{S}|\,\mathbf{e}_z$ of the finite sized sample. See Fig. 5.2 for details on $\mathcal{T}_{\sigma\bar{\sigma},\mathrm{avg}}/\mathcal{T}_{\mathrm{pristine}}$. My thanks to J. Wilhelm who performed the spinor DFT simulation of the finite ribbon[140]. [DFT details: Turbomole, basis set svp, spinor DFT with SOI]
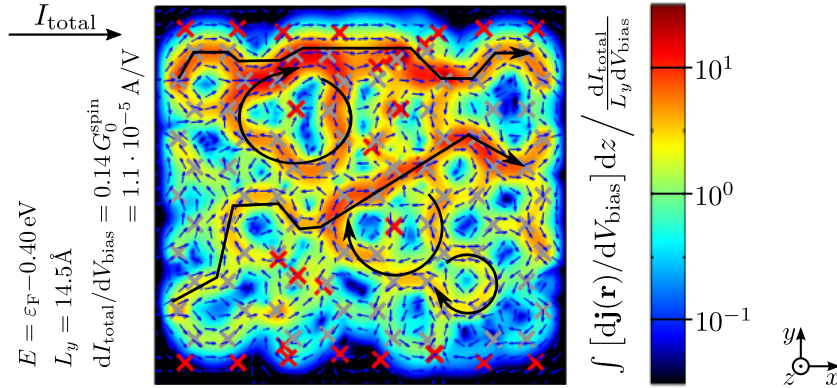
Figure 5.4: Local current density response (integrated over the out-of-plane direction) normalized to the average through current in the hydrogenated AGNR11 shown in Fig. 5.1b. The current exhibits very strong mesoscopic fluctuations that reflect in a logarithmic color scale covering three decades. Some interesting current paths are drawn in the picture for illustration: local current vortices exceeding the spatial average current by one order of magnitude (see dark red regions). Plot shows current amplitude (color), current direction (arrows), carbon atoms (gray crosses), and hydrogen atoms (red crosses). [DFT details: Turbomole, basis set svp, spinor DFT with SOI]

which we simulated the local current density for much larger ribbons but enforced a closed-shell electronic structure without SOI to reduce the computational effort. The characteristic features, i.e., current vortices and broad fluctuations, are the same in both cases; they emerge from full spin treatment including SOI as well as from spin restricted treatment. Therefore, we confirm that their appearance is a fundamental property of the scattering states in hydrogenated graphene flakes.

5.2.4 Comparison of different (approximate) groundstate spin configurations and their influence on transmission and local current density

We now examine if and how different levels of spin theory change the current picture of Fig. 5.4. For that purpose, we perform closed-shell, collinear open-shell and full spinor DFT calculations with FHI-AIMS and TURBOMOLE. Open-shell and spinor DFT simulations depend on the initial guess of the spin configuration since the KS equations are solved iteratively and only find local minima in the energy landscape. We use several reasonable guesses, such as an extended Hückel guess for open-shell calculations using TURBOMOLE[134]. The exact initial configurations are not important for our discussion and are deferred to the notes[B] section. The important point is that many possible spin configurations with (nearly) equal energy exist. In principle, we should accept only the configuration with the lowest total energy, but since our DFT treatment is not exact (remember the approximate functionals), and the energy differences are small ($100\,\mu\text{eV}$ to several meV per atom, see Tab. 5.1), the true groundstate realized in experiment might not have the lowest energy in approximate DFT. Therefore, we perform several simulations and compare the transport results.

We start with the transmission functions shown in Fig. 5.5. We sort the transmission curves into two categories:

- The **"closed-shell-like" category (blueish)** contains transmission functions with a peak near $E = \varepsilon_{\text{F}} - 0.4\,\text{eV}$ and $E = \varepsilon_{\text{F}} + 0.2\,\text{eV}$ with small transmission directly below ε_{F}, i.e., $\mathcal{T}(\varepsilon_{\text{F}} - 0.1\,\text{eV}) < 0.1$.

- The **"open-shell-like" category (reddish)** contains transmission functions with a peak near $E = \varepsilon_{\text{F}} - 0.15\,\text{eV}$ but small transmission directly above ε_{F}, i.e., $\mathcal{T}(\varepsilon_{\text{F}} + 0.2\,\text{eV}) < 0.1$.

This classification was chosen since the two categories show distinct additional features, e.g., peaks at different positions. For nearly all energies, all curves of one category are above all curves of the other category.

Most interestingly, the transmission of the open-shell calculation (B) using FHI-AIMS lies in the closed-shell category despite a total spin of $S_z = 1\hbar$, see Tab. 5.1. Also, the SOI calculation (b) using TURBOMOLE has a nearly vanishing total spin but belongs to the open-shell category. From that, we conclude that the total spin is not a good indicator for transport in hydrogenated graphene ribbons.

Next, we investigate the local current density response at six energies, marked by arrows in the transmission plot, Fig. 5.5. Inside each category, the current pattern and the current magnitude normalized to the transmission always match (see Appx. E.1 for all plots). Between the two categories, the current patterns do not match for all energies, see Fig. 5.6 for an example. Even if the current patterns differ, their qualitative features—current vortices and broad fluctuations—are present in all cases. They emerge from the full spin treatment including SOI as well as from the closed-shell treatment. Thus, we conclude that these qualitative features are generic and do not depend on the exact groundstate configuration. They are also correctly reproduced in (much cheaper) spin-restricted closed-shell simulations.
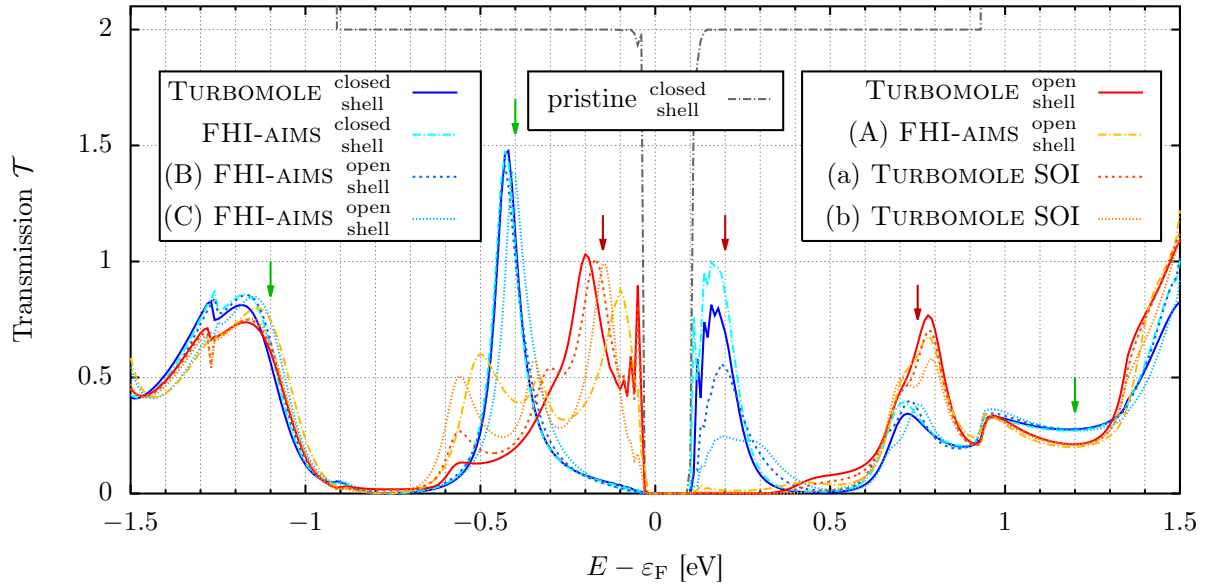
Figure 5.5: Total transmission for different DFT calculations comparing different levels of theory: open-shell, closed-shell, and 2-component spinor calculation including spin-orbit interaction (SOI). All transmission curves can be categorized as either "closed-shell-like" (bluish) or "open-shell-like" (reddish). The arrows represent energy values for which the current density response has been calculated; green/red arrows refer to current patterns which match/differ for the two categories. The current patterns inside each category match qualitatively.
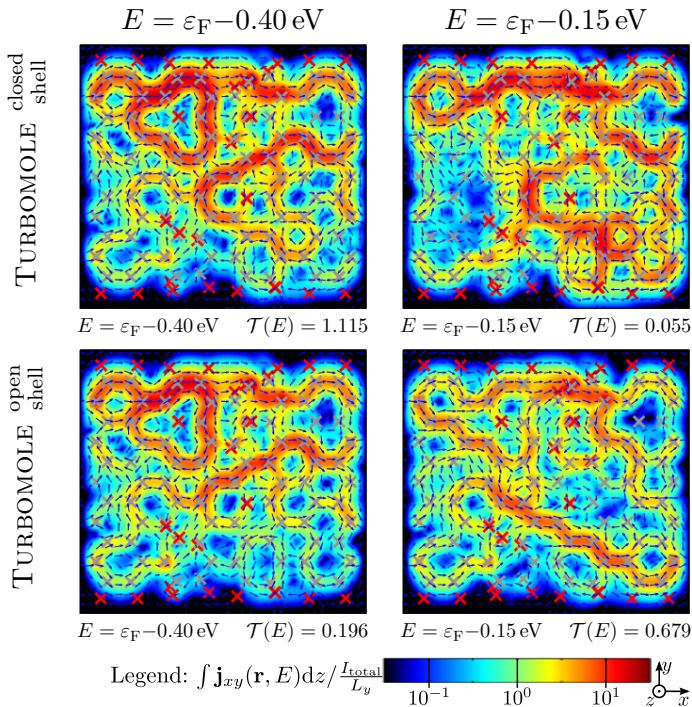
Figure 5.6: The current density for two different energies, $E - \varepsilon_F = -0.40\,\text{eV}/-0.15\,\text{eV}$; one for each category.

	$\Delta E_0[\,\text{eV}]$	$S_z[\hbar]$
FHI-AIMS $^{\text{closed}}_{\text{shell}}$	0	0
(A) FHI-AIMS $^{\text{open}}_{\text{shell}}$	-0.478	1.91
(B) FHI-AIMS $^{\text{open}}_{\text{shell}}$	-0.016	0.05
(C) FHI-AIMS $^{\text{open}}_{\text{shell}}$	-0.310	1.08

	$\Delta E_0[\,\text{eV}]$	$S_z[\hbar]$
TURBOMOLE $^{\text{closed}}_{\text{shell}}$	0	0
TURBOMOLE $^{\text{open}}_{\text{shell}}$	-0.626	1

	$\Delta E_0[\,\text{eV}]$	$\mathbf{S}[\hbar]$
(a) T. SOI	0	$\begin{pmatrix} -0.163 \\ -0.044 \\ +0.860 \end{pmatrix}$
(b) T. SOI	-0.014	$\begin{pmatrix} -0.097 \\ +0.021 \\ -0.041 \end{pmatrix}$

Table 5.1: Comparison of DFT ground state energies E_0 of the finite (uncoupled) cluster and of the overall spin.[C]

5.3 Application: wide hydrogenated graphene ribbons including spin magnetism

In this section, we investigate how different levels of spin theory influence the qualitative transport features in larger hydrogenated AGNRs. We are motivated by recent studies that indicate that hydrogen adsorbates on graphene ribbons are indeed magnetic[103, 172–176]. Therefore, one must ask in what sense the spin-unpolarized results of Chap. 4 remain valid when spin effects are included. As one can already speculate from the results of the previous section, we find that generic transport features do not depend on the exact spin groundstate configuration, also not in larger hydrogenated AGNRs.

For this investigation, we apply closed-shell and open-shell DFT to a medium sized ribbon, an AGNR8x41 with 20% hydrogen (as used in Chap. 4, see Fig. 4.1b for the atomic structure). For such system sizes, we are already unable to perform a spinor DFT calculation. Even collinear open-shell calculations are computational tedious because of a very slow SCF convergence due to many possible spin configurations with (nearly) equal energy. The larger the system gets, the more low lying spin excitation exist in a given energy window; making the SCF convergence extremely costly for larger systems. Physically, this is the same effect as in a spin glass[177]: flipping a single spin is energetically hardly suppressed if neighboring spins are also flipped. Thus, finding the electronic groundstate of such systems is hard.

In Fig. 5.7, we show the total transmission $\mathcal{T}$ and the magnetic response dm_z/dV_{bias} simulated by a closed-shell (CS) and two open-shell (OS) calculations (A and B) with different initial spin configurations.[D] As before, all three simulations converge to different local minima in the energy landscape and therefore the transport properties differ. The total energy of the OS simulations is only slightly—1.42 eV and 2.78 eV—below the CS case. This corresponds to only a few meV per atom, and one should consider all three spin configurations as energetically equal due to approximations in the DFT functionals.

For all three systems, the transmission $\mathcal{T}$ and magnetic response dm_z/dV_{bias} differ quantitatively. Nevertheless, the qualitative features are the same in all cases. A pronounced peak structure in $\mathcal{T}$ and dm_z/dV_{bias} exists in the vicinity of the Fermi energy. The magnetic response shows the usual sign changes near antiresonances. Also, the magnitude of the magnetic response peaks is similar in all three cases. If anything, the magnetic response peaks are slightly higher for CS, but also slightly sharper so that the magnitude of the energy-integrated magnetization coincides again.

Remark: We also investigated the current density pattern $\mathbf{j}(\mathbf{r}, E)$ and the current distributions functions $\mathcal{P}[\ln j_i/j_{\text{avg;y}}]$ of the OS simulations directly (not shown). We found no contradiction to any results presented in this thesis.
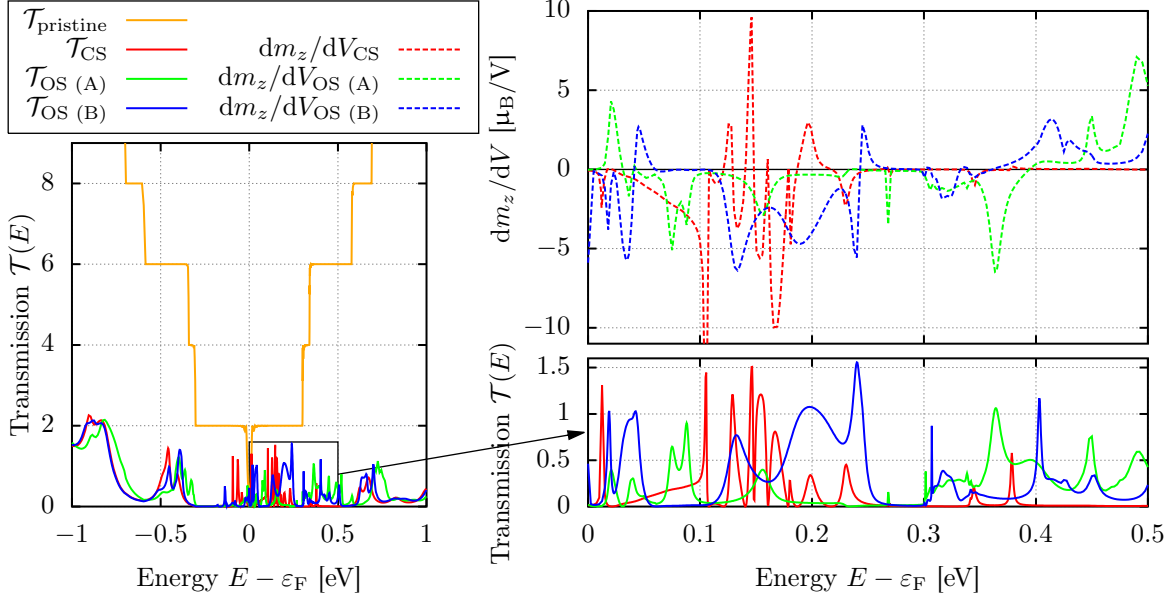
Figure 5.7: Total transmission and total magnetic response, comparing a closed-shell with two different open-shell DFT simulations. The transmission and the magnetic response include both spin channels. The transmission shows a fine peak structure in a wide energy window for all three cases (left panel). A zoom-in of the transmission (lower right panel) and the magnetic response (upper right panel) show three quantitatively different cases, which still show the same generic features: a peak structure of the transmission and several sign changes in the magnetic response.

[DFT details: FHI-AIMS, basis set `tier1`, closed and open-shell. Closed shell quantities have been multiplied by the spin degeneracy factor 2. The clipped peak in dm_z/dV_{CS} at $E - \varepsilon_F = 0.105$ eV reaches $-22.1 \, \mu_B/V$.]

Summary

On the one hand, we showed that the exact spin groundstate configuration has an immediate influence on the local current pattern. We are therefore unable to predict the exact current paths through hydrogenated graphene ribbons. [Even if the DFT transport would predict exact current paths, one would not expect them to reproduce the physical current path in experiment since there is no formal connection for the general case between the KS current density and the physical one (see discussion in Sec. 2.2).] On the other hand, we showed that qualitative features—transmission peaks, sign changes in the magnetic response, and current vortices—remain valid, independent of the level of spin theory. The results indicate that (much cheaper) closed-shell calculations—ignoring local spin polarization—already allow for qualitatively correct predictions of the local current density. That justifies the closed-shell treatment of large hydrogenated ribbons, as performed in Chap. 4. These closed-shell results are correct on a qualitative level.

Notes to chapter 5

The notes are for completeness, reproducibility and to help interested readers understand all the fine technical details.

^A In the AGNR11 with a single hydrogen adatom (Fig. 5.1a), only the hydrogen atom and the four nearest carbon atoms were structurally relaxed. In the AGNR11 with 12 hydrogen adatoms (Fig. 5.1b), the central AGNR4x11 (44 carbon atoms and 12 adsorbed hydrogen atoms) was structurally relaxed. (page 94)

^B As initial spin configuration for the different DFT calculations of Sec. 5.2.4 we used:

(A) FHI-aims open-shell: a spin moment μ_B on each hydrogen atom (all pointing in the same direction),

(B) FHI-aims open-shell: a spin moment μ_B on each hydrogen atom, pointing alternatingly in spin up and spin down direction,

(C) FHI-aims open-shell: a partial spin moment of $0.1\mu_B$ on each carbon and hydrogen atom (all pointing in the same direction),

(a) Turbomole SOI: an extended Hückel guess with fast simulated thermal annealing using the parameter `$fermi tmstrt=300 tmend=10 tmfac=0.95 hlcrt=0.5 stop=1.0E-3`,

(b) Turbomole SOI & Turbomole open-shell: an extended Hückel guess with slow simulated thermal annealing using the parameter `$fermi tmstrt=300 tmend=10 tmfac=0.98 hlcrt=0.5 stop=1.0E-3`.

The resulting total spin moments after SCF convergence are given in Tab. 5.1. (page 98)

^C We made sure to only compare energies which are calculated by the same code with the same basis set because otherwise the differences are due to differences in the calculation scheme and not of physical origin. In that sense, a closed-shell calculation is equivalent to an open-shell calculation where both spin channels are forced to be the same. As energy zero point, we chose the energy of the closed-shell calculation (if available; otherwise, we chose a random reference point). The ground state DFT energies used as references points are

FHI-aims closed-shell: $E_0 = -137514.8234$ eV,

Turbomole closed-shell: $E_0 = -137549.2636$ eV,

Turbomole SOI: $E_0 = -137599.2168$ eV.

They are given only for completeness. (page 99)

^D As initial spin configuration for the open-shell (OS) simulations shown in Fig. 5.7 we used

(A): a spin moment μ_B on each hydrogen atom (all pointing in the same direction),

(B): a spin moment μ_B on each hydrogen atom, pointing alternatingly in spin up and spin down direction.

After SCF convergence, the resulting total spin moments of the entire structures are (A) $S_z = 21.06\hbar$ and (B) $S_z = 4.64\hbar$. (page 100)

6 Magnetic feedback: Self-consistency in the induced orbital magnetism

In this chapter, we study magnetic feedback effects on the transport behavior in hydrogenated AGNRs. The magnetic field induced by orbital currents couples to both, electron charge and spin. Therefore, magnetic feedback effects can—at least in principle—significantly reduce ring currents (Lenz's law) or alter the current density pattern altogether. To discuss these effects, we first determine (Sec. 6.1) how an external magnetic field acts on the electron's motion and its spin. We present a method that includes the magnetic field into DFT a posteriori by calculating its action on the Kohn-Sham states. In Sec. 6.2, we employ this approach to hydrogenated AGNRs, and discuss the feedback of the induced magnetic field on the transmission function. We estimate that the magnetic feedback is minor for the system sizes considered and can be ignored in most cases. This result is supported by a numerical calculation which shows changes in the transmission in the order of $\mathcal{O}(10^{-9})$.

6.1 Theory: influence of magnetic fields

A magnetic field couples to electrons in two ways. First, it couples to the charge influencing the motion by the Lorentz force. Second, it also couples to the spin via a Zeeman term $\mathbf{S} \cdot \mathbf{B}$, favoring an anti-alignment between spin $\mathbf{S}$ and magnetic field $\mathbf{B}$.

Lorentz force: principle of minimal coupling

We include the Lorentz force by employing the principle of minimal coupling, substituting the kinetic momentum operator $\hat{\mathbf{p}}$ by $\hat{\boldsymbol{\pi}} = \hat{\mathbf{p}} - q\mathbf{A}(\hat{\mathbf{r}})$ with electron charge $q = -e$ and vector potential $\mathbf{A}$. The Lorentz interaction

$$\Delta \hat{\mathcal{H}}^{\text{Lorentz}} = \frac{\hat{\boldsymbol{\pi}}^2}{2m} - \left. \frac{\hat{\boldsymbol{\pi}}^2}{2m} \right|_{\mathbf{A}=0} = \frac{-q[\mathbf{A}(\hat{\mathbf{r}}) \cdot \hat{\mathbf{p}} + \hat{\mathbf{p}} \cdot \mathbf{A}(\hat{\mathbf{r}})]}{2m} + \frac{q^2 \mathbf{A}^2(\hat{\mathbf{r}})}{2m} \tag{6.1}$$

is given by the difference between the kinetic energy with and without vector potential $\mathbf{A}$.

Zeeman interaction: $\mathbf{S} \cdot \mathbf{B}$

The Zeeman interaction couples spin to the magnetic field. The corresponding Hamiltonian reads

$$\Delta \hat{\mathcal{H}}^{\text{Zeeman}} = \gamma \int \hat{\mathbf{S}}(\mathbf{r}) \cdot \mathbf{B}(\mathbf{r}) \, \mathrm{d}^3 \mathbf{r} \tag{6.2}$$

with the gyromagnetic ratio $\gamma = \frac{q}{m}$ for the electron spin (including the g-factor $g = 2$ and electron charge $q = -e$). Writing the spin-density operator $\hat{\mathbf{S}}(\mathbf{r}) = \frac{\hbar}{2} \delta(\mathbf{r} - \hat{\mathbf{r}}) \hat{\boldsymbol{\sigma}}$ in terms of Pauli-matrices σ_i, the Zeeman interaction in spin representation is explicitly given as

$$\Delta \hat{\mathcal{H}}^{\text{Zeeman}} = \frac{q\hbar}{2m} \hat{\boldsymbol{\sigma}} \cdot \mathbf{B}(\hat{\mathbf{r}}) = \frac{q\hbar}{2m} \begin{pmatrix} B_z(\hat{\mathbf{r}}) & B_{xy}^*(\hat{\mathbf{r}}) \\ B_{xy}(\hat{\mathbf{r}}) & -B_z(\hat{\mathbf{r}}) \end{pmatrix} \tag{6.3}$$

with $B_{xy} := B_x + \mathrm{i} B_y$.

Incorporating the magnetic field into DFT

The magnetic field does not couple directly to the electron density. Therefore, incorporating the magnetic field into DFT is not straightforward. The standard way is to employ current density functional theory (CDFT)[178, 179]. In that case, the exchange-correlation functional $E_{\text{xc}}[n, \mathbf{s}, \mathbf{j}]$ not only depends on the density $n(\mathbf{r})$ and the spin density $\mathbf{s}(\mathbf{r})$, but also on the current density $\mathbf{j}(\mathbf{r})$ (see Appx. B.2 for a DFT overview). That means, that in addition to the external fields $\mathbf{A}_{\text{ext}}(\mathbf{r})$ and $\mathbf{B}_{\text{ext}}(\mathbf{r})$, there are new exchange-correlation potentials $\mathbf{A}_{\text{xc}}(\mathbf{r}) = \delta E_{\text{xc}} / \delta \mathbf{j}(\mathbf{r})$ and $\mathbf{B}_{\text{xc}}(\mathbf{r}) = \delta E_{\text{xc}} / \delta \mathbf{s}(\mathbf{r})$ that act on the Kohn-Sham (KS) system [in addition to the standard exchange-correlation potential $v_{\text{ex}}(\mathbf{r}) = \delta E_{\text{xc}} / \delta n(\mathbf{r})$].

Formally, CDFT—as standard DFT—is exact as long as the exchange-correlation functional E_{xc} is exact. In practice, useful approximate functionals for CDFT are much more problematic than in standard DFT. For that reason, we do not use CDFT to include the magnetic field. Instead, we include the magnetic field ad-hoc by applying the above Hamiltonians directly to the KS states, i.e., we calculate the matrix elements with respect to the orthonormal basis set $|\tilde{\varphi}_i\rangle$, using $\hat{\mathbf{p}} = -\mathrm{i}\hbar \boldsymbol{\nabla}$ in real space. The Lorentz Hamiltonian,

$$\begin{aligned} \Delta \mathbf{H}_{ij}^{\text{Lorentz}} &:= \langle \tilde{\varphi}_i | \Delta \hat{\mathcal{H}}^{\text{Lorentz}} | \tilde{\varphi}_j \rangle \\ &= \frac{1}{2m} \int \tilde{\varphi}_i^*(\mathbf{r}) \Big\{ \mathrm{i}\hbar q [\mathbf{A}(\mathbf{r}) \cdot \boldsymbol{\nabla} + \boldsymbol{\nabla} \cdot \mathbf{A}(\mathbf{r})] + q^2 \mathbf{A}^2(\mathbf{r}) \Big\} \tilde{\varphi}_j(\mathbf{r}) \mathrm{d}^3 \mathbf{r} \,, \end{aligned} \tag{6.4}$$

and the Zeeman interaction,

$$\begin{aligned} \Delta \mathbf{H}_{ij}^{\text{Zeeman}} &:= \langle \tilde{\varphi}_i | \Delta \hat{\mathcal{H}}^{\text{Zeeman}} | \tilde{\varphi}_j \rangle \\ &= \frac{q\hbar}{2m} \int \tilde{\varphi}_i^*(\mathbf{r}) \, \hat{\boldsymbol{\sigma}} \cdot \mathbf{B}(\mathbf{r}) \, \tilde{\varphi}_j(\mathbf{r}) \mathrm{d}^3 \mathbf{r} \,, \end{aligned} \tag{6.5}$$

then contain spatial derivatives and integrals which are solved numerically (see Appx. F.1 for details). Compared to CDFT, our approach has the advantage that it fits seamlessly into our framework (as presented in Chap. 2) that relies on groundstate DFT. No drastic code changes are necessary, only the two Hamiltonian matrices $\Delta \mathbf{H}^{\text{Lorentz}}$ and $\Delta \mathbf{H}^{\text{Zeeman}}$ need to be calculated. Both matrices are then directly added to the KS Green's function of the device region, i.e., new terms (marked in blue) are added to Eq. (2.7) which becomes

$$\mathbf{G}(E)^{-1} = \mathbf{G}_0^{\text{KS}}(E)^{-1} - \mathbf{\Sigma}_{\text{L}}(E) - \mathbf{\Sigma}_{\text{R}}(E) - \Delta \mathbf{H}^{\text{Lorentz}} - \Delta \mathbf{H}^{\text{Zeeman}}. \tag{6.6}$$

Our method does not accommodate for energy contributions induced by large changes in the groundstate density due to the applied magnetic field. (Such terms would be included in CDFT.) Therefore, our method fails for large density changes, i.e., in the limit of very strong applied magnetic fields. On the other hand, our method should include all relevant physics for weak to moderate magnetic fields.

Remark: The principle of minimal coupling also affects the definition of the current density operator

$$\mathbf{j}(\mathbf{r}, E) = \frac{1}{2\pi} \frac{\hbar}{2m} \lim_{\mathbf{r}' \to \mathbf{r}} (\mathbf{\nabla}_{\mathbf{r}'} - \mathbf{\nabla}_{\mathbf{r}}) G^{<}(\mathbf{r}, \mathbf{r}', E) + \frac{\text{i}}{2\pi} \frac{q}{m} \mathbf{A}(\mathbf{r}) \, G^{<}(\mathbf{r}, \mathbf{r}, E) \tag{6.7}$$

which acquires new a term proportional to the vector potential $\mathbf{A}$. Please refer to Appx. F.2 for the derivation.

6.2 Application: self-consistency effects in graphene ribbons

In this section, we apply the presented formalism to investigate self-consistency effects of the induced magnetic field in large hydrogenated AGNRs. In principle, the induced magnetic field feeds back into the electronic structure and thereby also affects the current density with an expected tendency to suppress it (Lenz's law). We can solve this self-consistency iteratively, i.e., we start by calculating the current density in the absence of magnetic fields. Then the magnetic field induced by the current density is calculated. In the next step, the current density is recalculated in the presence of the induced magnetic field. These steps are iterated until convergence is achieved.

In our formalism, self-interaction effects are included, i.e., the magnetic contribution induced by the motion of a single electron also acts back on the motion of this electron. On the one hand, the self-interaction is unphysical and should be removed. On the other hand, the self-interaction effect is negligible if we apply a bias voltage V_{bias} that averages over many electrons. In this case, the relevant level spacing is given by the level spacing Δ_{lead} of the leads which is significantly smaller than the level spacing Δ of the device. We will work in the hierarchy, $eV_{\text{bias}} \gg \Delta \gg \Delta_{\text{lead}}$. Therefore, the self-interaction should not matter for a qualitative understanding and an estimation of the order of the effect.

6.2.1 Estimation of the magnetic flux

First, we estimate the order of the magnetic flux related to the induced magnetic field. Second, we use the magnetic flux to estimate the influence of self-consistency on the transmission function.

For an hydrogenated AGNR, we expect an induced magnetic field is in the order of $B_0 \sim 10\,\mathrm{mT}$ for a finite bias voltage $V_{\mathrm{bias}} = 1\,\mathrm{V}$, cf. Fig. 4.14b. For a small system, we expect that most vortices encircle only a few carbon rings. Thus, we multiply the magnetic field by the area $A_{\mathrm{ring}} \approx 3.5 \text{Å}^2$ of a single carbon ring. This gives the magnetic flux per carbon ring,

$$\Phi = A_{\mathrm{ring}} \cdot B_0 \sim 10^{-7}\,\Phi_0\,, \tag{6.8}$$

which is significantly smaller than the magnetic flux quantum $\Phi_0 = h/e \approx 4.1 \cdot 10^5\ \text{TÅ}^2$ (for single-charged electrons). The magnetic flux can be used to estimate the influence of self-consistency on the transmission function in the following way: We expect significant effects on the transmission function only if the electrons pick up phases in the order of 2π. Such a phase is realized if the electron encircle an area containing a full flux quantum Φ_0. Therefore, we predict that magnetic feedback effects on the transmission function are in the order of $\mathcal{O}(10^{-7})$ if single ring vortices dominate. For a larger effect, one can assume that the dominating ring currents encircle several rings. To get a magnetic flux of the order of a full flux quantum, the system size must reach 1–$10\,\mu\mathrm{m}$. Whether such a system still features fully phase-coherent transport or not is—at the very least—arguable. [The upper end of the mesoscopic regime is usually seen at such length scales.] Thus, also in that case, we do not expect large self-consistency effects but for a different reason.

6.2.2 Numerical calculation

Wide ribbons: hydrogenated AGNR8×41

We now apply our method (cf. sec:SC:theory) to calculate the self-consistency effects in a hydrogenated AGNR8×41 as shown in Fig. 4.1b with bias voltage $V_{\mathrm{bias}} = 1\,\mathrm{V}$. The current density and the induced magnetic field (without self-consistent iteration) can be found in Fig. 4.14. Since we expect a small effect, we only calculate the first iteration step. In Fig. 6.1, we plot the transmission $\mathcal{T}_0$ of the zeroth iteration and the deviation $\Delta\mathcal{T} = |\mathcal{T}_0 - \mathcal{T}_1|$ from the transmission $\mathcal{T}_1$ after the first iteration step. We find that the magnitude of the change is below 10^{-9}; at most energies $\Delta\mathcal{T}$ is even smaller. In the current density, we cannot reproduce any deviation since the numerical error of the numerically performed basis function derivatives is also of the order $\mathcal{O}(10^{-10})$. Therefore, we conclude that self-consistency in the magnetic field has only a very minor influence on the total transmission function and can be neglected in most cases.

Narrow ribbon: AGNR5 with a single nitrogen substituent

We close with an additional numerical example, a narrow AGNR5 with a single nitrogen substituent as presented in Sec. 3.2.2. We calculate the self-consistency effect for a bias voltage of $V_{\mathrm{bias}}{=}1.145\,\mathrm{V}$. This bias voltage coincides with the maximal energy range between the Fermi
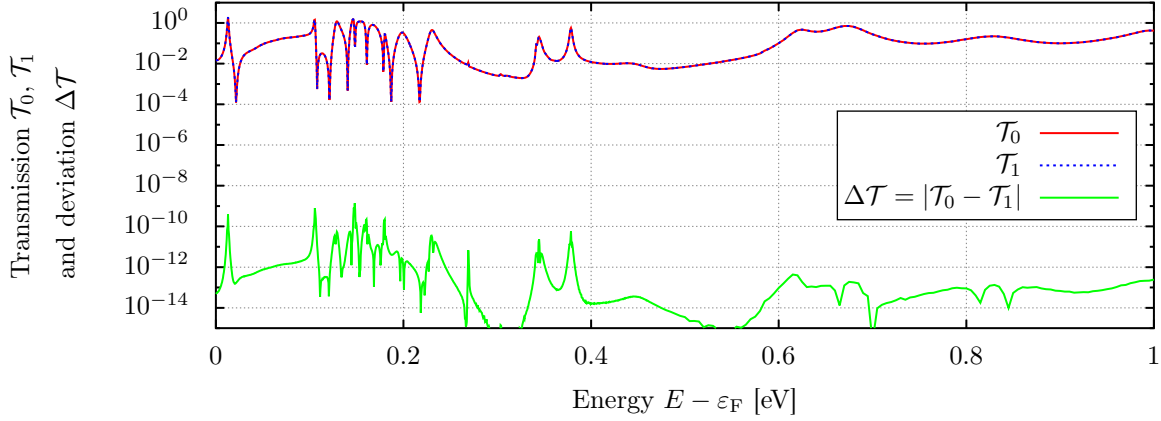
Figure 6.1: Comparison of the total transmission (both spin channels) after zero and after one iteration in the self-consistency cycle. We include $\Delta \mathbf{H}^{\text{Lorentz}}$ and $\Delta \mathbf{H}^{\text{Zeeman}}$ on top of a spin-unpolarized DFT calculation of hydrogenated AGNR8×41, see Fig. 4.1b for the atomic geometry. The transmission $\mathcal{T}_0$ is taken after zero iterations, i.e., without applying any magnetic field. The transmission $\mathcal{T}_1$ is calculated after one iteration, i.e., with applying the magnetic field induced by the current density of the zeroth iteration with $V_{\text{bias}} = 1\,\text{V}$. Both transmission functions coincide in the plot. The deviation $\Delta \mathcal{T} = |\mathcal{T}_0 - \mathcal{T}_1|$ reaches values up to 10^{-9}. In all cases, the antiresonances, i.e. the downward peaks, are not fully resolved due to a finite energy raster of $\delta E = 0.5\,\text{meV}$.
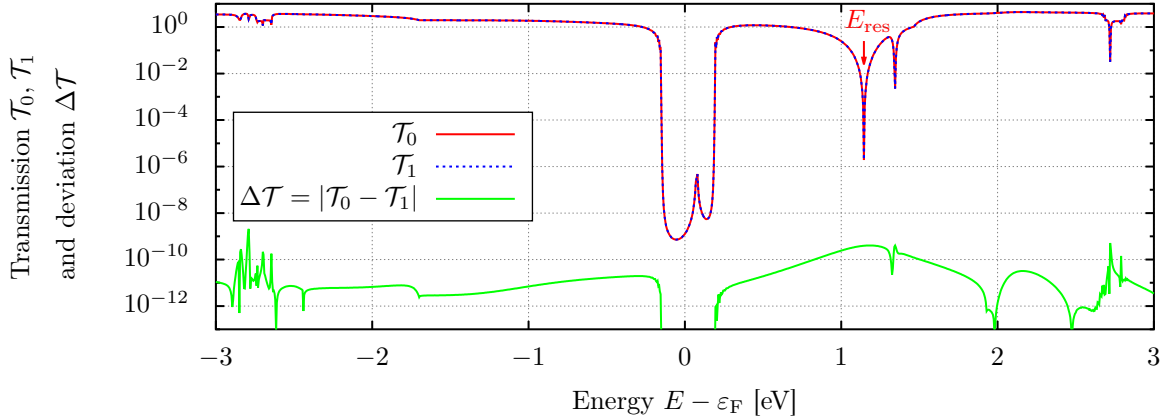
Figure 6.2: Comparison of the total transmission (both spin channels) after zero and after one iteration in the self-consistency cycle. We include $\Delta \mathbf{H}^{\text{Lorentz}}$ and $\Delta \mathbf{H}^{\text{Zeeman}}$ on top of a spin-unpolarized DFT calculation of AGNR5 with a nitrogen substituent, see Fig. 3.7a (pos. 3) for the atomic geometry. The transmission $\mathcal{T}_0$ is taken after zero iterations, i.e., without applying any magnetic field. The transmission $\mathcal{T}_1$ is calculated after one iteration, i.e., with applying the magnetic field induced by the current density of the zeroth iteration with $V_{\text{bias}} = 1.145\,\text{V}$ (integration from Fermi energy to the antiresonance E_{res}). Both transmission functions coincide in the plot. The deviation $\Delta \mathcal{T} = |\mathcal{T}_0 - \mathcal{T}_1|$ reaches values up to 10^{-9}. In all cases, the antiresonances, i.e. the downward peaks, are not fully resolved due to a finite energy raster of $\delta E = 5\,\text{meV}$. The transmission does not vanish completely inside the band gap (but is reduced by nine orders of magnitude) due to the limited length of the lead system in x-direction. This methodological artifact is due to a small numerical difference between the exact lead-induced self-energy and our approximation scheme (see decimation technique in Sec. 2.1.3).
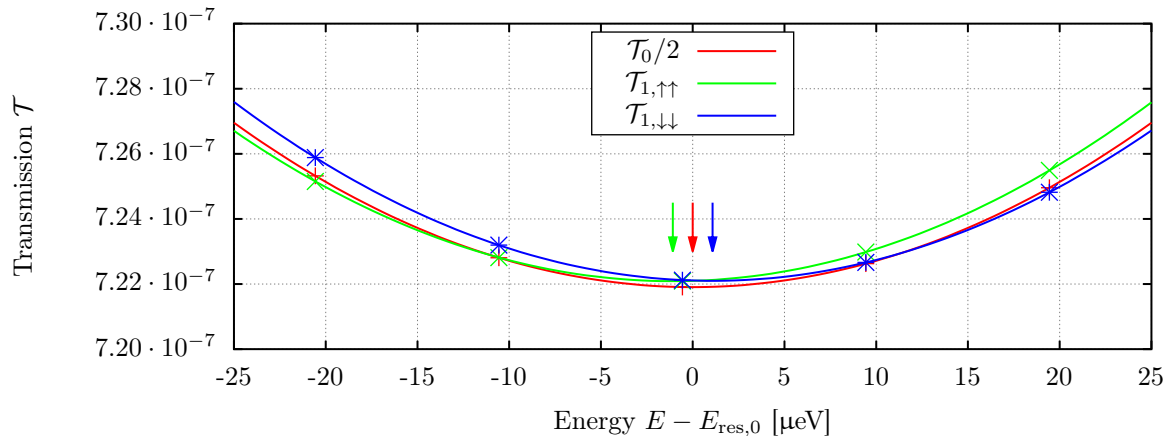
Figure 6.3: Comparison of the transmission functions in a small energy range near the antiresonance $E = E_{res}$. This is a zoom-in of Fig. 6.2 with the transmission $\mathcal{T}_1$ split into its spin-resolved components, i.e., $\mathcal{T}_1 = \sum_{\sigma\sigma'} \mathcal{T}_{1,\sigma\sigma'}$. The spin off-diagonal component $\mathcal{T}_{1,\uparrow\downarrow}$ and $\mathcal{T}_{1,\downarrow\uparrow}$ are not shown since they are in the order $\mathcal{O}(10^{-20})$ (and below) for all energies $E - \varepsilon_F \in [-3\,\text{eV}, +3\,\text{eV}]$. The data is marked by crosses, the solid lines are quadratic fits near the antiresonance. The respective minimum of each parabola is marked by a colored arrow.

energy ε_F and the antiresonance energy E_{res}. At the latter, the induced magnetic field response changes its sign. In other words, V_{bias}=1.145 V is the bias voltage with the largest induced magnetic field in this system (see Fig. 3.11 for current density and induced magnetic field).

In Fig. 6.2, the total transmission for zero and one self-consistency iteration are compared. The two transmission curves virtually coincide. Their difference only reaches values up to $\mathcal{O}(10^{-9})$, and thus, also for this system, the self-consistency effects on the total transmission are negligible.

If one is interested in the spin-resolved quantities, i.e., the spin-resolved transmission, the picture changes. In Fig. 6.3, the total transmission $\mathcal{T}_0$ without any spin polarization is compared to the spin-resolved transmission $\mathcal{T}_{1,\sigma\sigma'}$ for one self-consistency iteration. The difference in the spin channels of $\mathcal{T}_{1,\sigma\sigma}$ are solely due to the self-consistency effect of the induced magnetic field. Recall that the AGNR5 with nitrogen substituent stays completely flat, i.e., the system features a z-mirror symmetry. Thus, the in-plane magnetic field components B_x and B_y are suppressed. This is expressed in small spin-flip transmission values $\mathcal{T}_{1,\uparrow\downarrow}$ and $\mathcal{T}_{1,\downarrow\uparrow}$ below $\mathcal{O}(10^{-20})$ for all investigated energies. The out-of-plane component B_z alone can only induce spin-diagonal energy shifts, cf. Eq. (6.3). We observe such a shift of the spin resolved transmission curves in the order of $2\,\mu\text{eV}$. Although small, it reaches the order of the intrinsic spin-orbit interaction in pristine graphene, where the latter opens a gap of $24\,\mu\text{eV}$ at the Dirac points[180]. [The gap is larger by an additional factor of about 20 in hydrogenated graphene[159].]

Thus, self-consistency effects on the spin-resolved transmission function are mainly described by small energy shifts. These induced energy shifts may become relevant compared to intrinsic spin-orbit interaction. This is consistent with our discussion in Sec. 4.1.4 of current-induced spin relaxation, where we found that the induced magnetic field acting on the electron spins might compete with other sources of spin relaxation.

7 Chapter 7
Conclusion & Outlook

In this thesis, we applied density functional theory (DFT) in combination with non-equilibrium Green's function (NEGF) techniques to study the spatial structure of scattering states in graphene nanoribbons. For that purpose, we presented a formalism which calculates the electron current density $\mathbf{j}(\mathbf{r})$ and the induced orbital field $\mathbf{B}(\mathbf{r})$. A large emphasis was placed on parallelization, so that an efficient scaling for up to 1000 CPU cores is achieved on a supercomputer. Although, we have applied our implementation solely to graphene nanoribbons, it is in no way restricted to carbon based materials. Further transport studies, especially computationally expensive ones, can rely on our implementation also for other classes of materials.

We have employed our machinery to pristine and disordered armchair graphene nanoribbons (AGNRs). Even in pristine ribbons, we found highly inhomogeneous current density patterns: streamline patterns. They arise as a consequence of quantum confinement in the transverse direction, as can be explained with simple zone-folding arguments. The current pattern displays a threefold periodicity in the ribbon width. In pristine AGNRs($3m-1$), i.e. the number of carbon atoms in transverse direction is $N_{\mathrm{C}} = 3m-1$ ($m \in \mathbb{N}$), these streamlines are separated by (almost) vanishing current flows. We found that these streamline patterns intuitively explain the strong position dependence of impurities in graphene ribbons. An impurity has only a strong influence on the transport behavior if positioned inside the streamlines of the pristine ribbon. That way, changing the position of an impurity—even by a single lattice constant—can lead to qualitatively different transport scenarios. This effect was well-known before[81, 99–102], but we provide an intuitive explanation in terms of streamlines. This result can also be understood as a manifestation of a strong spatial structure in the scattering states of mesoscopic devices.

The strong spatial structure in the scattering states is even more evident if scattering centers exist. We observed a tendency to form ring currents, current vortices, which induce orbital magnetism. This tendency is independent of the atomistic details in the structure: it exist for single impurities in narrow AGNRs as well as for finite impurity concentrations in large AGNRs; irrespective of local spin polarization, lattice relaxation effects, or magnetic backfeed. We could trace the origin of these ring currents to asymmetries in the possible interference paths by using a two-path (toy)

model. From that, we conclude that loop currents are expected in all generic situations with phase-coherent charge transport in the presence of broken spatial symmetries, such as brought about by disorder.[A] Hence, current vortices should be a generic feature of transport through mesoscopic devices, whose implications have hardly been touched upon by now.

Our investigations aim at situations, where interaction effects can be modelled qualitatively by mean field interactions, so that a single-particle picture remains valid. In this case, we expect the general *qualitative* features of our DFT transport simulations to be representative of the real physical system. For our results, that means that the qualitative features of the scattering states—tendencies to form ring currents or streamline patterns—are of physical origin. However, the exact physical current density pattern for a given atomic structure might deviate from the presented simulation results.

In this thesis, we discussed orbital magnetism and induced spin relaxation as examples. Both effects are experimentally relevant. We propose to measure orbital magnetism by an NMR experiment performed under an applied bias voltage. The coupling of the induced magnetic field to the hydrogens' nuclear spins should allow to study the evolution of the current vortices experimentally. Alternatively, one could measure the total induced magnetization m_z, which is effectively the average rotation sense of all current vortices. We predict a total magnetization of $\sqrt{\langle m_z^2 \rangle} \sim 1\,\mu_\mathrm{B} \cdot \sqrt{V_\mathrm{bias}/\mathrm{V}}$ that scales with the square root of the bias voltage, independent of the system size. Additionally, the random magnetic fields induce a new spin-relaxation channel—spin relaxation by bias-induced orbital magnetism—which may be relevant especially for graphene spintronics[103].

Our findings are not restricted to charge transport. The underlying idea is very general: scattering states of mesoscopic samples have an inner, non-trivial structure than can lead to pattern formation. An additional example is heat transport: Meair *et al.* have recently proposed the concept of a local temperature applicable to an out-of-equilibrium situation[181]. In a mesoscopic device connected to several reservoirs, the local particle density receives contributions from the scattering states originating from the different reservoirs. If the reservoirs exhibit different temperatures, the device will show local temperature fluctuations. Hot regions have dominant particle contributions from the hot reservoir, while colder regions receive more contributions from the colder reservoir.

As possible future applications, we think of nanoscopic devices. It might be possible to engineer the impurity positions so that all current vortices in a given, perhaps periodic, nanostructure rotate in the same direction. In such a case, magnetic moments would not (partly) cancel each other but instead add up, so that a large total moment could be observed. Applying an alternating voltage, such a device would act as a nano-transmitter. For such a nanodevice, the knowledge of an inhomogeneous heat flow is also important since heat affects the device operations, and must be disposed somehow. To cool efficiently, one must know where overheating is critical.

Another area for future research are three dimensional structures. We expect that our results—at least partially—transfer to the third dimension since the physical mechanism relies on quantum interference which only depends on the existence of asymmetric paths through the device. So far,

it is unknown how the additional (spatial) degree of freedom influences the formation of current vortices; one might expect a seemingly random orientation of the induced local magnetic moments, i.e., ring vortices exist in all spatial directions. Until now, the atomistic structure of the current paths in three-dimensions was even more ignored than in lower dimensions. Impurities, e.g. in a p- or n-doped silicon crystal, were responsible only for changing the chemical potential and adjusting the number of charge carriers. Their influence on the microscopic current path through the wire was of minor importance. With the on-going effort of miniaturization—following approximately[B] Moore's law[182]—the transport behavior in integrated circuits (IC) will be governed by quantum effects stemming from individual scattering centers. Since 2014, Intel mass-produces its CPUs using the 14-nm technology; the next steps (10-nm, 7-nm, 5-nm) are already in preparation. Although the numbers must be taken with a grain of salt,[C] it is clear that the miniaturization cannot continue forever while relying on (semi)-classical transport theory. Quantum interference effects and non-trivial current patterns—as discussed in this thesis—will become important, in one way or another.

Notes to chapter 7

The notes are for completeness, reproducibility and to help interested readers understand all the fine technical details.

[A] As usual, system symmetries govern what effects can be observed in principle. With spatial symmetries (inversion or mirror symmetry) intact, no ring currents are possible because both senses of rotation are equivalent. Such a degeneracy can be lifted in several ways, e.g., by the presence of impurities, boundary effects, or by an applied external magnetic field. (page 110)

[B] In 1965, Moore predicted an exponential growth of the number of components in integrated circuits (IC) when producing for minimal costs per component. His prediction aimed at a timescale of about 10 years. Today, Moore's law is mainly used as a marketing scheme by Intel (cofounded by Moore) and is applied to (nearly) every quantity in computer hardware which grows (roughly) exponentially: most prominently the number of transistors per chip, the transistor density and the computing power. The growth rates vary; most quantities approximately double every 18–24 months. (page 111)

[C] In principle, the length in *14-nm technology* refers to the *average half-pitch* being defined as half the distance between identical features. In practice, it is often criticized that hardly anything in a chip is 14 nm wide, and that the main usage of these numbers is marketing. Nevertheless, the numbers give the correct order for the involved length scales. (page 111)

A

Nomenclature & Conventions

A.1 Graphene nanoribbons: nomenclature & construction

Graphene nanoribbons

Graphene consists of carbon atoms arranged in a regular hexagonal lattice. We work with finite graphene nanoribbons (GNRs) whose borders are hydrogen-terminated, i.e., hydrogen atoms are placed as continuation of the hexagonal lattice (but with a reduced bond distance).

Armchair and zigzag boundaries

There are two types of regular boundaries for GNRs: armchair and zigzag (cf. Fig. A.1). Long GNRs featuring only one boundary type are either called armchair graphene nanoribbon (AGNRs) or zigzag graphene nanoribbons (ZGNRs). Pristine AGNRs are usually spin-unpolarized[114], whereas pristine ZGNRs facilitate spin-separation[138]. In this thesis, we focus on AGNRs.

Nomenclature: AGNRN_{C} & AGNR$N_{\mathrm{x}} \times N_{\mathrm{y}}$

We label pristine AGNRs consisting of N_{C} carbon atoms in the transverse direction (y-direction) by AGNRN_{C}. When placing impurities on the AGNRs, the nomenclature AGNR$N_{\mathrm{x}} \times N_{\mathrm{y}}$ refers to the size of the functionalized area. In Fig. A.1 an AGNR4x11 functionalized with 27.3% hydrogen atoms is displayed. The carbon atoms of the pristine continuation in x-direction are not counted since the transport formalism extends the pristine areas semi-infinitely anyway.

Construction

We construct hydrogenated AGNRs in the following way. We start with a structure consisting of a regular hexagonal carbon lattice with bond length $d_{\mathrm{CC}} = 1.439$ Å. The hydrogen atoms terminating the ribbon are placed as continuation of the hexagonal lattice but with a bond distance of $d_{\mathrm{CH}} = 1.0954$ Å. Both values are taken from a relaxation of a small 14×14 graphene-ribbon calculation in TURBOMOLE[134] using a SVP basis set. Then, adsorbed hydrogen atoms are randomly placed vertically above or below random carbon atoms (of the functionalized area) with a bond distance of d_{CH}. In the unrelaxed structure, the carbon atoms (with the adsorbed hydrogen atoms) are moved out of the graphene plane by 0.5 Å to represent the sp³-hybridization. This unrelaxed structure serves as a template.

To get a relaxed structure, we structurally relax all atoms of the functionalized area (device region excluding contact region) using DFT as implemented in FHI-AIMS[130] until all atomic forces drop below 10^{-2} eV/ Å.

Coordinate system

Throughout this work, we always place the AGNR in the xy-plane at $z = 0$. The transport direction is the x-direction, with an (electron) particle current flowing from $-x$ to $+x$.
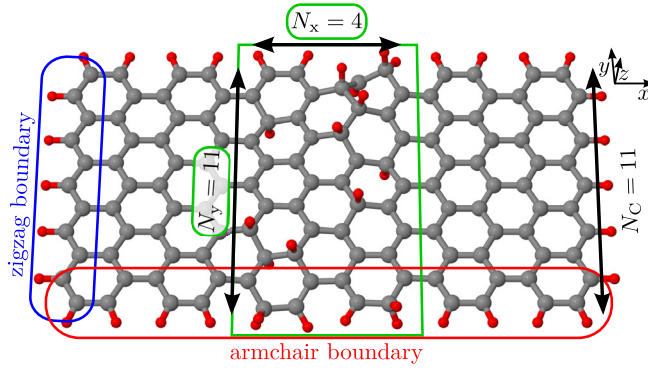
Figure A.1: Hydrogen terminated graphene nanoribbon showing zigzag (blue box) and armchair boundaries (red box). In the center (green box), a functionalized area of an AGNR4×11 carries 12 additional hydrogen atoms.

AGNRN_C	ε_{HL}	$\Delta\varepsilon$
AGNR5	$-3.9855\,\text{eV}$	0
AGNR14	$-4.1411\,\text{eV}$	$64\,\text{meV}$
AGNR20	$-4.1691\,\text{eV}$	$46\,\text{meV}$
AGNR29	$-4.1767\,\text{eV}$	$35\,\text{meV}$
AGNR41	$-4.2054\,\text{eV}$	$35\,\text{meV}$
AGNR42	$-4.2168\,\text{eV}$	$35\,\text{meV}$
AGNR43	$-4.2023\,\text{eV}$	$29\,\text{meV}$
AGNR59	$-4.2215\,\text{eV}$	$31\,\text{meV}$
AGNR83	$-4.2412\,\text{eV}$	$83\,\text{meV}$

$\left[\text{DFT details: FHI-AIMS, basis set \texttt{tier1}, closed-shell}\right]$

Table A.1: HOMO-LUMO average ε_{HL} and shift $\Delta\varepsilon$ for determination of the Fermi energy $\varepsilon_F = \varepsilon_{HL} + \Delta\varepsilon$ in pristine AGNRs.

A.2 Determination of Fermi energy ε_F

In this thesis, most energies are given with respect to the Fermi energy ε_F of the corresponding pristine AGNRN_C. To determine the Fermi energy, we use the following procedure: First, the average energy ε_{HL} of the highest occupied (HOMO) and lowest unoccupied (LUMO) molecular orbital of a finite pristine ribbon [see e.g. Fig. 2.4 (bottom) for AGNR5] serves as an estimate. Then, the transmission function $\mathcal{T}$ of the infinitely extended pristine AGNR is calculated. Last, a correcting shift $\Delta\varepsilon$ is introduced so that the Fermi energy $\varepsilon_F = \varepsilon_{HL} + \Delta\varepsilon$ lies in the bandgap, $\mathcal{T} = 0$, of the infinite AGNR. The estimates of ε_{HL} for several AGNRs and corresponding shifts $\Delta\varepsilon$ are given in Tab. A.1.

A.3 Abbreviations used in this thesis

AB Aharonov-Bohm effect[60]
ABC Absorbing Boundary Conditions
AFM Atomic Force Microscope
AGNR Armchair Graphene NanoRibbon
B-P86 Becke-Perdew functional[183, 184]
CDFT Current Density Functional Theory[178, 179]
DFT (groundstate) Density Functional Theory
DMRG Density Matrix Renormalization Group
DOS Density Of States
DT Decimation Technique
IV current-voltage
    (from symbols I [current] and V [voltage])
LDA Local Density Approximations
    (class of DFT functionals)
LDOS Local Density Of States
LTEM Lorentz Transmission Electron Microscopy
MCBJ Mechanically Controllable Break Junction

NEGF Non-Equilibrium Green's Function formalism
NMR Nuclear Magnetic Resonance
GGA Generalized Gradient Approximations
    (class of DFT functionals)
GNR Graphene NanoRibbon
GW GW approximation
KS Kohn-Sham
HF Hartree-Fock
PBE Perdew-Burke-Ernzerhof functional[151]
SCF Self-Consistent Field (in the DFT)
SIAM Single Impurity Anderson Model
SOI Spin Orbit Interaction
STM Scanning Tunneling Microscopy
SQUID Superconducting Quantum Interference Device
TB Tight-Binding method
QA Quantization Axis (for the spin)
QD Quantum Dot
ZGNR Zigzag Graphene NanoRibbon

A.4 Unit system: atomic units

Our transport code uses atomic units internally (abbreviation: a.u.). In atomic units, the following quantities are set to unity and serve as basis units: the electron mass $m_e = 1$, the reduced Planck constant $\hbar = 1$, the vacuum permittivity (times 4π) $4\pi\varepsilon_0 = 1$, and the elementary charge $e = 1$.

Derived units are formed by combinations of these base units. Examples are the Hartree energy Ha $= m_e e^4/(4\pi\epsilon_0\hbar)^2 \approx 27.21\,\text{eV}$, and the Bohr radius $a_0 = 4\pi\varepsilon_0\hbar^2/(m_e e^2) \approx 0.53\text{Å}$. Another example is the magnetic moment whose base unit in a.u. is two times the Bohr magneton, i.e., a.u. $= e\hbar/m_e = 2\,\mu_B$.

B

Transport method: Calculation of the local current density

This appendix contains additional material that complements Chap. 2. It features a short overview of Green's functions (Appx. B.1) and of DFT including employed basis functions (Appx. B.2). Next, the structure of the implementation (Appx. B.3) and essential optimization (Appx. B.4) are presented. Finally, the appendix lists additional convergence checks (Appx. B.5) to further support the analyses of Chap. 2.

B.1 Green's function formalism: retarded and advanced Green's function

We give a short overview of Green's functions for reference. Similar (and much more extended) overviews can be found in any standard textbook[76, 185, 186].

Definition in Time-Domain

The Green's function $\mathbf{G}(t)$ to the one-particle Schrödinger equation

$$\mathrm{i}\hbar\partial_t|\psi(t)\rangle = \hat{\mathcal{H}}|\psi(t)\rangle \qquad \text{(B.1)}$$

is defined as solution of the equation

$$\left(\mathrm{i}\hbar\partial_t - \hat{\mathcal{H}}\right)\mathbf{G}(t) = \delta(t)\,. \qquad \text{(B.2)}$$

For a time-independent Hamiltonian $\hat{\mathcal{H}}$, there are two linearly independent solutions, $\mathbf{G}_0^+$ and $\mathbf{G}_0^-$:

$$\mathbf{G}^\pm(t) = \begin{cases} \mp\dfrac{\mathrm{i}}{\hbar}\mathrm{e}^{-\frac{\mathrm{i}}{\hbar}\hat{\mathcal{H}}t}, & \text{for } t \gtrless 0 \\ 0, & \text{for } t \lessgtr 0\,. \end{cases} \qquad \text{(B.3)}$$

$\mathbf{G}^+$ ($\mathbf{G}^-$) is called the *retarded* (*advanced*) Green's function since it is able to construct the full time-dependent solution $|\psi(t)\rangle$ when only knowing a single past (future) point t_0.

$$|\psi(t)\rangle = \pm\mathrm{i}\hbar\mathbf{G}^\pm(t - t_0)|\psi(t_0)\rangle \qquad t \gtrless t_0\,. \qquad \text{(B.4)}$$

Since the Green's function can be used to propagate a state in time, it's often also called *propagator*. In this thesis, the retarded Green's function $\mathbf{G}^+$ is usually just called $\mathbf{G}$.

Fourier Transformation to Energy Domain

For a time-independent problem (homogeneity in time), it is useful to perform a Fourier transformation to energy domain, i.e.,

$$\mathbf{G}^\pm(E) = \int\limits_{-\infty}^{+\infty} \mathrm{d}t\; \mathrm{e}^{+\frac{\mathrm{i}}{\hbar}Et}\; \mathrm{e}^{\mp\eta t/\hbar}\; \mathbf{G}^\pm(t) \qquad \text{(B.5)}$$

where we already introduced an infinitesimal small parameter $\eta > 0$ (see red term) to ensure the convergence

of the integral at $t \to +\infty$ and $t \to -\infty$ for the retarded and advanced Green's function, respectively. The convergence at the other integral limit is trivial since the Green's function $\mathbf{G}^{\pm}(t)$ is zero for $t \lessgtr 0$.

Formally performing the integration leads to

$$\mathbf{G}^{\pm}(E) = \left[E - \hat{\mathcal{H}} \pm \mathrm{i}\eta \right]^{-1} \qquad \text{(B.6)}$$

where the inversion can be defined as matrix inversion if the operator $\hat{\mathcal{H}}$ is written in some (finite) basis.

The inverse Fourier transformation

$$\mathbf{G}^{\pm}(t) = \int\limits_{-\infty}^{+\infty} \frac{\mathrm{d}E}{2\pi\hbar} \, \mathrm{e}^{-\frac{\mathrm{i}}{\hbar} E t} \, \mathbf{G}^{\pm}(E) \qquad \text{(B.7)}$$

can be performed via contour integration. For $t > 0$ ($t < 0$) the integration contour can be closed in the lower (upper) complex plane. Formally, $\mathbf{G}^{\pm}(E)$ has a single pole at $E = \hat{\mathcal{H}} \mp \mathrm{i}\eta$ and we recover the original definition in Eq. (B.3).

Observables

As example for an observable, the density of states operator $\hat{\rho}$ is calculated as

$$
\begin{aligned}
\hat{\rho}(E) &= \sum_i \delta(E - E_i)|i\rangle\langle i| \stackrel{E_i|i\rangle = \hat{\mathcal{H}}|i\rangle}{=} \delta(E - \hat{\mathcal{H}}) \\
&= \frac{1}{\pi} \frac{\eta}{(E - \hat{\mathcal{H}})^2 + \eta^2} = -\frac{1}{\pi} \operatorname{Im} \frac{1}{E - \hat{\mathcal{H}} + \mathrm{i}\eta} \quad \text{(B.8)} \\
&= -\frac{1}{\pi} \operatorname{Im} \mathbf{G}^+ \,,
\end{aligned}
$$

where in the second line, we used a Lorentzian $\frac{1}{\pi}\frac{\eta}{x^2 + \eta^2}$ to represent the delta distribution $\delta(x)$ in the limit of infinitesimal η.

B.2 Density functional theory

Density functional theory (DFT) is probably the most successful theory to calculate the electronic structure of atoms, molecules and solid states from *ab initio*. Here, only the most important ideas of DFT can be presented. Thus, for simplicity, this overview ignores spin and external magnetic fields. For a full length description, please refer to the literature, e.g. Ref. [168, including references].

B.2.1 General framework

Born-Oppenheimer approximation

As most *ab initio* methods, standard DFT treats the atomic cores as classic potentials in a Born-Oppenheimer approximation[187]. Thus, their interaction with the electrons is included in an external potential $v_{\mathrm{ex}}(\mathbf{r}, \{\mathbf{R}_i\})$ which acts on the electron positions $\mathbf{r}$ and depends on the core positions $\mathbf{R}_i$ only as parameters. Geometric relaxations are possible, by iteratively changing and improving the core position $\mathbf{R}_i$ in each DFT towards the energetically most stable configuration. In the following, the dependence on the core position is suppressed in the external potential $v_{\mathrm{ex}}(\mathbf{r})$.

The full many-body Hamiltonian $\hat{\mathcal{H}}$ for n_{el} electrons is then given by

$$\hat{\mathcal{H}} = \hat{\mathcal{T}} + \hat{\mathcal{V}}_{\mathrm{int}} + \int \mathrm{d}\mathbf{r} \, v_{\mathrm{ex}}(\mathbf{r}) \, \hat{n}(\mathbf{r}) \,, \qquad \text{(B.9)}$$

where $\hat{\mathcal{T}}$ is the kinetic energy operator. The interaction term $\hat{\mathcal{V}}_{\mathrm{int}}$ is the Coulomb interaction, an isotropic and homogeneous two-body interaction, i.e., $\hat{\mathcal{V}}_{\mathrm{int}} = \frac{1}{2}\sum_{ij} v(|\hat{\mathbf{r}}_i - \hat{\mathbf{r}}_j|)$. The external potential $v_{\mathrm{ex}}(\mathbf{r})$ directly couples to the electron density $n(\mathbf{r})$.

Hohenberg-Kohn theorem

The foundation of DFT is laid by the Hohenberg-Kohn theorem[188]. For fixed $\hat{\mathcal{V}}_{\mathrm{int}}$ (and fixed $\hat{\mathcal{T}}$, n_{el}), the Hohenberg-Kohn theorem ensures a one-to-one-to-one correspondence between the external potential $v_{\mathrm{ex}}(\mathbf{r})$, the groundstate wavefunction $\Psi(\{\mathbf{r}_i\})$, and the groundstate density $n(\mathbf{r})$:

$$v_{\mathrm{ex}}(\mathbf{r}) \Leftrightarrow \Psi(\{\mathbf{r}_i\}) \Leftrightarrow n(\mathbf{r}) \qquad \text{for fixed } \hat{\mathcal{V}}_{\mathrm{int}} \,. \quad \text{(B.10)}$$

The path $v_{\mathrm{ex}}(\mathbf{r}) \Rightarrow \Psi(\{\mathbf{r}_i\}) \Rightarrow n(\mathbf{r})$ is trivial since it describes the canonical method: definition of the Hamiltonian (using $v_{\mathrm{ex}}(\mathbf{r})$), solving it for the groundstate wavefunction $\Psi(\{\mathbf{r}_i\})$ and calculating the groundstate density $n(\mathbf{r}) = \langle\Psi|\hat{n}(\mathbf{r})|\Psi\rangle$. The reverse direction is the

important part of the Hohenberg-Kohn theorem (a nice proof is given by Levy[189]). It allows us to ignore the full many-body wavefunction $\Psi(\{\mathbf{r}_i\})$, which is usually too complicated to be calculated anyway, and work solely with the groundstate density $n(\mathbf{r})$. The price to pay is that all physical quantities are now functionals of the groundstate density. This is possible since the groundstate density already uniquely defines all observables due to the one-to-one correspondence.

The functional $E[n]$ for the groundstate energy is (at least formally) given by

$$E[n] := \min_{\substack{|\Psi\rangle \\ \langle\Psi|\hat{n}(\mathbf{r})|\Psi\rangle = n(\mathbf{r})}} \langle\Psi|\hat{\mathcal{H}}|\Psi\rangle \tag{B.11}$$

$$= \underbrace{\min_{\substack{|\Psi\rangle \\ \langle\Psi|\hat{n}(\mathbf{r})|\Psi\rangle = n(\mathbf{r})}} \langle\Psi|\hat{\mathcal{T}} + \hat{\mathcal{V}}_{\text{int}}|\Psi\rangle}_{E'[n]} + \int d\mathbf{r}\, v_{\text{ex}}(\mathbf{r})\, n(\mathbf{r})\,.$$

Given a certain groundstate density, one (formally) constructs all many-body wavefunctions Ψ which reproduce the correct density, $\langle\Psi|\hat{n}(\mathbf{r})|\Psi\rangle \overset{!}{=} n(\mathbf{r})$. The groundstate energy is the minimum energy of all such constructed wavefunctions. In the second line, we separated the term containing the external potential $v_{\text{ex}}(\mathbf{r})$. This is essential because the remaining functional $E'[n]$ is *universal* in the sense that it does not depend on the external potential $v_{\text{ex}}(\mathbf{r})$, and can (at least formally) be

constructed once and for all. Then, the true groundstate density to any external potential $v_{\text{ex}}(\mathbf{r})$ can be found by minimizing the functional $E[n]$ with respect to the density $n(\mathbf{r})$, i.e., $\frac{\delta E[n]}{\delta n(\mathbf{r})} \overset{!}{=} 0$

Kohn-Sham method

So far, it is unclear how to use DFT in practice since the exact energy functional is unknown and probably too complicated to be ever written down more explicitly than above. Direct approximations of the energy functionals are challenging, usually too challenging. Here, the Kohn-Sham (KS) method[190] comes into play. It made DFT as successful as it is today. The KS method constructs a fictitious *non-interacting* system, the KS system, and employs it to approximate the kinetic energy operator $\hat{\mathcal{T}}$ which is hard to deal with otherwise.

So, the groundstate density is represented by the sum of orthonormal KS states ψ_n^{KS}:

$$n(\mathbf{r}) = \sum_l f_l |\psi_l^{\text{KS}}(\mathbf{r})|^2\,, \qquad \left(\sum_l f_l = n_{\text{el}}\right). \tag{B.12}$$

Formally, the occupation numbers f_l are either zero or one and the sum can be restricted to terms with $f_l = 1$.[1] Using the KS states, the universal energy functional is separated into three terms:

$$E'[n] = \sum_l f_l \int d\mathbf{r}\, \left(\psi_l^{\text{KS}}(\mathbf{r})\right)^* \underbrace{\frac{-\hbar^2}{2m}\Delta}_{\text{single particle kinetic energy } \hat{t}_{\text{kin}}} \psi_l^{\text{KS}}(\mathbf{r}) \quad + \quad \underbrace{\frac{1}{2}\int d\mathbf{r}\, v_{\text{H}}(\mathbf{r})\, n(\mathbf{r})}_{\text{Hartree-potential}} \quad + \quad \underbrace{E_{\text{xc}}[n]}_{\text{exchange-correlation functional}}\,. \tag{B.13}$$

The first term serves as an approximation to the total kinetic energy. The second term includes the most obvious interaction effect via the Hartree-potential $v_{\text{H}}(\mathbf{r}) = \int d\mathbf{r}'\, v(|\mathbf{r} - \mathbf{r}'|)\, n(\mathbf{r}')$. This includes unphysical self-interaction effects since every single electron interacts with the total electron density (which also includes the contribution of that single electron). Everything else (including corrections to the kinetic energy and the cancellation of the self-interaction) is put into the *exchange-correlation functional* $E_{\text{xc}}[n]$. In that sense, Eq. (B.13)

is still exact since it only defines $E_{\text{xc}}[n]$.[2]

The new problem is to search for the set of KS states $\{\psi_l^{\text{KS}}(\mathbf{r})\}$ which minimize $E[n]$. This variational problem leads to the *Kohn-Sham equations*:

$$\hat{\mathcal{H}}^{\text{KS}}|\psi_l^{\text{KS}}\rangle = \varepsilon_l|\psi_l^{\text{KS}}\rangle\,,$$
$$\hat{\mathcal{H}}^{\text{KS}} = \hat{t}_{\text{kin}} + \hat{v}_{\text{ex}} + \hat{v}_{\text{H}} + \hat{v}_{\text{xc}}\,. \tag{B.14}$$

The Lagrange-multiplier ε_l was introduced to ensure the correct normalization of the KS states ψ_l^{KS}. The func-

---

[1] In practice, fractional occupation numbers are useful to improve convergence of the SCF cycle (see end of paragraph) as they provide a way to avoid a sharp distinction between occupied and unoccupied states near the Fermi energy. A sharp distinction is usually numerically unstable in early steps of the SCF cycle.

[2] Formally, the exchange-correlation functional $E_{\text{xc}}[n]$ also depends directly on the KS states ψ_l^{KS} since it must include corrections to the kinetic energy term. In the end, only $E'[n]$ does solely depend on the groundstate density.

tional derivative of the exchange correlation functional is called the exchange correlation potential $\hat{v}_{\mathrm{xc}}$:

$$\hat{v}_{\mathrm{xc}} = \frac{\delta E_{\mathrm{xc}}[n]}{\delta n(\hat{\mathbf{r}})}. \tag{B.15}$$

Since the Hartree potential $v_{\mathrm{H}}(\mathbf{r})$ and the exchange-correlation potential $v_{\mathrm{xc}}(\mathbf{r})$ depend on the density $n(\mathbf{r})$, the KS equations are usually solved iteratively (which is then called the *self-consistent field (SCF) cycle*).

The KS equations, Eq. (B.14), look temptingly like a single particle time-independent Schrödinger equation for non-interacting particles. Understandably, $\hat{\mathcal{H}}^{\mathrm{KS}}$ is therefore called the KS Hamiltonian, ε_l are the KS energies, and the KS states ψ_l^{KS} refer to fictitious KS particles. This analogy must *not* be taken to far: formally all the KS quantities are fictitious, although some relations to the physical interacting electron system exists, e.g., the KS energy of the highest occupied orbital (HOMO) coincides with the (negative) ionization potential[191–193].

Approximation of the exchange-correlation functional

Until this point, the DFT is still exact but hardly useful in practice since the exchange correlation functional E_{xc} is unknown. For practical purposes, there exist several widely used approximations, most prominently, the local density approximations (LDA) and the generalized gradient approximations (GGA):

$$E_{\mathrm{xc}}[n] \approx \int \mathrm{d}\mathbf{r}\, E_{\mathrm{xc}}^{\mathrm{LDA}}\Big(n(\mathbf{r})\Big), \tag{B.16}$$

$$E_{\mathrm{xc}}[n] \approx \int \mathrm{d}\mathbf{r}\, E_{\mathrm{xc}}^{\mathrm{GGA}}\Big(n(\mathbf{r}), \boldsymbol{\nabla} n(\mathbf{r})\Big). \tag{B.17}$$

In LDA, the functional dependence is expressed as a simple spatial integral whose integrand only depends on the local density value $n(\mathbf{r})$ at that point. Additionally, the first density gradient is include in GGA schemes.

In this thesis, we use two well-established GGAs: the Perdew-Burke-Ernzerhof functional (PBE)[151] (using the DFT package FHI-AIMS[130]) and the Becke-Perdew functional (B-P86)[183, 184] (using the DFT package TURBOMOLE[134]).

B.2.2 Basis sets: overview of local basis functions used in this thesis

Both DFT codes used in this thesis, FHI-AIMS and TURBOMOLE, use atom centered local basis functions $|\varphi_j\rangle$ to represent the Kohn-Sham orbitals $|\psi_i^{\mathrm{KS}}\rangle = \sum_j |\varphi_j\rangle c_{ji}$. Their basis functions $\varphi_i(\mathbf{r}) = \langle \mathbf{r}|\varphi_i\rangle$ are represented in a radial-angular decomposition,

$$\varphi_i(\mathbf{r}) = R_i(r) Y_{lm}(\theta, \phi), \tag{B.18}$$

with real-values spherical harmonics Y_{lm} that ensure real-valued basis functions everywhere. (The angular indices $l(i)$, $m(i)$ are functions of the overall basis index i.) Anticipating time reversal invariance[3] of the KS system, real-valued basis functions mean that all expansion coefficients c_{ji} stay real as well.

FHI-AIMS uses numeric atom-centered orbitals (NAO)[130] as basis functions. The radial part $u_i(r) = R_i(r) \cdot r$ is numerically tabulated on a logarithmic grid. We employ a cubic spline interpolation for intermediate values. These basis functions used throughout this thesis are ordered in tiers with increasing precision, ranging from `tier1` (double-ζ) through `tier2` (triple-ζ) up to `tier3` (quadruple-ζ). By default, we use the `light` default species settings (corresponding to `tier1` for carbon atoms) and only switch to `tight` default species settings (corresponding to `tier2`) for convergence checks.

TURBOMOLE uses contracted Gaussian type orbitals (CGTO)[194, 195] as basis functions. The radial part is given by

$$R_i(r) = r^l \sum_p^{P_i} d_p \exp(-\eta_p r^2), \tag{B.19}$$

where P_i Gaussians with exponents η_p are contracted using the weights d_p. The basis functions used in this thesis are (with increasing precision) of double-ζ (split-valence, DEF2-SVP) and triple-ζ quality with polarization functions (DEF2-TZVP, DEF2-TZVPP), and the corresponding Coulomb-fitting basis sets within the resolution of identity approximation[196–198]. The basis sets are abbreviated by SVP, TZVP, TZVPP.

---

[3]Time reversal invariance is, for example, broken by spin-orbit interaction (SOI). Then, the expansion coefficients become complex, see Chap. 5 for an investigation of SOI in graphene nanoribbons.

B.3 Implementation overview

B.3.1 Program structure

Before discussing the program performance (Appx. B.3.2), we present the task flow, see Fig. B.1. The code is structured into several modules, which operate independently. The modules' outputs (and therefore the inputs for the next module) are either saved on the hard disk or kept directly in memory.

The most important modules (from top to bottom in Fig. B.1) are:

ExtractSubSystem: In two separate instances of this module, the Kohn-Sham Hamiltonian for the device and the lead region is reconstructed. When using several MPI processes, only the first one (rank 0) is performing the work; the results are broadcasted to all other MPI processes.

CalcSelfEnergy: For each energy point E, the self-energy $\mathbf{\Sigma}_{\mathrm{L/R}}$ for the lead is constructed (or read from hard disk if it was constructed earlier).

CalcTransmission: To calculate the transmission, we first diagonalize the central part of the device region (cf. Sec. B.4.5) using all MPI processes via ScaLAPACK[199]. Next, the different energy points are distributed to the different MPI processes. For each energy point E, the self-energies $\mathbf{\Sigma}_{\mathrm{L/R}}(E)$ are used to calculate the retarded Green's function $\mathbf{G}(E)$, the transmission $\mathcal{T}(E)$ and the density of states $\rho(E)$.

The time $t_{\mathbf{G}}$ for constructing the Green's function and calculating the transmission includes constructing the indices, applying the self-energy and—most notably—the matrix inversion and matrix multiplication. Since these things are separated in the code, we calculate $t_{\mathbf{G}} := T_{\mathcal{T}} - t_{\mathbf{H}} - t_{\mathrm{diag}} - t_{\mathbf{\Sigma}}$ where $T_{\mathcal{T}}$ is the total wall time of the complete program run. The lower t are measured using an in-code timing mechanism. (See Fig. B.1 (left) for definition of the timing symbols).

CalcLocalCurrent: The Keldysh Green's function $\mathbf{G}^{<}$ is used to calculate the spectrally resolved non-equilibrium particle number $n(E)$. The local current density $\mathbf{j}(\mathbf{r}, E)$, the divergence $\mathbf{\nabla} \cdot \mathbf{j}(\mathbf{r}, E)$, the local density of states $\rho(\mathbf{r}, E)$ and the spectrally resolved non-equilibrium local density $n(\mathbf{r}, E)$ are rastered on a rectilinear grid. Again, the timing for reconstructing the Green's function includes all necessary overhead, i.e., $t_{\mathbf{G}^{<}} := T_{\mathbf{r}} - t_{\mathbf{H}} - t_{\mathbf{\Sigma}} - t_{(\mathbf{r})}$.

If the number of MPI processes exceeds the number of energy points (probably because we use a very fine grid for the local quantities), the energy points are not distributed but all MPI processes calculate all energy points. This leads to an overhead since the self-energy and the Green's functions are calculated redundantly. The rastering of the local quantities, i.e. the grid points, are then distributed over all MPI processes.

MagneticField: As an optional post-processing module, the magnetic field $\mathbf{B}(\mathbf{r}, E)$, the vector potential $\mathbf{A}(\mathbf{r}, E)$ and the magnetic moment $\mathbf{m}(E)$ induced by the current density $\mathbf{j}(\mathbf{r})$ can be calculated. This module in not included in the detailed performance analysis below and therefore no timing symbol is given.

There are additional modules for post-processing, e.g., `IntegrateEnergy`, `IncludeMagneticFeedback`, `IntegrateGFs`, `CalcSpectrum`, `WriteASCII`; please refer to the program documentation for details (e.g. run `TSaint --config`).

B.3.2 Parallelization and performance measurements

In Fig. B.2, we present detailed measurements of the performance of our transport code for realistic system sizes. In the tests, we distinguish between calculation of the transmission and of local observables. Trans-mission calculations ($\mathcal{T}(E)$) also include the density of states $\rho(E)$. Local observables are the local current density $\mathbf{j}(\mathbf{r}, E)$ but also its divergence $\mathbf{\nabla} \cdot \mathbf{j}(\mathbf{r}, E)$, the non-equilibrium density $n(\mathbf{r}, E)$ and the local density

Timing symbols	Programm flow		Parallelization via MPI	via threads
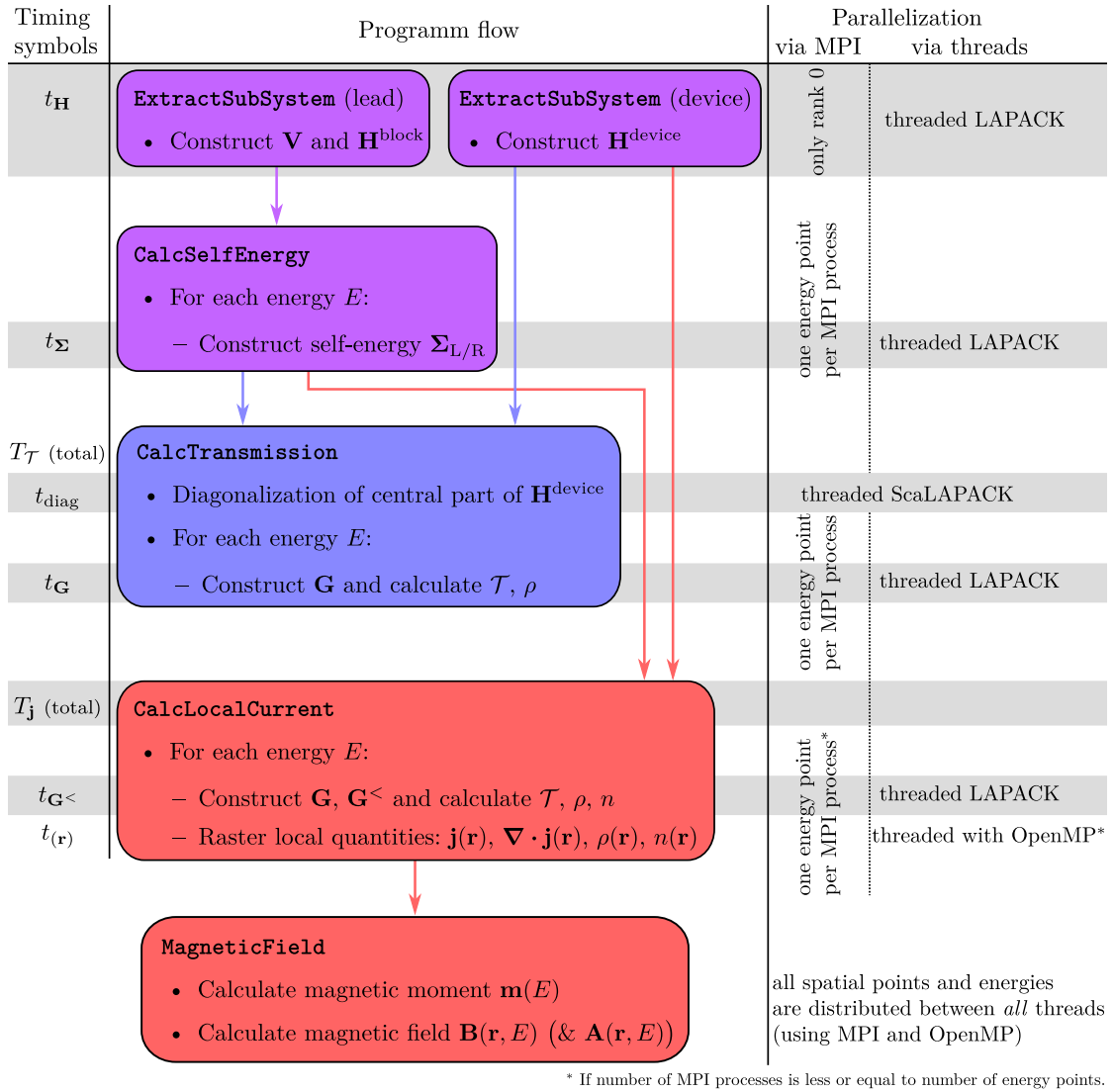
Figure B.1: Center: The main modules are depicted in separate boxes. The two most common module sequences are depicted in blue (transmission calculation) and red (current density and magnetic field calculation). Both sequences include the reconstruction of the KS Hamiltonian and the calculation of the self-energies (purple). Transmission calculations ($\mathcal{T}(E)$) also include the density of states $\rho(E)$. Current density calculations ($\mathbf{j}(\mathbf{r}, E)$) additionally include the current divergence $\boldsymbol{\nabla} \cdot \mathbf{j}(\mathbf{r}, E)$, the non-equilibrium density $n(\mathbf{r}, E)$ and the local density of states $\rho(\mathbf{r}, E)$. Left: the timing symbols used in the following for performance analyzation, cf. Fig. B.2. Right: Overview of the parallelization techniques used in each module to allow the use of many (up to thousand) CPUs.

of states $\rho(\mathbf{r}, E)$. In Fig. B.2a, the wall time for calculating $N_E = 128$ separate transmission and density of states values is plotted depending on the number of basis functions N. The test system are the same hydrogen-saturated AGNRs as shown in Fig. 2.18.

The total time $T_{\mathcal{T}}(N)$ is divided into four groups ($t_{\mathbf{H}}$, t_{diag}, $t_{\boldsymbol{\Sigma}}$, $t_{\mathbf{G}}$, cf. Fig. B.1). The calculation of the lead self-energy [via 200 iterations in the decimation technique (cf. Sec. 2.1.3)] depends directly on the number of basis functions N_{lead} of a block ("slice") of the lead; it only indirectly depends on the basis functions N of the device region. Thus, the dependence on the former is plotted separately. The main effort for a transmission

(a) Transmission: $\mathcal{O}(N^n)$-scaling (P=32)

(b) Local observables: $\mathcal{O}(N^n)$-scaling (P=32)
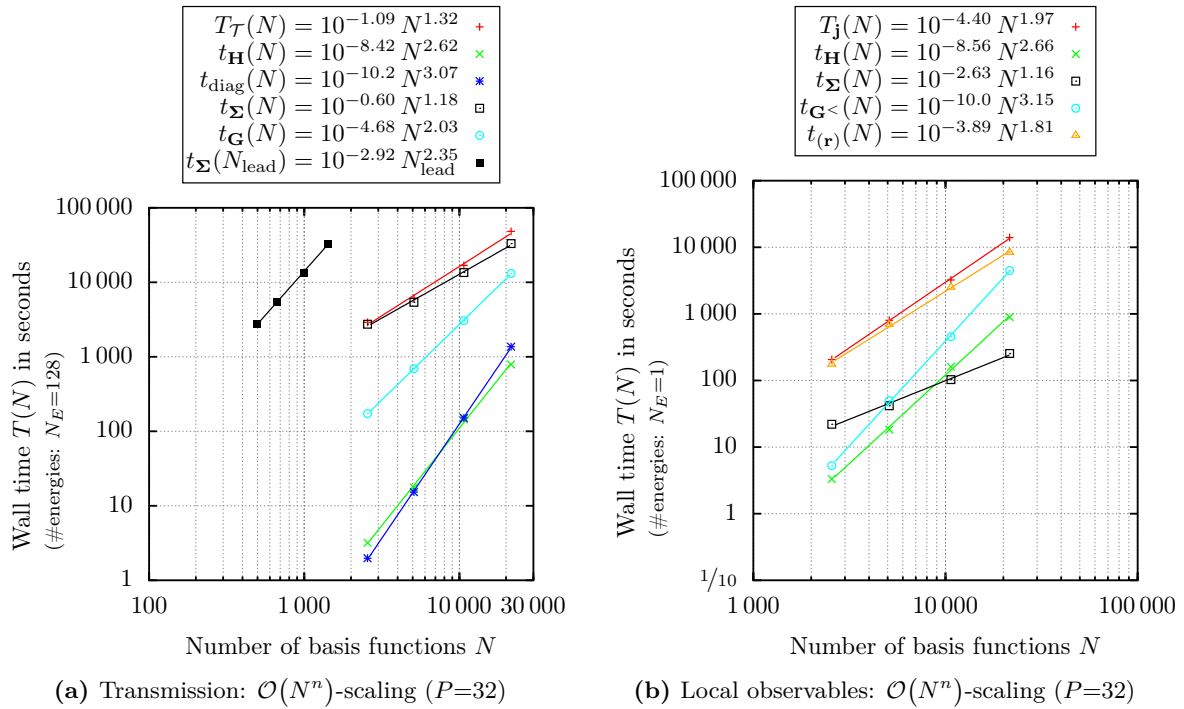
Figure B.2: $\mathcal{O}(N^n)$-scaling: Performance measurements with varying system size for a transmission (upper plot) and local observable (lower plot) calculation for a fixed number of CPU cores (P=32). Symbols: number of basis functions N, number of energy points N_E, number of CPU cores P.

(a) Transmission: MPI-Speedup (p=8)

(b) Local observables: MPI-Speedup (p=8)
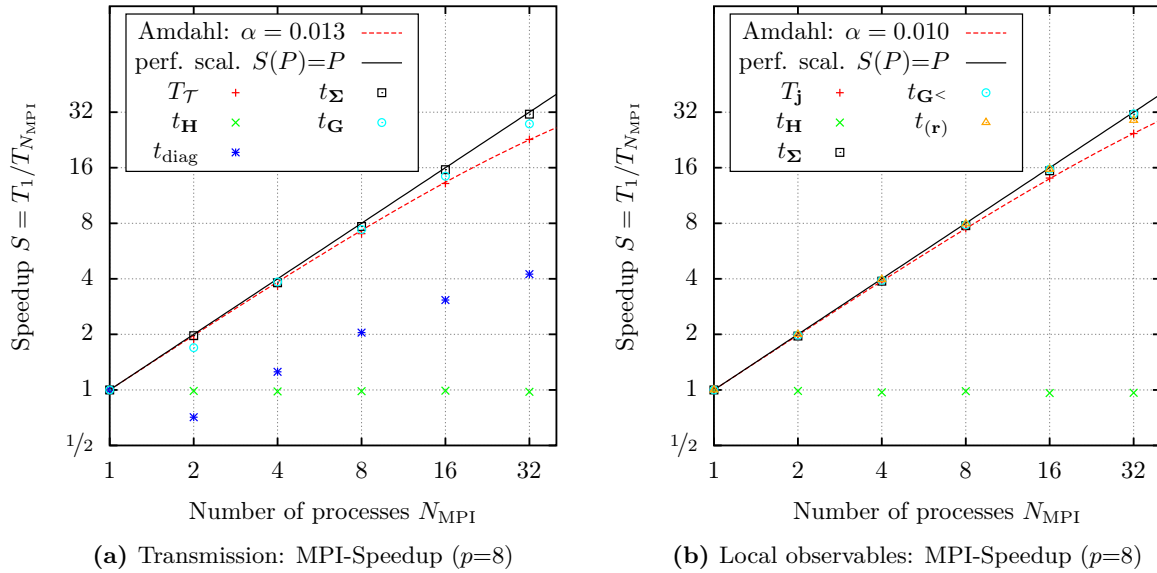
Figure B.3: MPI-parallelization: Speedup for a fixed system size (735 (21×35) carbon atoms) and for a fixed number of CPU cores per MPI process (p=8). Left: Speedup for transmission calculations. Right: Speedup for local observable calculation. Symbols are the same as in Fig. B.2. p is the number of CPU cores per MPI process, and N_{MPI} is the number of MPI processes ($P = p\,N_{\mathrm{MPI}}$).

calculation is reconstructing the self-energy; therefore it makes sense to save them on the hard disk if several different impurity configurations are processed which all use the same leads. Then, the main effort is spent for reconstructing the Green's function ($t_{\mathbf{G}}$). The diagonalization (t_{diag}, see Sec. B.4.5) does not significantly contribute to the overall effort for the available system sizes since it is performed only once and not for every energy point.

In Fig. B.3b, the analogue is plotted for a single ($N_E{=}1$) current density calculation. The number of grid points used is proportional to the system size (one grid point every 0.2 Å, 31 in z-direction). We first note, that the main effort is dominated by rastering the local quantities ($t_{(\mathbf{r})}$). We were able to optimize local observable calculation to scale below N^2 employing the locality of

the basis functions.[4]

In Fig. B.3, we discuss the parallelization efficiency of the transmission calculation and current density calculation for a fixed system size (735 (21×35) carbon atoms). The speedup S for many MPI processes compared to a single process is shown and compared to Amdahl's law: $T_{N_{\text{MPI}}} = T_1 \left(\alpha + \frac{1-\alpha}{N_{\text{MPI}}} \right)$, $\alpha \approx 1\%$. We see a good scalability for the total wall time, the self-energy construction and the Green's function construction ($T_{\mathcal{T}}$, $t_{\mathbf{\Sigma}}$, $t_{\mathbf{G}}$). The reconstruction of the KS Hamiltonian ($t_{\mathbf{H}}$) does not speedup since only the first MPI process is involved (cf. Fig. B.1). For the diagonalization, we even observe that using two processes (using ScaLAPACK) is slower than using only one process (using LAPACK). Therefore, our code now only uses ScaLAPACK starting with 4 MPI processes.

B.3.3 Numerical parameters

In Table B.1, we list the numerical parameters of the largest calculation performed for hydrogenated graphene flakes. First, the graphene flake is structurally relaxed using FHI-AIMS until the remaining forces decrease below 10^{-2} eV/ Å. This is, by far, the most expensive part of the calculation. Then a final DFT run for the relaxed structure is performed and the output

written to disk. This is used by AITRANSS to perform a wide scan over the transmission function (the self-energies $\mathbf{\Sigma}$ are pre-calculated since they only depend on the system size, not on the impurity configuration). Eventually, a few interesting energy points are taken from the transmission function and the current density is calculated at those energy points.

	FHI-AIMS		AITRANSS	
	Relaxation	DFT	Transmission[a]	Current density[b]
numbers of processes N_{MPI}	3600	384	16	6
cores per process p	1	1	12	24
total number of cores P	3600	384	192	144
number of nodes n	150	16	8	6
wall time T_{wall}	77.9h[c]	5.52h	5.68h	9.86h
core hours T_{cores}	280 500h	2 120h	1 090h	1 420h
memory usage per process $\mathcal{M}$	0.72 GiB	0.72 GiB	52.7 GiB	76.3 GiB
memory usage per node $\mathcal{M}_{\text{node}}$	17.2 GiB	17.2 GiB	105.5 GiB	76.3 GiB

[a] Transmission $\mathcal{T}(E)$ has been calculated at 2423 energies values.
[b] The current density $\mathbf{j}(\mathbf{r}, E)$ has been calculated at 6 energies values.
[c] The relaxation calculation was broken down into several jobs, each with a wall time below 24h.

Table B.1: An overview of the calculations performed on Cray XC40 (Hornet) for the largest graphene flake feasible (with 2479 carbon atoms) whose central 34×59 carbon atoms have been functionalized with hydrogen (compare with Fig. 4.8). Note that some information is redundant, i.e., $P = p\,N_{\text{MPI}} = 24\,n$, $T_{\text{cores}} = T_{\text{wall}}P$, $\mathcal{M}_{\text{node}} = \mathcal{M}N_{\text{MPI}}/n$.

---

[4]Naively the evaluation of the current or its divergence, see Eq. (2.30) and Eq. (2.31), scales with N^3 since the number of spatial grid points $\mathbf{r}$ scales linearly, for constant grid spacing, and the summation of i, j gives additional N^2. Please, refer to Sec. B.4.4 for optimization details.

B.4 Implementation details

B.4.1 A word on the Löwdin orthogonalization

Technically, the underlying DFT codes work with non-orthogonal basis sets $|\varphi_i\rangle$. Internally, the Kohn-Sham (KS) orbitals $|\psi_i^{\mathrm{KS}}\rangle$ are represented by expansion coefficients c_{ji} with respect to the non-orthogonal basis set, i.e., $|\psi_i^{\mathrm{KS}}\rangle = \sum_j |\varphi_j\rangle c_{ji}$.

We use the (symmetric) overlap matrix $S_{ij} = \langle\varphi_i|\varphi_j\rangle$ to calculate the orthogonal set of basis functions $|\tilde{\varphi}_i\rangle$ via the Löwdin-orthogonalization[136] procedure, i.e., $|\tilde{\varphi}_i\rangle = \sum_j |\varphi_j\rangle \left[S^{-1/2}\right]_{ji}$. The "square root" $S^{1/2}$ is defined by the positive square roots of the eigenvalues in eigenbasis representation. The expansion coefficients are transformed as well: $\tilde{c}_{ik} = \sum_j \left[S^{1/2}\right]_{ij} c_{jk}$. The Löwdin-orthonormalized basis set $|\tilde{\varphi}_i\rangle$ is the orthogonal basis set which minimizes the squared distance $\sum_i \int |\varphi_i(\mathbf{r}) - \tilde{\varphi}_i(\mathbf{r})|^2 \, \mathrm{d}^3\mathbf{r}$ to the original basis set $|\varphi_i\rangle$[200]. In particular, that means that the orthonormalized basis function $|\tilde{\varphi}_i\rangle$ is still localized around the same atom core as $|\varphi_i\rangle$.

The full KS Hamiltonian $\hat{\mathcal{H}}_0^{\mathrm{KS}}$ is then reconstructed

$$\hat{\mathcal{H}}_0^{\mathrm{KS}} = \sum_n |\psi_n^{\mathrm{KS}}\rangle \varepsilon_n^{\mathrm{KS}} \langle\psi_n^{\mathrm{KS}}| = \sum_{ij} |\tilde{\varphi}_i\rangle \mathbf{H}_{0,ij}^{\mathrm{KS}} \langle\tilde{\varphi}_j|\,, \tag{B.20}$$

which is written with respect to the orthonormal basis as

$$\mathbf{H}_{0,ij}^{\mathrm{KS}} = \sum_n \tilde{c}_{in}\, \varepsilon_n^{\mathrm{KS}} \left[\tilde{c}^T\right]_{nj}\,. \tag{B.21}$$

In the main part, we always worked with the Löwdin-orthonormalized basis set $|\tilde{\varphi}_i\rangle$; even when calculating local observables [cf. Eq. (2.30),(2.31)].

In practice, it is computational advantageous to transform the Green's functions to the non-orthogonal basis set, e.g., $\check{\mathbf{G}} = S^{-1/2}\mathbf{G}S^{-1/2}$, and calculate the local observables using the original non-orthogonal basis set. For the calculation of the current density, this means:

$$\mathbf{j}(\mathbf{r}, E) = \frac{1}{2\pi}\frac{\hbar}{m}\sum_{ij} \tilde{\varphi}_i(\mathbf{r})\overset{\mathrm{as}}{\mathbf{G}}{}_{ij}^< \left(\boldsymbol{\nabla}\tilde{\varphi}_j(\mathbf{r})\right), \tag{B.22}$$

$$= \frac{1}{2\pi}\frac{\hbar}{m}\sum_{\substack{ii'\\jj'}} \varphi_{i'}(\mathbf{r})\underbrace{S_{i'i}^{-1/2}\overset{\mathrm{as}}{\mathbf{G}}{}_{ij}^<(E)S_{jj'}^{-1/2}}_{=:\,\overset{\mathrm{as}}{\check{\mathbf{G}}}{}_{i'j'}^<}\left(\boldsymbol{\nabla}\varphi_{j'}(\mathbf{r})\right).$$

Going to the second line, we replaced the orthonormal basis set $\tilde{\varphi}_i(\mathbf{r})$ with the original set $\varphi_i(\mathbf{r})$ using the overlap matrix S.

Technical remark: Please note, that the primed indices of Eq. (B.22) run (in principle) over all N_{DFT} non-orthogonal basis functions $|\varphi_i\rangle$ of the underlying DFT calculation whereas the unprimed indices only run over the N basis functions $|\tilde{\varphi}_i\rangle$ used to represent the device region. At first glance, the two numbers are the same since we constructed the later basis set as linear combination of the former. But, the device region is usually represented only by a $N{\times}N$-subblock of the total $N_{\mathrm{DFT}}{\times}N_{\mathrm{DFT}}$ KS Hamiltonian. By extracting this subblock, we only take a subset of the orthogonal basis set $|\tilde{\varphi}_i\rangle$, i.e., $N < N_{\mathrm{DFT}}$. Especially near the borders of the device region, non-orthogonal basis functions centered outside reach into the device region and are therefore partly contained in the (restricted) orthogonal basis set. Due to that reason, the (technical) matrix dimension of $\check{\mathbf{G}}$ is larger that the matrix dimension of $\mathbf{G}$ and a rectangular subblock of the overall overlap matrix S is needed in $\check{\mathbf{G}} = S^{-1/2}\mathbf{G}S^{-1/2}$.

Overview over local observables

For convenience, we list all implemented local observables: the local current density $\mathbf{j}(\mathbf{r}, E)$, its divergence, the non-equilibrium local density $n(\mathbf{r}, E)$ and the local density of states $\rho(\mathbf{r}, E)$; all spectrally resolved:

$$\mathbf{j}(\mathbf{r}, E) = \frac{1}{2\pi}\frac{\hbar}{2m}\lim_{\mathbf{r}'\to\mathbf{r}}(\boldsymbol{\nabla}_{\mathbf{r}'} - \boldsymbol{\nabla}_{\mathbf{r}})G^<(\mathbf{r}, \mathbf{r}', E)$$
$$= \frac{1}{2\pi}\frac{\hbar}{m}\sum_{ij} \varphi_i(\mathbf{r})\overset{\mathrm{as}}{\check{\mathbf{G}}}{}_{ij}^< \left(\boldsymbol{\nabla}\varphi_j(\mathbf{r})\right), \tag{B.23}$$

$$\boldsymbol{\nabla}\cdot\mathbf{j}(\mathbf{r}, E) = \frac{1}{2\pi}\frac{\hbar}{m}\sum_{ij} \varphi_i(\mathbf{r})\overset{\mathrm{as}}{\check{\mathbf{G}}}{}_{ij}^< \left(\boldsymbol{\nabla}\cdot\boldsymbol{\nabla}\varphi_j(\mathbf{r})\right), \tag{B.24}$$

$$n(\mathbf{r}, E) = -\frac{\mathrm{i}}{2\pi}G^<(\mathbf{r}, \mathbf{r}, E)$$
$$= -\frac{\mathrm{i}}{2\pi}\sum_{ij} \varphi_i(\mathbf{r})\overset{\mathrm{sym}}{\check{\mathbf{G}}}{}_{ij}^< \varphi_j(\mathbf{r}), \tag{B.25}$$

$$\rho(\mathbf{r}, E) = -\frac{1}{\pi}\operatorname{Im} G(\mathbf{r}, \mathbf{r}, E)$$
$$= -\frac{1}{\pi}\sum_{ij} \varphi_i(\mathbf{r})\operatorname{Im}\check{\mathbf{G}}_{ij}\,\varphi_j(\mathbf{r}). \tag{B.26}$$

The checked versions, e.g., $\check{\mathbf{G}}$, always denote the quantities with respect to the non-orthogonal basis set, i.e., $\check{\mathbf{G}} = S^{-1/2}\mathbf{G}S^{-1/2}$.

$$\overset{\text{sym}}{\mathbf{G}}{}^{<}_{ij} := \frac{1}{2}\Big(\mathbf{G}^{<}_{ij} + \mathbf{G}^{<}_{ji}\Big) = \frac{1}{2}\Big(\mathbf{G}^{<}_{ij} - (\mathbf{G}^{<}_{ij})^{*}\Big) = i\,\mathrm{Im}\,\mathbf{G}^{<}_{ij},$$
$$\text{(B.27)}$$

$$\overset{\text{as}}{\mathbf{G}}{}^{<}_{ij} := \frac{1}{2}\Big(\mathbf{G}^{<}_{ij} - \mathbf{G}^{<}_{ji}\Big) = \frac{1}{2}\Big(\mathbf{G}^{<}_{ij} + (\mathbf{G}^{<}_{ij})^{*}\Big) = \mathrm{Re}\,\mathbf{G}^{<}_{ij}.$$
$$\text{(B.28)}$$

Remark: Since the Keldysh Green's function $\mathbf{G}^{<}$ is anti-Hermitian, cf. Eq. (2.12), the symmetric and antisymmetric parts are given by the imaginary and real part, respectively:

B.4.2 Optimization overview

In this section, we present the most important optimizations used throughout our code development. These are implementation details, but nevertheless, they are important to anyone who either wants to to improve/modify the code or plans to write a separate framework to transport through large systems.

In the following sections, several optimizations are presented whose performance impact is summarized in Tab. B.2. The table lists the increase in wall time and memory consumption when a specific optimization is removed from the code. Each optimization is labeled by a short keyword which is used in the respective section headings.

The optimization ZerosInSigma (cf. Sec. B.4.3), exploiting the block structure of the self-energy, is straightforward but reduces the construction of the Green's function by over a factor of ten. The technically most difficult (but also very important) optimiza-

tion is probably SpaceBlocks (cf. Sec. B.4.4) without which current calculations for systems with more than 1000 atoms would become impossible. But also the optimization MatrixInverse (cf. Sec. B.4.5) is quite handy because it allows for quick (and perhaps finer in energy domain) transmission scans before turning to more expensive current density calculations. Note that all three optimization have a larger impact for the 812-atom-system compared to the 398-atom-system. This makes them especially important for large systems.

The optimization measurements have been performed with realistic system data (cf. Appx. B.3.2) so that size-related bugs and problems already appeared during testing and could be solved early on. Prominent bottlenecks/problems related to the large system size were:

- The matrix outputs of FHI-aims are by default written as text files which is inefficient (in terms

Optimization	Changed Quantity	398 atoms		812 atoms	
ZerosInSigma: $\mathcal{T}$ [a]	Energy loop: $t_{\mathbf{G}}$	$\times 13.3$	203s →2705s	$\times 19.0$	1342s →25482s
	Memory: $\mathcal{M}_{\mathcal{T}}$	$\times 2.0$	1141MiB →2307MiB	$\times 2.1$	4845MiB →9945MiB
ZerosInSigma: $\mathbf{j}$ [a]	Energy loop: $t_{\mathbf{G}<}$	$\times 1.9$	664s →1263s	$\times 2.9$	754s →2179s
	Memory: $\mathcal{M}_{\mathbf{j}}$	$\times 1.5$	1669MiB →2459MiB	$\times 1.5$	7143MiB →10615MiB
SpaceBlocks: $\mathbf{j}$	Local quantities: $t_{(\mathbf{r})}$	$\times 18.3$	557s →10177s	$\times 41.1$	1845s →75811s
MatrixInverse: $\mathcal{T}$ [a]	Energy loop: $t_{\mathbf{G}}$	$\times 7.0$	203s →1414s	$\times 10.6$	1342s →14264s
	Memory: $\mathcal{M}_{\mathcal{T}}$	$\times 1.3$	1141MiB →1450MiB	$\times 1.3$	4845MiB →6230MiB

Table B.2: Increase in wall time and memory consumption when specific optimizations *are removed* from the code. To get a feeling for the the dependence on the system size, two different sizes are shown. The computational parameters and the systems are identical to the ones used in Fig. B.2a and Fig. B.2b. Symbols are used to distinguish transmission ($\mathcal{T}$) and current density ($\mathbf{j}$) calculations. [a] The self-energy was read from hard disk.

of disk memory but also in terms of CPU time). Especially for large systems, this became a bottleneck and we switched to writing the matrix data directly to a HDF5-file[137], which is a structured but binary file format.

- Reading and writing from and to the hard disk (I/O) becomes terrible slow if it is done in small portions (or unnecessary from multiple processes). To solve that, we read the whole matrix data using a single system call (using HDF5-parallel when available). Also, all I/O-related work in the module `ExtractSubSystem` is is done in one process (rank 0) and only the results are broadcasted to other MPI processes.

- It is problematic (i.e. some MPI implementations crash) to send data larger than 2 GiB via MPI in a single call, even if the number of elements is significantly below $2^{31}-1$. In such cases, our code automatically sends the data using multiple MPI calls.

B.4.3 Optimization ZEROSINSIGMA: exploiting the block structure of self-energy Σ and broadening matrix Γ

Formally, transmission $\mathcal{T}$ and Keldysh Green's function $\mathbf{G}^<$ are calculated as:

$$\mathcal{T}(E) = \mathrm{Tr}\{\mathbf{\Gamma}_\mathrm{L}\,\mathbf{G}\,\mathbf{\Gamma}_\mathrm{R}\,\mathbf{G}^\dagger\}\,, \qquad \text{cf. Eq. (2.8)} \quad (B.29)$$

$$\mathbf{G}^<(E) = \mathrm{i}\mathbf{G}\mathbf{\Gamma}_\mathrm{L}\mathbf{G}^\dagger\,. \qquad \text{cf. Eq. (2.12)} \quad (B.30)$$

In practice, the matrices $\mathbf{\Gamma}_\mathrm{L/R} = \mathrm{i}(\mathbf{\Sigma}_\mathrm{L/R} - \mathbf{\Sigma}_\mathrm{L/R}^\dagger)$ contain a lot of zeros. Their non-vanishing entries belong to the left/right contact areas of the device region. This block structure is evident if one partitions the device region into three regions: left contact area (L), right contact area (R) and the remaining central part of the device (C). In the basis (L/C/R), the matrices $\mathbf{\Gamma}_\mathrm{L/R}$ then read:

$$\mathbf{\Gamma}_\mathrm{L} = \begin{pmatrix} \tilde{\mathbf{\Gamma}}_\mathrm{L} & 0 & 0 \\ 0 & 0 & 0 \\ 0 & 0 & 0 \end{pmatrix}\,, \qquad \mathbf{\Gamma}_\mathrm{R} = \begin{pmatrix} 0 & 0 & 0 \\ 0 & 0 & 0 \\ 0 & 0 & \tilde{\mathbf{\Gamma}}_\mathrm{R} \end{pmatrix}\,. \tag{B.31}$$

Working with the (unnecessarily large) matrices $\mathbf{\Gamma}_\mathrm{L/R}$ is computationally inefficient. It is much more efficient to also partition the retarded Green's function $\mathbf{G}$ into blocks, i.e.,

$$\mathbf{G} = \begin{pmatrix} \mathbf{G}_\mathrm{LL} & \mathbf{G}_\mathrm{LC} & \mathbf{G}_\mathrm{LR} \\ \mathbf{G}_\mathrm{CL} & \mathbf{G}_\mathrm{CC} & \mathbf{G}_\mathrm{CR} \\ \mathbf{G}_\mathrm{RL} & \mathbf{G}_\mathrm{RC} & \mathbf{G}_\mathrm{RR} \end{pmatrix}\,, \quad \mathbf{G}_\mathrm{FL} := \begin{pmatrix} \mathbf{G}_\mathrm{LL} \\ \mathbf{G}_\mathrm{CL} \\ \mathbf{G}_\mathrm{RL} \end{pmatrix}\,. \tag{B.32}$$

Here, we already defined $\mathbf{G}_\mathrm{FL}$ as the submatrix of $\mathbf{G}$ where the first index refers to the full (F) device region but the second index is restricted to the left (L) contact region.

Using these shrunken matrices, the transmission $\mathcal{T}$ and Keldysh Green's function $\mathbf{G}^<$ is calculated as:

$$\mathcal{T}(E) = \mathrm{Tr}\{\tilde{\mathbf{\Gamma}}_\mathrm{L}\,\mathbf{G}_\mathrm{LR}\,\tilde{\mathbf{\Gamma}}_\mathrm{R}\,[\mathbf{G}_\mathrm{LR}]^\dagger\}\,, \tag{B.33}$$

$$\mathbf{G}^<(E) = \mathrm{i}\mathbf{G}_\mathrm{FL}\tilde{\mathbf{\Gamma}}_\mathrm{L}[\mathbf{G}_\mathrm{FL}]^\dagger\,. \tag{B.34}$$

Remark on complexity: Using this technique, the computational complexity for calculating transmission and Keldysh Green's function is reduced from $\mathcal{O}(N^3)$ [Eq. (B.29),(B.30)] to $\mathcal{O}(n^3)$ [Eq. (B.33)] and $\mathcal{O}(nN^2)$ [Eq. (B.34)], respectively. N and n denote the number of basis functions in the device region and the left contact region, respectively.

B.4.4 Optimization SPACEBLOCKS: dividing space into blocks

Here, we discuss how to evaluate the formulas for space-depending local quantities like the current density

$$\mathbf{j}(\mathbf{r}, E) \propto \sum_{ij} \varphi_i(\mathbf{r}) \overset{\text{as}}{\mathbf{G}}{}^<_{ij} \left(\boldsymbol{\nabla} \varphi_j(\mathbf{r}) \right). \qquad (B.35)$$

In principle, the double sum runs over *all N* basis functions of the underlying DFT simulation. Additionally, for constant grid spacing, the number of spatial grid points **r** scales linearly with system size. Thus, naively, the evaluation of the local quantities scales with N^3. But each basis function is localized around some atom, i.e., it is nonzero only in a small area. This can be exploited in the following way.

First, we define $r_{\max}$ as the maximal extent of all basis functions, i.e., each basis function is zero at points which are further away from its central atom than $r_{\max}$. Second, the 3D space is divided into little cubes with edge length $r_{\max}/n$, see Fig. B.4 (n is an integer). When calculating any local quantity inside the blue shaded

area, the only basis functions taken into account are centered around atoms in the green (and blue) shaded area. All other basis functions do not contribute in the blue shaded area.

Hence, the the cubes of length $r_{\max}/n$ are distributed to the separate MPI processes. The integer n is chosen such that every MPI process can work on at least five cubes since some cubes are cheap since no or hardly any grid points are contained. Then, for each inner (blue) cube, we restrict the Green's function $\mathbf{G}^<$ to the basis functions corresponding to atoms in the extended (green) shaded area.

Remark: To measure the wall time in Tab. B.2 without this optimization for 812 atoms, we needed to double the grid spacing (taking only every eighth grid point) and used linear extrapolation to approximate $t_{(\mathbf{r})}$ for the full grid.
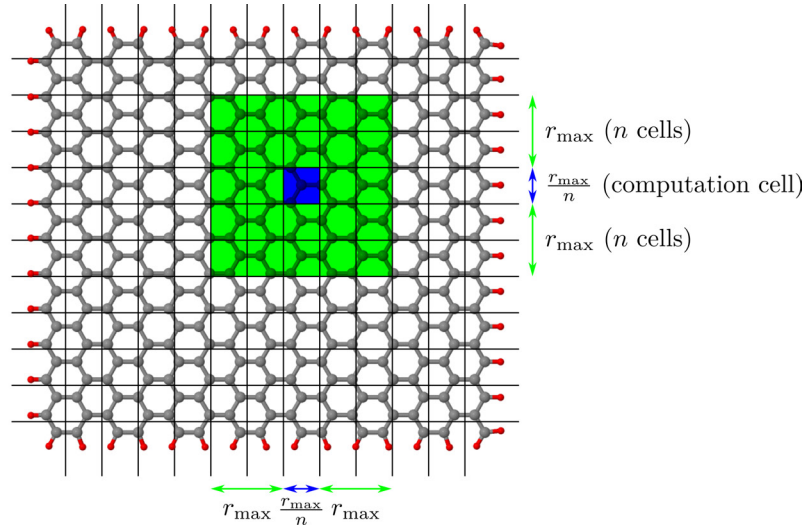
Figure B.4: Dividing space into 156 (13×12x1) non-overlapping blocks, exemplary for a graphene flake with 398 atoms. (2D-Model with $n = 2$, $r_{\max} = 5.05\,\text{Å}$)

B.4.5 Optimization MATRIXINVERSE: calculating the Green's function inverse

As the self-energy can be read from hard disk, the most expensive part in a transmission calculation is the matrix inversion in calculating the retarded Green's function $\mathbf{G}$, cf. Eq. (2.23). According to Fig. B.2a, $\mathbf{G}$ can be constructed in $\mathcal{O}(N^2)$ whereas a textbook matrix inversion scales[5] as $\mathcal{O}(N^3)$ and would therefore dominate for large systems anyway. The quadratic scaling shown in Fig. B.2a is possible when calculating $\mathbf{G}(E)$ for many different energies. Exploiting the structure of the Green's function, one can pre-diagonalize parts of

the Hamiltonian so that the residual work per energy point resides in $\mathcal{O}(N^2)$.

Partitioning of the Green's function: We first transform the Hamiltonian so that it is diagonal in the regions where the self-energies $\boldsymbol{\Sigma}$ are zero. Thus, we resort the indices of the Green's function such that the self-energy contribution of the leads only appear in subblock $\mathbf{D}$, i.e.,

$$
\begin{aligned}
\mathbf{G}^{-1} &= E\mathbb{1} - \mathbf{H} - \boldsymbol{\Sigma}_L(E) - \boldsymbol{\Sigma}_R(E) \\
&= \begin{pmatrix} E\mathbb{1}_{\mathrm{AA}} - \mathbf{H}_{\mathrm{AA}} & -\mathbf{H}_{\mathrm{AD}} \\ -\mathbf{H}_{\mathrm{DA}} & E\mathbb{1}_{\mathrm{DD}} - \mathbf{H}_{\mathrm{DD}} - \boldsymbol{\Sigma}_L(E) - \boldsymbol{\Sigma}_R(E) \end{pmatrix}^{-1} =: \begin{pmatrix} \mathbf{A} & \mathbf{B} \\ \mathbf{C} & \mathbf{D} \end{pmatrix}^{-1},
\end{aligned}
\tag{B.36}
$$

with the subscripts AA, AD, DA, DD denoting the restriction to the respective matrix subspace.

As advantage of this division, the only non-trivial energy dependence appears in subblock $\mathbf{D} = E\mathbb{1}_{\mathrm{DD}} - \mathbf{H}_{\mathrm{DD}} - \boldsymbol{\Sigma}_L(E) - \boldsymbol{\Sigma}_R(E)$. The block $\mathbf{A}$ can be diagonalized for all energies in a single eigenvalue problem: the eigenvalues are given by $\tilde{\mathbf{A}} = E\mathbb{1} - \tilde{\mathbf{H}}_{\mathrm{AA}}$ where $\tilde{\mathbf{H}}_{\mathrm{AA}}$ denotes the eigenvalues of $\mathbf{H}_{\mathrm{AA}}$. The transformation matrix $\mathbf{V}$ ($\tilde{\mathbf{H}}_{\mathrm{AA}} = \mathbf{V}^{-1}\mathbf{H}_{\mathrm{AA}}\mathbf{V}$) is constructed by filling its columns with the (right) eigenvectors of $\mathbf{H}_{\mathrm{AA}}$. The

off-diagonal blocks also stay energy independent, e.g., $\tilde{\mathbf{B}} = -\mathbf{V}^{-1}\mathbf{H}_{\mathrm{AD}}$.

General matrix: For the matrix inversion, we first tend to a general matrix which we divide into four blocks

$$
\begin{pmatrix} \mathbf{A} & \mathbf{B} \\ \mathbf{C} & \mathbf{D} \end{pmatrix},
\tag{B.37}
$$

so that the submatrices $\mathbf{A}$ and $\mathbf{D}$ are square matrices. The inverse is given by

$$
\begin{pmatrix} \mathbf{A} & \mathbf{B} \\ \mathbf{C} & \mathbf{D} \end{pmatrix}^{-1} = \begin{pmatrix} \mathbf{A}^{-1}(\mathbb{1} + \mathbf{B}\mathbf{E}^{-1}\mathbf{C}\mathbf{A}^{-1}) & -\mathbf{A}^{-1}\mathbf{B}\mathbf{E}^{-1} \\ -\mathbf{E}^{-1}\mathbf{C}\mathbf{A}^{-1} & \mathbf{E}^{-1} \end{pmatrix} \text{ with } \mathbf{E} := \mathbf{D} - \mathbf{C}\mathbf{A}^{-1}\mathbf{B}
\tag{B.38}
$$

as is easily checked by direct matrix multiplication. Next, we transform $\mathbf{A}$ into diagonal form $\tilde{\mathbf{A}}$, e.g., $\mathbf{A} = \mathbf{V}\tilde{\mathbf{A}}\mathbf{V}^{-1}$. This makes the calculation of the inverse $\tilde{\mathbf{A}}^{-1}$ trivial and we get:

$$
\begin{pmatrix} \mathbf{A} & \mathbf{B} \\ \mathbf{C} & \mathbf{D} \end{pmatrix}^{-1} = \begin{pmatrix} \mathbf{V}\tilde{\mathbf{A}}^{-1}(\mathbb{1} + \tilde{\mathbf{B}}\mathbf{E}^{-1}\tilde{\mathbf{C}}\tilde{\mathbf{A}}^{-1})\mathbf{V}^{-1} & -\mathbf{V}\tilde{\mathbf{A}}^{-1}\tilde{\mathbf{B}}\mathbf{E}^{-1} \\ -\mathbf{E}^{-1}\tilde{\mathbf{C}}\tilde{\mathbf{A}}^{-1}\mathbf{V}^{-1} & \mathbf{E}^{-1} \end{pmatrix} \text{ with } \mathbf{E} := \mathbf{D} - \tilde{\mathbf{C}}\tilde{\mathbf{A}}^{-1}\tilde{\mathbf{B}}
\tag{B.39}
$$

---

[5]The direct textbook matrix multiplication algorithm indeed scales cubically. But there exist more complicated algorithms with complexity below cubic but, of course, still above quadratic, like the Strassen algorithm with $\approx \mathcal{O}(N^{2.8})$[201]. In practise, implementations often still use a direct cubic scaling version of the matrix product since it is easier optimized to the hardware and wins for small to medium matrix sizes. For large matrix sizes, choosing more sophisticated algorithm is usually a trade-off between speed and accuracy since the faster algorithms are usually numerically less stable. For the sake of simplicity, we simply assume cubic scaling of the algorithms. However, the discussed tendency is still correct even for modified scalings.

using the abbreviations $\tilde{\mathbf{C}} := \mathbf{C}\mathbf{V}$ and $\tilde{\mathbf{B}} := \mathbf{V}^{-1}\mathbf{B}$.

Exploiting symmetries of $\mathbf{G}$: In general, the Hamiltonian $\mathbf{H}$ is Hermitian and the self-energies $\boldsymbol{\Sigma}$ are non-Hermitian. In most cases, we can restrict ourselves to a real symmetric Hamiltonian and complex symmetric self-energies. In that case, the Green's function $\mathbf{G}$ is also (complex) symmetric, $\tilde{\mathbf{B}}$ and $\tilde{\mathbf{C}}$ are related by transposition, the eigenvalue problem simplifies to a real symmetric one[6] which makes the transformation matrix $\mathbf{V}$ orthogonal, i.e., $\mathbf{V}^{-1} = \mathbf{V}^T$.

Basis change for non-local quantities: If we are only interested in non-local quantities like the transmission or the density of states, we can go a step further. Such quantities do not dependent on the spatial basis and we can transform the Green's function so that the Hamiltonian is diagonal in the subblock $\mathbf{A}$:

$$\mathbf{G} \to \mathbf{S}^{-1}\mathbf{G}\mathbf{S}, \qquad \mathbf{S} = \begin{pmatrix} \mathbf{V} & 0 \\ 0 & \mathbb{1}_{\mathrm{DD}} \end{pmatrix}. \qquad \text{(B.40)}$$

In practise, we indirectly perform this transformation by omitting the respective factors of $\mathbf{V}$ in Eq. (B.39). All in all, the inverse is given by:

$$\mathbf{G} = \begin{pmatrix} \tilde{\mathbf{A}}^{-1}(\mathbb{1} + \tilde{\mathbf{B}}\mathbf{E}^{-1}\tilde{\mathbf{B}}^T\tilde{\mathbf{A}}^{-1}) & -\tilde{\mathbf{A}}^{-1}\tilde{\mathbf{B}}\mathbf{E}^{-1} \\ \left[-\tilde{\mathbf{A}}^{-1}\tilde{\mathbf{B}}\mathbf{E}^{-1}\right]^T & \mathbf{E}^{-1} \end{pmatrix} \text{ with } \mathbf{E} := \mathbf{D} - \tilde{\mathbf{B}}^T\tilde{\mathbf{A}}^{-1}\tilde{\mathbf{B}} \qquad \text{(B.41)}$$

using the abbreviation $\tilde{\mathbf{B}} := \mathbf{V}^T\mathbf{B}$.

Optimization traits: In Eq. (B.41), no matrix operations for matrices of size of $\mathbf{H}_{\mathrm{AA}}$ appear (except for the initial eigenvalue problem): the inverse $\tilde{\mathbf{A}}^{-1}$ is trivial since $\tilde{\mathbf{A}}$ is diagonal. Therefore, this optimization is extremely useful for large systems where the coupling regions to the leads are only a small part of the overall system, i.e., $N_{\mathrm{A}} \gg N_{\mathrm{D}}$ with $N_{\mathrm{A/D}}$ denoting the size of the square matrices $\mathbf{A}, \mathbf{D}$, respectively.

For a short complexity analysis, we assume that multiplication and eigenvalue problem of $N \times N$-matrices have computational complexity $\mathcal{O}(N^3)$. Then, the naive direct matrix inversion used to calculate the Green's function has complexity $\mathcal{O}((N_{\mathrm{A}}+N_{\mathrm{D}})^3) \overset{N_{\mathrm{A}} \gg N_{\mathrm{D}}}{\to} \mathcal{O}(N_{\mathrm{A}}^3)$.

In the above optimization, the complexity of the preparation process containing the eigenvalue problem and

the calculation of $\tilde{\mathbf{B}}$ is $\mathcal{O}(N_{\mathrm{A}}^3 + N_{\mathrm{A}}^2 N_{\mathrm{D}}) \overset{N_{\mathrm{A}} \gg N_{\mathrm{D}}}{\to} \mathcal{O}(N_{\mathrm{A}}^3)$. All the following inversions using Eq. (B.41) only are of complexity $\mathcal{O}(N_{\mathrm{D}}^3 + N_{\mathrm{A}}N_{\mathrm{D}}^2 + N_{\mathrm{A}}) \overset{N_{\mathrm{A}} \gg N_{\mathrm{D}}}{\to} \mathcal{O}(N_{\mathrm{A}}N_{\mathrm{D}}^2)$. The summands stand for inversion of $\mathbf{E}$, products of $N_{\mathrm{A}} \times N_{\mathrm{D}}$-matrices with $N_{\mathrm{D}} \times N_{\mathrm{D}}$-matrices like $\tilde{\mathbf{B}}\mathbf{E}^{-1}$ and inversion of $\tilde{\mathbf{A}}$, respectively.

Strictly speaking, the optimization still scales cubically in N_{A} due to the initially eigenvalue problem. Nevertheless, for energy sweeps over the density of states or the transmission, the complexity of each inversion step dominates and whose effort could be reduced to complexity $\mathcal{O}(N_{\mathrm{A}}N_{\mathrm{D}}^2)$ for large systems, cf. Fig. B.2a[7]

As stated above, the optimization only applies for non-local quantities. For local quantities like current densities, the transformation matrices $\mathbf{V}$ cannot be omitted from Eq. (B.39) and we are back to cubic complexity.

---

[6]For real symmetric eigenvalue problems, implementations such as ScaLAPACK[199] or ELPA[133] exist that parallelize over many computational nodes. To the best of my knowledge, no efficient and numerically stable parallelized implementation exists for the general eigenvalue problem.

[7]For the AGNRs used for Fig. B.2a, the central part scales linearly, $N_{\mathrm{A}} \in \mathcal{O}(N)$, but the contact regions scale with the square root, $N_{\mathrm{D}} \in \mathcal{O}(\sqrt{N})$ because they only grow transverse to the transport direction but not in transport direction. This gives the observed overall complexity $\mathcal{O}(N^2 = N_{\mathrm{A}}N_{\mathrm{D}}^2)$.

B.5 Additional convergence tests for the transmission and current density

B.5.1 Transmission coefficient in pristine AGNR5

To test the damping model (see Sec. 2.1.3) and the extraction procedure (e.g. in Fig. 2.5b), we compare the transmission as calculated with different parametrizations of the damping rate $\eta(\mathbf{r})$ with the (numerically) exact result (derived from a band-structure calculation). Our test systems are pristine armchair nanoribbons with width of five carbon atoms (AGNR5). To this end, we define the root mean square deviation $\Delta\mathcal{T}_{\mathrm{rms}}$:

$$\Delta\mathcal{T}_{\mathrm{rms}} = \sqrt{\frac{1}{\Delta E} \int_{E_1}^{E_2} \left[\Delta\mathcal{T}(E)\right]^2 \mathrm{d}E} \ , \qquad (B.42)$$

$$\Delta E = E_2 - E_1 \qquad E_{1/2} = \varepsilon_{\mathrm{F}} \mp 3\,\mathrm{eV} \ . \qquad (B.43)$$

The integral is evaluated on an energy grid with spacing $\Delta = 0.1\,\mathrm{eV}$; $\Delta\mathcal{T}(E)$ denotes the difference of the calculated transmission and the number of bands in the bandstructure in the interval $(E-\Delta, E+\Delta)$, formally

$$\Delta\mathcal{T}(E) = \min_{\tilde{E}\in(E-\Delta,E+\Delta)} |\mathcal{T}_{\mathrm{calc}}(E) - N_{\mathrm{bands}}(\tilde{E})| \ ,$$
$$(B.44)$$

where $N_{\mathrm{bands}}(\tilde{E})$ is the number of bands at energy $\tilde{E}$. Tab. B.3 lists the deviations of the transmission func-

tions for the pristine AGNR5 (see Sec. 2.2.2) for different parametrizations of the damping rate $\eta(\mathbf{r})$, see Eq. (2.24).

We have therefore checked that when the leakage rate is sufficiently large ($\eta_0 \approx 0.1 - 1\,\mathrm{Ha}$) and is smoothly reduced to zero near the device region ($\kappa L \approx 8 - 64$), exact results (in this case a step-like transmission function) can be recovered as long as the leads are long enough ($M \approx 50 - 200$). As a rule of thumb, the length of the total system should exceed its width at least by a factor of $L/W \approx 10 - 25$.

If these conditions are mistreated, more drastic effects arise, such as standing waves reflecting from the lead boundaries. For illustration, Fig. B.5 focuses on these effects induced by poorly chosen damping models. Finite values of η at the device-to-lead interface cause back-reflection of waves. The latter happens for a step-function parametrization as well as for too large damping at the interface ($\kappa L \leq 4$).

number of unit cells		damping model		
M	$\Delta\mathcal{T}_{\mathrm{rms}}$	model		$\Delta\mathcal{T}_{\mathrm{rms}}$
1	$3.7 \cdot 10^{-1}$	$\eta_0 = 0.1\,\mathrm{Ha}$		$6.6 \cdot 10^{-3}$
5	$1.2 \cdot 10^{-1}$	$\eta_0 = 0.5\,\mathrm{Ha}$	$\kappa L = 16$	$2.3 \cdot 10^{-3}$
10	$2.7 \cdot 10^{-2}$	$\boldsymbol{\eta_0 = 1.0\,\mathrm{Ha}}$		$\boldsymbol{6.6 \cdot 10^{-4}}$
50	$6.9 \cdot 10^{-3}$		$\kappa L = 4$	$2.6 \cdot 10^{-1}$
100	$8.3 \cdot 10^{-3}$		$\kappa L = 8$	$2.6 \cdot 10^{-3}$
200	$\boldsymbol{6.6 \cdot 10^{-4}}$	$\eta_0 = 1.0\,\mathrm{Ha}$	$\boldsymbol{\kappa L = 16}$	$\boldsymbol{6.6 \cdot 10^{-4}}$
			$\kappa L = 32$	$7.8 \cdot 10^{-3}$
			$\kappa L = 64$	$1.8 \cdot 10^{-3}$
		$\eta_{\mathrm{step},0} = 0.1\,\mathrm{Ha}$	$\eta_{\mathrm{step}}(x)$	$5.4 \cdot 10^{-1}$
		$\eta_{\mathrm{step},0} = 1.0\,\mathrm{Ha}$		$6.6 \cdot 10^{-1}$

Table B.3: Variation of the calculated transmission coefficients (measured with respect to conducting bands, cf. Fig. 2.6a) with different parametrizations of the damping rate $\eta(\mathbf{r})$, see Eq. (2.24). The default values taken in our production runs are listed in underlined bold. Entries leading to acceptable results are marked in green, unacceptable ones are marked in red. Left: Variation with the number of blocks M used in each lead. Right: Variation with damping rate $\eta(\mathbf{r})$. Different values for the parameters η_0 (top) and κ (center) of the damping rate from Eq. (2.25) are tested, as well as a step-function parametrization $\eta_{\mathrm{step}}(d) = \eta_{\mathrm{step},0} \cdot \Theta(d)$ (bottom).
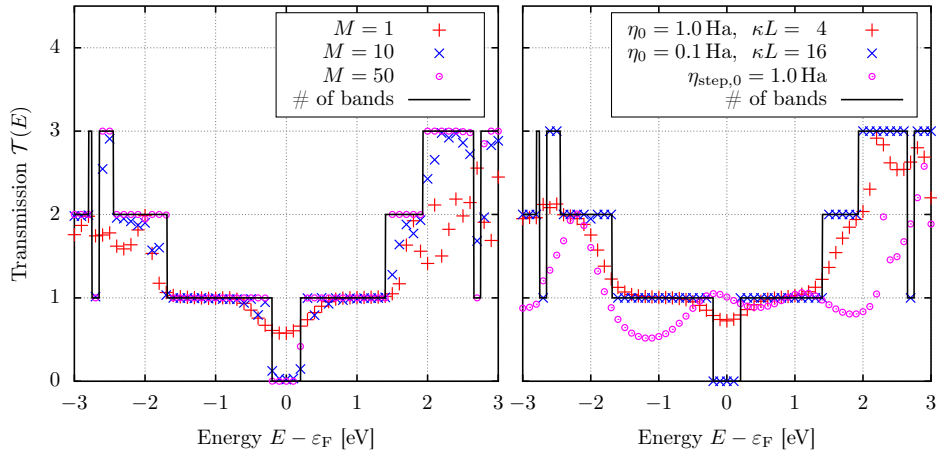
Figure B.5: Transmission $\mathcal{T}$ of a pristine AGNR5 for several damping models including non-converged ones for illustration. The exact value, the number of bands from a bandstructure calculation, is plotted as solid line. Left: The length of the leads (number of building blocks M) is varied (the remaining parameters are the default values: $\eta_0 = 1\,\mathrm{Ha}$, $\kappa L = 16$). For too short leads ($M \leq 10$), the steps in the transmission function are not fully developed, yet. Right: The length of the leads is fixed ($M = 200$), but the parametrization of the leakage rate $\eta(\mathbf{r}_i)$ is varied, i.e., to a step function (constant at $\eta_{\mathrm{step},0}$ in the leads but zero in the device region; magenta circle markers) which shows standing wave patterns due to reflection at the interface.

B.5.2 Local current densities in pristine AGNR5

This section contains additional convergence tests for local currents in pristine AGNR5. They turn out very similar to the discussion offered in Sec. 2.3.2 for the AGNR5 with a single nitrogen substituent.

In Figs. B.6 and B.7, the dependence of the current density in pristine AGNR5 on the basis set size is shown.

As in the case with a nitrogen scatterer (cf. Sec. 2.3.2), the divergence decreases rapidly for increasing basis set size (tier1 → tier2 → tier3; SVP → TZVP → TZVPP).

Again, the current density $\mathbf{j}(\mathbf{r})$ as well as its divergence and its integral over a yz-plane converged in the limit of large basis sets (cf. Fig. B.8a and Fig. B.8b).

Artificial current sources and sinks in the contact region

When coupling to the leads, the current density artificially appears and disappears; as seen in Fig. B.9 in terms of the divergence pattern $\boldsymbol{\nabla} \cdot \mathbf{j}(\mathbf{r}, E)$ in the left contact region. The self-energy $\boldsymbol{\Sigma}_{\mathrm{L}}$ effectively behaves as a current source with a spatial structure which becomes more complicated for large basis sets. Therefore, the calculated current density represents the physical current density only in regions away from the contact

region, i.e., in the center of the device region, but not in the model electrodes. The effect of the self-energy can even spread a little further into the device region since the basis function have a finite extension. Thus, in our convergence tests, we only compared the current density in a smaller region (dashed orange box in Fig. 2.7), which is one additional carbon ring away from the contact region.

(a) $|\mathbf{j}_{xy}(\mathbf{r}, E)|$ – FHI-AIMS `tier1` (b) $|\mathbf{j}_{xy}(\mathbf{r}, E)|$ – FHI-AIMS `tier2` (c) $|\mathbf{j}_{xy}(\mathbf{r}, E)|$ – FHI-AIMS `tier3`

(d) $\boldsymbol{\nabla} \cdot \mathbf{j}(\mathbf{r}, E)$ – FHI-AIMS `tier1` (e) $\boldsymbol{\nabla} \cdot \mathbf{j}(\mathbf{r}, E)$ – FHI-AIMS `tier2` (f) $\boldsymbol{\nabla} \cdot \mathbf{j}(\mathbf{r}, E)$ – FHI-AIMS `tier3`
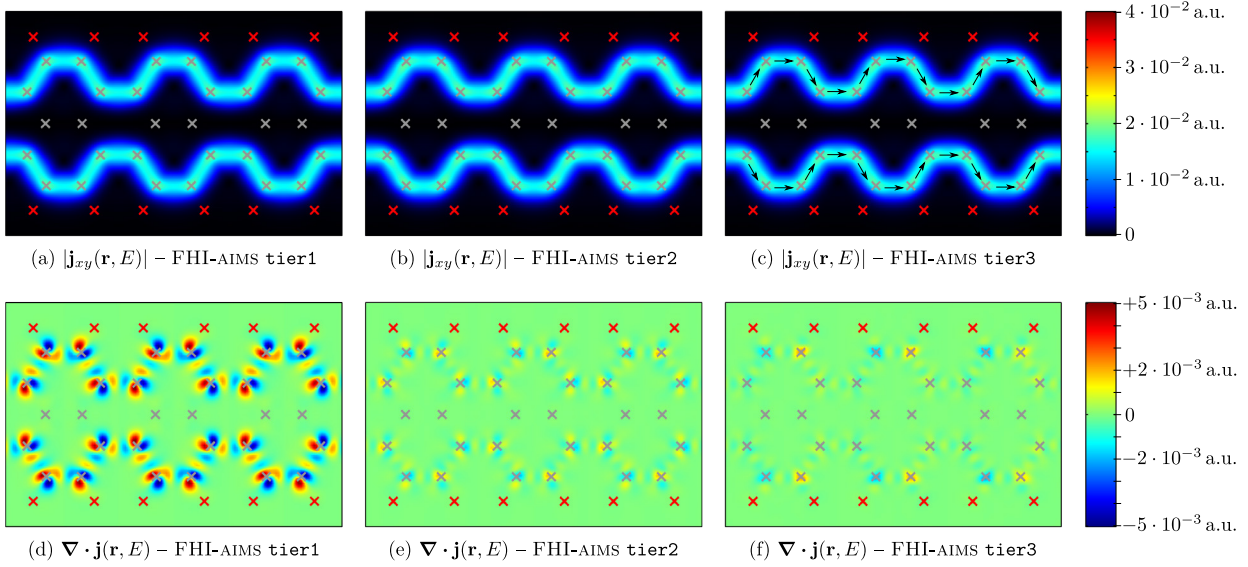
Figure B.6: (a)-(c): Variation of the in-plane current density $\mathbf{j}_{xy}(\mathbf{r}, E)$ with increasing size of the basis set for a pristine AGNR5 at a plane $z = 0.4\,\text{Å}$ above the carbon atoms at perfect transmission, $\mathcal{T}(E) = 1$ (Energy: $E = \varepsilon_\mathrm{F} + 1\,\text{eV}$). The current direction is indicated by black arrows for the largest basis set. (d)-(f): The divergence $\boldsymbol{\nabla} \cdot \mathbf{j}(\mathbf{r}, E)$ belonging to the respective current pattern in (a)-(c). The divergence converges very rapidly with increasing size of the basis set. Divergence errors have a very small impact on the current pattern. All plots were calculated using FHI-AIMS.

(a) $|\mathbf{j}_{xy}(\mathbf{r}, E)|$ – TURBOMOLE SVP (b) $|\mathbf{j}_{xy}(\mathbf{r}, E)|$ – TURBOMOLE TZVP (c) $|\mathbf{j}_{xy}(\mathbf{r}, E)|$ – TURBOMOLE TZVPP

(d) $\boldsymbol{\nabla} \cdot \mathbf{j}(\mathbf{r}, E)$ – TURBOMOLE SVP (e) $\boldsymbol{\nabla} \cdot \mathbf{j}(\mathbf{r}, E)$ – TURBOMOLE TZVP (f) $\boldsymbol{\nabla} \cdot \mathbf{j}(\mathbf{r}, E)$ – TURBOMOLE TZVPP
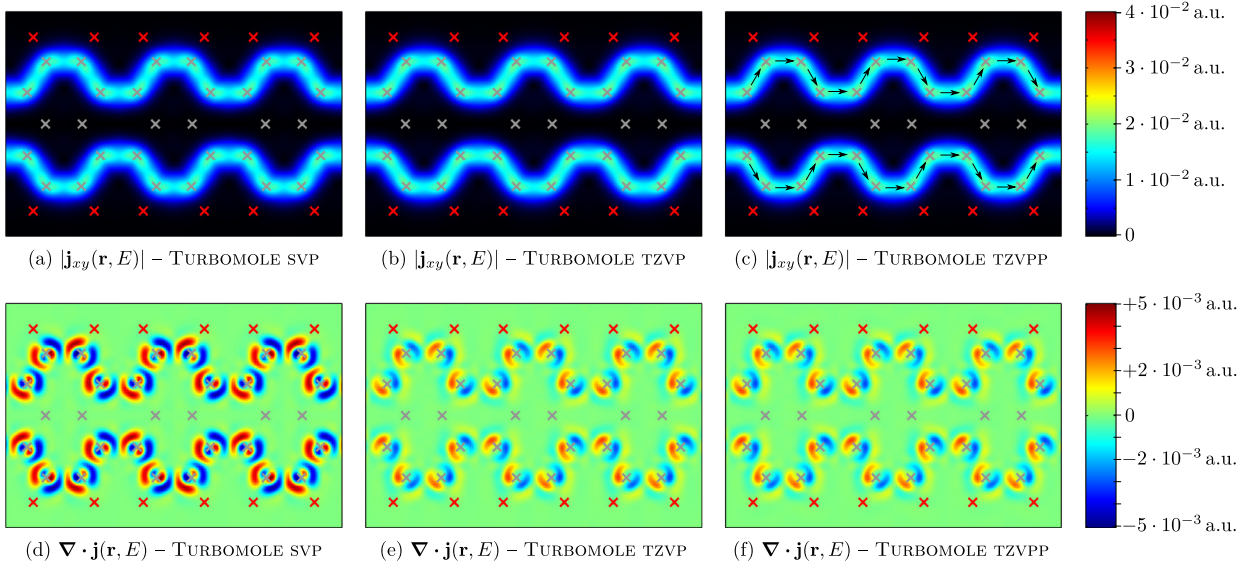
Figure B.7: Analog to Fig. B.6 but calculated using TURBOMOLE.

(a)　　　　　　　　**(b)**
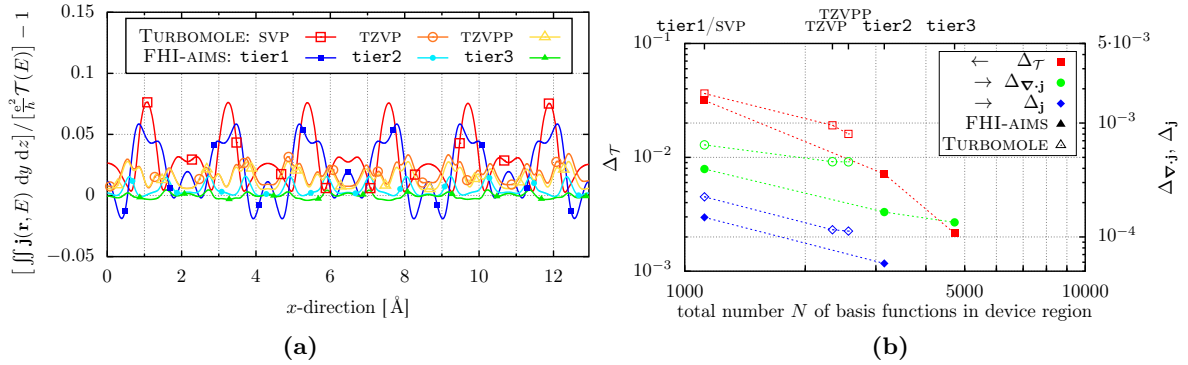
Figure B.8: (a): Relative deviation between the local current density (as plotted in Fig. B.6 and B.7) integrated over a yz-plane and the total current given by the transmission function. For clarity, only the markers of every 12th sampling point are shown. (b): Convergence analyses of the local currents shown in Fig. B.6 and B.7 with respect to the basis set using FHI-AIMS (closed markers) and TURBOMOLE (open markers). The root mean square deviations Δ_X are plotted over the number of basis functions per carbon atom ($\Delta_{\mathcal{T}}$ on left y-axis; $\Delta_{\mathbf{j}}$ and $\Delta_{\nabla \cdot \mathbf{j}}$ on right y-axis). All error measures decrease when increasing the basis set size. The different basis sets contain different number of basis functions per hydrogen/carbon/nitrogen atom: `tier1`/SVP: 5/14/14; TZVP: 6/31/31; TZVPP: 14/31/31; `tier2`: 15/39/39: `tier3`: 31/55/55.

(a) $\nabla \cdot \mathbf{j}(\mathbf{r}, E)$ − FHI-AIMS `tier1`　(b) $\nabla \cdot \mathbf{j}(\mathbf{r}, E)$ − FHI-AIMS `tier2`　(c) $\nabla \cdot \mathbf{j}(\mathbf{r}, E)$ − FHI-AIMS `tier3`
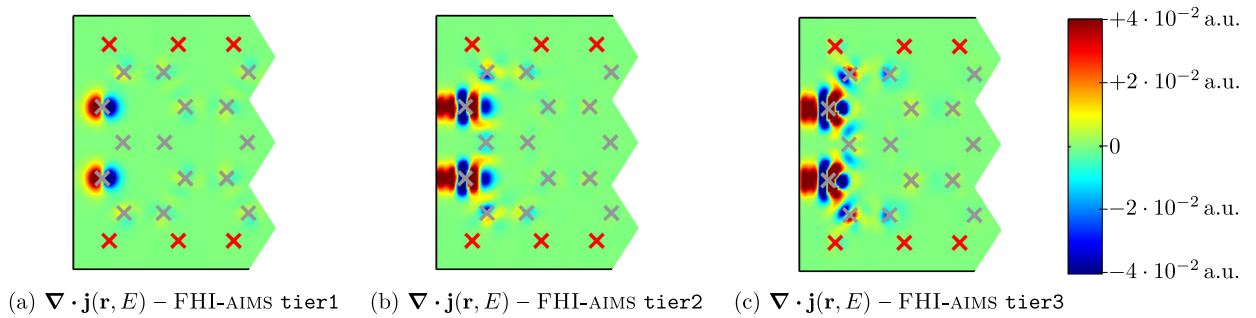
Figure B.9: The current divergence $\nabla \cdot \mathbf{j}(\mathbf{r}, E)$ in the left contact region (coupled to the left lead) for a pristine AGNR5 at a plane $z = 0.4\,\text{Å}$ above the carbon atoms. The self-energy $\mathbf{\Sigma}_\mathrm{L}$ effectively behaves as a current source with a spatial structure which becomes more complicated for large basis sets. Please note the different scale which is larger by about one order of magnitude than all the other divergence plots in this thesis.

B.5.3 Local current densities in AGNR5 with a single nitrogen substituent

In the main part, we have shown a basis set comparison of the current density in AGNR5 with a single nitrogen substituent in Fig. 2.9. Here, plots with additional basis sets are shown in Figs. B.11 and B.12 for completeness.

B.5.4 Local current density in hydrogenated AGNR41 (20% hydrogen adsorbates)

Fig. B.10 shows the basis set dependence of the current density at an energy point, where the transmission itself is not yet fully converged, but small energy shifts are noticeable in the transmission peaks (cf. blue arrow in Fig. 2.14). In this situation, the current density still exhibit a dependence on the basis set size. The main qualitative feature remain: current vortices are still present and stable. Also quantitative features are sustained; the overall scale is the same and the current still exhibits the mesoscopic fluctuations in the same order of magnitude exceeding the average current by two orders of magnitude, cf. the logarithmic color scale. Hence, we are unable to predict the concrete current path at a certain energy point. We can still make senseful predictions about statistic properties of the current densities (such as magnitude of the fluctuations or their mean value), even though the transmission function is not yet converged with respect to the basis set size.
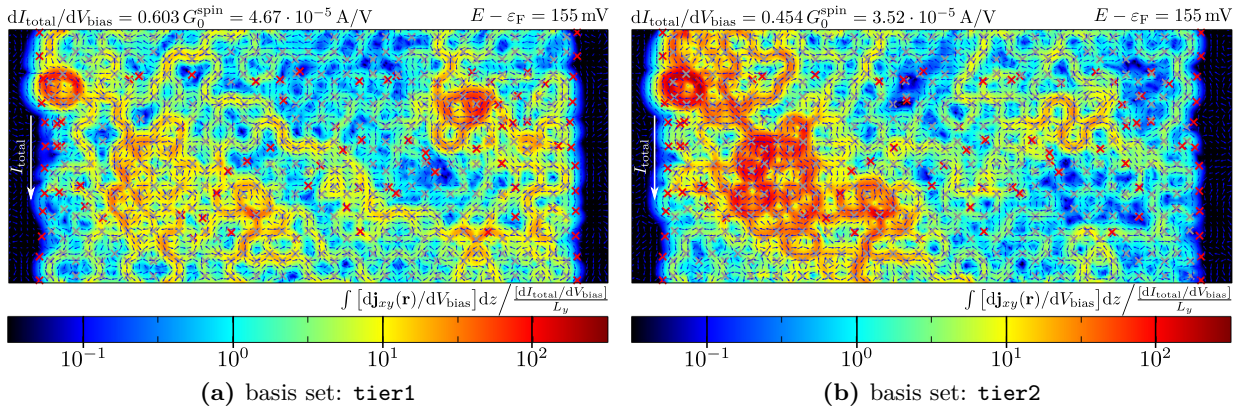
Figure B.10: Basis set comparison of the local current density response (integrated over the out-of-plane direction) in the AGNR41 of Fig. 2.12 at energy $E=\varepsilon_F+155\,\text{meV}$ (blue arrow in Fig. 2.14). The current density is plotted relative to average current density I/L_y, with width $L_y = 5.19\,\text{nm}$. Plot shows current amplitude (color), current direction (arrows), carbon atoms (gray crosses) and hydrogen atoms (red crosses).

(a) $|\mathbf{j}_{xy}(\mathbf{r}, E)|$ – FHI-AIMS tier1

(b) $|\mathbf{j}_{xy}(\mathbf{r}, E)|$ – FHI-AIMS tier2

(c) $|\mathbf{j}_{xy}(\mathbf{r}, E)|$ – FHI-AIMS tier3

(d) $\boldsymbol{\nabla} \cdot \mathbf{j}(\mathbf{r}, E)$ – FHI-AIMS tier1

(e) $\boldsymbol{\nabla} \cdot \mathbf{j}(\mathbf{r}, E)$ – FHI-AIMS tier2

(f) $\boldsymbol{\nabla} \cdot \mathbf{j}(\mathbf{r}, E)$ – FHI-AIMS tier3
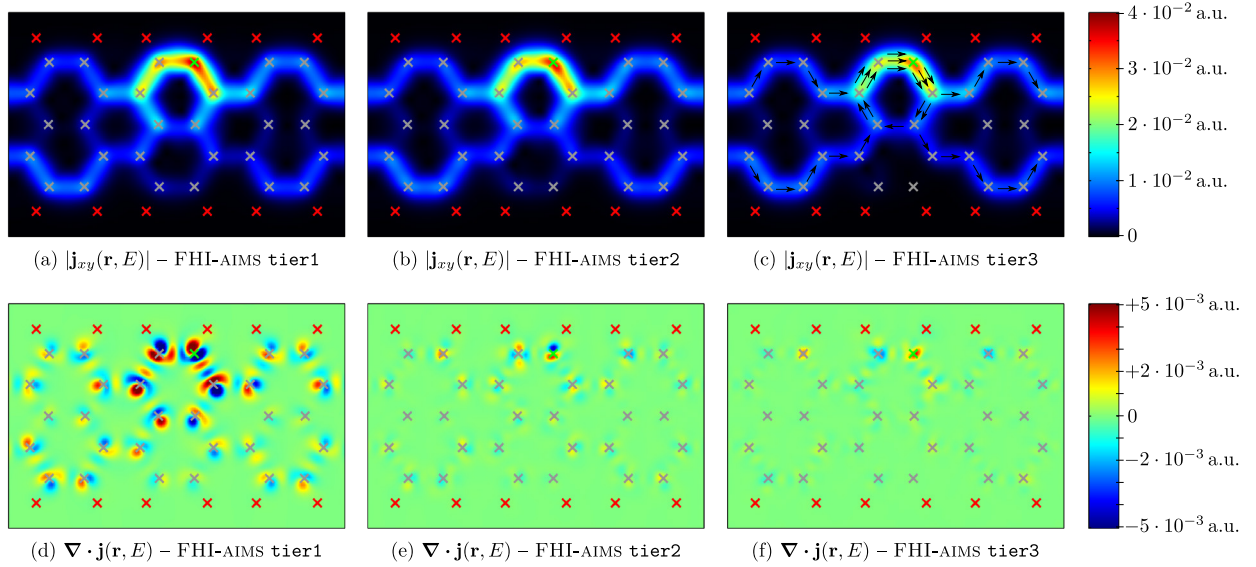
Figure B.11: (a)-(c): Variation of the in-plane current density $\mathbf{j}_{xy}(\mathbf{r}, E)$ with increasing size of the basis set for an AGNR5 with one nitrogen substituent (green cross) at a plane $z = 0.4\,\text{Å}$ above the carbon atoms restricted in x-direction to the central region near the nitrogen impurity (dash orange box in Fig. 2.7). The current density carries half a conductance quantum, $\mathcal{T}(E) = 0.5$, in all cases; the energy E is varied such that all plots share the same transmission value, see colored arrows in Fig. 2.8 for exact position. The current direction is indicated by black arrows for the largest basis set. (d)-(f): The divergence $\boldsymbol{\nabla} \cdot \mathbf{j}(\mathbf{r}, E)$ belonging to the respective current pattern in (a)-(c). The divergence converges very rapidly with increasing size of the basis set. Divergence errors have a very small impact on the current pattern. All plots were calculated using FHI-AIMS.

(a) $|\mathbf{j}_{xy}(\mathbf{r}, E)|$ – TURBOMOLE svp

(b) $|\mathbf{j}_{xy}(\mathbf{r}, E)|$ – TURBOMOLE tzvp

(c) $|\mathbf{j}_{xy}(\mathbf{r}, E)|$ – TURBOMOLE tzvpp

(d) $\boldsymbol{\nabla} \cdot \mathbf{j}(\mathbf{r}, E)$ – TURBOMOLE svp

(e) $\boldsymbol{\nabla} \cdot \mathbf{j}(\mathbf{r}, E)$ – TURBOMOLE tzvp

(f) $\boldsymbol{\nabla} \cdot \mathbf{j}(\mathbf{r}, E)$ – TURBOMOLE tzvpp
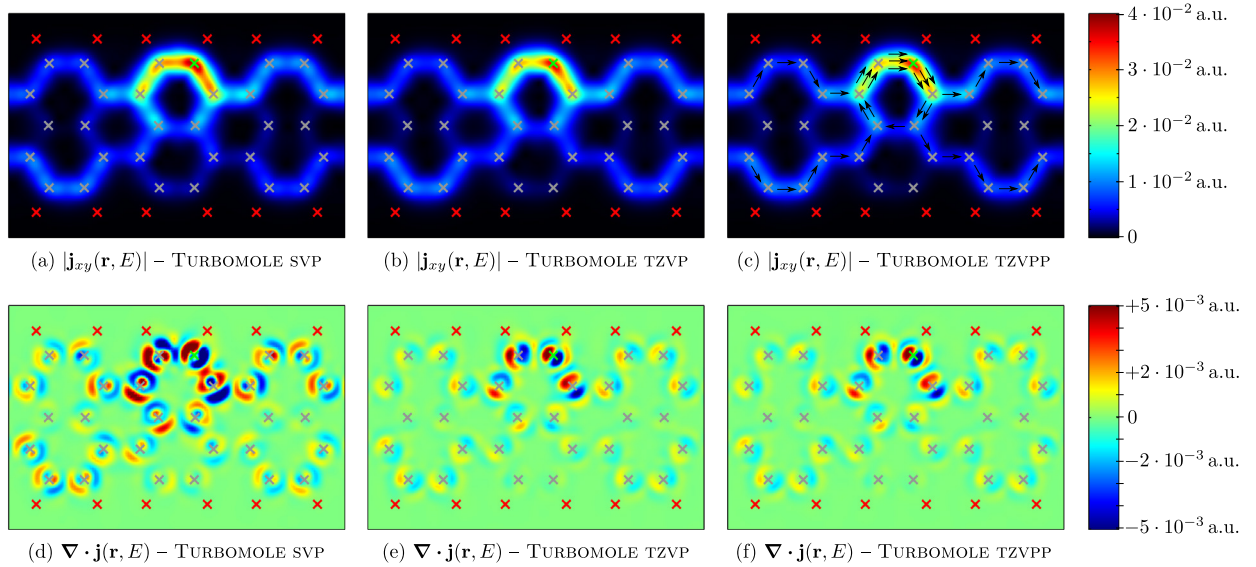
Figure B.12: Analog to Fig. B.11 but calculated using TURBOMOLE.

C

Application I: Narrow armchair graphene nanoribbons

This appendix contains additional material that complements Chap. 3, e.g., additional material on the behavior of streamlines in the bulk limit (Appx. C.1) as well as additional plots for ring currents near antiresonances for AGNR5 with a single nitrogen substituent (Appx. C.2). Next, a continuity equation for "bond currents" is derived from a general TB Hamiltonian (Appx. C.3). The scattering phase of a simple linear TB chain with an on-site potential is derived in Appx. C.4. Finally, the appendix closes with symmetry consideration preventing the emergence of ring currents (Appx. C.5).

C.1 Bulk limit investigations for current patterns in pristine ribbons

C.1.1 Energy window for observation of streamlines

In Tab. C.1, we check the estimate

$$\Delta E_{\mathcal{T}=1} \approx \frac{25\,\text{eV}}{N_{\text{C}}} \qquad \text{for } N_{\text{C}} \gg 1 \qquad \text{(C.1)}$$

used in the Sec. 3.1.3 to estimate the energy range in which streamlines exist. The energy range $\Delta E_{\mathcal{T}=1}$ is defined as the energy range with $\mathcal{T}(E) = 1$ and we expect a $1/N_{\text{C}}$ behavior for the energy interval $\mathcal{T}(E) = 1$ since the (discrete) transverse wavevectors $k_{y,m}$ scale with $1/N_{\text{C}}$. Thus, the product $\Delta E_{\mathcal{T}=1} \cdot N_{\text{C}}$ (last table column) should be constant for $N_{\text{C}} \gg 1$. As mentioned in the main text, the streamline patterns in the current density in AGNRs($3m-1$) only appear at energies E with a single fully transparent channel. For higher/lower energies, with two or more current channels, the patterns are more complicated.

One should not attach to much importance to the exact numerical values since they are strongly functional/method dependent. For example, for AGNR14, we report two different values which were calculated by using different (but very similar) functionals using different DFT codes.

C.1.2 Streamline patterns in the bulk limit

In Sec. 3.1.3, we stressed that we see no indication that the streamline pattern vanishes for wide ribbons. In Fig. C.1, a cut at constant x and z through the streamlines in AGNR5/8/11/14/17 is shown. The current density is scaled by the number m of streamlines. That way, the curves coincide. We conclude that, the streamlines remain for wide AGNR($3m-1$); only the weight is distributed over all m streamlines. Please note that the small negative values for j_x occurring in Fig. C.1 indicate small current eddies with backflow.

$N_C = 3m-1$	m	$\Delta E_{\mathcal{T}=1}$	$\Delta E_{\mathcal{T}=1} \cdot N_C$
5^a	2	2.63 eV	13.2 eV
8^a	3	2.20 eV	17.6 eV
11^a	4	1.75 eV	19.3 eV
14^a	5	1.48 eV	20.7 eV
14^b	5	1.42 eV	19.8 eV
17^a	6	1.20 eV	20.4 eV
20^b	7	1.06 eV	21.2 eV
29^b	10	0.778 eV	22.6 eV
41^b	14	0.585 eV	24.0 eV
59^b	20	0.426 eV	25.1 eV
83^b	28	0.304 eV	25.3 eV

[a] TURBOMOLE, SVP basis set, B-P86-functional
[b] FHI-AIMS, `tier1` basis set, PBE-functional
both closed-shell

Table C.1: Testing the dependence of $\Delta E_{\mathcal{T}=1}$ on N_C for $N_C = (3m-1)$. $\Delta E_{\mathcal{T}=1}$ is defined as the energy range when only one band in an AGNRN_C is present and therefore perfect streamline patterns are expected. My thanks to J. Wilhelm who performed the numerical calculations for the cases labeled with [a][140].
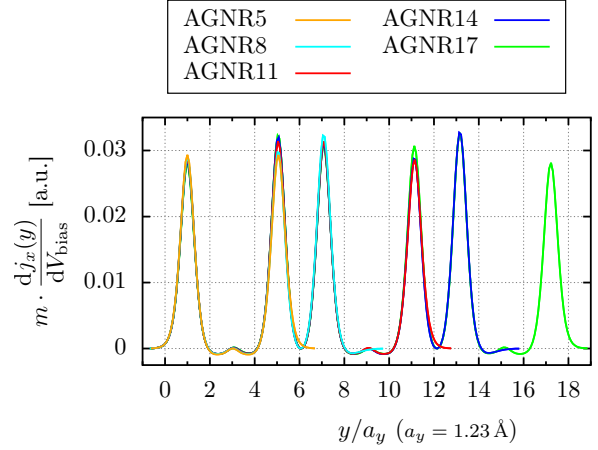
Figure C.1: A xz-cut through the current density response scaled by the number of streamlines m for different pristine AGNRs($3m-1$). The x-component j_x is shown at $\mathcal{T} = 1$, at $z = 0.5$Å, and $x = x_1$, see Fig. 3.1a. Each AGNR($3m-1$) shows m peaks. The origin of the y-axis is chosen so that $y/a_y = 1$ coincides with the first peak. My thanks to J. Wilhelm who performed the numerical calculations[140].
[DFT details: TURBOMOLE, basis set SVP, closed-shell]
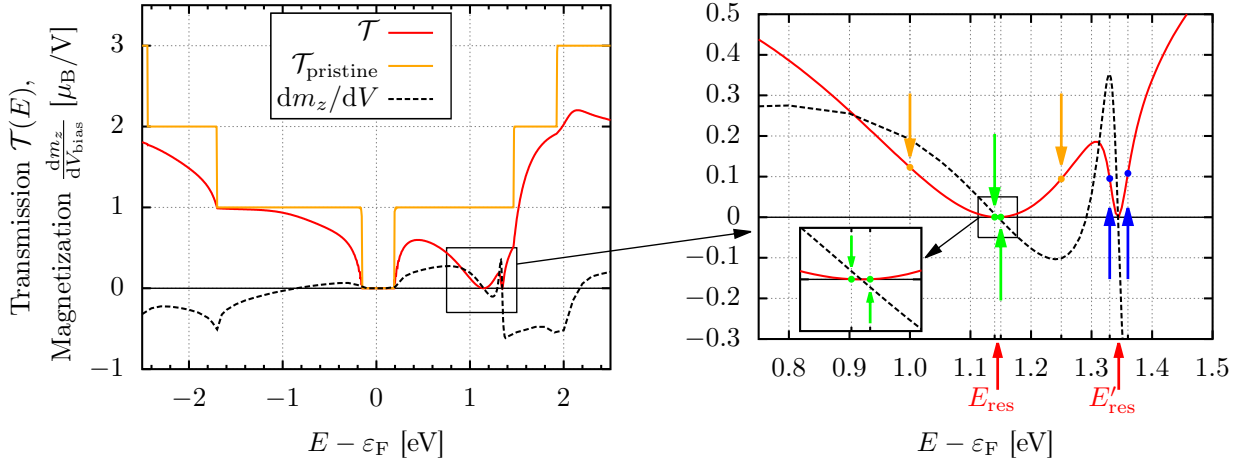
Figure C.2: Transmission function (solid red) and magnetization per bias dm_z/dV_{bias} (perpendicular to the graphene plane, dashed black) for the AGNR5 with nitrogen at position 3. The plot is identical to Fig. 3.10, except that additional energies are marked by colored arrows. The orange arrows mark the energy for the current response already plotted in Figs. 3.8c and 3.8d, respectively. The green arrows refer to the current response in Figs. C.3a and C.3b. The blue arrows refer to the Figs. C.3c and C.3d.
[DFT details: FHI-AIMS, basis set `tier1`, closed-shell]

C.2 Additional ring current investigations for ribbons with a single nitrogen

In this section, we list additional current density responses at selected energy points to further support our analyses of ring currents near antiresonances as discussed in Sec. 3.2.2. The selected energy points are labeled by colored arrows in the magnifications of Fig. C.2. The energy points always appear in pairs, one below and one above an antiresonance.

The current densities for the orange marked energy points are already shown in the main text, in Fig. 3.8c and Fig. 3.8d.

The green marked energy points refer to the ring currents shown in Fig. C.3a and Fig. C.3b. These energies

are very close to the antiresonance and the ring currents exceed the remaining average through current by a factor of 1000. The latter is therefore not visible in the current density plots anymore and we see a perfect reversal of the ring current pattern. The slightly different scale is due to slightly different transmission values, i.e., the chosen energy points are not exactly symmetric to the antiresonance.

The remaining two ring current patterns, Fig. C.3c and Fig. C.3d (blue marked energies in Fig. C.2), deal with a second (sharper) antiresonance at E'_{res}. Again, we see a reversal of the rotation sense. Thus, we conclude that these direction changes are a generic feature.

(a) nitrogen at pos. 3, $E-\varepsilon_{\mathrm{F}} = 1.14\,\mathrm{eV}$, $E < E_{\mathrm{res}}$

(b) nitrogen at pos. 3, $E-\varepsilon_{\mathrm{F}} = 1.15\,\mathrm{eV}$, $E > E_{\mathrm{res}}$

(c) nitrogen at pos. 3, $E-\varepsilon_{\mathrm{F}} = 1.33\,\mathrm{eV}$, $E < E'_{\mathrm{res}}$

(d) nitrogen at pos. 3, $E-\varepsilon_{\mathrm{F}} = 1.36\,\mathrm{eV}$, $E > E'_{\mathrm{res}}$

Figure C.3: (a–b) Local current density response (integrated over the out-of-plane direction) normalized to the average through current of AGNR5 with a single nitrogen substituent (green cross). The plots are for slightly different energy points (see green arrows in Fig. C.2), (a) below and (b) above the antiresonance E_{res}. (c–d) Equivalent to (a–b) but for energy below and above the second (sharper) antiresonance E'_{res} (see blue arrows in Fig. C.2). [DFT details: FHI-AIMS, basis set `tier1`, closed-shell]

C.3 Bond currents in tight-binding models: derivation of the continuity equation in a tight-binding model

In this section, we derive a continuity equation for tight-binding (TB) models. On that basis, we define "bond currents", current contributions which flow from one TB site to another, and which obey this TB continuity equation.

First, let us assume that the system is described by an effective single particle Hamiltonian

$$\hat{\mathcal{H}} = \sum_{i,j} h_{ij}\, c_i^\dagger c_j\,, \qquad (C.2)$$

with a general matrix h_{ij}. We do not (yet) impose any conditions to h_{ij}; not even hermiticity. The fermionic operators c_i comply with the usual anti-commutation relations

$$\left\{ c_i^\dagger, c_j \right\} = \delta_{ij} \qquad \text{and} \qquad \left\{ c_i, c_j \right\} = 0\,. \qquad (C.3)$$

The time-dependence of the one-particle wavefunction

$$|\psi\rangle = \sum_n \psi_n c_n^\dagger |0\rangle \qquad (C.4)$$

follows from the Schrödinger equation

$$\mathrm{i}\hbar\partial_t|\psi\rangle = \hat{\mathcal{H}}|\psi\rangle \qquad \text{and} \qquad -\mathrm{i}\hbar\partial_t\langle\psi| = \langle\psi|\hat{\mathcal{H}}^\dagger\,. \quad (C.5)$$

Next, we calculate the time-derivative of the density ρ_l of site l ($\rho_l := \langle c_l^\dagger c_l\rangle$):

$$\begin{aligned}
\partial_t\rho_l &= \partial_t\langle\psi|c_l^\dagger c_l|\psi\rangle \\
&= \left(\underbrace{\partial_t\langle\psi|}\right)c_l^\dagger c_l|\psi\rangle + \langle\psi|c_l^\dagger c_l\left(\underbrace{\partial_t|\psi\rangle}\right) \\
&\qquad \overset{(C.5)}{=} \tfrac{\mathrm{i}}{\hbar}\langle\psi|\hat{\mathcal{H}}^\dagger \qquad\qquad\quad \overset{(C.5)}{=} -\tfrac{\mathrm{i}}{\hbar}\hat{\mathcal{H}}|\psi\rangle \\
&\overset{(C.2)}{=} \frac{\mathrm{i}}{\hbar}\sum_{ij}\left(h_{ij}^*\langle\psi|c_j^\dagger c_i\,c_l^\dagger c_l|\psi\rangle - h_{ij}\langle\psi|c_l^\dagger c_l\,c_i^\dagger c_j|\psi\rangle\right) \\
&= \frac{2}{\hbar}\sum_{ij}\mathrm{Im}\left(h_{ij}\langle\psi|c_l^\dagger c_l\,c_i^\dagger c_j|\psi\rangle\right) \\
&\overset{(C.4)}{=} \frac{2}{\hbar}\sum_{ijnm}\mathrm{Im}\left(h_{ij}\underbrace{\langle 0|c_m c_l^\dagger c_l\,c_i^\dagger c_j c_n^\dagger|0\rangle}_{\delta_{ml}\,\delta_{li}\,\delta_{jn}}\psi_m^*\psi_n\right) \\
&= \frac{2}{\hbar}\sum_j\mathrm{Im}\,h_{lj}\psi_l^*\psi_j \overset{(C.7)}{=} \frac{2}{\hbar}\sum_j\mathrm{Im}\,h_{lj}\langle c_l^\dagger c_j\rangle \quad (C.6)
\end{aligned}$$

In the last line, we applied the identity

$$\begin{aligned}
\langle c_i^\dagger c_j\rangle &= \langle\psi|c_i^\dagger c_j|\psi\rangle \qquad\qquad\qquad\qquad (C.7) \\
&\overset{(C.4)}{=} \sum_{nm}\psi_m^*\psi_n\underbrace{\langle 0|c_m c_i^\dagger c_j c_n^\dagger|0\rangle}_{\delta_{mi}\,\delta_{jn}} = \psi_i^*\psi_j\,.
\end{aligned}$$

Now, we insert a Hamiltonian describing a pure nearest-neighbor TB model, i.e.,

$$h_{ij} = \begin{cases} -t_{ij} & \text{if } \langle i,j\rangle \quad (i \text{ and } j \text{ are nearest neighbors})\,, \\ 0 & \text{else}\,. \end{cases} \qquad (C.8)$$

That way, we arrive at a continuity equation

$$\partial_t\rho_l \overset{(C.6)}{=} -\frac{2}{\hbar}\sum_{\substack{i \\ \text{if }\langle l,i\rangle}}\mathrm{Im}\,t_{li}\langle c_l^\dagger c_i\rangle =: -\sum_{\substack{i \\ \text{if }\langle l,i\rangle}} j_{l\to i}\,. \quad (C.9)$$

Here, we used that a continuity equation of the form

$$\partial_t\rho_l = \text{"}-\mathrm{div}\,j_l\text{"} \qquad (C.10)$$

must hold, and we identify the sum of all currents $j_{l\to i}$ flowing away from site l as the divergence. That way, we can define the current $j_{l\to i}$ flowing from site l to site i (with site l and i being nearest neighbors) as:

$$\boxed{j_{l\to i} := \frac{2}{\hbar}\mathrm{Im}\,t_{li}\langle c_l^\dagger c_i\rangle} \qquad \text{if } \langle l,i\rangle\,. \qquad (C.11)$$

Source and sink terms

Adding an on-site energy term to the model, $\Delta h_{ij} = \delta_{ij}\,\varepsilon_i$, we get

$$\partial_t\rho_l + \sum_{\substack{i \\ \text{if }\langle l,i\rangle}} j_{l\to i} \overset{(C.6)}{=} \frac{2}{\hbar}\sum_j\mathrm{Im}\,\underbrace{\Delta h_{lj}\langle c_l^\dagger c_j\rangle}_{\mathrm{Im}\,\varepsilon_l\langle c_l^\dagger c_l\rangle = \mathrm{Im}(\varepsilon_l)\rho_l} \qquad (C.12)$$

as a correction to Eq. (C.9). By defining a source/sink-term

$$\sigma := \frac{2}{\hbar}\mathrm{Im}(\varepsilon_l)\rho_l\,, \qquad (C.13)$$

we can write the full continuity equation as

$$\partial_t\rho_l + \sum_{\substack{i \\ \text{if }\langle l,i\rangle}} j_{l\to i} = \sigma\,. \qquad (C.14)$$

Please note, that σ is only non-zero if we add an imaginary part to the on-site energy ε_l. Then, the Hamiltonian $\hat{\mathcal{H}}$ is no longer Hermitian because it includes damping terms. Such damping terms occur, for example, when including effects of leads via a self-energy.

Remark: Instead of $c_i^\dagger$ and c_j (used in multi-particle physics) one can also use $|i\rangle$ and $\langle j|$ (used in single-particle physics) directly. This basically means to use single particle states $|n\rangle = c_n^\dagger |0\rangle$ and to project the Hamiltonian to these single-particle states. Then Eq. (C.2) and Eq. (C.4) become

$$\hat{\mathcal{H}} = \sum_{i,j} h_{ij} \, |i\rangle\langle j| \qquad (\text{C.15})$$

and

$$|\psi\rangle = \sum_n \psi_n |n\rangle \,, \qquad (\text{C.16})$$

respectively. The resulting bond currents in this single particle formulation read

$$\boxed{j_{l\to i} := \frac{2}{\hbar} \, \mathrm{Im}\, t_{li} \langle\psi|l\rangle\langle i|\psi\rangle} \qquad \text{if } \langle l,i\rangle \,. \qquad (\text{C.17})$$

C.4 Linear tight-binding chain with a single on-site potential

In this section, we calculate the scattering phase of transport through a linear tight-binding (TB) chain with a single one-site potential ε_0. Similar to Sec. 3.3.1, the Hamiltonian is defined by

$$\hat{\mathcal{H}} = -t \sum_{n=-\infty}^{\infty} \Big[|n\rangle\langle n{+}1| + |n{+}1\rangle\langle n| \Big] + \varepsilon_0 |0\rangle\langle 0| \,. \tag{C.18}$$

We search for eigenstates which include an incoming wave $|\psi_{\mathrm{in}}\rangle = \sum_{n=1}^{\infty} \mathrm{e}^{+ik(-n)} |{-}n\rangle$ with wavevector k, thereby effectively restricting the energy $E = -2t\cos k$ to the band of the TB chain: $E \in [-2t, 2t]$. Hence, we make the ansatz

$$|\psi\rangle = \sum_{n=1}^{\infty} \left[\Big(\mathrm{e}^{+ik(-n)} + r\mathrm{e}^{-ik(-n)} \Big) |{-}n\rangle + \phi\mathrm{e}^{+ikn}|n\rangle \right] + \phi|0\rangle \tag{C.19}$$

which includes 2 free parameters: the reflexion amplitude r and the transmission amplitude ϕ. Enforcing the state to be an eigenstate of the Hamiltonian, we get two conditions:

$$\phi \overset{!}{=} 1 + r \,, \qquad (\text{C.20a})$$

$$-t(\mathrm{e}^{-ik} + r\mathrm{e}^{+ik} + \phi\mathrm{e}^{+ik}) + \varepsilon_0\phi \overset{!}{=} E\phi \,. \qquad (\text{C.20b})$$

Solving this linear set of equations gives

$$\phi = \frac{1}{1 + \mathrm{i}\frac{\varepsilon_0}{2t\sin k}} \,, \qquad (\text{C.21a})$$

$$r = \phi - 1 = \frac{-\mathrm{i}\frac{\varepsilon_0}{2t\sin k}}{1 + \mathrm{i}\frac{\varepsilon_0}{2t\sin k}} = \frac{\varepsilon_0}{2it\sin k - \varepsilon_0} \,. \qquad (\text{C.21b})$$

The transmission $\mathcal{T}$, given by the squared absolute value of the transmission amplitude ϕ, is

$$\mathcal{T} = |\phi|^2 = \frac{1}{1 + \left[\dfrac{\varepsilon_0}{2t\sin k} \right]^2} \,, \qquad (\text{C.22})$$

and does not depend on the sign of ε_0, only on the amplitude. The scattering phase φ, however, given by

$$\tan\varphi := \frac{\mathrm{Im}\,\phi}{\mathrm{Re}\,\phi} = -\frac{\varepsilon_0}{2t\sin k} \,, \qquad (\text{C.23})$$

depends also on the sign of ε_0. The dependence on the sign is important for Sec. 3.3.1, because it explains how an antiresonance can be formed in a two-path model with opposite on-site potential in the paths.

C.5 How symmetry can prevent the emergence of ring currents

In this section, we explain how a perfect symmetry relation between the different paths of two-path models as discussed in Sec. 3.3 can lead to a suppression of the ring currents. To this end, Fig. C.4 (left) shows the most general system—we know of—where a symmetry relation suppresses the creation of any backflow currents. The system features two identical paths (labeled by the sub-Hamiltonian **h**) whose couplings to the leads differs only by a scalar constant s. Of course, the case of equal hopping, $s = 1$, is included.

For convenience, we diagonalize the subsystem **h**, see Fig. C.4 (right). Then, each path consists of several states of energy $\mathfrak{e}_i$ with (potentially) different couplings $\mathfrak{t}_i'$, $\mathfrak{t}_i''$ to the leads. The current $j_{\mathrm{T/B}}$ can be split into its contribution $j_{\mathrm{T/B},i}$ through the states $\mathfrak{e}_i$. For the basis functions, we use the same nomenclature as in Eq. (3.8), except that every eigenstate $\mathfrak{e}_i$ belongs to its own basis functions $|T_i\rangle$ and $|B_i\rangle$ at the top and bottom path, respectively.

For each state $\mathfrak{e}_i$, an eigenstate $|\chi_i\rangle$ with energy $\mathfrak{e}_i$ of the overall structure (including leads) is given by

$$|\chi_i\rangle = s|T_i\rangle - |B_i\rangle\,. \tag{C.24}$$

This eigenstate has no contributions at the leads and is therefore not part of an incoming wave. And since it is an eigenstate of the overall Hamiltonian, it is also not mixed in by the time evolution. Hence, each transport/scattering state ψ is orthogonal to it:

$$\langle\psi|\chi_i\rangle \overset{!}{=} 0\,. \tag{C.25}$$

Thus, a general scattering state is written as

$$|\psi\rangle = \underbrace{\sum_{n=1}^{\infty}\left[\left(\mathrm{e}^{+\mathrm{i}k(-n)} + r\mathrm{e}^{-\mathrm{i}k(-n)}\right)|-n\rangle + \phi\mathrm{e}^{+\mathrm{i}kn}|n\rangle\right]}_{\text{incoming, reflected and transmitted wave as before}} + \underbrace{\sum_i c_i\left(|T_i\rangle + s^*|B_i\rangle\right)}_{\text{most general term allowed by } \langle\psi|\chi_i\rangle \overset{!}{=} 0} \tag{C.26}$$

with some constants c_i. This relates the contribution in the top and bottom path by

$$\langle\psi|B_i\rangle = s\langle\psi|T_i\rangle\,. \tag{C.27}$$

Again, we calculate the bond current between two neighboring sites i and j (connected by the hopping element t_{ij}) as $j_{i\to j} := \frac{2}{\hbar}\,\mathrm{Im}\,t_{ij}\langle\psi|i\rangle\langle j|\psi\rangle$. The currents through the states $\mathfrak{e}_i$ of the top/bottom path are then given by

$$j_{\mathrm{T},i} := j_{\mathrm{T},i\to1} = \frac{2}{\hbar}\,\mathrm{Im}\,\mathfrak{t}_i''\langle\psi|T_i\rangle\langle1|\psi\rangle\,, \tag{C.28}$$

and

$$\begin{aligned}
j_{\mathrm{B},i} := j_{\mathrm{B},i\to1} &= \frac{2}{\hbar}\,\mathrm{Im}\,s^*\mathfrak{t}_i''\langle\psi|B_i\rangle\langle1|\psi\rangle\\
&\overset{\text{(C.27)}}{=}\frac{2}{\hbar}\,\mathrm{Im}\,|s|^2\mathfrak{t}_i''\langle\psi|T_i\rangle\langle1|\psi\rangle\,. \tag{C.29}
\end{aligned}$$

Hence, the currents through the top and bottom path are related by a constant prefactor:

$$\mathbf{j}_{\mathrm{B}}(E) = |s|^2\,\mathbf{j}_{\mathrm{T}}(E) \qquad \forall E\,. \tag{C.30}$$

This behavior is seen in Fig. 3.14b and Fig. 3.14d, where the top and bottom currents are related by an energy-independent constant.
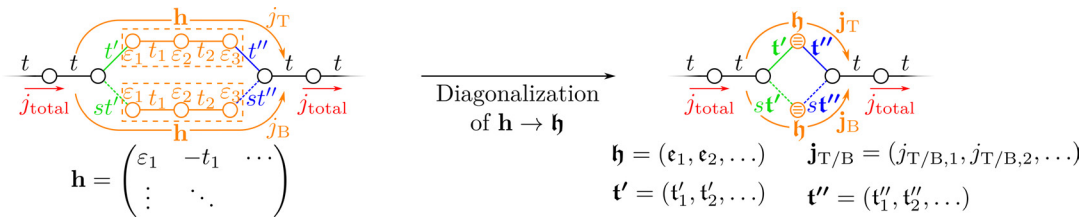
Figure C.4: A general TB two-path model where the symmetry suppresses the creation of backflow currents.

D

Application II:
Graphene with hydrogen adsorbates

This appendix contains additional material that complements Chap. 4. First, we estimate the average level spacing of hydrogenated AGNRs in Appx. D.1. Additional material on the current density is divided into three sections: the three-dimensional spatial dependence (Appx. D.2), the spatial autocorrelation (Appx. D.4), and the evolution under an applied bias voltage (Appx. D.3). In Appx. D.5, we discuss details about the distribution function, ranging from definitions over analytical calculations to additional examples. Last, in Appx. D.6 and Appx. D.7, a selection of the raw data is shown which was used to analyze the dependence on AGNR size and impurity concentration.

D.1 Level-spacing of hydrogenated AGNRs (20% hydrogen concentration)

In this section, we estimate the level spacing of hydrogenated AGNRs for fixed hydrogen concentration. For that purpose, we employ several AGNRs (as shown in Fig. 4.7) with 20% hydrogen adsorbates. The level spacing Δ is calculated as average over an interval of $1\,\mathrm{eV}$ near the Fermi energy, i.e.,

$$\Delta = 1\,\mathrm{eV} \left/ \int_{\varepsilon_{\mathrm{F}}-0.5\,\mathrm{eV}}^{\varepsilon_{\mathrm{F}}+0.5\,\mathrm{eV}} \rho(E)\,\mathrm{d}E \right. . \qquad \text{(D.1)}$$

In the density of states $\rho(E)$, we only include the states of the functionalized area which excludes the pristine contact regions.[1] In general, the level spacing is inversely proportional to the number of states which in turn is proportional to the system size. We parametrize the system size by the number of carbon atoms N which reside in the functionalized area. We thus expect a $1/N$ dependence for the level spacing. A fit to the DFT data estimates

$$\Delta = \frac{c_\Delta}{N} \qquad \text{with } c_\Delta = 15.1\,\mathrm{eV}, \qquad \text{(D.2)}$$

as shown in Fig. D.1.

---

[1] Technically, we use the Green's function $\mathbf{G}(E)$ of the device region (cf. Eq. (2.23)) to calculate the density of states $\rho_{\mathrm{device}}(E)$ of the whole device region (including two pristine contact regions). We use the converged Green's function $\mathbf{G}^m(E)$ of a single building block of the lead (cf. Eq. (2.18)) to calculate the density of states $\rho_{\mathrm{block}}(E)$ of one lead block. [We use the Green's function of the last iteration, i.e., $m = M - 1$, cf. Eq. (2.18).] Then, the density of states of the functionalized area (without the two contact regions) is estimated as $\rho(E) = \rho_{\mathrm{device}}(E) - 2\,\rho_{\mathrm{block}}(E)$.
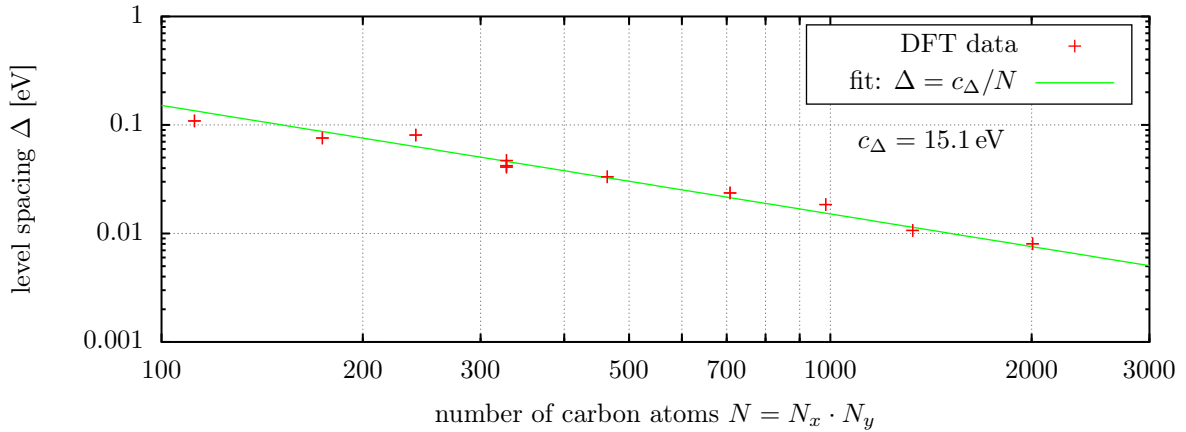
Figure D.1: Level spacing of AGNRs($N_x \times N_y$) with 20% hydrogen depending on the system size. The AGNRs are shown in Fig. 4.7. The level spacing Δ is calculated as average over an interval of $1\,\text{eV}$ near the Fermi energy, i.e., $\Delta = 1\,\text{eV} \Big/ \int_{\varepsilon_\text{F}-0.5\,\text{eV}}^{\varepsilon_\text{F}+0.5\,\text{eV}} \rho(E)\,\text{d}E$. The number of carbon atoms $N = N_x \cdot N_y$ only includes the carbon atoms in the functionalized area, i.e., the pristine contact regions are not counted.

D.2 Three-dimensional spatial dependence of current density and magnetic field in AGNR8×41

D.2.1 Current density response

In the main body, we mostly integrate the current density over the out-of-plane direction (z-direction). In this section, we discuss the z-dependence of the current density response in a hydrogenated AGNR8×41 with 20% hydrogen adsorbates (as shown in Fig. 4.1b). The transmission function was depicted in Fig. 4.2b and features many sharp peaks. We calculate the current density response at energy $E = \varepsilon_\text{F} + 155\,\text{meV}$ related to the center of a transmission peak. In Fig. D.2a, we show the integrated current density as commonly presented in the main body. It exhibits the usual strong mesoscopic fluctuations reflecting in a logarithmic color scale covering 4 decades. The cuts in Figs. D.2b and D.2c show that the current density has the general tendency to be symmetric to the carbon plane. Nevertheless, there are also regions where the current above and below the carbon plane flows in opposite directions, thereby forming small vortices. These vortices also induce magnetic fields; this time in x- and y-direction, which are discussed in the next section.

D.2.2 Magnetic field response

In the main body, we restricted ourselves to the magnetic field in z-direction because the other components are suppressed by an (approximate) z-mirror symmetry. In Fig. D.3, the magnetic field response for the current density response (shown in Fig. D.2) is shown at three different heights: below ($z=-1.5$Å), at ($z=0$Å), and above ($z=+1.5$Å) the carbon plane.

The x and y-components show a strong z-dependence, with a different sign below and above the carbon plane. For a perfect z-mirror symmetry, the contributions above the carbon plane are opposite to the ones below, $B_{x/y}(+z) = -B_{x/y}(-z)$. The remaining fluctuations in the (averaged) carbon plane (Figs. D.3d and D.3e) are evidence of the slightly broken z-mirror symmetry of the system configuration.

The z-component of the magnetic field shows a very weak z-dependence. Basically, all features at $z=0$Å are still present at $z=\pm1.5$Å. This is explained by the divergence condition, $\partial_z B_z + \cdots = 0$, which reduces the z-dependence of B_z.

In the main body, we focused on B_z since we expect the contributions of B_x, B_y on the electronic wavefunctions to average out because of the strong z-dependence and the sign change at $z=0$Å. We expect the main contributions from B_z. [Of course, all components are numerically included in Chap. 6 nevertheless.]

$$\mathrm{d}I_{\text{total}}/\mathrm{d}V_{\text{bias}} = 0.603\, G_0^{\text{spin}} = 4.67 \cdot 10^{-5}\,\text{A/V} \qquad L_y = 51.9\,\text{Å} \qquad E - \varepsilon_{\text{F}} = 155\,\text{meV}$$

(a) $\mathbf{j}_{xy}$: xy-view, integrated over z

(b) $\mathbf{j}_{yz}$: yz-cut at $x=x_0$

(c) $\mathbf{j}_x$: yz-cut at $x=x_0$
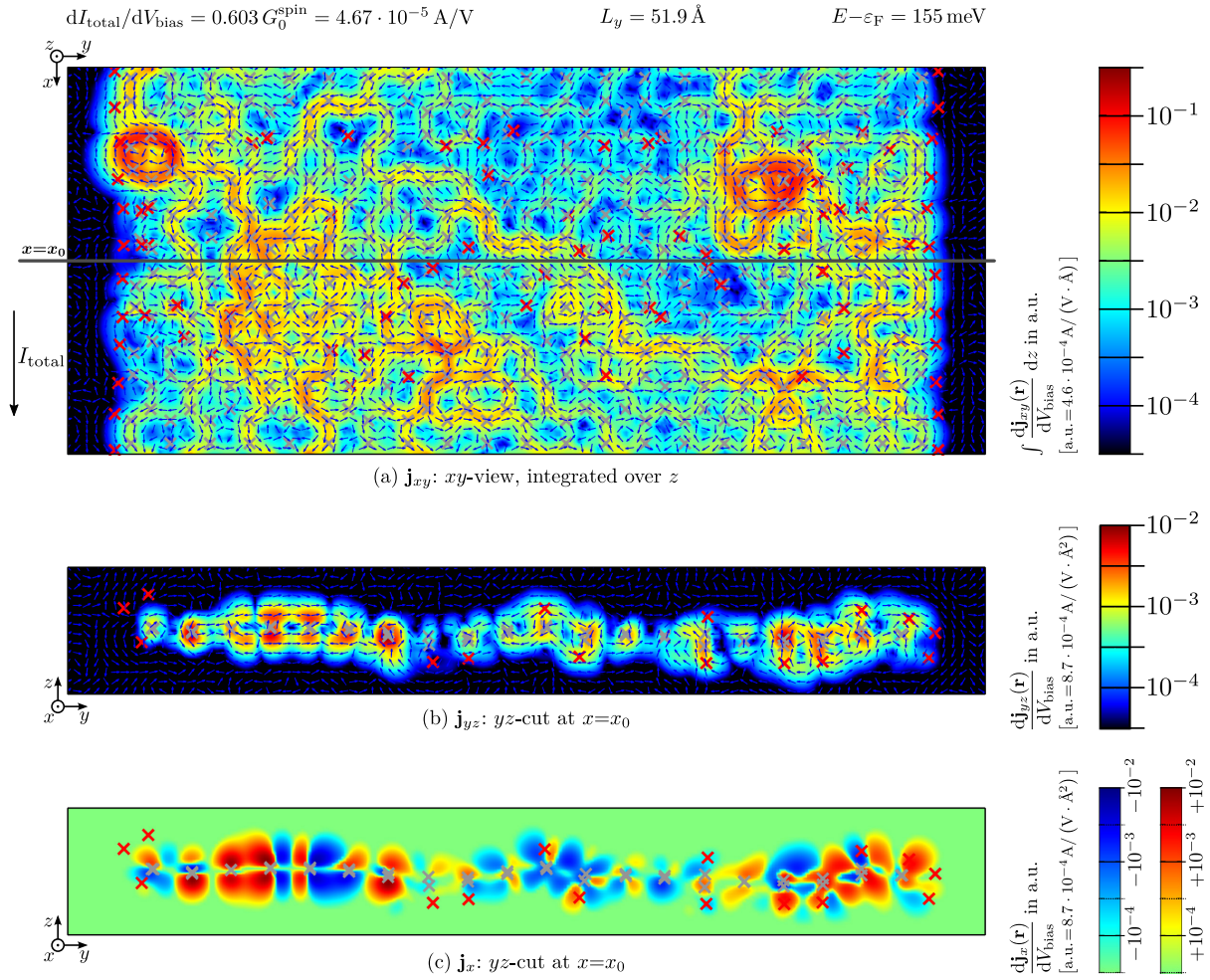
Figure D.2: Local current density response for the hydrogenated AGNR8×41 shown in Fig. 4.1b at energy $E = \varepsilon_{\text{F}} + 155\,\text{meV}$. Plot shows current amplitude (color), current direction (arrows), carbon atoms (gray crosses), and hydrogen atoms (red crosses). (a) In-plane current pattern in an xy-view, integrated over the z as commonly presented also in the main body. (b/c) A cut through the current density at $x = x_0$, as marked in (a). The current components parallel (j_y and j_z) and perpendicular (j_x) to the cut are shown in panel (b) and (c), respectively. Only atoms within 1Å of the cut are marked by crosses in the yz-cut.

$\mathrm{d}I_{\mathrm{total}}/\mathrm{d}V_{\mathrm{bias}} = 0.603\, G_0^{\mathrm{spin}} = 4.67 \cdot 10^{-5}\,\mathrm{A/V}$ $\hspace{4cm}$ $E - \varepsilon_{\mathrm{F}} = 155\,\mathrm{meV}$

(a) $\mathrm{d}B_x/\mathrm{d}V$ at $z{=}{-}1.5\text{Å}$ $\hspace{2cm}$ (b) $\mathrm{d}B_y/\mathrm{d}V$ at $z{=}{-}1.5\text{Å}$ $\hspace{2cm}$ (c) $\mathrm{d}B_z/\mathrm{d}V$ at $z{=}{-}1.5\text{Å}$

(d) $\mathrm{d}B_x/\mathrm{d}V$ at $z{=}0\text{Å}$ $\hspace{2.5cm}$ (e) $\mathrm{d}B_y/\mathrm{d}V$ at $z{=}0\text{Å}$ $\hspace{2.5cm}$ (f) $\mathrm{d}B_z/\mathrm{d}V$ at $z{=}0\text{Å}$

(g) $\mathrm{d}B_x/\mathrm{d}V$ at $z{=}{+}1.5\text{Å}$ $\hspace{2cm}$ (h) $\mathrm{d}B_y/\mathrm{d}V$ at $z{=}{+}1.5\text{Å}$ $\hspace{2cm}$ (i) $\mathrm{d}B_z/\mathrm{d}V$ at $z{=}{+}1.5\text{Å}$

I_{total} $\qquad$ $\frac{\mu_0 \mathrm{d}I_{\mathrm{total}}}{4\pi L_y \mathrm{d}V_{\mathrm{bias}}} = 0.90\,\mathrm{mT/V}$ $\qquad$ $\left[\mathrm{d}B_z(\mathbf{r})/\mathrm{d}V_{\mathrm{bias}}\right] \Big/ \frac{\mu_0 \mathrm{d}I_{\mathrm{total}}}{4\pi L_y \mathrm{d}V_{\mathrm{bias}}}$

$-10^2 \qquad -10^1 \qquad -10^0 \qquad +10^0 \qquad +10^1 \qquad +10^2$
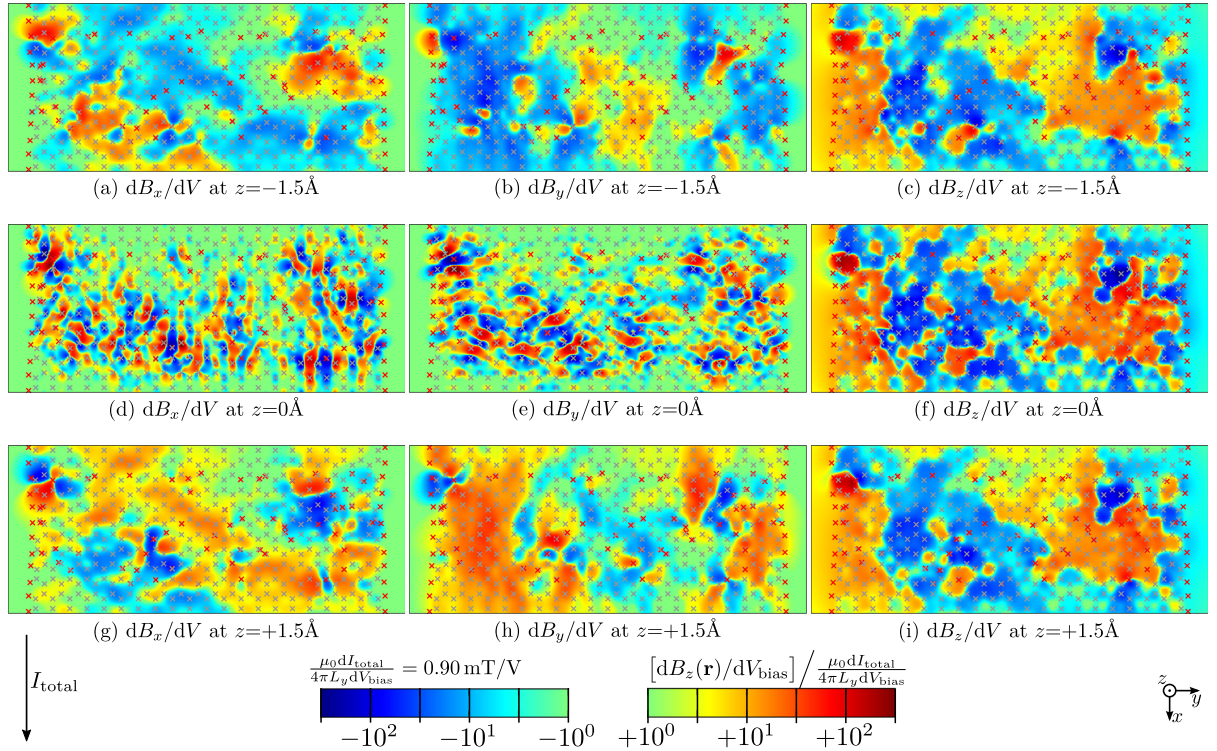
Figure D.3: The magnetic field response $\mathrm{d}\mathbf{B}/\mathrm{d}V_{\mathrm{bias}}$ induced by the current configuration presented in Fig. D.2. The magnetic field is shown at three different heights, $z{=}{-}1.5\text{Å}$ (panel a/b/c), $z{=}0\text{Å}$ (panel d/e/f), and $z{=}{+}1.5\text{Å}$ (panel g/h/i); corresponding to below, at, and above the average carbon plane, respectively. The x- and y-components show a strong z-dependence with an (approximate) sign change at $z{=}0\text{Å}$. On the other hand, the z-component hardly depends on the z-direction.

D.3 Current evolution when increasing the bias voltage

In Sec. 4.2.3, we discussed the evolution of the current density with increasing bias voltage using the moments of the distribution function, cf. Fig. 4.15 (center).

In Fig. D.4, we provide explicit plots of the current density for increasing bias voltage. For small bias voltages, an increase of the bias voltage significantly changes the current pattern, e.g., from $V_{\mathrm{bias}} = 50\,\mathrm{mV}$ to $V_{\mathrm{bias}} = 100\,\mathrm{mV}$ (Fig. D.4a to Fig. D.4b). For large bias voltages, an increase hardly perturbs the pattern, e.g., from $V_{\mathrm{bias}} = 200\,\mathrm{mV}$ to $V_{\mathrm{bias}} = 250\,\mathrm{mV}$ (Fig. D.4d to Fig. D.4e). From that behavior, we conclude that each

transport state carrying current vortices of the same order. Adding additional transport states (by increasing the bias voltages) only significantly changes the current pattern if the number of transport states to start with was small.

The magnetic field for a bias voltages of $V_{\mathrm{bias}} = 250\,\mathrm{mV}$ is shown in Fig. D.4f. The magnetic field strongly varies and changes sign from region to region. The field gradient reaches $200\,\mathrm{mT}\,\mathrm{V}^{-1}\,\mathrm{nm}^{-1}$ which is reduced by about a factor of 5 when compared with the response to an infinitesimal small bias voltage (cf. Fig. D.3f).

(a) $\int \mathbf{j}_{xy}(\mathbf{r})\,\mathrm{d}z$ for $V_{\mathrm{bias}} = 50\,\mathrm{mV}$

(b) $\int \mathbf{j}_{xy}(\mathbf{r})\,\mathrm{d}z$ for $V_{\mathrm{bias}} = 100\,\mathrm{mV}$

(c) $\int \mathbf{j}_{xy}\,\mathrm{d}z$ for $V_{\mathrm{bias}} = 150\,\mathrm{mV}$

(d) $\int \mathbf{j}_{xy}\,\mathrm{d}z$ for $V_{\mathrm{bias}} = 200\,\mathrm{mV}$

(e) $\int \mathbf{j}_{xy}\,\mathrm{d}z$ for $V_{\mathrm{bias}} = 250\,\mathrm{mV}$

(f) $B_z(x, y, z = 0)$ for $V_{\mathrm{bias}} = 250\,\mathrm{mV}$
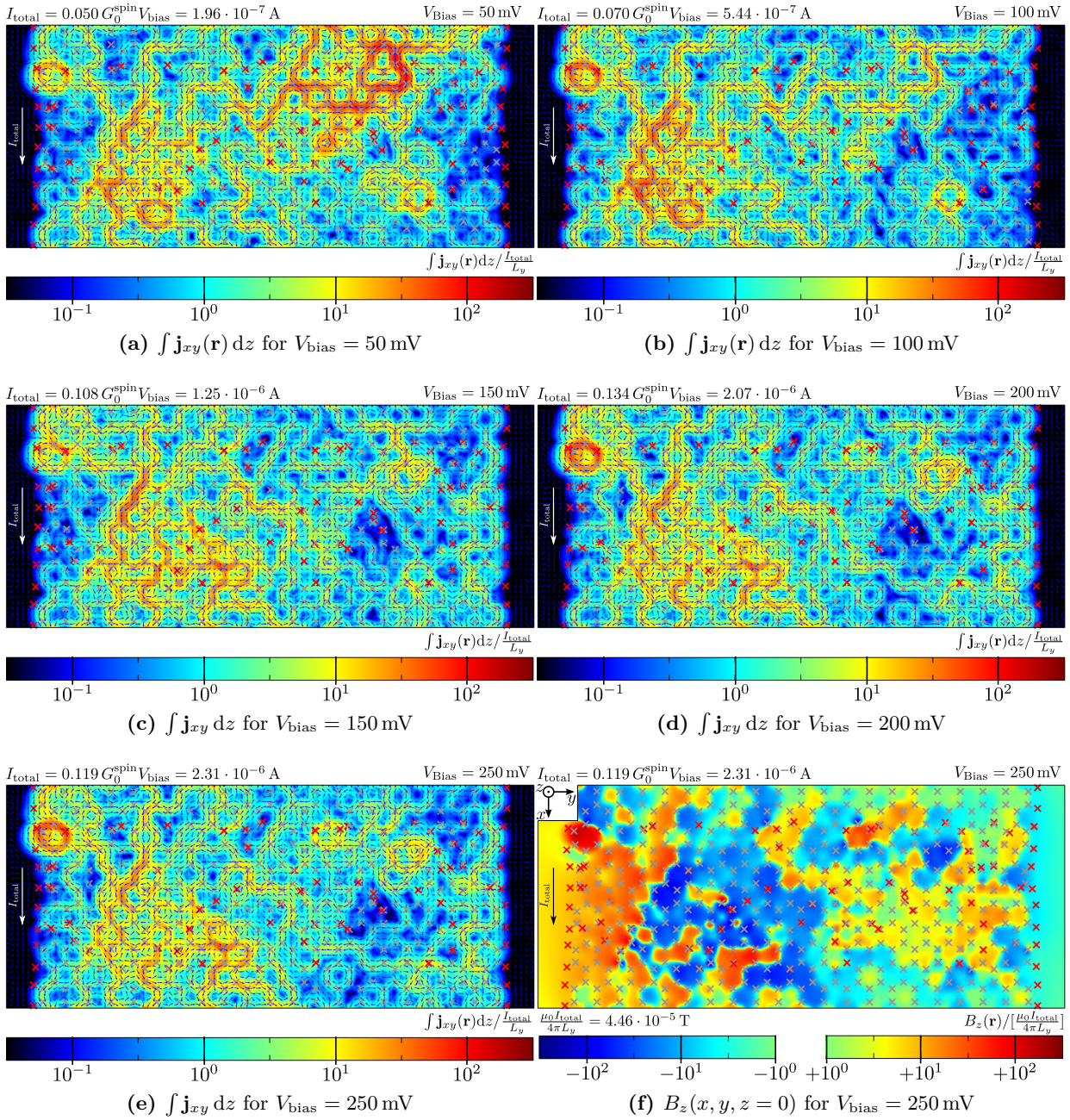
Figure D.4: (a-e) Local current density (integrated over the out-of-plane direction) in the hydrogenated AGNR8×41 of Fig. 4.1b with increasing bias voltage V_{bias}. Plots show current amplitude (color), current direction (arrows), carbon atoms (gray crosses) and hydrogen atoms (red crosses). (f) Magnetic field B_z (in out-of-plane direction) induced by the current distribution plotted in (e) for a bias voltage of $V_{\mathrm{bias}} = 250\,\mathrm{mV}$.

D.4 Spatial autocorrelation function of the current density

D.4.1 Theory

In the main body, in Fig. 4.3a, the current density response $\mathbf{j}^\diamond := \mathrm{d}\mathbf{j}/\mathrm{d}V_{\text{bias}}$ of a hydrogenated AGNR16×83 was shown. The current pattern displayed many seemingly random current vortices. To quantify this "randomness", we ask the following question: what is the spatial autocorrelation function for the current density and how fast does it decay?

The spatial autocorrelation function $J_{ab}(\boldsymbol{\delta})$ of the current density response is given by

$$
\begin{aligned}
J_{ab}(\boldsymbol{\delta}) &= \Big\langle j_a(\mathbf{r})\, j_b(\mathbf{r}+\boldsymbol{\delta}) \Big\rangle \\
&= \frac{1}{V} \int_V \mathrm{d}^3\mathbf{r}\, j_a(\mathbf{r})\, j_b(\mathbf{r}+\boldsymbol{\delta}),
\end{aligned}
\tag{D.3}
$$

where the integration volume V is restricted to a cuboid of dimensions $L_x = 38.8\text{Å}$, $L_y = 97.2\text{Å}$, and $L_z = 10.0\,\text{Å}$. The cuboid includes only the functionalized area of the AGNR without the border regions.[2] The integration borders in z-direction, $z = \pm 5\text{Å}$, are arbitrary. To remove this arbitrary dependence, we define a normalized autocorrelation function

$$
\tilde{J}_{ab}(\boldsymbol{\delta}) := \frac{J_{ab}(\boldsymbol{\delta})}{\sqrt{J_{aa}(\mathbf{0})\, J_{bb}(\mathbf{0})}},
\tag{D.4}
$$

so that $\tilde{J}_{aa}(\mathbf{0}) = 1$.

To avoid the evaluation of the integral in Eq. (D.3) for every value of $\boldsymbol{\delta}$, we evaluate the autocorrelation function by a double Fourier transformation, i.e.,

$$
\begin{aligned}
J_{ab}(\boldsymbol{\delta}) &= \Big\langle j_a(\mathbf{r})\, j_b(\mathbf{r}+\boldsymbol{\delta}) \Big\rangle \\
&= \mathcal{F}^{-1}\Big(\mathcal{F}\big(j_a(\mathbf{r})\big)\, \mathcal{F}\big(j_b(\mathbf{r})\big)^* \Big).
\end{aligned}
\tag{D.5}
$$

That way, a periodicity of the current density pattern is assumed which, of course, the current density in hydrogenated AGNR16×83 does not possess. The induced errors are of the order $2\delta_i/L_i$. Thus, we expect only small errors for $\delta_x \lesssim 8\text{Å}$, $\delta_y \lesssim 12\text{Å}$, and $\delta_z \lesssim 2.5\text{Å}$.

D.4.2 AGNR16×83 functionalized by 20% hydrogen adatoms

The autocorrelation function $\tilde{J}_{xx}$ of the current density $j_x^\diamond$ (in transport direction) of a hydrogenated AGNR16×83 is shown in Fig. D.5a. We observe a very fast decay which seems to be modulated by additional oscillations, i.e., $\tilde{J}_{xx} \sim e^{-\delta/\xi} \cdot \cos(\lambda\delta)$. The correlation

(a) $\tilde{J}_{xx}(\boldsymbol{\delta})$

(b) $\tilde{J}_{xx}(\boldsymbol{\delta})$
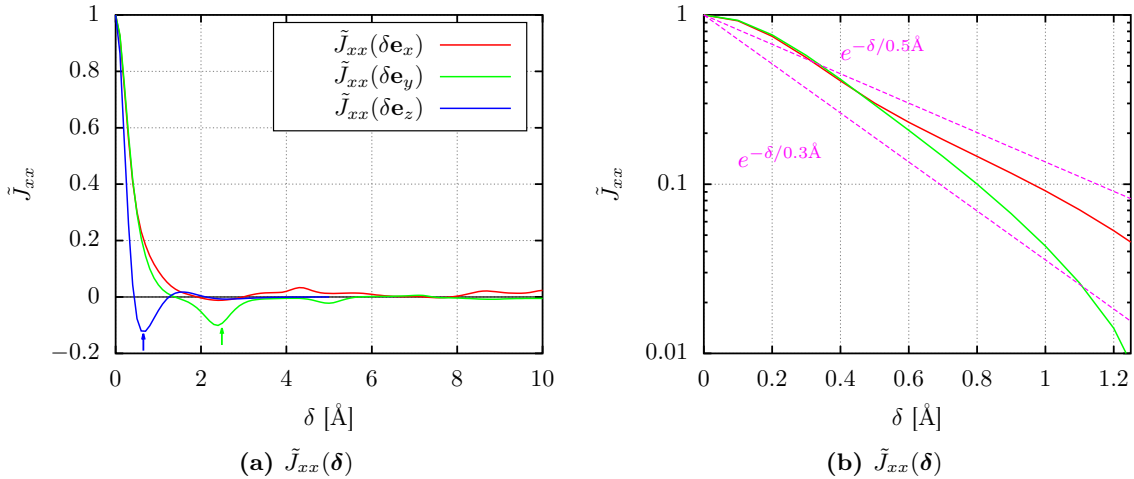
Figure D.5: Spatial autocorrelation functions $\tilde{J}_{xx}$ for the current density $j_x^\diamond$ in transport direction in a hydrogenated AGNR16×83 (as presented in Fig. 4.3a). The arrows at $0.65\,\text{Å}$ and $2.49\,\text{Å}$ (width of carbon ring) mark significant oscillations in the correlation functions, hinting at current vortices.

---

[2]The exclusion of the boundary areas is performed with the same procedure as used for the suppression of the boundary effects in the distribution functions, cf. A_{cut} in Appx. D.5.3, Fig. D.9c.

length ξ is estimated in Fig. D.5b for the in-plane current components as $\xi = 0.3 - 0.5$ Å. The sign changes in the autocorrelation function are especially important because they hint at tendencies to form ring currents around single carbon rings, i.e., the current density $j_x^\diamond$ at two points which are separated by one carbon ring, $\boldsymbol{\delta} = 2.94$Å $\mathbf{e}_y$, show a preference to align antiparallel. The negative peak in z-direction (blue arrow) predicts a tendency to also form small current vortices along the z-direction. The effect of a current density running in opposite direction above and below the graphene plane is neglected in the main part by integrating over z-direction.

For completeness, all autocorrelation components are shown in Fig. D.6. The off-diagonal correlators $\tilde{J}_{ab}$, $a \neq b$, should tend to zero for averaging either over a single large disordered AGNR or over several randomly disordered AGNRs. The modulations in Fig. D.6d-f are estimates for the influence of the concrete impurity configuration. Thus, any features in the diagonal correlators $\tilde{J}_{aa}$ below 0.05 are probably not of general origin

but depend on the exact impurity configuration.

Thus, all in all, the autocorrelation functions support the tendency to form vortices in the current density.

D.4.3 Pristine AGNR41

In Fig. D.7, the diagonal autocorrelators for a stream-line pattern of pristine AGNR24×41 is shown.[3] The off-diagonal correlations $\tilde{J}_{xy}$, $\tilde{J}_{xz}$, $\tilde{J}_{yz}$ are numerically zero, i.e., in the order of 10^{-6} and below. We ensured that the integration volume V is chosen in such a way that the current pattern is indeed exactly periodic. Thus, no spurious contributions are introduced by the Fourier transformation.

The perfect periodicity of the streamlines is reflected in the autocorrelation functions for $\boldsymbol{\delta} \parallel \mathbf{e}_x$ and $\boldsymbol{\delta} \parallel \mathbf{e}_y$. The periodicity lengths a_x and a_y, marked with colored arrows, naturally coincide with the periodicity length of the streamline patterns. Interestingly, in out-of-plane

(a) $\tilde{J}_{xx}(\boldsymbol{\delta})$ **(b)** $\tilde{J}_{yy}(\boldsymbol{\delta})$ **(c)** $\tilde{J}_{zz}(\boldsymbol{\delta})$

(d) $\tilde{J}_{xy}(\boldsymbol{\delta})$ **(e)** $\tilde{J}_{xz}(\boldsymbol{\delta})$ **(f)** $\tilde{J}_{yz}(\boldsymbol{\delta})$
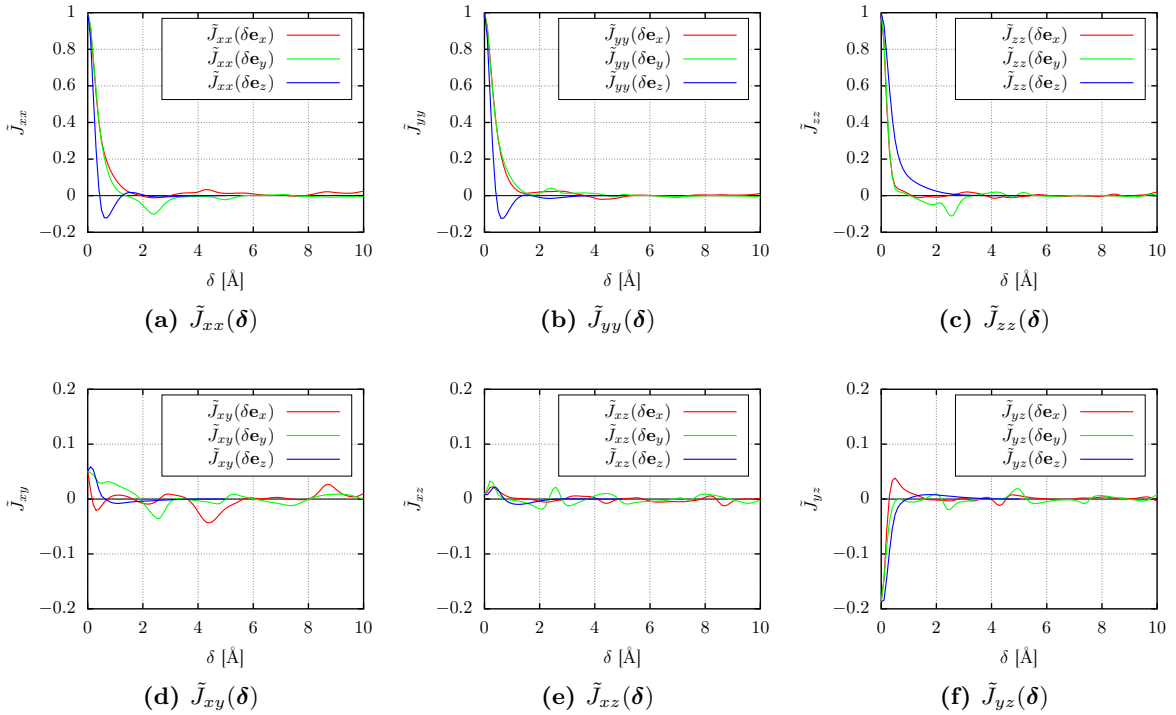
Figure D.6: Spatial autocorrelation functions $\tilde{J}_{ab}$ for the current density in a hydrogenated AGNR16×83 (as presented in Fig. 4.3a).

---

[3]The streamline patterns in pristine AGNRs are discussed in detail in Sec. 3.1. Due to the periodicity in the ribbon width, the autocorrelation functions presented are the same of any AGNRN_C with $N_C = 3m - 1$.
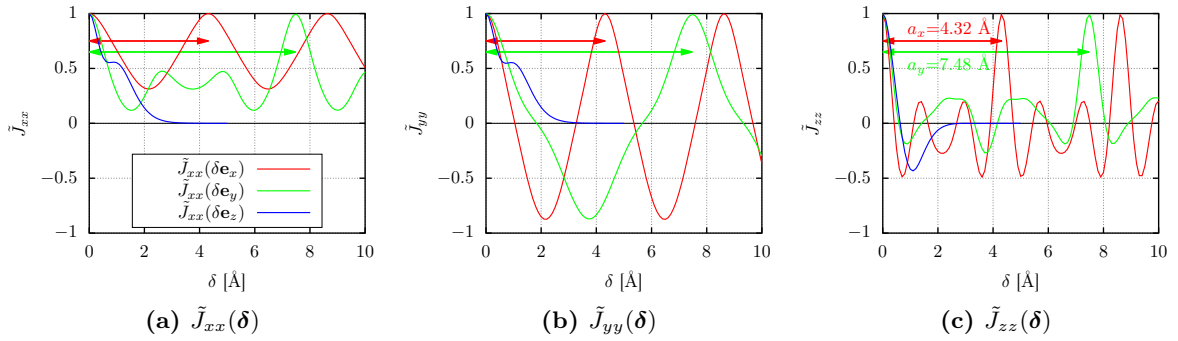
Figure D.7: Spatial autocorrelation functions $\tilde{J}_{aa}$ for the streamline pattern seen in pristine AGNR($3m-1$). The off-diagonal correlations J_{xy}, J_{xz}, J_{yz} are numerically zero, i.e., in the order of 10^{-6} and below.

direction, $\boldsymbol{\delta} \parallel \mathbf{e}_z$, the autocorrelation function decays significantly slower than in the hydrogenated AGNR, cf. Sec. D.4.2. While in pristine AGNRs the current density is always the same above and below the carbon plane, it may (and does) differ in hydrogenated AGNRs in some spatial regions, cf. Appx. D.2, Figs. D.2b and D.2c.

D.5 Distribution functions

In this section, we cover details of the distribution functions which have been omitted from the main part. We start with formal definitions in Appx. D.5.1. In Appx. D.5.2, we analytically calculate the expectation of equivalent vector components if the vector magnitude follows a lognormal distribution. Next, the procedure how to suppress border contributions is discussed (Appx. D.5.3). We close with further examples of distribution functions of the current density in Appx. D.5.4.

D.5.1 Normal and lognormal distribution & deviations from distributions

Normal distribution

A normal or Gaussian distribution is given by

$$\mathcal{P}_{\text{normal}}(x) = \frac{1}{\sqrt{2\pi}\sigma} \exp\left[-\frac{(x-\mu)^2}{2\sigma^2} \right]. \qquad (D.6)$$

It is solely parameterized by its mean value μ,

$$\mu = \int x\, \mathcal{P}(x)\, dx\,, \qquad (D.7)$$

and its width σ,

$$\sigma^2 = \int (x-\mu)^2\, \mathcal{P}(x)\, dx\,. \qquad (D.8)$$

Lognormal distribution

A quantity x follows a lognormal distribution if the logarithm $\ln x$ follows a normal distribution, i.e.,

$$\mathcal{P}_{\text{lognormal}}(\ln x) = \frac{1}{\sqrt{2\pi}\sigma} \exp\left[-\frac{(\ln x - \mu)^2}{2\sigma^2} \right]. \quad (D.9)$$

It is also solely parameterized by its mean value μ and width σ, both with respect to the logarithm of x.

Deviation from a lognormal distribution

For classification of the distribution functions, we use the mean value μ and the width σ. These two values do not ensure that a quantity follows a normal or lognormal distribution. Historically, we used higher moments (skewness ν, kurtosis ω and excess kurtosis $\gamma = \omega - 3$) to quantify deviations from a (log)normal distribution. We found this procedure to be insufficient because it neglects all differences in higher moments. Therefore, to quantify the deviation of a (nu-

merically calculated) distribution function $\mathcal{P}(\ln x)$ from the lognormal-distribution $\mathcal{P}_{\mathrm{lognormal}}(\ln x)$, we define a deviation measure $\Delta_{\mathcal{P}_{\ln x}}$ that uses the complete range in which the distribution function $\mathcal{P}(\ln x)$ is reliable. We define $\Delta_{\mathcal{P}_{\ln x}}$ as the logarithmic root mean square deviation between the two distributions with an additional cutoff Λ which cuts off statistical unlikely unreliable values:

$$\Delta_{\mathcal{P}_{\ln x}} = \sqrt{\frac{1}{2\sqrt{2\sigma^2\Lambda}} \int\limits_{\ln \mu - \sqrt{2\sigma^2\Lambda}}^{\ln \mu + \sqrt{2\sigma^2\Lambda}} \mathrm{d}\ln x \, \left| \ln \mathcal{P}(\ln x) - \ln \mathcal{P}_{\mathrm{lognormal}}(\ln x) \right|^2} \qquad (\mathrm{D.10})$$

In this procedure, the lognormal distribution $\mathcal{P}_{\mathrm{lognormal}}(\ln x)$ is parameterized by the mean μ and the standard deviation σ of $\mathcal{P}(\ln x)$. This exactly corresponds to the deviation of the distribution $\mathcal{P}(\ln x)$ to a (downward opening) parabola in double-logarithmic

plots like Figs. D.10 and D.11. We arbitrarily set the cutoff to $\Lambda = 2.5$. The integration bounds $\ln \mu \pm \sqrt{2\sigma^2\Lambda}$ are set in such a way that only values more likely than $\mathrm{e}^{-\Lambda}/\sqrt{2\pi\sigma^2}$ are taken into account.

Deviation from a uniform distribution

For quantities that are expected to follow a uniform distribution

$$\mathcal{P}_{\mathrm{uniform}}(x) = \begin{cases} \frac{1}{b-a} & x \in [a, b] \\ 0 & \mathrm{else} \end{cases} , \qquad (\mathrm{D.11})$$

we define a deviation measure $\Delta_{\mathcal{P}_{\mathrm{uniform}}}$ as the relative

root mean square deviation, i.e.,

$$\Delta_{\mathcal{P}_{\mathrm{uniform}}} = \sqrt{\frac{1}{b-a} \int_a^b \mathrm{d}x \, \left(\frac{\mathcal{P}(x) - \mathcal{P}_{\mathrm{uniform}}}{\mathcal{P}_{\mathrm{uniform}}} \right)^2} . \qquad (\mathrm{D.12})$$

In this thesis, we use this measure for angle distributions, $\mathcal{P}(\varphi)$ and $\mathcal{P}(\cos\theta)$. The related deviation measures are named $\Delta_{\mathcal{P}_\varphi}$ and $\Delta_{\mathcal{P}_{\cos\theta}}$, respectively.

D.5.2 Lognormal distribution of a vector quantity

In this section, we analyze a 3-component vector $\mathbf{j}$ whose magnitude $j = |\mathbf{j}|$ follows a lognormal distribution. We assume that the angles defining the component

$j_x = j\sin\theta\cos\varphi$, $j_y = j\sin\theta\sin\varphi$, and $j_z = j\cos\theta$ are equally distributed, i.e., $\mathcal{P}(\varphi) = 1/2\pi$ and $\mathcal{P}(\cos\theta) = 1/2$. For that case, we provide an analytic expression

(a) linear scale

(b) logarithmic scale
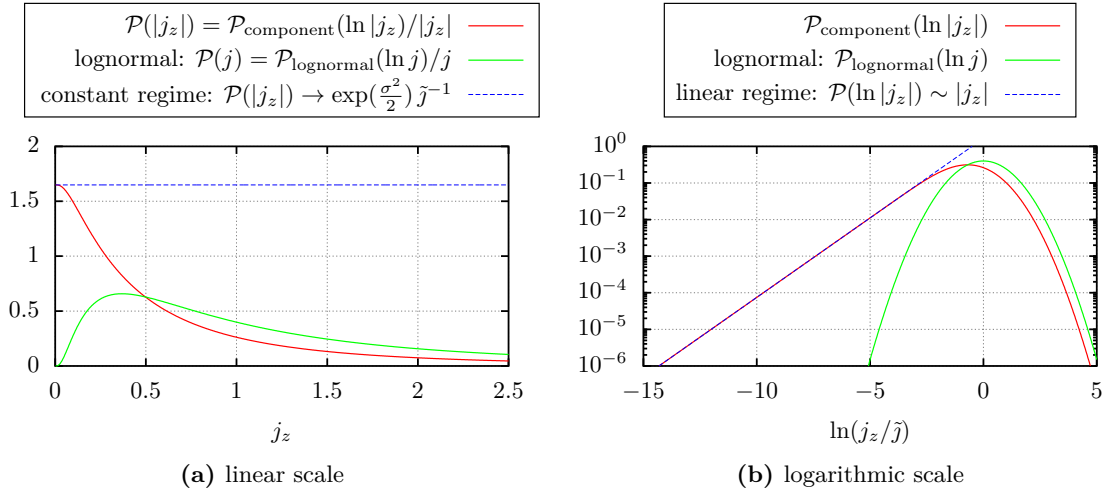
Figure D.8: Distribution functions $\mathcal{P}_{\text{component}}$ and $\mathcal{P}_{\text{lognormal}}$ for a linear and logarithmic scale. [Numerical parameters: $\tilde{j} = 1$, $\sigma = 1$.]

for the expectation value of a single vector component of $\mathbf{j}$.

To start, let the amplitude j follow a lognormal distri-

bution with mean value $\mu = \ln \tilde{j}$ and width σ:

$$\mathcal{P}(\ln j) = \frac{1}{\sqrt{2\pi}\sigma} \exp\left[- \frac{(\ln j - \ln \tilde{j})^2}{2\sigma^2} \right]. \qquad \text{(D.13)}$$

Then, the distribution function of the logarithm of a single component, e.g. $\ln |j_z|$, is given by

$$\mathcal{P}(\ln |j_z|) = \underbrace{\int_0^{2\pi} \mathrm{d}\varphi \, \mathcal{P}(\varphi)}_{1} \int_{-1}^{+1} \mathrm{d}\cos\theta \, \underbrace{\mathcal{P}(\cos\theta)}_{1/2} \int_{-\infty}^{+\infty} \mathrm{d}\ln j \, \mathcal{P}(\ln j) \, \delta\Big(\ln |j_z| - \ln(|j\cos\theta|) \Big) . \qquad \text{(D.14)}$$

The φ-integral evaluates to unity (due to normalization). The Dirac delta function forces the amplitude j to equal $j = |j_z/\cos\theta|$. This happens twice (for $\pm\cos\theta$); by including a factor of 2, we can restrict $\cos\theta$ to positive values:

$$\mathcal{P}(\ln |j_z|) = \frac{1}{\sqrt{2\pi}\sigma} \int_0^{+1} \mathrm{d}\cos\theta \, \exp\left[- \frac{(\ln |j_z/\cos\theta| - \ln \tilde{j})^2}{2\sigma^2} \right]. \qquad \text{(D.15)}$$

The integral can be simplified using the substitution

$$t = \frac{\ln |j_z/\cos\theta| - \ln \tilde{j}}{\sqrt{2}\sigma} + \frac{\sigma}{\sqrt{2}}, \qquad \text{(D.16)}$$

$$\frac{\mathrm{d}\cos\theta}{\mathrm{d}t} = -\sqrt{2}\sigma \, e^{-\sqrt{2}\sigma t + \sigma^2} \frac{j_z}{\tilde{j}}, \qquad \text{(D.17)}$$

leading to

$$\boxed{\mathcal{P}(\ln |j_z|) = \frac{e^{\frac{\sigma^2}{2}}}{2} \frac{|j_z|}{\tilde{j}} \, \mathrm{erfc}\left(\frac{\sigma}{\sqrt{2}} + \frac{1}{\sqrt{2}\sigma} \ln \frac{|j_z|}{\tilde{j}} \right)} \qquad \text{(D.18)}$$

where we have introduced the complementary error function $\mathrm{erfc}(x)$,

$$\mathrm{erfc}(x) = \frac{2}{\sqrt{\pi}} \int_x^\infty e^{-t^2} \, \mathrm{d}t. \qquad \text{(D.19)}$$

In the main body of this thesis, we refer to $\mathcal{P}(\ln |j_z|)$ as $\mathcal{P}_{\text{component}}$. Its behavior is shown in Fig. D.8 (red curve) for a logarithmic and linear scale. For comparison, a lognormal distribution is shown (in green) as well. For large values, both distributions are similar. For small values, $\mathcal{P}_{\text{component}}$ shows a much heavier tail.

Limiting behavior of $\mathcal{P}_{\text{component}}$

The limiting behavior can be reproduced analytically. Employing the limits for $x \to \pm\infty$ of the complementary error function,

$$\lim_{x \to -\infty} \text{erfc}(x) = 2 \,, \qquad (D.20)$$

and

$$\lim_{x \to +\infty} \text{erfc}(x) = \frac{e^{-x^2}}{x\sqrt{\pi}} \,, \qquad (D.21)$$

the distribution functions limiting behavior is given by

$$\lim_{\ln|j_z| \to -\infty} \mathcal{P}(\ln|j_z|) = e^{\frac{\sigma^2}{2}} \frac{|j_z|}{\tilde{j}} \propto |j_z| \,, \qquad (D.22)$$

$$\lim_{\ln|j_z| \to +\infty} \mathcal{P}(\ln|j_z|) \propto \exp\left[-\frac{(\ln|j_z| - \ln\tilde{j})^2}{2\sigma^2} \right] \,. \qquad (D.23)$$

Thus, for small values, a *linear* regime exists, whereas a lognormal distribution is recovered for large values.

Remark: The linear regime for small values translates to a constant regime on a non-logarithmic scale since the linear term drops out when transforming the distribution function:

$$\mathcal{P}_{|j_z|}(|j_z|) = \mathcal{P}_{\ln|j_z|}(\ln|j_z|) \underbrace{\frac{d\ln|j_z|}{d|j_z|}}_{\frac{1}{|j_z|}} \,. \qquad (D.24)$$

D.5.3 Current density distribution function: suppressing border contributions

In Chap. 4, we plot several distribution functions of the current density. We focus on the bulk limit; therefore we want to suppress border contributions. In this section, we provide the details on the procedure how the borders effects are reduced.

We start with the current density response in three dimensional space, e.g., the current density response is rastered in a cuboid with corners ($x_{\text{min/max}}, y_{\text{min/max}} \pm 3\text{Å}, z_0 \pm 4\text{Å}$), where $x_{\text{min/max}}$ is the minimal and maximal x-coordinate of any atom in the device region (including contact regions). $z_0 = 0$ refers to the average carbon plane. The distribution function of the current density rastered that way is shown in Fig. D.9a. We see very long tails for small values. We account the tail to an exponential decay of the current density in z-direction "outside" the AGNR. If the decay is indeed exponential, the distribution function of the logarithmic current density should go to a constant for small values. [That this still happens for smaller values is unlikely because the employed basis functions in the DFT cannot represent long exponential tails.] Apart from the long tail clouding any interesting details, this definition is also problematic since the height L_z of the ribbon is not well-defined. [Here, we have used the height of the rastered box, $L_z = 8\text{Å}$.]

To remove the long tails, we integrate the current density over z-direction. The corresponding distribution function is shown in Fig. D.9b. The tails are already significantly reduced. The drop-off at smaller values is probably due to the finite precision used in the numerical integration (double precision $\varepsilon = 2.2 \cdot 10^{-16}$, $\ln\varepsilon = -36.05$). There is still a heavy shoulder for small values. These values can be attributed to contributions at the y-border of the AGNR where the current contributions also decay exponentially.

To remove this border effects, and simultaneously reduce the influence of the pristine leads, the integrated current density is restricted to a rectangular area A_{cut} which is one carbon ring (2.878Å) distance away from from the outer hydrogen atoms and from the contact region (cf. Fig. D.9d). The obtained distribution of the current density is shown in Fig. D.9c. The current magnitude follows the lognormal distribution and the vector components follow $\mathcal{P}_{\text{component}}$.

For the distributions of the magnetic field, we apply a modified procedure. The magnetic field is not integrated but restricted to the average carbon plane, $z = 0$. In x/y-direction, it is also restricted to the area A_{cut}.

(a) Current density response $\mathbf{j}^{\diamond}(\mathbf{r})$

(b) Integrated current density response $\int \mathrm{d}z\, \mathbf{j}^{\diamond}(\mathbf{r})$

(c) Integrated and restricted to $(x,y) \in A_{\mathrm{cut}}$

(d) Cutting procedure
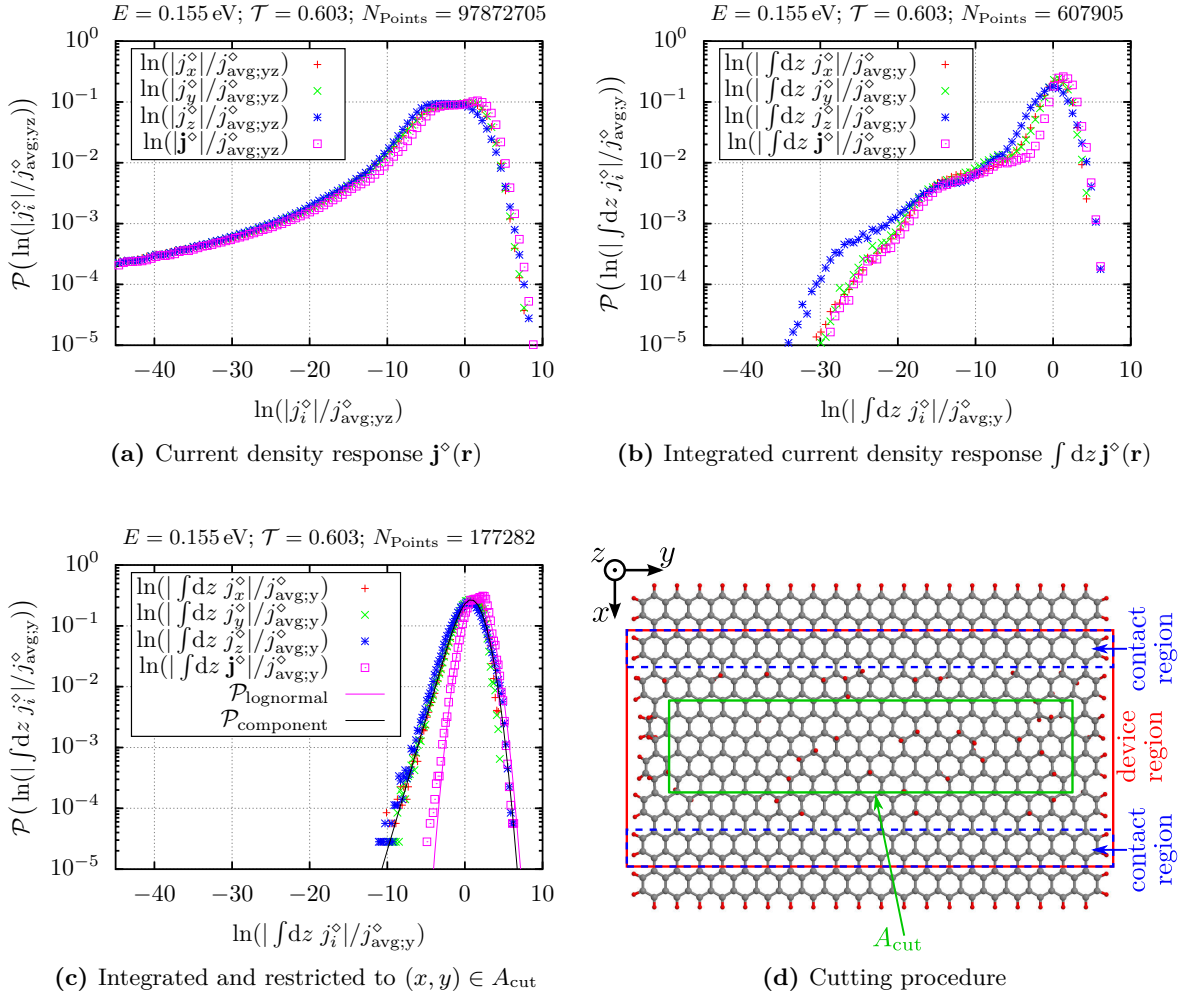
Figure D.9: (a) Distribution function for the current density response $\mathbf{j}^{\diamond} = \mathrm{d}\mathbf{j}/\mathrm{d}V_{\mathrm{bias}}$ normalized to the average through current per width and height, $j^{\diamond}_{\mathrm{avg;yz}} = \mathrm{d}I_{\mathrm{total}}/(L_y L_z \mathrm{d}V_{\mathrm{bias}})$. The number of points N_{points} used to approximate the distribution function is shown in the plot title. (b) The current density response is integrated over the z-direction and normalized to the average through current per width, $j^{\diamond}_{\mathrm{avg;y}} = \mathrm{d}I_{\mathrm{total}}/(L_y \mathrm{d}V_{\mathrm{bias}})$. (c) The current density response is integrated over the z-direction and additionally restricted to the region A_{cut}. (d) Geometry of the ribbon showing the definition of A_{cut}.

D.5.4 Further distribution functions for simulated current densities

Hydrogenated AGNR8×41: infinitesimal bias voltage

In Fig. D.10, distribution functions for infinitesimal bias voltages in hydrogenated AGNR8×41 (20% hydrogen concentration) are shown. In both cases, the magnitude of the current density follows a lognormal distribution, although the transmission differs by two decades ($\mathcal{T} = 0.6$ and $\mathcal{T} = 0.004$). The main effect of a low transmission value is that the distribution is shifted to higher values. This is because the current density is normalized to the average through current $j^{\diamond}_{\mathrm{avg;y}} = \mathrm{d}I_{\mathrm{total}}/(L_y \mathrm{d}V_{\mathrm{bias}})$. The latter vanishes faster at an antiresonance with $\mathcal{T} \to 0$, so that the ratio increases.

Hydrogenated AGNR8×41: finite bias voltage

In Fig. D.11, the distribution functions for two different bias voltages V_{bias} are shown. Different bias voltages mean that the current contributions of the different number of transport states $N = \int_{\varepsilon_{\mathrm{F}}}^{\varepsilon_{\mathrm{F}} + eV_{\mathrm{bias}}} \rho(E)\, \mathrm{d}E$

are included: $N_a = 14$ and $N_b = 36$ for panels (a) and (b), respectively. In both cases, the magnitude of the current density follows a lognormal distribution. The width of the lognormal distribution decreases for a larger number of states. Naively, from a simple summation of random quantities, one might expect a square root dependence, i.e., $\sigma \propto 1/\sqrt{N}$. The data, however, suggest that the decay of the width is much slower; specifically, the decay of the widths, $\sigma_b/\sigma_a = 1.06/1.23 = 0.86$, is slower than the decay of the (inverse) square root of the number of states, $\sqrt{N_a/N_b} = \sqrt{14/36} = 0.62$.

Pristine AGNR41

The current density distribution and the distributions of the related angles of pristine AGNR41 are shown in Fig. D.12. As usual, the current density is normalized to the average through current. The distribution shows only few values above 0 and no tails for larger (positive) values, i.e., only very few values exceed the average through current.

(a) High transmission: $\mathcal{T} = 0.6$

(b) Low transmission: $\mathcal{T} = 0.004$
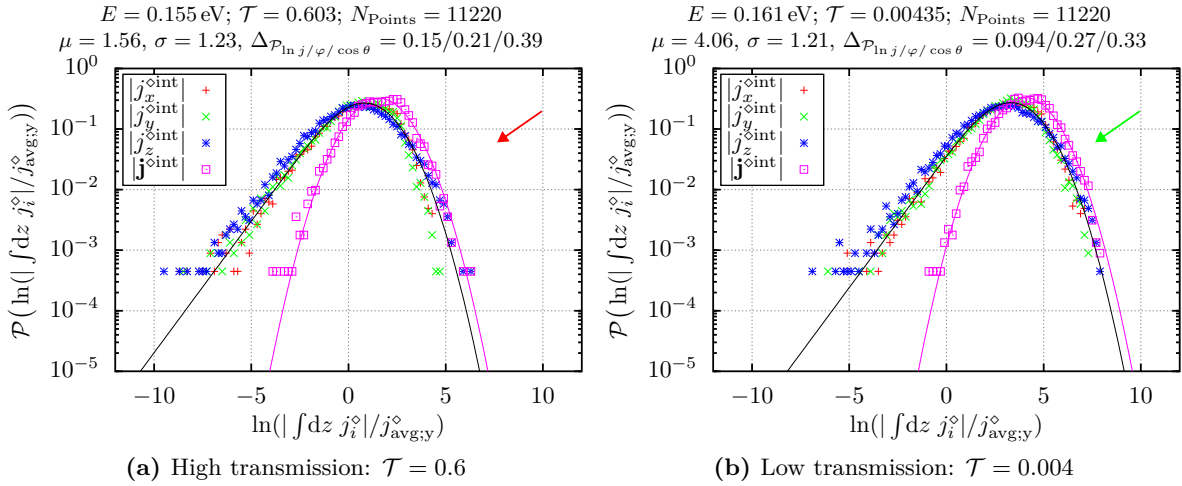
Figure D.10: Distribution functions for the current density response $\mathbf{j}^{\diamond} = \mathrm{d}\mathbf{j}/\mathrm{d}V_{\mathrm{bias}}$ taken at (a) high and (b) low transmission values. The current density is integrated over the z-direction and normalized to the average through current $j^{\diamond}_{\mathrm{avg;y}} = \mathrm{d}I_{\mathrm{total}}/(L_y \mathrm{d}V_{\mathrm{bias}})$. The colored arrows refer to Fig. 4.15 (top), where they mark the energy at which the current density response is taken. The magenta parabola is a lognormal distribution $\mathcal{P}_{\mathrm{lognormal}}$ parametrized by the mean μ and the width σ given in the plot titles. The expectation for a single vector component, $\mathcal{P}_{\mathrm{component}}$, is given by a black line.

(a) voltage V_{bias}=0.42 V – states N_a=14

(b) voltage V_{bias}=1.6 V – states N_b=36
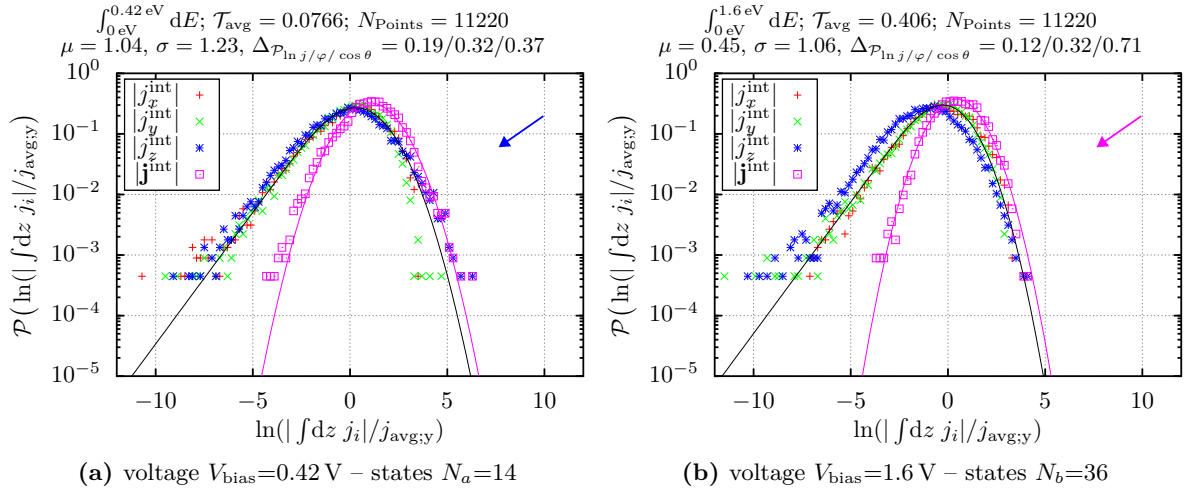
Figure D.11: Distribution functions for the current density **j** at two different bias voltages. The current density is integrated over the z-direction and normalized to the average through current $j_{\text{avg;y}} = I_{\text{total}}/L_y$. The colored arrows refer to Fig. 4.15 (center), where they mark the energy range over which the current density is integrated. The magenta parabola is a lognormal distribution $\mathcal{P}_{\text{lognormal}}$ parametrized by the mean μ and the width σ given in the plot titles. The expectation for a single vector component, $\mathcal{P}_{\text{component}}$, is given by the black line.

(a) Current density distribution in pristine AGNR41

(b) Angle distributions in pristine AGNR41
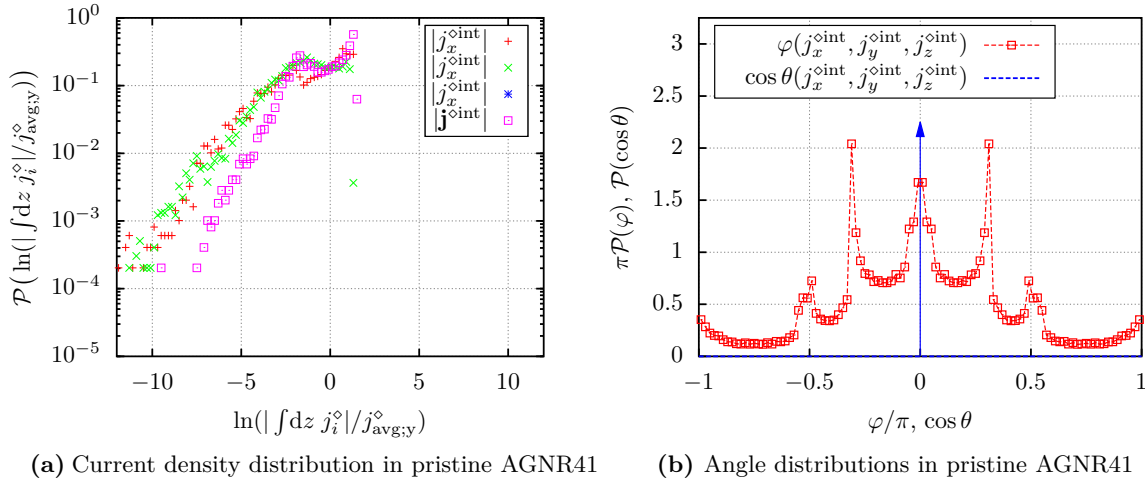
Figure D.12: (a) Distribution functions for the current density response $\mathbf{j}^{\diamond} = \text{d}\mathbf{j}/\text{d}V_{\text{bias}}$. The current density is integrated over the z-direction and normalized to the average through current $j^{\diamond}_{\text{avg;y}} = \text{d}I_{\text{total}}/(L_y \text{d}V_{\text{bias}})$. Because of the exact z-mirror symmetry, the value of $\int j_z \, \text{d}z$ is always exactly zero. (b) The related distribution for the angles. Because of the exact z-mirror symmetry, only $\cos\theta = 0$ is allowed, leading to a Dirac delta function $\mathcal{P}(\cos\theta)=\delta(\cos\theta)$.

D.6 Raw data: magnetization response $\mathbf{d}m_z/\mathbf{d}V_{\mathbf{bias}}$

In Sec. 4.3, especially in Fig. 4.19, we analyzed the system size dependence of the magnetic response dm_z/dV_{bias}. For that purpose, for each system size, we calculated the magnetic response for several energies E_i featuring high transmission values (see Appx. D.7 for the transmission curves). The raw values are shown in Tab. D.1.

The average values

$$\left\langle \frac{dm_z}{dV_{\mathrm{bias}}} \right\rangle = \frac{1}{N} \sum_{i=1}^{N} \frac{dm_z(E_i)}{dV_{\mathrm{bias}}} \qquad (D.25)$$

as well as the standard deviations

$$\sigma_{dm_z/dV_{\mathrm{bias}}} = \sqrt{ \frac{1}{N-1} \sum_{i=1}^{N} \left[\left\langle \frac{dm_z}{dV_{\mathrm{bias}}} \right\rangle - \frac{dm_z(E_i)}{dV_{\mathrm{bias}}} \right]^2 }$$
$$(D.26)$$

are shown in Tab. D.2.

System	$E - \varepsilon_{\mathrm{F}}$	dm_z/dV_{bias}
AGNR6×29	$-1.3150\,\mathrm{eV}$	$+0.6611\,\mu_{\mathrm{B}}/\mathrm{V}$
	$-0.5115\,\mathrm{eV}$	$-0.8719\,\mu_{\mathrm{B}}/\mathrm{V}$
	$-0.0605\,\mathrm{eV}$	$+0.3792\,\mu_{\mathrm{B}}/\mathrm{V}$
	$+0.1835\,\mathrm{eV}$	$-4.2071\,\mu_{\mathrm{B}}/\mathrm{V}$
	$+0.2130\,\mathrm{eV}$	$+2.9794\,\mu_{\mathrm{B}}/\mathrm{V}$
	$+0.3910\,\mathrm{eV}$	$+11.9696\,\mu_{\mathrm{B}}/\mathrm{V}$
AGNR8×41	$-0.3030\,\mathrm{eV}$	$+9.3981\,\mu_{\mathrm{B}}/\mathrm{V}$
	$-0.1400\,\mathrm{eV}$	$-3.6439\,\mu_{\mathrm{B}}/\mathrm{V}$
	$-0.0950\,\mathrm{eV}$	$+18.8951\,\mu_{\mathrm{B}}/\mathrm{V}$
	$+0.0070\,\mathrm{eV}$	$-4.3672\,\mu_{\mathrm{B}}/\mathrm{V}$
	$+0.0590\,\mathrm{eV}$	$-1.4230\,\mu_{\mathrm{B}}/\mathrm{V}$
	$+0.0865\,\mathrm{eV}$	$-4.1040\,\mu_{\mathrm{B}}/\mathrm{V}$
AGNR12×59	$-0.3330\,\mathrm{eV}$	$+5.3899\,\mu_{\mathrm{B}}/\mathrm{V}$
	$-0.0725\,\mathrm{eV}$	$-4.3827\,\mu_{\mathrm{B}}/\mathrm{V}$
	$+0.0155\,\mathrm{eV}$	$-10.8772\,\mu_{\mathrm{B}}/\mathrm{V}$
	$+0.0440\,\mathrm{eV}$	$+6.8316\,\mu_{\mathrm{B}}/\mathrm{V}$
	$+0.0660\,\mathrm{eV}$	$+12.5626\,\mu_{\mathrm{B}}/\mathrm{V}$
	$+0.1820\,\mathrm{eV}$	$-7.5150\,\mu_{\mathrm{B}}/\mathrm{V}$
	$+0.2115\,\mathrm{eV}$	$-11.3322\,\mu_{\mathrm{B}}/\mathrm{V}$
AGNR16×83	$-0.1835\,\mathrm{eV}$	$-17.0402\,\mu_{\mathrm{B}}/\mathrm{V}$
	$-0.1040\,\mathrm{eV}$	$-40.4304\,\mu_{\mathrm{B}}/\mathrm{V}$
	$-0.0450\,\mathrm{eV}$	$-10.6666\,\mu_{\mathrm{B}}/\mathrm{V}$
	$+0.0975\,\mathrm{eV}$	$+12.0678\,\mu_{\mathrm{B}}/\mathrm{V}$
	$+0.1225\,\mathrm{eV}$	$+13.4251\,\mu_{\mathrm{B}}/\mathrm{V}$
	$+0.2195\,\mathrm{eV}$	$+10.0110\,\mu_{\mathrm{B}}/\mathrm{V}$

System	$E - \varepsilon_{\mathrm{F}}$	dm_z/dV_{bias}
AGNR8×14	$-0.9090\,\mathrm{eV}$	$-0.3929\,\mu_{\mathrm{B}}/\mathrm{V}$
	$-0.7540\,\mathrm{eV}$	$-0.3992\,\mu_{\mathrm{B}}/\mathrm{V}$
	$-0.4675\,\mathrm{eV}$	$-1.0914\,\mu_{\mathrm{B}}/\mathrm{V}$
	$+0.2730\,\mathrm{eV}$	$+0.6555\,\mu_{\mathrm{B}}/\mathrm{V}$
	$+0.5610\,\mathrm{eV}$	$+5.3023\,\mu_{\mathrm{B}}/\mathrm{V}$
	$+0.8710\,\mathrm{eV}$	$-1.3445\,\mu_{\mathrm{B}}/\mathrm{V}$
AGNR12×20	$-0.5015\,\mathrm{eV}$	$-5.2491\,\mu_{\mathrm{B}}/\mathrm{V}$
	$-0.3060\,\mathrm{eV}$	$+3.9614\,\mu_{\mathrm{B}}/\mathrm{V}$
	$-0.2480\,\mathrm{eV}$	$-2.1956\,\mu_{\mathrm{B}}/\mathrm{V}$
	$+0.1820\,\mathrm{eV}$	$+4.2866\,\mu_{\mathrm{B}}/\mathrm{V}$
	$+0.2035\,\mathrm{eV}$	$-0.6291\,\mu_{\mathrm{B}}/\mathrm{V}$
	$+0.2170\,\mathrm{eV}$	$+3.6162\,\mu_{\mathrm{B}}/\mathrm{V}$
AGNR16×29	$-0.4625\,\mathrm{eV}$	$+6.9511\,\mu_{\mathrm{B}}/\mathrm{V}$
	$-0.3320\,\mathrm{eV}$	$-0.1153\,\mu_{\mathrm{B}}/\mathrm{V}$
	$-0.0105\,\mathrm{eV}$	$+3.6212\,\mu_{\mathrm{B}}/\mathrm{V}$
	$+0.1615\,\mathrm{eV}$	$-4.8307\,\mu_{\mathrm{B}}/\mathrm{V}$
	$+0.3925\,\mathrm{eV}$	$+3.4705\,\mu_{\mathrm{B}}/\mathrm{V}$
	$+0.4475\,\mathrm{eV}$	$+0.3718\,\mu_{\mathrm{B}}/\mathrm{V}$
AGNR24×41	$-1.0550\,\mathrm{eV}$	$-15.2517\,\mu_{\mathrm{B}}/\mathrm{V}$
	$-0.9350\,\mathrm{eV}$	$-0.8779\,\mu_{\mathrm{B}}/\mathrm{V}$
	$-0.7000\,\mathrm{eV}$	$+3.2307\,\mu_{\mathrm{B}}/\mathrm{V}$
	$+0.2485\,\mathrm{eV}$	$+10.5061\,\mu_{\mathrm{B}}/\mathrm{V}$
	$+0.2980\,\mathrm{eV}$	$-2.6444\,\mu_{\mathrm{B}}/\mathrm{V}$
	$+0.3130\,\mathrm{eV}$	$-3.9263\,\mu_{\mathrm{B}}/\mathrm{V}$
AGNR34×59	$-0.3660\,\mathrm{eV}$	$+2.7975\,\mu_{\mathrm{B}}/\mathrm{V}$
	$-0.3095\,\mathrm{eV}$	$+15.9137\,\mu_{\mathrm{B}}/\mathrm{V}$
	$-0.2650\,\mathrm{eV}$	$-19.3498\,\mu_{\mathrm{B}}/\mathrm{V}$
	$+0.1525\,\mathrm{eV}$	$+12.0663\,\mu_{\mathrm{B}}/\mathrm{V}$
	$+0.2125\,\mathrm{eV}$	$+0.5942\,\mu_{\mathrm{B}}/\mathrm{V}$
	$+0.2200\,\mathrm{eV}$	$-4.5360\,\mu_{\mathrm{B}}/\mathrm{V}$

Table D.1: The magnetic response dm_z/dV_{bias} taken at energies with high transmission values for several differently sized AGNR$N_x \times N_y$. The data is used in Fig. 4.19 to discuss the system size dependence of the magnetic response.

System	$\langle \mathrm{d}m_z/\mathrm{d}V_{\mathrm{bias}} \rangle$	$\sigma_{\mathrm{d}m_z/\mathrm{d}V_{\mathrm{bias}}}$
AGNR6×29	$+1.8184\,\mu_{\mathrm{B}}/\mathrm{V}$	$5.5018\,\mu_{\mathrm{B}}/\mathrm{V}$
AGNR8×41	$+2.4592\,\mu_{\mathrm{B}}/\mathrm{V}$	$9.5946\,\mu_{\mathrm{B}}/\mathrm{V}$
AGNR12×59	$-1.3319\,\mu_{\mathrm{B}}/\mathrm{V}$	$9.5179\,\mu_{\mathrm{B}}/\mathrm{V}$
AGNR16×83	$-5.4389\,\mu_{\mathrm{B}}/\mathrm{V}$	$21.3886\,\mu_{\mathrm{B}}/\mathrm{V}$

System	$\langle \mathrm{d}m_z/\mathrm{d}V_{\mathrm{bias}} \rangle$	$\sigma_{\mathrm{d}m_z/\mathrm{d}V_{\mathrm{bias}}}$
AGNR8×14	$+0.4550\,\mu_{\mathrm{B}}/\mathrm{V}$	$2.4745\,\mu_{\mathrm{B}}/\mathrm{V}$
AGNR12×20	$+0.6317\,\mu_{\mathrm{B}}/\mathrm{V}$	$3.9375\,\mu_{\mathrm{B}}/\mathrm{V}$
AGNR16×29	$+1.5781\,\mu_{\mathrm{B}}/\mathrm{V}$	$4.0502\,\mu_{\mathrm{B}}/\mathrm{V}$
AGNR24×41	$-1.4939\,\mu_{\mathrm{B}}/\mathrm{V}$	$8.5231\,\mu_{\mathrm{B}}/\mathrm{V}$
AGNR34×59	$+1.2476\,\mu_{\mathrm{B}}/\mathrm{V}$	$12.5911\,\mu_{\mathrm{B}}/\mathrm{V}$

Table D.2: The average and standard deviation of the magnetic responses $\mathrm{d}m_z/\mathrm{d}V_{\mathrm{bias}}$ listed in Tab. D.1.

D.7 Raw data: transmission & distribution functions

In Sec. 4.2.1 and Sec. 4.2.2, we investigated the dependence on the system size and on the impurity concentration, respectively, on the flow of the moments belonging to the distribution functions of the underlying current density. For that purpose, we calculated the transmission function for each system, and selected six energies which feature transmission peaks. For these six energies, the current density response and the associated distributions were calculated. Then, we averaged the moments over all six energies and discussed the flow in dependence on system size and hydrogen concentration (cf. Fig. 4.11 and Fig. 4.12).

In this appendix, we present a selection of the raw data. For each system, we show the transmission curve. The six selected energies are marked by red boxes. For one of these energies (marked by a filled red box), the corresponding distribution function of the current density is also plotted. Its mean value μ and width σ, as well as the deviation measures (as defined in Appx. D.5.1) are given in the title off each distribution function. In

all cases, a lognormal distribution $\mathcal{P}_{\mathrm{lognormal}}$ parameterized by mean μ and width σ is shown for comparison (solid magenta). The expectation $\mathcal{P}_{\mathrm{component}}$ for a single vector component (cf. Appx. D.5.2) is drawn as a solid black line.

In some systems, we also analyzed the relaxation effects (cf. Sec. 4.4). In that cases, a transmission function $\mathcal{T}_{\mathrm{unrelaxed}}$ for the unrelaxed ribbon is also plotted (dashed cyan).

On the following pages, the described selection of the raw data is shown for

- size dependence in Appx. D.7.1,
- impurity concentration variation in Appx. D.7.2,
- AGNR 41/42/43 dependence in Appx. D.7.3.

Afterwards, the statistical values of all distribution functions (same order as in Fig. D.13–Fig. D.18) are listed in Tab. D.3–Tab. D.5.

D.7.1 Size dependence

(a) AGNR8x14, 20% H

(b) AGNR12x20, 20% H

(c) AGNR16x29, 20% H

(d) AGNR24x41, 20% H (1)

(e) AGNR34x59, 20% H

(f) AGNR8x14, 20% H

(g) AGNR12x20, 20% H

(h) AGNR16x29, 20% H

(i) AGNR24x41, 20% H (1)

(j) AGNR34x59, 20% H
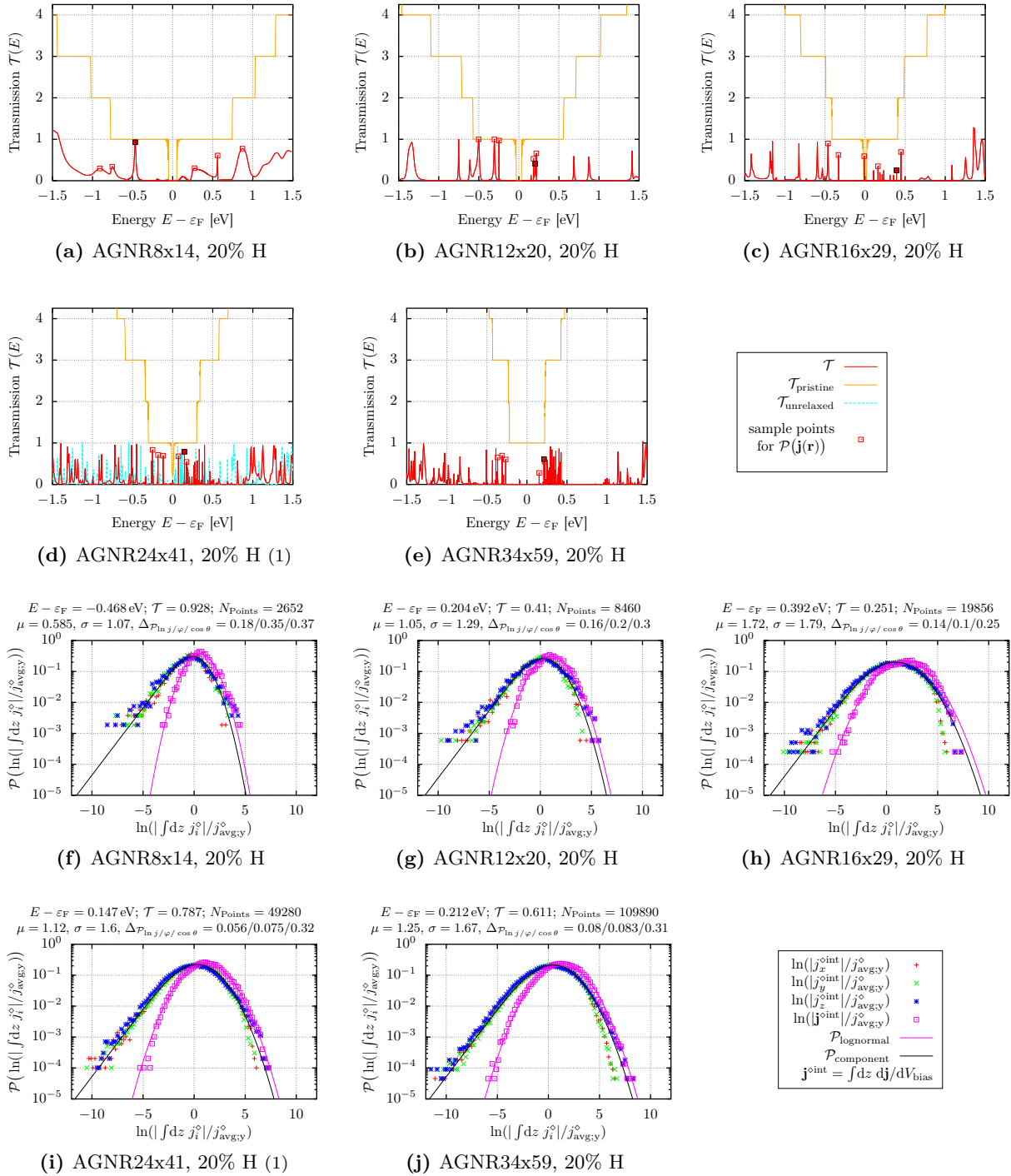
Figure D.13: Raw data for different sizes of square hydrogenated AGNRs (20% hydrogen, $L/W = 1$).

Size dependence (continued)

(a) AGNR6x29, 20% H

(b) AGNR8x41, 20% H (1)

(c) AGNR8x41, 20% H (2)

(d) AGNR12x59, 20% H

(e) AGNR16x83, 20% H

(f) AGNR6x29, 20% H

(g) AGNR8x41, 20% H (1)

(h) AGNR8x41, 20% H (2)

(i) AGNR12x59, 20% H

(j) AGNR16x83, 20% H
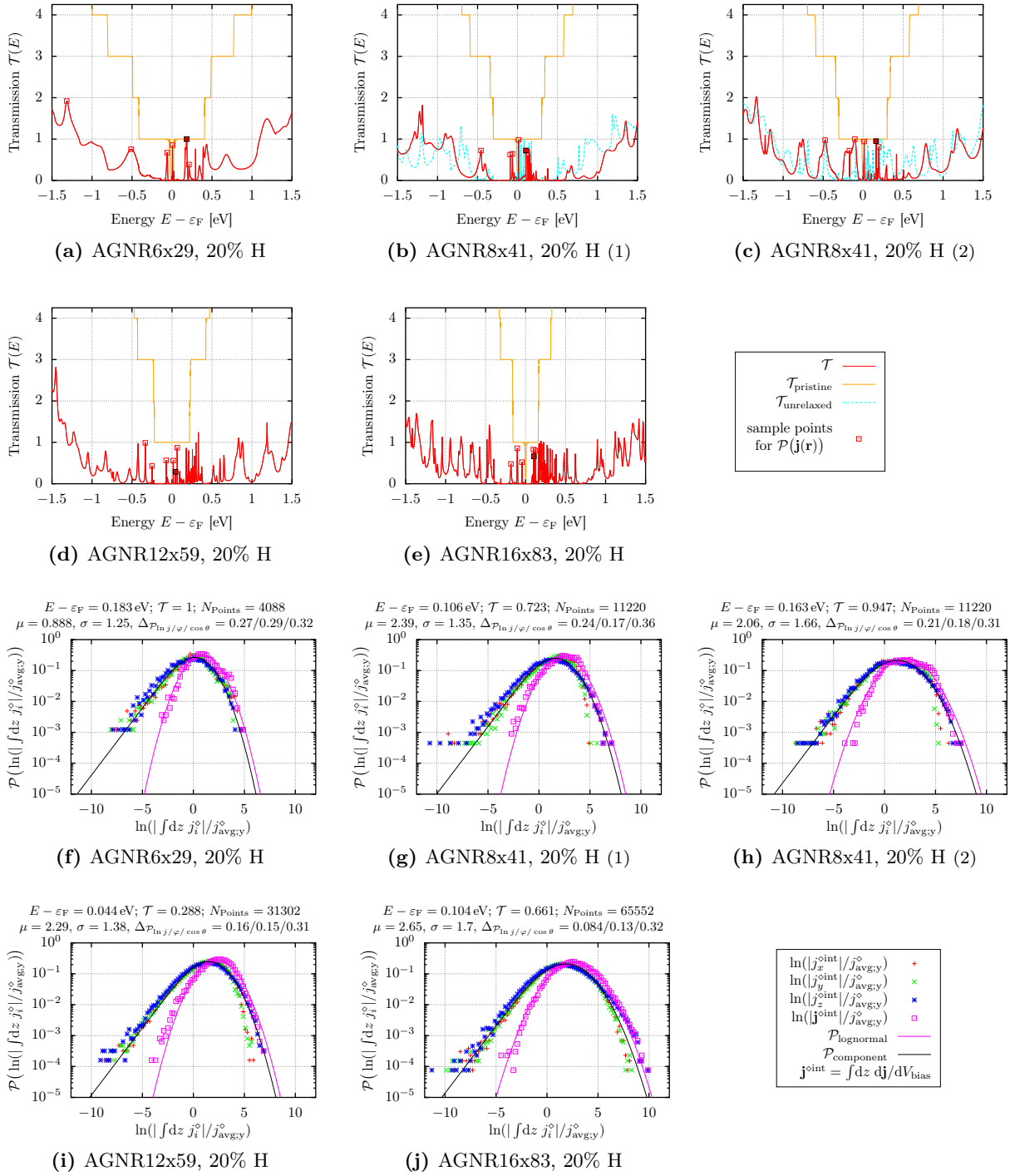
Figure D.14: Raw data for different sizes of wide hydrogenated AGNRs (20% hydrogen, $L/W = 3$).

D.7.2 Impurity concentration variation

(b) AGNR24x41, 1% H

(c) AGNR24x41, 5% H

(d) AGNR24x41, 10% H

(e) AGNR24x41, 20% H (1)

(f) AGNR24x41, 40% H

(g) AGNR24x41, 0% H

(h) AGNR24x41, 1% H

(i) AGNR24x41, 5% H

(j) AGNR24x41, 10% H

(k) AGNR24x41, 20% H (1)

(l) AGNR24x41, 40% H
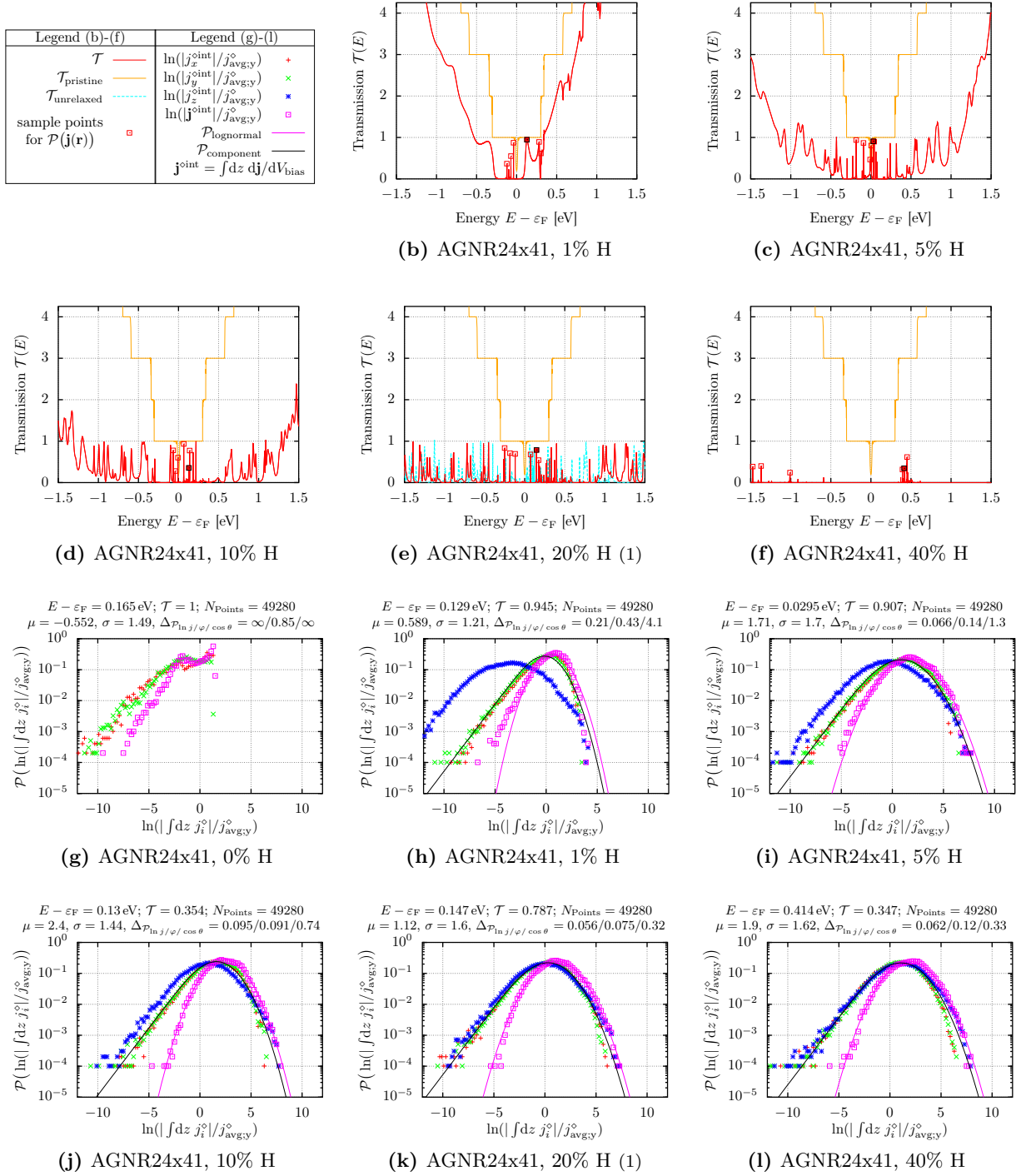
Figure D.15: Raw data for varying hydrogen concentration of a square AGNR24×41 ($L/W = 1$). (a) The transmission function $\mathcal{T}_{\mathrm{pristine}}$ of pristine AGNR has been omitted in favor of a legend since $\mathcal{T}_{\mathrm{pristine}}$ is shown in all other transmission plots anyway.

Impurity concentration variation (continued)

(b) AGNR8x41, 1% H

(c) AGNR8x41, 5% H

(d) AGNR8x41, 10% H

(e) AGNR8x41, 20% H (1)

(f) AGNR8x41, 40% H

(g) AGNR8x41, 0% H

(h) AGNR8x41, 1% H

(i) AGNR8x41, 5% H

(j) AGNR8x41, 10% H

(k) AGNR8x41, 20% H (1)

(l) AGNR8x41, 40% H
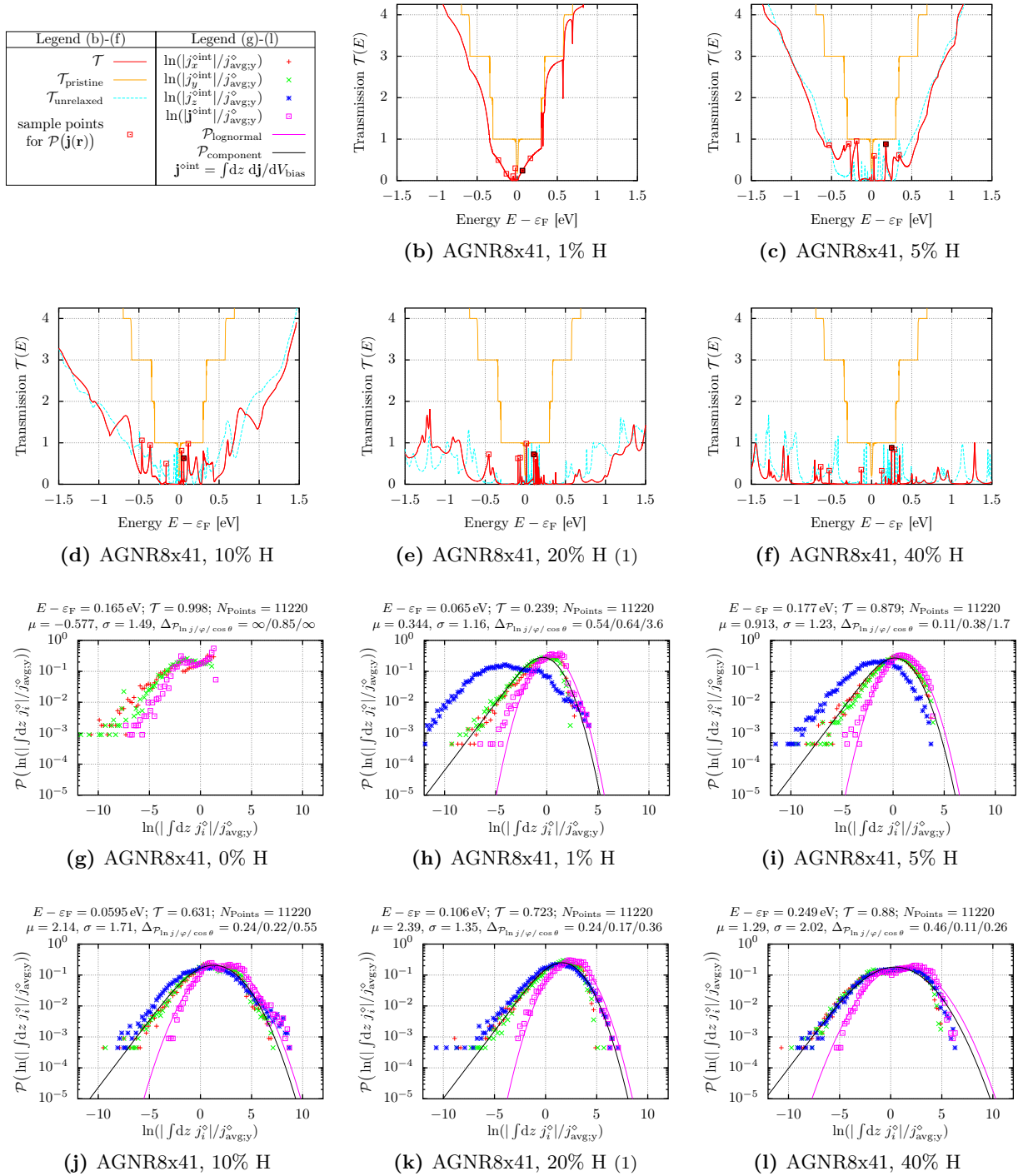
Figure D.16: Raw data for varying hydrogen concentration of a wide AGNR8×41 ($L/W = 3$). (a) The transmission function $\mathcal{T}_{\text{pristine}}$ of pristine AGNR has been omitted in favor of a legend since $\mathcal{T}_{\text{pristine}}$ is shown in all other transmission plots anyway.

D.7.3 AGNR 41/42/43 dependence

(a) AGNR24x41, 20% H (2)

(b) AGNR24x42, 20% H

(c) AGNR24x43, 20% H

(d) AGNR24x41, 20% H (2)

(e) AGNR24x42, 20% H

(f) AGNR24x43, 20% H

Figure D.17: Raw data for hydrogenated square AGNR24×41/42/43 (20% hydrogen, $L/W = 1$). Due to lack of space, the legend is not reproduced (see previous pages).

(a) AGNR8x41, 20% H (3)

(b) AGNR8x42, 20% H

(c) AGNR8x43, 20% H

(d) AGNR8x41, 20% H (2)

(e) AGNR8x42, 20% H

(f) AGNR8x43, 20% H

Figure D.18: Raw data for hydrogenated wide AGNR8×41/42/43 (20% hydrogen, $L/W = 3$). Due to lack of space, the legend is not reproduced (see previous pages).

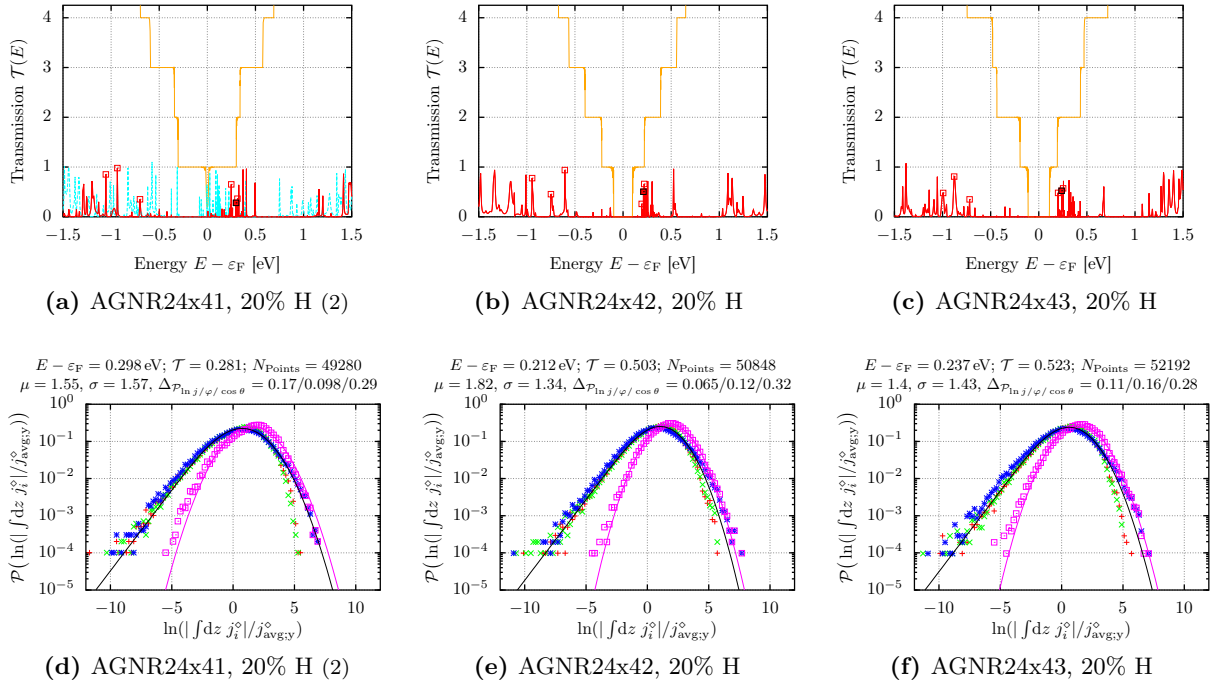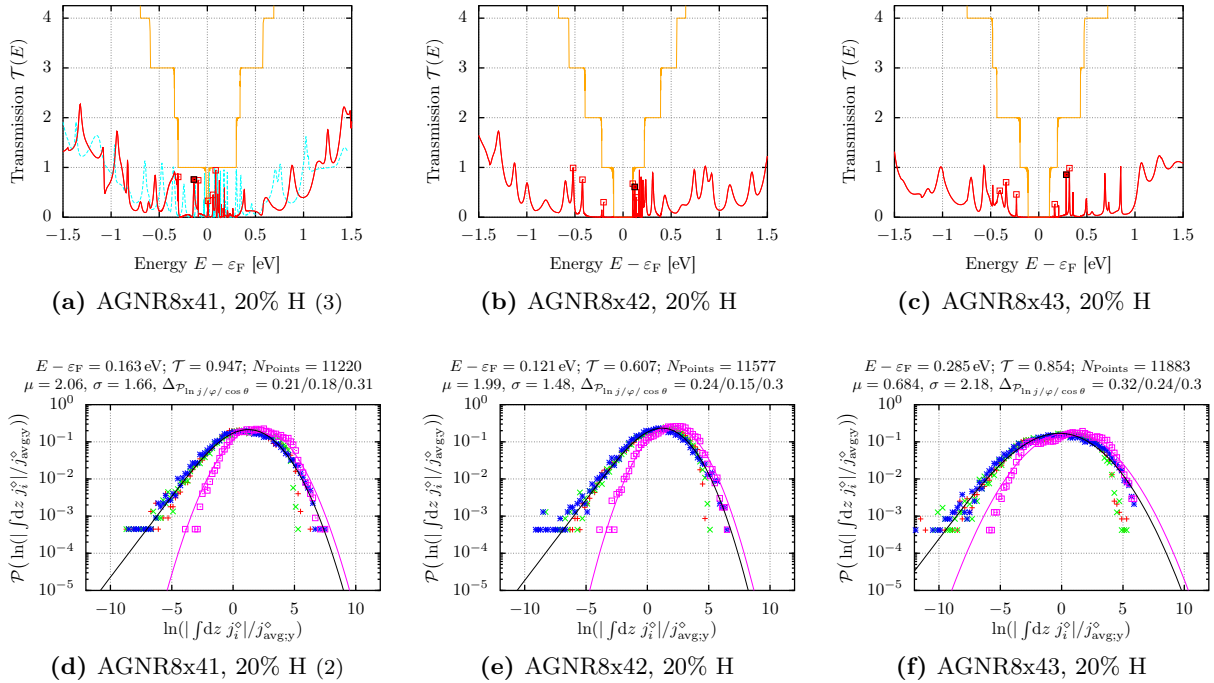| System	$E-\varepsilon_{\mathrm{F}}$	$\mathcal{T}(E)$	$\mathrm{d}m_z/\mathrm{d}V_{\mathrm{bias}}$	$\mu(\mathcal{P}_{\ln j})$	$\sigma(\mathcal{P}_{\ln j})$	$\Delta_{\mathcal{P}_{\ln j}}$	$\Delta_{\mathcal{P}_\varphi}$	$\Delta_{\mathcal{P}_{\cos\theta}}$
AGNR8x14 20% H	$-0.9090\,\mathrm{eV}$	0.2954	$-0.393\,\mu_{\mathrm{B}}/\mathrm{V}$	0.9981	1.3399	0.1277	0.5622	0.4008
	$-0.7540\,\mathrm{eV}$	0.3386	$-0.399\,\mu_{\mathrm{B}}/\mathrm{V}$	1.0436	1.2204	0.1463	0.4310	0.3487
	$-0.4675\,\mathrm{eV}$	0.9282	$-1.09\,\mu_{\mathrm{B}}/\mathrm{V}$	0.5851	1.0660	0.1841	0.3486	0.3660
	$+0.2730\,\mathrm{eV}$	0.3019	$+0.656\,\mu_{\mathrm{B}}/\mathrm{V}$	0.7021	1.5780	0.2104	0.3674	0.4230
	$+0.5610\,\mathrm{eV}$	0.6074	$+5.3\,\mu_{\mathrm{B}}/\mathrm{V}$	1.3262	1.6842	0.3986	0.3273	0.3145
	$+0.8710\,\mathrm{eV}$	0.7729	$-1.34\,\mu_{\mathrm{B}}/\mathrm{V}$	0.1926	1.1944	0.2088	0.3020	0.5124
AGNR12x20 20% H	$-0.5015\,\mathrm{eV}$	0.9987	$-5.25\,\mu_{\mathrm{B}}/\mathrm{V}$	0.8248	1.4275	0.5118	0.3367	0.3587
	$-0.3060\,\mathrm{eV}$	0.9961	$+3.96\,\mu_{\mathrm{B}}/\mathrm{V}$	0.5462	1.3121	0.1560	0.2717	0.3599
	$-0.2480\,\mathrm{eV}$	0.9697	$-2.2\,\mu_{\mathrm{B}}/\mathrm{V}$	1.7501	1.5494	0.2910	0.2297	0.3343
	$+0.1820\,\mathrm{eV}$	0.5302	$+4.29\,\mu_{\mathrm{B}}/\mathrm{V}$	2.1480	1.8125	0.1607	0.1951	0.3213
	$+0.2035\,\mathrm{eV}$	0.4099	$-0.629\,\mu_{\mathrm{B}}/\mathrm{V}$	1.0549	1.2896	0.1585	0.2004	0.3049
	$+0.2170\,\mathrm{eV}$	0.6599	$+3.62\,\mu_{\mathrm{B}}/\mathrm{V}$	2.1199	1.2513	0.1598	0.2137	0.2890
AGNR16x29 20% H	$-0.4625\,\mathrm{eV}$	0.8991	$+6.95\,\mu_{\mathrm{B}}/\mathrm{V}$	0.2877	1.5069	0.1248	0.1923	0.4254
	$-0.3320\,\mathrm{eV}$	0.6220	$-0.115\,\mu_{\mathrm{B}}/\mathrm{V}$	1.3861	1.4475	0.2137	0.2541	0.3783
	$-0.0105\,\mathrm{eV}$	0.5923	$+3.62\,\mu_{\mathrm{B}}/\mathrm{V}$	1.5744	1.2834	0.0883	0.2640	0.2958
	$+0.1615\,\mathrm{eV}$	0.3498	$-4.83\,\mu_{\mathrm{B}}/\mathrm{V}$	2.5073	1.3759	0.1452	0.1619	0.2360
	$+0.3925\,\mathrm{eV}$	0.2507	$+3.47\,\mu_{\mathrm{B}}/\mathrm{V}$	1.7150	1.7886	0.1436	0.1044	0.2549
	$+0.4475\,\mathrm{eV}$	0.6938	$+0.372\,\mu_{\mathrm{B}}/\mathrm{V}$	1.2879	1.3663	0.0822	0.2090	0.2792
AGNR24x41 20% H (1)	$-0.2505\,\mathrm{eV}$	0.8342	$-20.1\,\mu_{\mathrm{B}}/\mathrm{V}$	0.7483	1.9559	0.2368	0.0828	0.3037
	$-0.1840\,\mathrm{eV}$	0.7113	$-2.15\,\mu_{\mathrm{B}}/\mathrm{V}$	0.8334	1.6644	0.1106	0.1279	0.3347
	$-0.1190\,\mathrm{eV}$	0.6928	$+11.5\,\mu_{\mathrm{B}}/\mathrm{V}$	0.1997	2.0014	0.2715	0.1653	0.3251
	$+0.0730\,\mathrm{eV}$	0.6798	$+0.586\,\mu_{\mathrm{B}}/\mathrm{V}$	0.9204	1.5236	0.0957	0.1653	0.3530
	$+0.1470\,\mathrm{eV}$	0.7874	$-12.4\,\mu_{\mathrm{B}}/\mathrm{V}$	1.1230	1.5968	0.0561	0.0747	0.3218
	$+0.1730\,\mathrm{eV}$	0.5425	$+13.4\,\mu_{\mathrm{B}}/\mathrm{V}$	1.5941	1.4222	0.1312	0.1172	0.3204
AGNR34x59 20% H	$-0.3660\,\mathrm{eV}$	0.6509	$+2.8\,\mu_{\mathrm{B}}/\mathrm{V}$	0.5694	1.8873	0.2304	0.0866	0.3123
	$-0.3095\,\mathrm{eV}$	0.6958	$+15.9\,\mu_{\mathrm{B}}/\mathrm{V}$	0.0955	2.7016	0.4387	0.0542	0.3092
	$-0.2650\,\mathrm{eV}$	0.6025	$-19.3\,\mu_{\mathrm{B}}/\mathrm{V}$	0.0240	2.4259	0.4382	0.1262	0.3143
	$+0.1525\,\mathrm{eV}$	0.2778	$+12.1\,\mu_{\mathrm{B}}/\mathrm{V}$	-0.3291	2.7985	0.4070	0.0520	0.2788
	$+0.2125\,\mathrm{eV}$	0.6112	$+0.594\,\mu_{\mathrm{B}}/\mathrm{V}$	1.2548	1.6676	0.0798	0.0834	0.3063
	$+0.2200\,\mathrm{eV}$	0.5486	$-4.54\,\mu_{\mathrm{B}}/\mathrm{V}$	1.4540	1.7585	0.1655	0.0763	0.3074
AGNR6x29 20% H	$-1.3150\,\mathrm{eV}$	1.9199	$+0.661\,\mu_{\mathrm{B}}/\mathrm{V}$	-0.0772	1.0716	0.1441	0.5741	0.3294
	$-0.5115\,\mathrm{eV}$	0.7537	$-0.872\,\mu_{\mathrm{B}}/\mathrm{V}$	0.1620	1.3891	0.1897	0.4370	0.3911
	$-0.0605\,\mathrm{eV}$	0.6717	$+0.379\,\mu_{\mathrm{B}}/\mathrm{V}$	0.8367	1.8668	0.3861	0.3026	0.2268
	$+0.0075\,\mathrm{eV}$	0.8557	$+35.6\,\mu_{\mathrm{B}}/\mathrm{V}$	2.6981	1.6417	0.4607	0.4078	0.3253
	$+0.1835\,\mathrm{eV}$	0.9999	$-4.21\,\mu_{\mathrm{B}}/\mathrm{V}$	0.8882	1.2488	0.2716	0.2862	0.3162
	$+0.2130\,\mathrm{eV}$	0.3840	$+2.98\,\mu_{\mathrm{B}}/\mathrm{V}$	1.4008	1.1698	0.1619	0.2775	0.2721
AGNR8x41 20% H (1)	$-0.4570\,\mathrm{eV}$	0.7228	$+1.3\,\mu_{\mathrm{B}}/\mathrm{V}$	0.3925	1.3175	0.1332	0.4304	0.4266
	$-0.0925\,\mathrm{eV}$	0.6258	$-0.7\,\mu_{\mathrm{B}}/\mathrm{V}$	1.0056	1.5739	0.4354	0.2384	0.3782
	$-0.0640\,\mathrm{eV}$	0.6424	$-1.78\,\mu_{\mathrm{B}}/\mathrm{V}$	1.3494	1.7189	0.4096	0.2549	0.4783
	$+0.0130\,\mathrm{eV}$	0.9829	$-3.53\,\mu_{\mathrm{B}}/\mathrm{V}$	1.5689	1.3280	0.1140	0.3196	0.4066
	$+0.1055\,\mathrm{eV}$	0.7227	$-11.3\,\mu_{\mathrm{B}}/\mathrm{V}$	2.3864	1.3507	0.2441	0.1681	0.3642
	$+0.1290\,\mathrm{eV}$	0.6055	$+0.154\,\mu_{\mathrm{B}}/\mathrm{V}$	1.2690	1.6147	0.1515	0.2114	0.3220
AGNR8x41 20% H (2)	$-0.4750\,\mathrm{eV}$	0.9738	$+6.95\,\mu_{\mathrm{B}}/\mathrm{V}$	-0.4061	2.1427	0.3599	0.2161	0.3356
	$-0.1720\,\mathrm{eV}$	0.7209	$+4.69\,\mu_{\mathrm{B}}/\mathrm{V}$	1.3903	1.2021	0.2281	0.3220	0.4042
	$-0.1035\,\mathrm{eV}$	0.9979	$+7.16\,\mu_{\mathrm{B}}/\mathrm{V}$	0.1159	1.5548	0.2069	0.3285	0.4509
	$+0.0135\,\mathrm{eV}$	0.9421	$+5.05\,\mu_{\mathrm{B}}/\mathrm{V}$	1.2009	1.4521	0.3604	0.2647	0.4017
	$+0.1625\,\mathrm{eV}$	0.9471	$-0.397\,\mu_{\mathrm{B}}/\mathrm{V}$	2.0616	1.6557	0.2062	0.1767	0.3088
	$+0.1965\,\mathrm{eV}$	0.8127	$-2.26\,\mu_{\mathrm{B}}/\mathrm{V}$	2.3037	1.8516	0.2616	0.1236	0.2669
AGNR12x59 20% H	$-0.3330\,\mathrm{eV}$	0.9867	$+5.39\,\mu_{\mathrm{B}}/\mathrm{V}$	-0.0372	2.0210	0.1585	0.1278	0.3200
	$-0.2490\,\mathrm{eV}$	0.4289	$+3.89\,\mu_{\mathrm{B}}/\mathrm{V}$	0.5764	2.2753	0.2646	0.1111	0.3331
	$-0.0725\,\mathrm{eV}$	0.5645	$-4.38\,\mu_{\mathrm{B}}/\mathrm{V}$	1.0371	1.6456	0.0800	0.1586	0.3125
	$+0.0155\,\mathrm{eV}$	0.5584	$-10.9\,\mu_{\mathrm{B}}/\mathrm{V}$	0.1561	2.1050	0.2302	0.1209	0.3080
	$+0.0440\,\mathrm{eV}$	0.2878	$+6.83\,\mu_{\mathrm{B}}/\mathrm{V}$	2.2938	1.3797	0.1591	0.1491	0.3111
	$+0.0660\,\mathrm{eV}$	0.8691	$+12.6\,\mu_{\mathrm{B}}/\mathrm{V}$	1.9347	1.3538	0.0764	0.1161	0.2914
AGNR16x83 20% H	$-0.1835\,\mathrm{eV}$	0.4777	$-17\,\mu_{\mathrm{B}}/\mathrm{V}$	-1.8140	3.2002	0.4553	0.1311	0.3582
	$-0.1040\,\mathrm{eV}$	0.8578	$-40.4\,\mu_{\mathrm{B}}/\mathrm{V}$	-0.2820	2.6604	0.1961	0.0975	0.3385
	$-0.0450\,\mathrm{eV}$	0.5207	$-10.7\,\mu_{\mathrm{B}}/\mathrm{V}$	1.9658	2.4992	0.3215	0.0871	0.3592
	$+0.0975\,\mathrm{eV}$	0.8260	$+12.1\,\mu_{\mathrm{B}}/\mathrm{V}$	1.0578	1.7898	0.1670	0.0853	0.3029
	$+0.1040\,\mathrm{eV}$	0.6612	$+67.8\,\mu_{\mathrm{B}}/\mathrm{V}$	2.6474	1.7039	0.0840	0.1265	0.3228
	$+0.1225\,\mathrm{eV}$	0.8038	$+13.4\,\mu_{\mathrm{B}}/\mathrm{V}$	0.2501	2.3483	0.3133	0.0861	0.2957

Table D.3: Statistical data of the distribution funtions $\mathcal{P}_{\ln j} = \mathcal{P}[\ln|\mathbf{j}(E)|/j^{\diamond}_{\mathrm{avg;y}}]$. The corresponding transmission functions and selected distribution functions are shown in Fig. D.13–Fig. D.18

System	$E-\varepsilon_{\mathrm{F}}$	$\mathcal{T}(E)$	$\mathrm{d}m_z/\mathrm{d}V_{\mathrm{bias}}$	$\mu(\mathcal{P}_{\ln j})$	$\sigma(\mathcal{P}_{\ln j})$	$\Delta_{\mathcal{P}_{\ln j}}$	$\Delta_{\mathcal{P}_\varphi}$	$\Delta_{\mathcal{P}_{\cos\theta}}$
AGNR24x41 0% H	$-0.2350\,\mathrm{eV}$	0.9661	$-0.000613\,\mu_\mathrm{B}/\mathrm{V}$	-0.6173	1.5174	$+\infty$	0.8822	$+\infty$
	$-0.2350\,\mathrm{eV}$	0.9661	$-0.000613\,\mu_\mathrm{B}/\mathrm{V}$	-0.6173	1.5174	$+\infty$	0.8822	$+\infty$
	$-0.2350\,\mathrm{eV}$	0.9661	$-0.000613\,\mu_\mathrm{B}/\mathrm{V}$	-0.6173	1.5174	$+\infty$	0.8822	$+\infty$
	$+0.1650\,\mathrm{eV}$	1.0000	$+0.00706\,\mu_\mathrm{B}/\mathrm{V}$	-0.5519	1.4868	$+\infty$	0.8464	$+\infty$
	$+0.1650\,\mathrm{eV}$	1.0000	$+0.00706\,\mu_\mathrm{B}/\mathrm{V}$	-0.5519	1.4868	$+\infty$	0.8464	$+\infty$
	$+0.1650\,\mathrm{eV}$	1.0000	$+0.00706\,\mu_\mathrm{B}/\mathrm{V}$	-0.5519	1.4868	$+\infty$	0.8464	$+\infty$
AGNR24x41 1% H	$-0.1215\,\mathrm{eV}$	0.3679	$+1.08\,\mu_\mathrm{B}/\mathrm{V}$	1.2788	1.3892	0.0818	0.2952	3.3620
	$-0.0715\,\mathrm{eV}$	0.5502	$-23\,\mu_\mathrm{B}/\mathrm{V}$	1.4765	1.7882	0.1780	0.2542	3.6078
	$-0.0390\,\mathrm{eV}$	0.8731	$+29.3\,\mu_\mathrm{B}/\mathrm{V}$	0.8792	1.6367	0.1780	0.2144	3.4119
	$+0.1285\,\mathrm{eV}$	0.9452	$-1.53\,\mu_\mathrm{B}/\mathrm{V}$	0.5894	1.2053	0.2096	0.4345	4.0815
	$+0.2805\,\mathrm{eV}$	0.8925	$-34.7\,\mu_\mathrm{B}/\mathrm{V}$	0.4971	1.2252	0.3429	0.3520	4.1346
	$+0.3035\,\mathrm{eV}$	0.6146	$-4.65\,\mu_\mathrm{B}/\mathrm{V}$	0.1291	1.1223	0.4239	0.7161	4.3325
AGNR24x41 5% H	$-0.1835\,\mathrm{eV}$	0.9366	$+9.23\,\mu_\mathrm{B}/\mathrm{V}$	1.5195	1.4659	0.1035	0.1696	1.5146
	$-0.0930\,\mathrm{eV}$	0.8666	$-11.4\,\mu_\mathrm{B}/\mathrm{V}$	0.8846	1.5322	0.2009	0.1625	1.3365
	$-0.0095\,\mathrm{eV}$	0.4674	$-6.64\,\mu_\mathrm{B}/\mathrm{V}$	0.4203	1.5302	0.1947	0.3070	1.4530
	$+0.0025\,\mathrm{eV}$	0.8036	$-14.2\,\mu_\mathrm{B}/\mathrm{V}$	0.4923	1.6304	0.2440	0.2168	1.3837
	$+0.0295\,\mathrm{eV}$	0.9071	$+14.3\,\mu_\mathrm{B}/\mathrm{V}$	1.7116	1.7002	0.0661	0.1383	1.2550
	$+0.0410\,\mathrm{eV}$	0.8983	$-15.9\,\mu_\mathrm{B}/\mathrm{V}$	1.3704	1.4396	0.0900	0.1982	1.3205
AGNR24x41 10% H	$-0.0665\,\mathrm{eV}$	0.7768	$-5.65\,\mu_\mathrm{B}/\mathrm{V}$	1.2698	1.8946	0.2943	0.1302	0.8777
	$-0.0415\,\mathrm{eV}$	0.2789	$-12.7\,\mu_\mathrm{B}/\mathrm{V}$	1.3883	1.7472	0.3956	0.1244	0.9033
	$-0.0075\,\mathrm{eV}$	0.6004	$-8.5\,\mu_\mathrm{B}/\mathrm{V}$	0.9458	1.5103	0.5695	0.1949	0.8206
	$+0.0655\,\mathrm{eV}$	0.9340	$-7.54\,\mu_\mathrm{B}/\mathrm{V}$	1.6777	1.2955	0.1141	0.1678	0.7630
	$+0.1295\,\mathrm{eV}$	0.3542	$+15.9\,\mu_\mathrm{B}/\mathrm{V}$	2.4018	1.4354	0.0946	0.0911	0.7382
	$+0.1390\,\mathrm{eV}$	0.7732	$+6.48\,\mu_\mathrm{B}/\mathrm{V}$	2.2502	1.5160	0.0954	0.1110	0.6900
AGNR24x41 20% H (1)	$-0.2505\,\mathrm{eV}$	0.8342	$-20.1\,\mu_\mathrm{B}/\mathrm{V}$	0.7483	1.9559	0.2368	0.0828	0.3037
	$-0.1840\,\mathrm{eV}$	0.7113	$-2.15\,\mu_\mathrm{B}/\mathrm{V}$	0.8334	1.6644	0.1106	0.1279	0.3347
	$-0.1190\,\mathrm{eV}$	0.6928	$+11.5\,\mu_\mathrm{B}/\mathrm{V}$	0.1997	2.0014	0.2715	0.1653	0.3251
	$+0.0730\,\mathrm{eV}$	0.6798	$+0.586\,\mu_\mathrm{B}/\mathrm{V}$	0.9204	1.5236	0.0957	0.1653	0.3530
	$+0.1470\,\mathrm{eV}$	0.7874	$-12.4\,\mu_\mathrm{B}/\mathrm{V}$	1.1230	1.5968	0.0561	0.0747	0.3218
	$+0.1730\,\mathrm{eV}$	0.5425	$+13.4\,\mu_\mathrm{B}/\mathrm{V}$	1.5941	1.4222	0.1312	0.1172	0.3204
AGNR24x41 40% H	$-1.4750\,\mathrm{eV}$	0.3874	$-1.54\,\mu_\mathrm{B}/\mathrm{V}$	-0.0906	2.5091	0.3193	0.1756	0.2811
	$-1.3700\,\mathrm{eV}$	0.4011	$+0.686\,\mu_\mathrm{B}/\mathrm{V}$	0.6564	2.2802	0.2199	0.1929	0.2999
	$-1.0100\,\mathrm{eV}$	0.2411	$-2.23\,\mu_\mathrm{B}/\mathrm{V}$	0.0710	2.3313	0.2963	0.1666	0.3262
	$+0.3935\,\mathrm{eV}$	0.3170	$-1.34\,\mu_\mathrm{B}/\mathrm{V}$	1.0828	1.8347	0.0744	0.1410	0.3239
	$+0.4145\,\mathrm{eV}$	0.3475	$+0.0593\,\mu_\mathrm{B}/\mathrm{V}$	1.9014	1.6171	0.0625	0.1190	0.3264
	$+0.4515\,\mathrm{eV}$	0.6159	$+17.7\,\mu_\mathrm{B}/\mathrm{V}$	0.9223	2.1846	0.1396	0.0582	0.2685
AGNR8x41 0% H	$-0.2350\,\mathrm{eV}$	0.9960	$-0.000461\,\mu_\mathrm{B}/\mathrm{V}$	-0.6459	1.5270	$+\infty$	0.8943	$+\infty$
	$-0.2350\,\mathrm{eV}$	0.9960	$-0.000461\,\mu_\mathrm{B}/\mathrm{V}$	-0.6459	1.5270	$+\infty$	0.8943	$+\infty$
	$-0.2350\,\mathrm{eV}$	0.9960	$-0.000461\,\mu_\mathrm{B}/\mathrm{V}$	-0.6459	1.5270	$+\infty$	0.8943	$+\infty$
	$+0.1650\,\mathrm{eV}$	0.9985	$+0.00059\,\mu_\mathrm{B}/\mathrm{V}$	-0.5766	1.4921	$+\infty$	0.8544	$+\infty$
	$+0.1650\,\mathrm{eV}$	0.9985	$+0.00059\,\mu_\mathrm{B}/\mathrm{V}$	-0.5766	1.4921	$+\infty$	0.8544	$+\infty$
	$+0.1650\,\mathrm{eV}$	0.9985	$+0.00059\,\mu_\mathrm{B}/\mathrm{V}$	-0.5766	1.4921	$+\infty$	0.8544	$+\infty$
AGNR8x41 1% H	$-0.2350\,\mathrm{eV}$	0.4926	$-0.162\,\mu_\mathrm{B}/\mathrm{V}$	-0.0289	1.1504	0.6796	0.6694	3.7350
	$-0.1350\,\mathrm{eV}$	0.1636	$-0.0967\,\mu_\mathrm{B}/\mathrm{V}$	0.4143	1.0869	0.4952	0.5622	3.4943
	$-0.0510\,\mathrm{eV}$	0.1067	$-8.89\,\mu_\mathrm{B}/\mathrm{V}$	3.6144	1.3897	0.1587	0.6313	3.2301
	$-0.0240\,\mathrm{eV}$	0.3004	$+9.06\,\mu_\mathrm{B}/\mathrm{V}$	1.7593	1.4254	0.2359	0.3108	3.5352
	$+0.0650\,\mathrm{eV}$	0.2387	$-0.216\,\mu_\mathrm{B}/\mathrm{V}$	0.3443	1.1566	0.5409	0.6442	3.6143
	$+0.1650\,\mathrm{eV}$	0.5391	$-0.043\,\mu_\mathrm{B}/\mathrm{V}$	-0.0429	1.2553	0.7186	0.6793	3.7536
AGNR8x41 5% H	$-0.5290\,\mathrm{eV}$	0.8520	$+7.26\,\mu_\mathrm{B}/\mathrm{V}$	-0.0839	1.4013	0.4253	0.4324	1.4900
	$-0.2860\,\mathrm{eV}$	0.8881	$+2.41\,\mu_\mathrm{B}/\mathrm{V}$	0.6006	1.2023	0.1455	0.3987	1.7572
	$-0.1870\,\mathrm{eV}$	0.9531	$+3.97\,\mu_\mathrm{B}/\mathrm{V}$	0.4227	1.1900	0.1063	0.4130	1.6544
	$+0.0305\,\mathrm{eV}$	0.5963	$-2.95\,\mu_\mathrm{B}/\mathrm{V}$	2.0504	1.4798	0.1736	0.2363	1.5822
	$+0.1775\,\mathrm{eV}$	0.8791	$+9.31\,\mu_\mathrm{B}/\mathrm{V}$	0.9132	1.2268	0.1091	0.3764	1.7358
	$+0.3410\,\mathrm{eV}$	0.6183	$-0.262\,\mu_\mathrm{B}/\mathrm{V}$	0.7836	1.0711	0.3471	0.3962	1.7889
AGNR8x41 10% H	$-0.4625\,\mathrm{eV}$	1.0589	$-1.23\,\mu_\mathrm{B}/\mathrm{V}$	1.1717	1.2229	0.1139	0.3464	0.7319
	$-0.3600\,\mathrm{eV}$	0.9433	$+0.25\,\mu_\mathrm{B}/\mathrm{V}$	1.0028	1.0979	0.0833	0.2832	0.7433
	$-0.1605\,\mathrm{eV}$	0.4973	$-14.1\,\mu_\mathrm{B}/\mathrm{V}$	3.2432	1.4026	0.2171	0.2412	0.5881
	$+0.0320\,\mathrm{eV}$	0.8113	$-7.32\,\mu_\mathrm{B}/\mathrm{V}$	2.3310	1.4021	0.1418	0.2283	0.5276
	$+0.0595\,\mathrm{eV}$	0.6309	$-14.2\,\mu_\mathrm{B}/\mathrm{V}$	2.1408	1.7128	0.2359	0.2187	0.5542
	$+0.1150\,\mathrm{eV}$	0.9789	$+4.03\,\mu_\mathrm{B}/\mathrm{V}$	1.4525	1.2706	0.2097	0.4151	0.6562

Table D.4: Statistical data of the distribution funtions $\mathcal{P}_{\ln j} = \mathcal{P}[\ln|\mathbf{j}(E)|/j^\diamond_{\mathrm{avg;y}}]$. The corresponding transmission functions and selected distribution functions are shown in Fig. D.13–Fig. D.18

System	$E - \varepsilon_{\mathrm{F}}$	$\mathcal{T}(E)$	$\mathrm{d}m_z/\mathrm{d}V_{\mathrm{bias}}$	$\mu(\mathcal{P}_{\ln j})$	$\sigma(\mathcal{P}_{\ln j})$	$\Delta_{\mathcal{P}_{\ln j}}$	$\Delta_{\mathcal{P}_\varphi}$	$\Delta_{\mathcal{P}_{\cos\theta}}$
AGNR8x41 (1) 20% H	$-0.4570\,\mathrm{eV}$	0.7228	$+1.3\,\mu_{\mathrm{B}}/\mathrm{V}$	0.3925	1.3175	0.1332	0.4304	0.4266
	$-0.0925\,\mathrm{eV}$	0.6258	$-0.7\,\mu_{\mathrm{B}}/\mathrm{V}$	1.0056	1.5739	0.4354	0.2384	0.3782
	$-0.0640\,\mathrm{eV}$	0.6424	$-1.78\,\mu_{\mathrm{B}}/\mathrm{V}$	1.3494	1.7189	0.4096	0.2549	0.4783
	$+0.0130\,\mathrm{eV}$	0.9829	$-3.53\,\mu_{\mathrm{B}}/\mathrm{V}$	1.5689	1.3280	0.1140	0.3196	0.4066
	$+0.1055\,\mathrm{eV}$	0.7227	$-11.3\,\mu_{\mathrm{B}}/\mathrm{V}$	2.3864	1.3507	0.2441	0.1681	0.3642
	$+0.1290\,\mathrm{eV}$	0.6055	$+0.154\,\mu_{\mathrm{B}}/\mathrm{V}$	1.2690	1.6147	0.1515	0.2114	0.3220
AGNR8x41 40% H	$-0.6350\,\mathrm{eV}$	0.4228	$+3.74\,\mu_{\mathrm{B}}/\mathrm{V}$	0.0446	2.2411	0.3209	0.1288	0.2564
	$-0.5300\,\mathrm{eV}$	0.3296	$-1.98\,\mu_{\mathrm{B}}/\mathrm{V}$	0.8338	2.6668	0.5822	0.1720	0.3345
	$-0.1300\,\mathrm{eV}$	0.3509	$-0.546\,\mu_{\mathrm{B}}/\mathrm{V}$	0.9284	1.2390	0.0820	0.2814	0.2836
	$+0.1265\,\mathrm{eV}$	0.3282	$-7.06\,\mu_{\mathrm{B}}/\mathrm{V}$	2.1855	2.5937	0.6727	0.1880	0.2509
	$+0.2490\,\mathrm{eV}$	0.8799	$+3.09\,\mu_{\mathrm{B}}/\mathrm{V}$	1.2898	2.0213	0.4598	0.1096	0.2567
	$+0.2850\,\mathrm{eV}$	0.8366	$-0.0955\,\mu_{\mathrm{B}}/\mathrm{V}$	1.8489	1.6927	0.1867	0.1481	0.3058
AGNR24x41 (2) 20% H	$-1.0550\,\mathrm{eV}$	0.8519	$-15.3\,\mu_{\mathrm{B}}/\mathrm{V}$	0.9244	1.5035	0.1971	0.1935	0.2677
	$-0.9350\,\mathrm{eV}$	0.9788	$-0.878\,\mu_{\mathrm{B}}/\mathrm{V}$	0.6365	1.9117	0.1298	0.2053	0.2671
	$-0.7000\,\mathrm{eV}$	0.3517	$+3.23\,\mu_{\mathrm{B}}/\mathrm{V}$	0.9351	2.0595	0.2487	0.1177	0.2731
	$+0.2485\,\mathrm{eV}$	0.6520	$+10.5\,\mu_{\mathrm{B}}/\mathrm{V}$	2.5481	1.7024	0.0788	0.0775	0.2994
	$+0.2980\,\mathrm{eV}$	0.2808	$-2.64\,\mu_{\mathrm{B}}/\mathrm{V}$	1.5481	1.5655	0.1704	0.0977	0.2854
	$+0.3130\,\mathrm{eV}$	0.3649	$-3.93\,\mu_{\mathrm{B}}/\mathrm{V}$	1.2059	1.7076	0.0686	0.1260	0.2687
AGNR24x42 20% H	$-0.9450\,\mathrm{eV}$	0.7762	$+0.887\,\mu_{\mathrm{B}}/\mathrm{V}$	0.7803	1.4495	0.1050	0.1735	0.2905
	$-0.7500\,\mathrm{eV}$	0.4543	$+5.23\,\mu_{\mathrm{B}}/\mathrm{V}$	0.2808	1.7188	0.0671	0.2546	0.2840
	$-0.6050\,\mathrm{eV}$	0.9389	$+1.55\,\mu_{\mathrm{B}}/\mathrm{V}$	1.1803	1.3361	0.0644	0.1486	0.2928
	$+0.1935\,\mathrm{eV}$	0.2597	$-14.2\,\mu_{\mathrm{B}}/\mathrm{V}$	1.9346	1.3567	0.0449	0.1297	0.2872
	$+0.2120\,\mathrm{eV}$	0.5030	$-3.78\,\mu_{\mathrm{B}}/\mathrm{V}$	1.8167	1.3438	0.0653	0.1201	0.3182
	$+0.2195\,\mathrm{eV}$	0.6608	$-12.9\,\mu_{\mathrm{B}}/\mathrm{V}$	2.3175	1.5278	0.0676	0.1323	0.3036
AGNR24x43 20% H	$-0.9940\,\mathrm{eV}$	0.4797	$+6.04\,\mu_{\mathrm{B}}/\mathrm{V}$	0.8639	1.6235	0.2083	0.1406	0.2958
	$-0.8790\,\mathrm{eV}$	0.8087	$+0.429\,\mu_{\mathrm{B}}/\mathrm{V}$	-0.0320	2.0050	0.5707	0.2124	0.2682
	$-0.7190\,\mathrm{eV}$	0.3501	$+4.47\,\mu_{\mathrm{B}}/\mathrm{V}$	-0.1113	1.9987	0.5194	0.2294	0.2909
	$+0.2005\,\mathrm{eV}$	0.4804	$+1.6\,\mu_{\mathrm{B}}/\mathrm{V}$	0.8770	1.6464	0.2426	0.1246	0.2960
	$+0.2365\,\mathrm{eV}$	0.5232	$+1.39\,\mu_{\mathrm{B}}/\mathrm{V}$	1.3952	1.4271	0.1089	0.1621	0.2750
	$+0.2535\,\mathrm{eV}$	0.5719	$-3.37\,\mu_{\mathrm{B}}/\mathrm{V}$	1.0257	1.7548	0.3104	0.2037	0.2761
AGNR8x41 (2) 20% H	$-0.4750\,\mathrm{eV}$	0.9738	$+6.95\,\mu_{\mathrm{B}}/\mathrm{V}$	-0.4061	2.1427	0.3599	0.2161	0.3356
	$-0.1720\,\mathrm{eV}$	0.7209	$+4.69\,\mu_{\mathrm{B}}/\mathrm{V}$	1.3903	1.2021	0.2281	0.3220	0.4042
	$-0.1035\,\mathrm{eV}$	0.9979	$+7.16\,\mu_{\mathrm{B}}/\mathrm{V}$	0.1159	1.5548	0.2069	0.3285	0.4509
	$+0.0135\,\mathrm{eV}$	0.9421	$+5.05\,\mu_{\mathrm{B}}/\mathrm{V}$	1.2009	1.4521	0.3604	0.2647	0.4017
	$+0.1625\,\mathrm{eV}$	0.9471	$-0.397\,\mu_{\mathrm{B}}/\mathrm{V}$	2.0616	1.6557	0.2062	0.1767	0.3088
	$+0.1965\,\mathrm{eV}$	0.8127	$-2.26\,\mu_{\mathrm{B}}/\mathrm{V}$	2.3037	1.8516	0.2616	0.1236	0.2669
AGNR8x42 20% H	$-0.5190\,\mathrm{eV}$	0.9889	$+3.99\,\mu_{\mathrm{B}}/\mathrm{V}$	0.2983	1.8816	0.5599	0.2758	0.3551
	$-0.4220\,\mathrm{eV}$	0.7546	$-1.74\,\mu_{\mathrm{B}}/\mathrm{V}$	1.1456	1.1269	0.1238	0.4181	0.3719
	$-0.2030\,\mathrm{eV}$	0.3014	$+4.16\,\mu_{\mathrm{B}}/\mathrm{V}$	1.6527	1.2511	0.0789	0.1863	0.3927
	$+0.1010\,\mathrm{eV}$	0.6736	$-12.7\,\mu_{\mathrm{B}}/\mathrm{V}$	1.7054	1.6421	0.2117	0.1659	0.3055
	$+0.1215\,\mathrm{eV}$	0.6071	$-8.55\,\mu_{\mathrm{B}}/\mathrm{V}$	1.9947	1.4827	0.2368	0.1463	0.3027
	$+0.1345\,\mathrm{eV}$	0.3991	$-6.15\,\mu_{\mathrm{B}}/\mathrm{V}$	2.9117	1.7628	0.2115	0.1475	0.2975
AGNR8x43 20% H	$-0.4050\,\mathrm{eV}$	0.5309	$-5.36\,\mu_{\mathrm{B}}/\mathrm{V}$	-0.1026	1.8955	0.3651	0.2123	0.3520
	$-0.3400\,\mathrm{eV}$	0.7012	$+0.666\,\mu_{\mathrm{B}}/\mathrm{V}$	0.7839	1.4586	0.1365	0.2629	0.3298
	$-0.2320\,\mathrm{eV}$	0.4584	$+2.32\,\mu_{\mathrm{B}}/\mathrm{V}$	0.8506	2.0193	0.3039	0.2322	0.3154
	$+0.1655\,\mathrm{eV}$	0.2619	$-1.67\,\mu_{\mathrm{B}}/\mathrm{V}$	1.8803	1.8262	0.4697	0.1226	0.2703
	$+0.2855\,\mathrm{eV}$	0.8540	$+4.04\,\mu_{\mathrm{B}}/\mathrm{V}$	0.6839	2.1767	0.3244	0.2439	0.3016
	$+0.3185\,\mathrm{eV}$	0.9866	$+3.07\,\mu_{\mathrm{B}}/\mathrm{V}$	0.6351	1.7925	0.2857	0.1820	0.3057

Table D.5: Statistical data of the distribution funtions $\mathcal{P}_{\ln j} = \mathcal{P}[\ln |\mathbf{j}(E)|/j^\diamond_{\mathrm{avg;y}}]$. The corresponding transmission functions and selected distribution functions are shown in Fig. D.13–Fig. D.18

E

Spin effects

This appendix contains additional material that complements Chap. 5.

E.1 Comparison of different (approximate) groundstate spin configurations and their influence on transmission and local current density

In Sec. 5.2.4, we discussed spin effects on the (spin-unpolarized) current density response. For that purpose, we calculated the total transmission with different levels of spin theory (closed-shell, open-shell and spinor DFT). The transmission plot and the comparison of the DFT groundstate energies are reproduced for convenience in Fig. E.1 and Tab. E.1, respectively.

In this appendix, we present all current density patterns which are calculated for the energies as marked in Fig. E.1 by arrows. The current plots for the closed-shell and open-shell category are shown in Fig. E.2 and Fig. E.3, respectively. As claimed in the main body, in each category, the current density normalized to the transmission does not depend on the spin level of the calculation (for finite transmission values).

One noticeable example is given by the current pattern for $E=\varepsilon_{\mathrm{F}}+0.2\,\mathrm{eV}$ of the closed-shell category (Fig. E.2). Although the transmission value ranges from $\mathcal{T}=0.24$ to $\mathcal{T}=0.86$, the current pattern is virtually identical for all closed-shell cases.

For a (nearly) vanishing transmission, the current pattern is solely dominated by small local fluctuations which are sensitive to small differences in the simulations, as for example the exact spin configuration. An example is given by the current density pattern for $E=\varepsilon_{\mathrm{F}}+0.2\,\mathrm{eV}$ of the open-shell category (Fig. E.3). In this case, the current patterns differ. In all other cases, the current density normalized to the transmission only depends on the category but not on the exact simulation details.
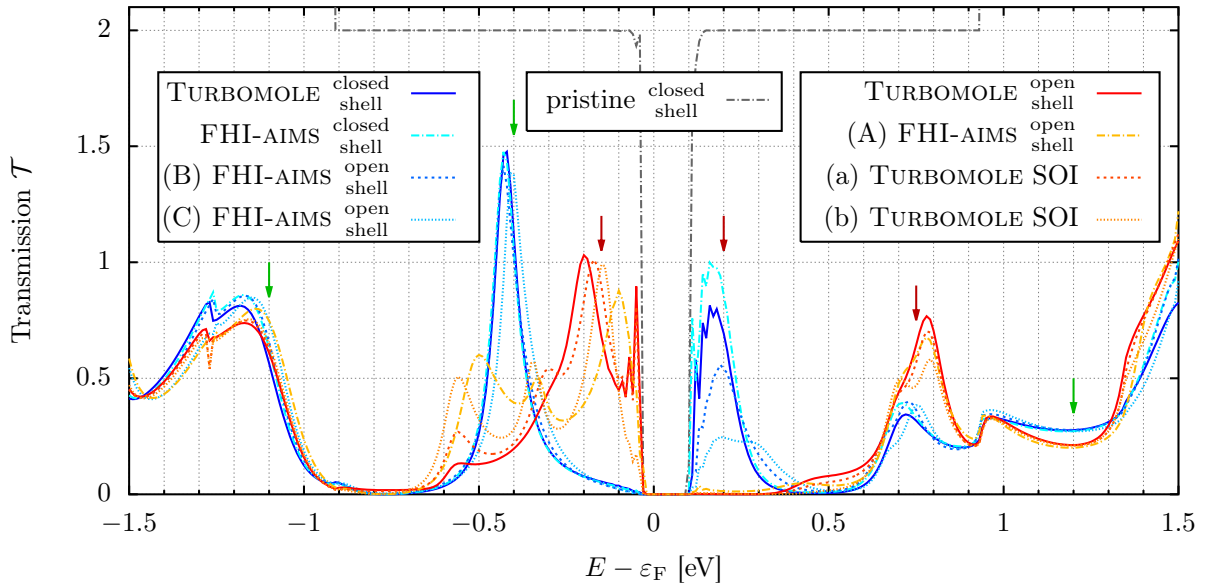
Figure E.1: Total transmission for different DFT calculations comparing different levels of theory: open-shell, closed-shell, and 2-component spinor calculation including spin-orbit interaction (SOI). All transmission curves can be categorized as either "closed-shell-like" (bluish) or "open-shell-like" (reddish). The arrows represent energy values for which the current density response has been calculated; green/red arrows refer to current patterns which match/differ for the two categories. The current patterns inside each category always match for non-vanishing transmission. The figure is a copy of Fig. 5.5, reproduced here for convenience.

	$\Delta E_0[\,\mathrm{eV}]$	$S_z[\hbar]$
FHI-AIMS $^{\mathrm{closed}}_{\mathrm{shell}}$	0	0
(A) FHI-AIMS $^{\mathrm{open}}_{\mathrm{shell}}$	-0.478	1.91
(B) FHI-AIMS $^{\mathrm{open}}_{\mathrm{shell}}$	-0.016	0.05
(C) FHI-AIMS $^{\mathrm{open}}_{\mathrm{shell}}$	-0.310	1.08

	$\Delta E_0[\,\mathrm{eV}]$	$\mathbf{S}[\hbar]$
(a) T. SOI	0	$\begin{pmatrix} -0.163 \\ -0.044 \\ +0.860 \end{pmatrix}$
(b) T. SOI	-0.014	$\begin{pmatrix} -0.097 \\ +0.021 \\ -0.041 \end{pmatrix}$

	$\Delta E_0[\,\mathrm{eV}]$	$S_z[\hbar]$
TURBOMOLE $^{\mathrm{closed}}_{\mathrm{shell}}$	0	0
TURBOMOLE $^{\mathrm{open}}_{\mathrm{shell}}$	-0.626	1

Table E.1: Comparison of DFT ground state energies E_0 of the finite (uncoupled) cluster and of the overall spin. We made sure to only compare energies which are calculated by the same code with the same basis set because otherwise the differences are due to differences in the calculation scheme and not of physical origin. In that sense, a closed-shell calculation is equivalent to an open-shell calculation where both spin channels are forced to be the same. As energy zero point, we chose the energy of the closed-shell calculation (if available; otherwise, we chose a random reference point). For information: the ground state DFT energies used as references points are: FHI-AIMS closed-shell: $E_0 = 137514.8234\,\mathrm{eV}$, TURBOMOLE closed-shell: $E_0 = 137549.2636\,\mathrm{eV}$, TURBOMOLE SOI: $E_0 = 137599.2168\,\mathrm{eV}$. The table is a copy of Tab. 5.1, reproduced here for convenience.
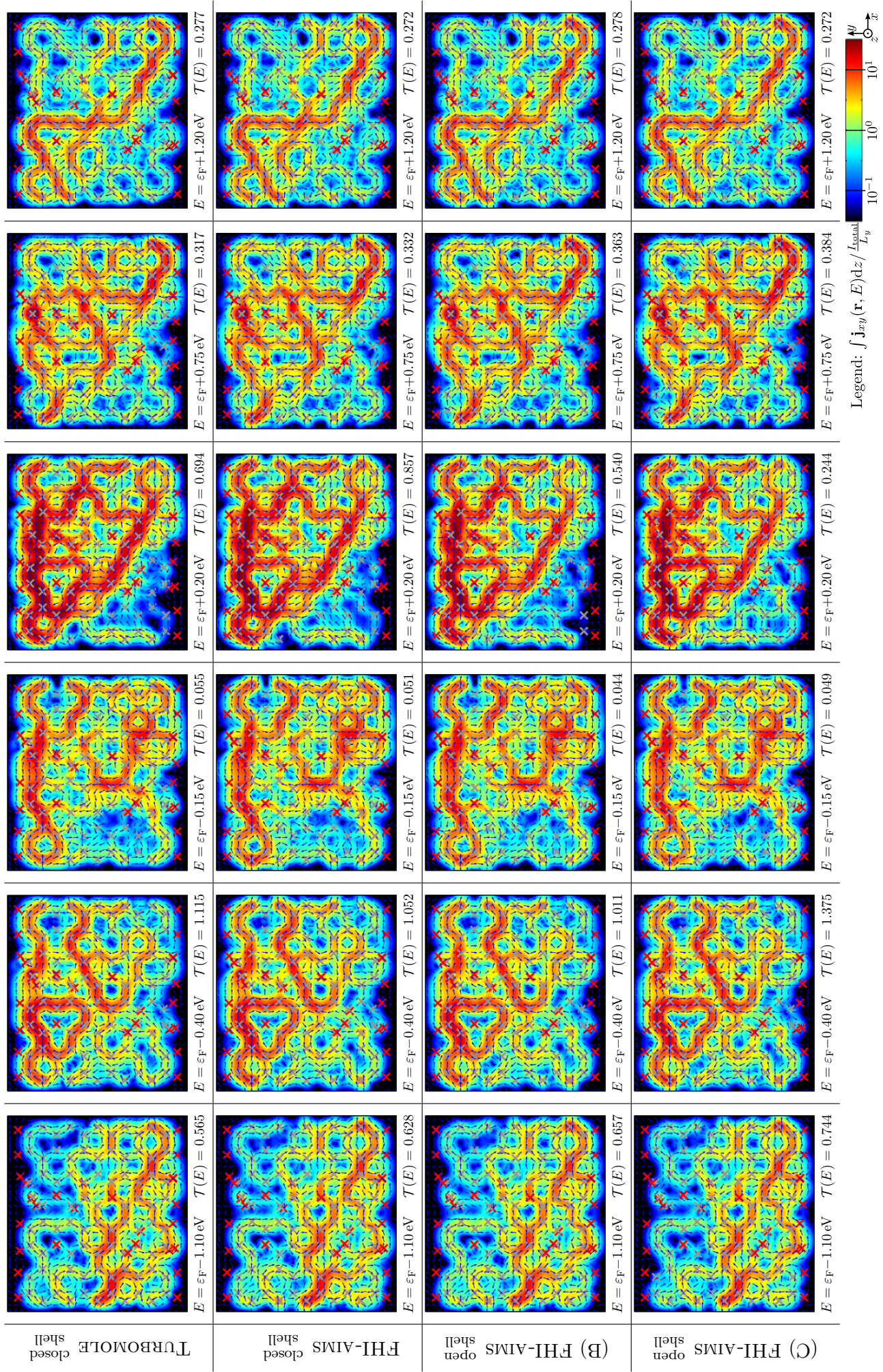
Figure E.2: The current density for six different energies for all calculations inside the "closed-shell-like" category. Note, how the current density per transmission is independent of the exact transmission value. Please refer to Fig. 5.5 for the transmission plot.
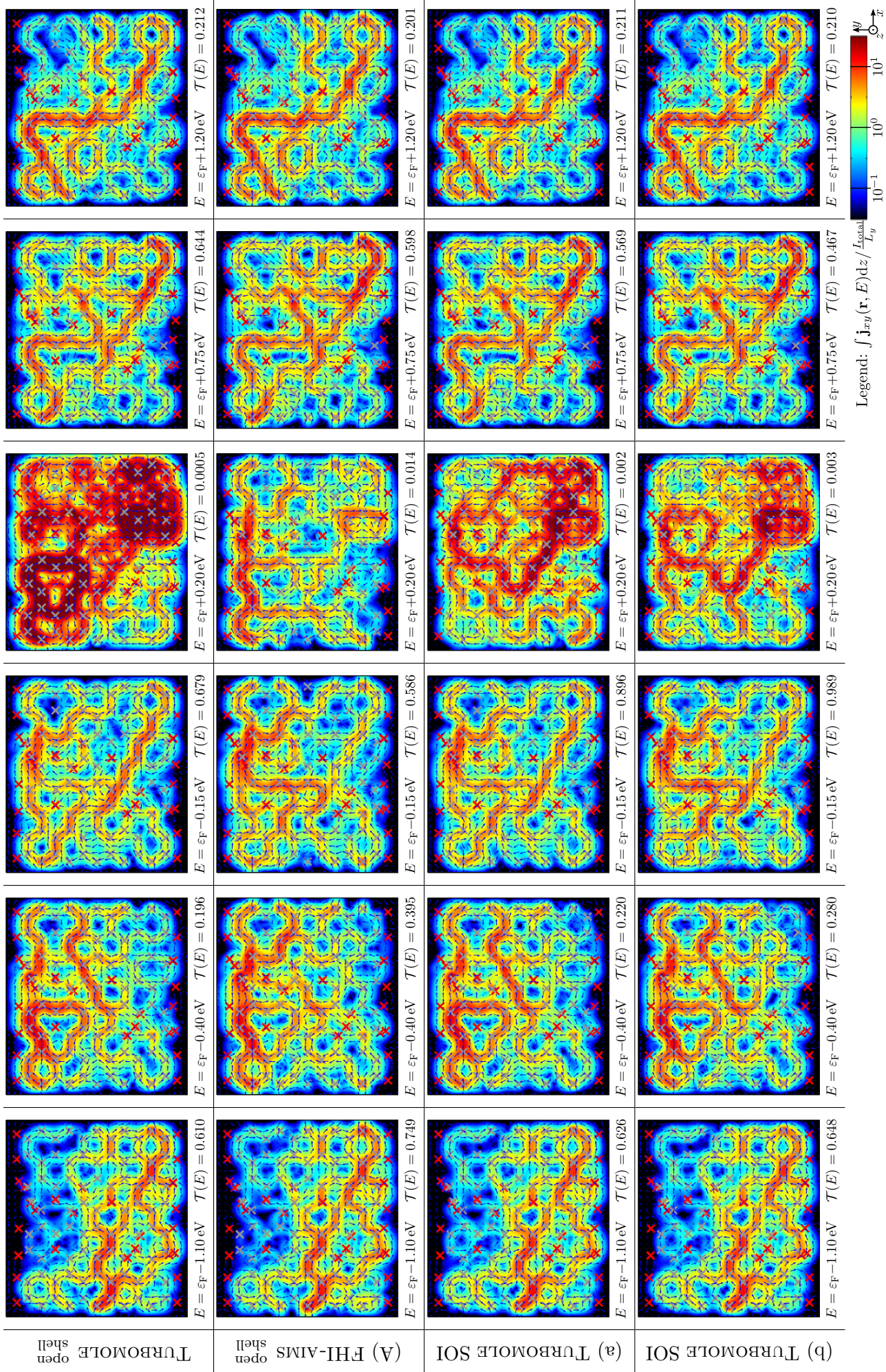
Figure E.3: The current density for six different energies for all calculations inside the "open-shell-like" category. For (nearly) vanishing transmission, e.g., at $E = \varepsilon_F + 0.2\,\text{eV}$, the current fluctuations dominate and are highly sensitive to the exact ground state configuration. Please refer to Fig. 5.5 for the transmission plot.

F Appendix F

Magnetic feedback: Self-consistency in the induced orbital magnetism

This appendix contains additional material that complements Chap. 6. In Appx. F.1, we shortly present implementation details on how the matrix elements for the magnetic influence on the electron motion and spin are calculated. A derivation of the current density operator with applied vector potential $\mathbf{A}$ is given in Appx. F.2.

F.1 Implementation details

Basis set transformation

In this section, we present how the matrix elements of type $\Delta \mathbf{H}_{ij}^{\mathrm{Lorentz}} := \langle \tilde{\varphi}_i | \Delta \hat{\mathcal{H}}^{\mathrm{Lorentz}} | \tilde{\varphi}_j \rangle$, see Eq. (6.4), are evaluated in our implementation. For that purpose, we write the orthogonal basis set $\tilde{\varphi}_i(\mathbf{r})$ in terms of the non-orthonormal basis $\varphi_j(\mathbf{r})$ used in the underlying DFT code,

$$\tilde{\varphi}_i(\mathbf{r}) = \sum_j \varphi_j(\mathbf{r}) \left[S^{-1/2} \right]_{ji}. \qquad \text{(F.1)}$$

The matrix element $\Delta \check{\mathbf{H}}^{\mathrm{Lorentz}}$ is evaluated in the non-orthogonal basis set,

$$\Delta \check{\mathbf{H}}_{ij}^{\mathrm{Lorentz}} = \langle \varphi_i | \Delta \hat{\mathcal{H}}^{\mathrm{Lorentz}} | \varphi_j \rangle \qquad \text{(F.2)}$$
$$= \frac{1}{2m} \int \varphi_i^*(\mathbf{r}) \Big\{ \mathrm{i}\hbar q [\mathbf{A}(\mathbf{r}) \cdot \boldsymbol{\nabla} + \boldsymbol{\nabla} \cdot \mathbf{A}(\mathbf{r})]$$
$$+ q^2 \mathbf{A}^2(\mathbf{r}) \Big\} \varphi_j(\mathbf{r}) \, \mathrm{d}^3\mathbf{r}$$

and then transformed back to the orthogonal basis set by

$$\Delta \mathbf{H}^{\mathrm{Lorentz}} = S^{-1/2} \, \Delta \check{\mathbf{H}}^{\mathrm{Lorentz}} \, S^{-1/2}. \qquad \text{(F.3)}$$

Internally, the matrix element is split,

$$\Delta \check{\mathbf{H}}_{ij}^{\mathrm{Lorentz}} = \Delta \check{\mathbf{h}}_{ij}^{\mathbf{A}} + (\Delta \check{\mathbf{h}}_{ji}^{\mathbf{A}})^* + \Delta \check{\mathbf{h}}_{ij}^{\mathbf{AA}}, \qquad \text{(F.4)}$$

into two auxiliary integrals,

$$\Delta \check{\mathbf{h}}_{ij}^{\mathbf{A}} = +\frac{\mathrm{i}\hbar q}{2m} \int \varphi_i(\mathbf{r}) \, \mathbf{A}(\mathbf{r}) \cdot [\boldsymbol{\nabla} \varphi_j(\mathbf{r})] \, \mathrm{d}^3\mathbf{r} \qquad \text{(F.5)}$$

and

$$\Delta \check{\mathbf{h}}_{ij}^{\mathbf{AA}} = +\frac{q^2}{2m} \int \varphi_i(\mathbf{r}) \, \mathbf{A}^2(\mathbf{r}) \, \varphi_j(\mathbf{r}) \, \mathrm{d}^3\mathbf{r}. \qquad \text{(F.6)}$$

For that purpose, we utilized that the vector potential and the basis set are real, $\mathbf{A}(\mathbf{r}) \in \mathbb{R}$ and $\varphi_i(\mathbf{r}) \in \mathbb{R}$. By employing integration by parts, the differential operators now act solely on the basis functions. These derivatives are calculated numerically with a precision of $\mathcal{O}(10^{-10})$, cf. Eq. (2.32).

Similarly, the Zeeman term $\Delta \mathbf{H}_{ij}^{\mathrm{Zeeman}} := \langle \tilde{\varphi}_i | \Delta \hat{\mathcal{H}}^{\mathrm{Zeeman}} | \tilde{\varphi}_j \rangle$, see Eq. (6.5), is internally calcu-

lated with respect to the non-orthonormal real basis set $\varphi_i(\mathbf{r})$:

$$\Delta\check{\mathbf{H}}_{ij}^{\text{Zeeman}} = \frac{q\hbar}{2m}\int \varphi_i(\mathbf{r})\begin{pmatrix} B_z(\mathbf{r}) & B_{xy}^*(\mathbf{r}) \\ B_{xy}(\mathbf{r}) & -B_z(\mathbf{r}) \end{pmatrix}\varphi_j(\mathbf{r})\,\mathrm{d}^3\mathbf{r}\,,$$
$$(F.7)$$

and then transformed back,

$$\Delta\mathbf{H}^{\text{Zeeman}} = \begin{pmatrix} S^{-1/2} & 0 \\ 0 & S^{-1/2} \end{pmatrix}\Delta\check{\mathbf{H}}^{\text{Zeeman}}\begin{pmatrix} S^{-1/2} & 0 \\ 0 & S^{-1/2} \end{pmatrix}.$$
$$(F.8)$$

To additionally reduce the computational effort, one can employ spin symmetries. In Eq. (F.7), only half of the components in $\Delta\check{\mathbf{H}}^{\text{Zeeman}}$ are independent. The others are determined by the symmetries

$$\left[\Delta\check{\mathbf{H}}^{\text{Zeeman}}\right]^{\uparrow\uparrow} = -\left[\Delta\check{\mathbf{H}}^{\text{Zeeman}}\right]^{\downarrow\downarrow} \qquad (F.9)$$

and

$$\left[\Delta\check{\mathbf{H}}^{\text{Zeeman}}\right]^{\uparrow\downarrow} = \left\{\left[\Delta\check{\mathbf{H}}^{\text{Zeeman}}\right]^{\downarrow\uparrow}\right\}^*, \qquad (F.10)$$

where the star * denotes complex conjugation.

Numerical Integration

For the numerical integration, we use a three-dimensional trapezoidal rule, i.e., we replace the integral by a sum over three-dimensional equidistant grid $\{\mathbf{r}_i\}$ with spacing δ:

$$\int \mathrm{d}^3\mathbf{r}\,F(\mathbf{r}) \rightarrow \delta^3\sum_{\mathbf{r}_i}F(\mathbf{r}_i)\,. \qquad (F.11)$$

In the integrals of type Eq. (F.2) and Eq. (F.7), the fastest varying parts of the integrand are the basis functions, not the magnetic field, nor the vector potential. To resolve the basis functions appropriately, we use a small spacing of $\delta = 0.05$Å (and below). We avoid an expensive calculation of the magnetic field and vector potential on such a fine grid (scaling with $\mathcal{O}(\delta^{-6})$, cf. Sec. 2.4). Instead we employ a larger grid spacing of $\delta = 0.2$Å to calculate the current density and the induced magnetic field and vector potential. Intermediate values are then estimated by a cubic spline interpolation as implemented in the GNU scientific library (GSL)[202].

Gauge invariance

A large spatial average $\langle\mathbf{A}\rangle$ of the vector potential shifts all energies without having an influence on observables, like energy differences or the magnetic field $\mathbf{B} = \boldsymbol{\nabla}\times\mathbf{A}$. In this thesis, we employ Gauge invariance to remove the spatial average $\langle\mathbf{A}\rangle$ of the vector potential, i.e., we replace $\mathbf{A} \rightarrow \mathbf{A} - \langle\mathbf{A}\rangle$. That choice also reduces the explicit contribution $\frac{q}{m}\mathbf{A}(\mathbf{r})|\Psi(\mathbf{r})|^2$ of the vector potential to the current density $\mathbf{j}(\mathbf{r})$, cf. Eq. (F.14).

F.2 Current density operator with applied vector potential $\mathbf{A}$

For completeness, we give a short derivation of the current operator. Classically, the current density operator is given by

$$\hat{\mathbf{j}}(\mathbf{r})\Big|_{\text{classic}} = \frac{\hat{\boldsymbol{\pi}}}{m}\delta(\mathbf{r}-\hat{\mathbf{r}})\,, \qquad (F.12)$$

with the kinetic momentum operator $\hat{\boldsymbol{\pi}}$. In quantum mechanics, one uses the symmetrized version

$$\hat{\mathbf{j}}(\mathbf{r}) = \frac{\{\hat{\boldsymbol{\pi}},\delta(\mathbf{r}-\hat{\mathbf{r}})\}}{2m} \qquad (F.13)$$

with $\{A,B\} = AB+BA$ denoting the anti-commutator. Employing the principle of minimal coupling, i.e. $\hat{\boldsymbol{\pi}} = \hat{\mathbf{p}} - q\mathbf{A}(\hat{\mathbf{r}})$, the expectation value of the current density

operator becomes

$$\mathbf{j}(\mathbf{r}) = \langle\Psi|\hat{\mathbf{j}}(\mathbf{r})|\Psi\rangle$$
$$= \frac{\hbar}{2m\mathrm{i}}\left(\Psi^*(\mathbf{r})\boldsymbol{\nabla}\Psi(\mathbf{r}) - \Psi(\mathbf{r})\boldsymbol{\nabla}\Psi^*(\mathbf{r})\right) \quad (F.14)$$
$$- \frac{q}{m}\mathbf{A}(\mathbf{r})|\Psi(\mathbf{r})|^2\,.$$

Transforming to energy domain and employing the Keldysh Green's function $G^<$, we get

$$\mathbf{j}(\mathbf{r},E) = \frac{1}{2\pi}\frac{\hbar}{2m}\lim_{\mathbf{r}'\to\mathbf{r}}(\boldsymbol{\nabla}_{\mathbf{r}'} - \boldsymbol{\nabla}_{\mathbf{r}})G^<(\mathbf{r},\mathbf{r}',E)$$
$$+ \frac{\mathrm{i}}{2\pi}\frac{q}{m}\mathbf{A}(\mathbf{r})\,G^<(\mathbf{r},\mathbf{r},E) \qquad (F.15)$$

as given in the main body. In the last term, we rewrote the density in terms of the Keldysh Green's function, $|\Psi(\mathbf{r},E)|^2 = n(\mathbf{r},E) = -\frac{\mathrm{i}}{2\pi}G^<(\mathbf{r},\mathbf{r},E)$.

Scientific Work

Publication List

- **M. Walz**, A. Bagrets, and F. Evers. *Local Current Density Calculations for Molecular Films from Ab Initio*. *J. Chem. Theory Comput.* **11**, 5161–5176 (2015).

- **M. Walz**, A. Bagrets, F. Evers, and I. Kondov. *Ab initio transport calculations for functionalized graphene flakes on a supercomputer*. In W. E. Nagel, D. H. Kröner, and M. M. Resch, eds., *High Performance Computing in Science and Engineering '15*. Springer, Berlin, Heidelberg (accepted, 2015).

- J. Wilhelm, **M. Walz**, and F. Evers. *Ab initio spin-flip conductance of hydrogenated graphene nanoribbons: Spin-orbit interaction and scattering with local impurity spins*. *Phys. Rev. B* **92**, 014405 (2015).

- **M. Walz**, J. Wilhelm, and F. Evers. *Current Patterns and Orbital Magnetism in Mesoscopic dc Transport*. *Phys. Rev. Lett.* **113**, 136602 (2014).

- J. Wilhelm, **M. Walz**, and F. Evers. *Ab initio quantum transport through armchair graphene nanoribbons: Streamlines in the current density*. *Phys. Rev. B* **89**, 195406 (2014).

- **M. Walz**, T. Zebrowski, J. Küchenmeister, and K. Busch. *B-spline modal method: A polynomial approach compared to the Fourier modal method*. *Opt. Express* **21**, 14683–14697 (2013).

- N. Bajales, S. Schmaus, T. Miyamashi, W. Wulfhekel, J. Wilhelm, **M. Walz**, M. Stendel, A. Bagrets, F. Evers, S. Ulas, B. Kern, A. Böttcher, and M. M. Kappes. *C_{58} on Au(111): A scanning tunneling microscopy study*. *J. Chem. Phys.* **138**, 104703 (2013).

- J. Wilhelm, **M. Walz**, M. Stendel, A. Bagrets, and F. Evers. *Ab initio simulations of scanning-tunneling-microscope images with embedding techniques and application to C58-dimers on Au(111)*. *Phys. Chem. Chem. Phys.* **15**, 6684–6690 (2013).

- **M. Walz**, T. Zebrowski, J. Küchenmeister, and K. Busch. *A B-spline modal method in comparison to the Fourier modal method*. *AIP Conf. Proc.* **1398**, 177–179 (2011).

Attended Conferences & Workshops

- 18th HLRS Results and Review Workshop, 5–6 October 2015, HLRS, Stuttgart, Germany
  Contribution: *Ab initio transport calculations for functionalized graphene flakes
  on a supercomputer* (Talk)

- Conference: DPG-Frühjahrstagung (SKM), 15–20 March 2015, Berlin, Germany
  Contribution: *Ab-initio simulations of local current flows in functionalized
  graphene flakes and ribbons* (Talk)

- Workshop: Scientific Visualization & GPU Programming using CUDA,
  20–24 October 2014, HLRS, Stuttgart, Germany

- Conference: DPG-Frühjahrstagung (SKM), 30 March–4 April 2014, Dresden, Germany
  Contribution: *Ab-initio simulations of local current flows in functionalized
  graphene flakes and ribbons* (Talk)

- Autumn School on Correlated Electrons: Emergent Phenomena in Correlated Matter,
  23–27 September 2013, Forschungszentrum Jülich, Germany
  Contribution: *Ab-initio transport calculations of functionalized graphene flakes* (Poster)

- Conference: Graphene Week 2013, 2–7 June 2013, Chemnitz, Germany
  Contribution: *Ab-initio transport calculations of functionalized graphene flakes* (Poster)

- Conference: DPG-Frühjahrstagung (SKM), 10–15 March 2013, Regensburg, Germany
  Contribution: *Ab-initio transport calculations of functionalized graphene flakes* (Talk)

- Workshop: Recent progress in Dynamical Mean-Field Theory and GW calculations,
  17–20 December 2012, IPCMS, Strasbourg, France

- Summer School on Magnetism and Spintronics in Molecular Nanostructures,
  16–22 September 2012, Ile de Porquerolles, France
  Contribution: *Towards ab-initio transport calculations of large graphene flakes* (Poster)

- Workshop: Density Functional Theory and Beyond with Numeric Atom-Centered Orbitals,
  28–31 August 2012, Free University Berlin, Germany
  Contribution: *Towards ab-initio transport calculations of large graphene flakes* (Poster)

- Workshop: Electronic Correlations and Disorder in Quantum Matter,
  31 March–3 April 2012, Karlsruhe, Germany

- Conference: Theoretical and Computational Nano-Photonics: TaCoNa-Photonics 2011,
  26-28 October 2011, Physikzentrum, Bad Honnef, Germany
  Contribution: *B-spline modal method in comparison to the Fourier modal method* (Poster)

Teaching Experience

- SS 2015:   Exercise to Introduction to Density functional theory: Fundamentals and applications

- SS 2014:   Exercise to Experimental Physics 6: Nuclei and Particles (Kerne und Teilchen)

- WS 2012/13: Exercise to Theoretical Physics E: Quantum Mechanics II (Quantenmechanik II)

- SS 2012:   Exercise to Theoretical Physics F: Statistical Mechanics (Statistische Mechanik)

- SS 2011:   Exercise to Theoretical Optics (Theoretische Optik)

- WS 2010/11: Exercise to Computer Application (Rechnernutzung)

- SS 2009:   Exercise to Theoretical Physics B: Classical Mechanics (Klassische Mechanik)

Thank You All

Acknowledgments

This thesis—as probably true for all theses—would not have been possible without the help of other people. In particular, I like to thank

- **Prof. Dr. Ferdinand Evers** for giving me the opportunity to work on this thesis in his research group and for supervising my work. He gave me the freedom and time to go my own way, but was always available when needed. Thank you especially for your support of my family.

- **Prof. Dr. Alexander Mirlin** for kindly agreeing to co-review this thesis.

- **Dr. Alexei Bagrets** for competent advices given whenever needed, especially concerning technical problems: compilation with (Intel) MPI, SCF convergence issues, . . .

- **Dr. Ivan Kondov** for managing the HLRS grant and forcing me to plan how to invest the computing time. Without his constant reminders, the computing project would never have reached 100% computing time.

- **Jan Wilhelm** and **Benedikt Schönauer** who did their master theses on topics closely related to this thesis. Thanks for a lot of helpful discussions. Your work has greatly influenced also this thesis. Without you, part of this thesis would not have been possible. A great thanks to J.W. who still pursued our joined publication, after he moved to Zürich to work on a different topic.

- **Dr. Kathrin Walz** for her endless support and patience.

- **Dr. Andreas Poenicke** and **Christian Seiler** for the best maintained computer system I ever worked with.

- the **High Performance Computing Center Stuttgart (HLRS)** for granting an enormous amount of computing time on their HERMIT/HORNET supercomputer.

In addition, I'd like to thank all proof-readers (in reverse alphabetical order): **Kathrin Walz**, **Jan Wilhelm**, **Benedikt Schönauer**, **Mathias Scheurer**, **Egor Kiselev**, **Ferdinand Kaplan**, **Nikolaos Kainaris**, **Mareike Hoyer**, **Ferdinand Evers**, **Ulf Briskot**, **Matthias Bard**, and **Kevin Atkinson**.

I am indebted to a whole group of coworkers (especially from the **CCMT group**, and my two affiliated institutes: **TKM** and **INT**). They provided a great amount of help, great years, a lot of fun, including (but not restricted to) barbecues, climbing, excursions, cakes, Christmas parties, PhD parties, and of course, mental support when nothing works as it should. . .

References

[1] G. Binnig, H. Rohrer, C. Gerber, and E. Weibel. *Surface Studies by Scanning Tunneling Microscopy. Phys. Rev. Lett.* **49**, 57–61 (1982). (cited on page 1)

[2] J. Tersoff and D. R. Hamann. *Theory of the scanning tunneling microscope. Phys. Rev. B* **31**, 805–813 (1985). (cited on page 1)

[3] J. M. Krans, J. M. van Ruitenbeek, V. V. Fisun, I. K. Yanson, and L. J. de Jongh. *The signature of conductance quantization in metallic point contacts. Nature* **375**, 767–769 (1995). (cited on page 1)

[4] M. A. Reed, C. Zhou, C. J. Muller, T. P. Burgin, and J. M. Tour. *Conductance of a Molecular Junction. Science* **278**, 252–254 (1997). (cited on page 1)

[5] J. P. Bergfield and M. A. Ratner. *Forty years of molecular electronics: Non-equilibrium heat and charge transport at the nanoscale. physica status solidi (b)* **250**, 2249–2266 (2013). (cited on page 1)

[6] D. M. Eigler, C. P. Lutz, and W. E. Rudge. *An atomic switch realized with the scanning tunnelling microscope. Nature* **352**, 600–603 (1991). (cited on page 1)

[7] C. Joachim, J. K. Gimzewski, and A. Aviram. . *Nature* **408**, 541–548 (2000). (cited on page 1)

[8] X. H. Qiu, G. V. Nazin, and W. Ho. *Mechanisms of Reversible Conformational Transitions in a Single Molecule. Phys. Rev. Lett.* **93** (2004). (cited on page 1)

[9] V. Meded, A. Bagrets, K. Fink, R. Chandrasekar, M. Ruben, F. Evers, A. Bernand-Mantel, J. S. Seldenthuis, A. Beukman, and H. S. J. van der Zant. *Electrical control over the Fe(II) spin crossover in a single molecule: Theory and experiment. Phys. Rev. B* **83** (2011). (cited on page 1)

[10] T. Miyamachi, M. Gruber, V. Davesne, M. Bowen, S. Boukari, L. Joly, F. Scheurer, G. Rogez, T. K. Yamada, P. Ohresser, E. Beaurepaire, and W. Wulfhekel. *Robust spin crossover and memristance across a single molecule. Nature Communications* **3**, 938 (2012). (cited on page 1)

[11] T. Ohto, I. Rungger, K. Yamashita, H. Nakamura, and S. Sanvito. *Ab initio theory for current-induced molecular switching: Melamine on Cu(001). Phys. Rev. B* **87** (2013). (cited on page 1)

[12] D. Horinek and J. Michl. *Surface-mounted altitudinal molecular rotors in alternating electric field: Single-molecule parametric oscillator molecular dynamics. Proceedings of the National Academy of Sciences* **102**, 14175–14180 (2005). (cited on page 1)

[13] P. Král and T. Seideman. *Current-induced rotation of helical molecular wires. The Journal of Chemical Physics* **123**, 184702 (2005). (cited on page 1)

[14] D. Dundas, E. J. McEniry, and T. N. Todorov. *Current-driven atomic waterwheels. Nat. Nanotechnol.* **4**, 99–102 (2009). (cited on page 1)

[15] J. S. Seldenthuis, F. Prins, J. M. Thijssen, and H. S. J. van der Zant. *An All-Electric Single-Molecule Motor. ACS Nano* **4**, 6681–6686 (2010). (cited on page 1)

[16] H. L. Tierney, C. J. Murphy, A. D. Jewell, A. E. Baber, E. V. Iski, H. Y. Khodaverdian, A. F. McGuire, N. Klebanov, and E. C. H. Sykes. *Experimental demonstration of a single-molecule electric motor. Nat. Nanotechnol.* **6**, 625–629 (2011). (cited on page 1)

[17] M. Mayor, H. B. Weber, J. Reichert, M. Elbing, C. von Hänisch, D. Beckmann, and M. Fischer. *Electric Current through a Molecular Rod—Relevance of the Position of the Anchor Groups. Angew. Chem. Int. Ed.* **42**, 5834–5838 (2003). (cited on pages 1, 2)

References

[18] J. R. Quinn, F. W. Foss, L. Venkataraman, M. S. Hybertsen, and R. Breslow. *Single-Molecule Junction Conductance through Diaminoacenes. J. Am. Chem. Soc.* **129**, 6714–6715 (2007). (cited on pages 1, 2)

[19] M. Kiguchi, H. Nakamura, Y. Takahashi, T. Takahashi, and T. Ohto. *Effect of Anchoring Group Position on Formation and Conductance of a Single Disubstituted Benzene Molecule Bridging Au Electrodes: Change of Conductive Molecular Orbital and Electron Pathway. J. Phys. Chem. C* **114**, 22254–22261 (2010). (cited on pages 1, 2)

[20] S. V. Aradhya, J. S. Meisner, M. Krikorian, S. Ahn, R. Parameswaran, M. L. Steigerwald, C. Nuckolls, and L. Venkataraman. *Dissecting Contact Mechanics from Quantum Interference in Single-Molecule Junctions of Stilbene Derivatives. Nano Lett.* **12**, 1643–1647 (2012). (cited on pages 1, 2)

[21] J. S. Meisner, S. Ahn, S. V. Aradhya, M. Krikorian, R. Parameswaran, M. Steigerwald, L. Venkataraman, and C. Nuckolls. *Importance of Direct Metal−π Coupling in Electronic Transport Through Conjugated Single-Molecule Junctions. J. Am. Chem. Soc.* **134**, 20440–20445 (2012). (cited on pages 1, 2)

[22] C. R. Arroyo, S. Tarkuc, R. Frisenda, J. S. Seldenthuis, C. H. M. Woerde, R. Eelkema, F. C. Grozema, and H. S. J. van der Zant. *Signatures of Quantum Interference Effects on Charge Transport Through a Single Benzene Ring. Angew. Chem. Int. Ed.* **52**, 3152–3155 (2013). (cited on pages 1, 2)

[23] H. Valkenier, C. M. Guédon, T. Markussen, K. S. Thygesen, S. J. van der Molen, and J. C. Hummelen. *Cross-conjugation and quantum interference: a general correlation? Phys. Chem. Chem. Phys.* **16**, 653–662 (2014). (cited on pages 1, 2)

[24] D. Z. Manrique, C. Huang, M. Baghernejad, X. Zhao, O. A. Al-Owaedi, H. Sadeghi, V. Kaliginedi, W. Hong, M. Gulcur, T. Wandlowski, M. R. Bryce, and C. J. Lambert. *A quantum circuit rule for interference effects in single-molecule electrical junctions. Nat. Commun.* **6**, 6389 (2015). (cited on pages 1, 2)

[25] M. Taniguchi, M. Tsutsui, R. Mogi, T. Sugawara, Y. Tsuji, K. Yoshizawa, and T. Kawai. *Dependence of Single-Molecule Conductance on Molecule Junction Symmetry. J. Am. Chem. Soc.* **133**, 11426–11429 (2011). (cited on page 1)

[26] C. M. Guédon, H. Valkenier, T. Markussen, K. S. Thygesen, J. C. Hummelen, and S. J. van der Molen. *Observation of quantum interference in molecular charge transport. Nat. Nanotechnol.* **7**, 305–309 (2012). (cited on page 1)

[27] H. Vazquez, R. Skouta, S. Schneebeli, M. Kamenetska, R. Breslow, L. Venkataraman, and M. Hybertsen. *Probing the conductance superposition law in single-molecule circuits with parallel paths. Nat. Nanotechnol.* **7**, 663–667 (2012). (cited on page 1)

[28] S. V. Aradhya and L. Venkataraman. *Single-molecule junctions beyond electronic transport. Nat. Nanotechnol.* **8**, 399–410 (2013). (cited on page 1)

[29] R. Baer and D. Neuhauser. *Phase Coherent Electronics: A Molecular Switch Based on Quantum Interference. J. Am. Chem. Soc.* **124**, 4200–4201 (2002). (cited on page 1)

[30] M. Ernzerhof, M. Zhuang, and P. Rocheleau. *Side-chain effects in molecular electronic devices. J. Chem. Phys.* **123**, 134704 (2005). (cited on page 1)

[31] C. A. Stafford, D. M. Cardamone, and S. Mazumdar. *The quantum interference effect transistor. Nanotechnology* **18**, 424014 (2007). (cited on page 1)

[32] D. Q. Andrews, G. C. Solomon, R. P. V. Duyne, and M. A. Ratner. *Single Molecule Electronics: Increasing Dynamic Range and Switching Speed Using Cross-Conjugated Species. J. Am. Chem. Soc.* **130**, 17309–17319 (2008). (cited on page 1)

[33] D. M. Cardamone, C. A. Stafford, and S. Mazumdar. *Controlling Quantum Transport through a Single Molecule. Nano Letters* **6**, 2422–2426 (2006). (cited on pages 1, 2)

[34] D. Rai, O. Hod, and A. Nitzan. *Magnetic fields effects on the electronic conduction properties of molecular ring structures. Phys. Rev. B* **85**, 155440 (2012). (cited on pages 1, 2)

[35] T. Markussen, R. Stadler, and K. S. Thygesen. *The Relation between Structure and Quantum Interference in Single Molecule Junctions. Nano Letters* **10**, 4260–4265 (2010). (cited on pages 1, 2)

[36] G. C. Solomon, C. Herrmann, T. Hansen, V. Mujica, and M. A. Ratner. *Exploring local currents in molecular junctions. Nat. Chem.* **2**, 223–228 (2010). (cited on pages 1, 2)

[37] D. A. Lovey and R. H. Romero. *Quantum interference through gated single-molecule junctions. Chemical Physics Letters* **530**, 86–92 (2012). (cited on pages 1, 2)

[38] M. Ratner. *A brief history of molecular electronics. Nat. Nanotechnol.* **8**, 378–381 (2013). (cited on pages 1, 2)

[39] M. G. Reuter and T. Hansen. *Communication: Finding destructive interference features in molecular transport junctions. J. Chem. Phys.* **141**, 181103 (2014). (cited on pages 1, 2)

[40] T. Markussen, J. Schiötz, and K. S. Thygesen. *Electrochemical control of quantum interference in anthraquinone-based molecular switches. J. Chem. Phys.* **132**, 224104 (2010). (cited on page 1)

[41] C. Haigh and R. Mallion. *Ring current theories in nuclear magnetic resonance. Prog. Nucl. Magn. Reson. Spectrosc.* **13**, 303–344 (1979). (cited on page 2)

[42] P. Lazzeretti. *Ring currents. Prog. Nucl. Magn. Reson. Spectrosc.* **36**, 1–88 (2000). (cited on page 2)

[43] J. A. N. F. Gomes and R. B. Mallion. *Aromaticity and Ring Currents. Chem. Rev.* **101**, 1349–1384 (2001). (cited on page 2)

[44] L. Pauling. *The Diamagnetic Anisotropy of Aromatic Molecules. J. Chem. Phys.* **4**, 673 (1936). (cited on page 2)

[45] K. Lonsdale. *Magnetic Anisotropy and Electronic Structure of Aromatic Molecules. Proceedings of the Royal Society A: Mathematical, Physical and Engineering Sciences* **159**, 149–161 (1937). (cited on page 2)

[46] J. D. Memory. *High-Resolution NMR Spectra of Polycyclic Hydrocarbons. J. Chem. Phys.* **45**, 3567 (1966). (cited on page 3)

[47] T. B. Cobb. *High-Resolution NMR Spectra of Polycyclic Hydrocarbons. II. Pentacyclic Compounds. J. Chem. Phys.* **47**, 2020 (1967). (cited on page 3)

[48] C. Haigh and R. Mallion. *Proton magnetic resonance of 3, 4-benzopyrene at 100 and 220 Mcps. J. Mol. Spectrosc.* **29**, 478–485 (1969). (cited on page 3)

[49] C. Haigh and R. Mallion. *Proton magnetic resonance of planar condensed benzenoid hydrocarbons. Mol. Phys.* **18**, 737–750 (1970). (cited on page 3)

[50] C. Haigh, R. Mallion, and E. Armour. *Proton magnetic resonance of planar condensed benzenoid hydrocarbons. Mol. Phys.* **18**, 751–766 (1970). (cited on page 3)

[51] P. Lazzeretti and F. Taddei. *Semi-empirical calculations of the magnetic properties of condensed hydrocarbons. J. Chem. Soc., Faraday Trans. 2* **68**, 839 (1972). (cited on page 3)

[52] R. Zanasi, P. Lazzeretti, M. Malagoli, and F. Piccinini. *Molecular magnetic properties within continuous transformations of origin of the current density. J. Chem. Phys.* **102**, 7150 (1995). (cited on page 3)

[53] E. Steiner and P. W. Fowler. *Ring currents in aromatic hydrocarbons. Int. J. Quantum Chem.* **60**, 609–616 (1996). (cited on page 3)

[54] R. Zanasi and P. Lazzer. *Ring current model of the naphthalene molecule. Mol. Phys.* **92**, 609–618 (1997). (cited on page 3)

[55] P. W. Fowler, E. Steiner, B. Cadioli, and R. Zanasi. *Distributed-Gauge Calculations of Current Density Maps, Magnetizabilities, and Shieldings for a Series of Neutral and Dianionic Fused Tetracycles: Pyracylene ($C_{14}H_8$), Acepleiadylene ($C_{16}H_{10}$), and Dipleiadiene ($C_{18}H_{12}$). J. Phys. Chem. A* **102**, 7297–7302 (1998). (cited on page 3)

[56] G. Merino, T. Heine, and G. Seifert. *The Induced Magnetic Field in Cyclic Molecules. Chem.-Eur. J.* **10**, 4367–4371 (2004). (cited on page 3)

[57] J. Hey, D. Leusser, D. Kratzert, H. Fliegl, J. M. Dieterich, R. A. Mata, and D. Stalke. *Heteroaromaticity approached by charge density investigations and electronic structure calculations. Phys. Chem. Chem. Phys.* **15**, 20600 (2013). (cited on page 3)

[58] K. Wakabayashi, M. Fujita, H. Ajiki, and M. Sigrist. *Electronic and magnetic properties of nanographite ribbons. Phys. Rev. B* **59**, 8271–8282 (1999). (cited on page 3)

[59] M. P. Johansson, J. Jusélius, and D. Sundholm. *Sphere Currents of Buckminsterfullerene. Angew. Chem. Int. Ed.* **44**, 1843–1846 (2005). (cited on page 3)

[60] Y. Aharonov and D. Bohm. *Significance of Electromagnetic Potentials in the Quantum Theory. Phys. Rev.* **115**, 485–491 (1959). (cited on pages 3, 114)

[61] B. Josephson. *Possible new effects in superconductive tunnelling. Phys. Lett.* **1**, 251–253 (1962). (cited on page 3)

[62] P. W. Anderson and J. M. Rowell. *Probable Observation of the Josephson Superconducting Tunneling Effect. Phys. Rev. Lett.* **10**, 230–232 (1963). (cited on page 3)

[63] R. C. Jaklevic, J. Lambe, A. H. Silver, and J. E. Mercereau. *Quantum Interference Effects in Josephson Tunneling. Phys. Rev. Lett.* **12**, 159–160 (1964). (cited on page 3)

[64] R. C. Jaklevic, J. J. Lambe, J. E. Mercereau, and A. H. Silver. *Superconducting circuit components and method for use as transducing device* (1968). US Patent 3,363,200. (cited on page 3)

[65] M. Büttiker, Y. Imry, and R. Landauer. *Josephson behavior in small normal one-dimensional rings. Physics Letters A* **96**, 365–367 (1983). (cited on page 3)

[66] R. Landauer and M. Büttiker. *Resistance of Small Metallic Loops. Phys. Rev. Lett.* **54**, 2049–2052 (1985). (cited on page 3)

[67] R. A. Webb, S. Washburn, C. P. Umbach, and R. B. Laibowitz. *Observation of $\frac{h}{e}$ Aharonov-Bohm Oscillations in Normal-Metal Rings. Phys. Rev. Lett.* **54**, 2696–2699 (1985). (cited on page 3)

[68] S. Russo, J. B. Oostinga, D. Wehenkel, H. B. Heersche, S. S. Sobhani, L. M. K. Vandersypen, and A. F. Morpurgo. *Observation of Aharonov-Bohm conductance oscillations in a graphene ring. Phys. Rev. B* **77** (2008). (cited on page 3)

[69] V. M. Fomin, ed. *Physics of Quantum Rings.* Springer, Berlin, Heidelberg (2014). (cited on page 3)

[70] L. P. Lévy, G. Dolan, J. Dunsmuir, and H. Bouchiat. *Magnetization of mesoscopic copper rings: Evidence for persistent currents. Phys. Rev. Lett.* **64**, 2074–2077 (1990). (cited on page 3)

[71] V. Chandrasekhar, R. A. Webb, M. J. Brady, M. B. Ketchen, W. J. Gallagher, and A. Kleinsasser. *Magnetic response of a single, isolated gold loop. Phys. Rev. Lett.* **67**, 3578–3581 (1991). (cited on page 3)

[72] R. Landauer. *Spatial Variation of Currents and Fields Due to Localized Scatterers in Metallic Conduction. IBM J. Res. Dev.* **1**, 223–231 (1957). (cited on pages 3, 10)

[73] M. Büttiker, Y. Imry, R. Landauer, and S. Pinhas. *Generalized many-channel conductance formula with application to small rings. Phys. Rev. B* **31**, 6207–6215 (1985). (cited on pages 3, 10)

[74] Y. Meir and N. S. Wingreen. *Landauer formula for the current through an interacting electron region. Phys. Rev. Lett.* **68**, 2512–2515 (1992). (cited on page 3)

[75] S. Datta. *Electronic transport in mesoscopic systems.* Cambridge University Press, Cambridge [u.a.], first ed. (2007). (cited on page 3)

[76] M. Di Ventra. *Electrical transport in nanoscale systems.* Cambridge University Press, Cambridge [u.a.], first ed. (2008). (cited on pages 3, 10, 115)

[77] L. P. Zârbo and B. K. Nikolić. *Spatial distribution of local currents of massless Dirac fermions in quantum transport through graphene nanoribbons. Europhys. Lett.* **80**, 47001 (2007). (cited on pages 3, 50)

[78] S. B. Kumar, M. B. A. Jalil, S. G. Tan, and G. Liang. *The effect of magnetic field and disorders on the electronic transport in graphene nanoribbons. J. Phys.: Condens. Mat.* **22**, 375303 (2010). (cited on pages 3, 50)

[79] J. Mabillard, T. Can, and D. K. Morr. *Spatial current patterns, dephasing and current imaging in graphene nanoribbons. New J. Phys.* **16**, 013054 (2014). (cited on pages 3, 50)

[80] A. Cresti, D. Van Tuan, D. Soriano, A. W. Cummings, and S. Roche. *Multiple Quantum Phases in Graphene with Enhanced Spin-Orbit Coupling: From the Quantum Spin Hall Regime to the Spin Hall Effect and a Robust Metallic State. Phys. Rev. Lett.* **113**, 246603 (2014). (cited on pages 3, 50)

[81] J.-Y. Yan, P. Zhang, B. Sun, H.-Z. Lu, Z. Wang, S. Duan, and X.-G. Zhao. *Quantum blockade and loop current induced by a single lattice defect in graphene nanoribbons. Phys. Rev. B* **79**, 115403 (2009). (cited on pages 3, 4, 50, 109)

[82] Y. Zhang, J.-P. Hu, B. A. Bernevig, X. R. Wang, X. C. Xie, and W. M. Liu. *Quantum blockade and loop currents in graphene with topological defects. Phys. Rev. B* **78**, 155413 (2008). (cited on pages 3, 50)

[83] Y.-Y. Zhang, J. Hu, B. A. Bernevig, X. R. Wang, X. C. Xie, and W. M. Liu. *Impurities in graphene. phys. stat. sol. (a)* **207**, 2726–2738 (2010). (cited on pages 3, 50)

[84] R. Tuovinen, E. Perfetto, G. Stefanucci, and R. van Leeuwen. *Time-dependent Landauer-Büttiker formula: Application to transient dynamics in graphene nanoribbons.* *Phys. Rev. B* **89**, 085131 (2014). (cited on page 3)

[85] P. Rickhaus, P. Makk, M.-H. Liu, E. Tóvári, M. Weiss, R. Maurand, K. Richter, and C. Schönenberger. *Snake trajectories in ultraclean graphene p–n junctions.* *Nat. Commun.* **6**, 6470 (2015). (cited on page 3)

[86] N. Tsuji, S. Takajo, and H. Aoki. *Large orbital magnetic moments in carbon nanotubes generated by resonant transport.* *Phys. Rev. B* **75** (2007). (cited on page 3)

[87] D. Rai, O. Hod, and A. Nitzan. *Circular Currents in Molecular Wires.* *J. Phys. Chem. C* **114**, 20583–20594 (2010). (cited on page 3)

[88] M. Ernzerhof, H. Bahmann, F. Goyer, M. Zhuang, and P. Rocheleau. *Electron Transmission through Aromatic Molecules.* *J. Chem. Theory Comput.* **2**, 1291–1297 (2006). (cited on page 3)

[89] A. Pecchia, G. Penazzi, L. Salvucci, and A. D. Carlo. *Non-equilibrium Green's functions in density functional tight binding: method and applications.* *New. J. Phys.* **10**, 065022 (2008). (cited on pages 4, 9)

[90] M. Brandbyge, J.-L. Mozos, P. Ordejón, J. Taylor, and K. Stokbro. *Density-functional method for nonequilibrium electron transport.* *Phys. Rev. B* **65**, 165401 (2002). (cited on pages 4, 9)

[91] A. Rocha, V. García-Suárez, S. Bailey, C. Lambert, J. Ferrer, and S. Sanvito. *Spin and molecular electronics in atomically generated orbital landscapes.* *Phys. Rev. B* **73**, 085414 (2006). (cited on pages 4, 9)

[92] I. Rungger and S. Sanvito. *Algorithm for the construction of self-energies for electronic transport calculations based on singularity elimination and singular value decomposition.* *Phys. Rev. B* **78**, 035407 (2008). (cited on pages 4, 9)

[93] A. Calzolari, N. Marzari, I. Souza, and M. Buongiorno Nardelli. *Ab initio transport properties of nanostructures from maximally localized Wannier functions.* *Phys. Rev. B* **69**, 035108 (2004). (cited on pages 4, 9)

[94] M. Brandbyge, J.-L. Mozos, P. Ordejón, J. Taylor, and K. Stokbro. *Density-functional method for nonequilibrium electron transport.* *Phys. Rev. B* **65**, 165401 (2002). (cited on pages 4, 9)

[95] J. Taylor, H. Guo, and J. Wang. *Ab initio modeling of quantum transport properties of molecular electronic devices.* *Phys. Rev. B* **63**, 245407 (2001). (cited on pages 4, 9)

[96] F. Evers, F. Weigend, and M. Koentopp. *Conductance of molecular wires and transport calculations based on density-functional theory.* *Phys. Rev. B* **69**, 235411 (2004). (cited on pages 4, 9)

[97] A. Bagrets. *Spin-Polarized Electron Transport Across Metal–Organic Molecules: A Density Functional Theory Approach.* *J. Chem. Theory Comput.* **9**, 2801–2815 (2013). (cited on pages 4, 16, 18)

[98] A. Arnold, F. Weigend, and F. Evers. *Quantum chemistry calculations for molecules coupled to reservoirs: Formalism, implementation, and application to benzenedithiol.* *J. Chem. Phys.* **126**, 174101 (2007). (cited on pages 4, 16, 18)

[99] B. Biel, X. Blase, F. Triozon, and S. Roche. *Anomalous Doping Effects on Charge Transport in Graphene Nanoribbons.* *Phys. Rev. Lett.* **102** (2009). (cited on pages 4, 50, 109)

[100] A. López-Bezanilla, F. Triozon, and S. Roche. *Chemical Functionalization Effects on Armchair Graphene Nanoribbon Transport.* *Nano Letters* **9**, 2537–2541 (2009). (cited on pages 4, 50, 109)

[101] I. Deretzis, G. Fiori, G. Iannaccone, and A. L. Magna. *Effects due to backscattering and pseudogap features in graphene nanoribbons with single vacancies.* *Phys. Rev. B* **81** (2010). (cited on pages 4, 50, 109)

[102] A. López-Bezanilla and S. Roche. *Embedded boron nitride domains in graphene nanoribbons for transport gap engineering.* *Phys. Rev. B* **86** (2012). (cited on pages 4, 50, 109)

[103] W. Han, R. K. Kawakami, M. Gmitra, and J. Fabian. *Graphene spintronics.* *Nat. Nanotechnol.* **9**, 794–807 (2014). (cited on pages 5, 100, 110)

[104] L. Fritz and M. Vojta. *The physics of Kondo impurities in graphene.* *Rep. Prog. Phys.* **76**, 032501 (2013). (cited on page 5)

[105] R. R. Nair, M. Sepioni, I.-L. Tsai, O. Lehtinen, J. Keinonen, A. V. Krasheninnikov, T. Thomson, A. K. Geim, and I. V. Grigorieva. *Spin-half paramagnetism in graphene induced by point defects.* *Nat Phys* **8**, 199–202 (2012). (cited on page 5)

References

[106] J. Wilhelm, M. Walz, M. Stendel, A. Bagrets, and F. Evers. *Ab initio simulations of scanning-tunneling-microscope images with embedding techniques and application to C58-dimers on Au(111)*. Phys. Chem. Chem. Phys. **15**, 6684–6690 (2013). (cited on pages 6, 16)

[107] N. Bajales, S. Schmaus, T. Miyamashi, W. Wulfhekel, J. Wilhelm, M. Walz, M. Stendel, A. Bagrets, F. Evers, S. Ulas, B. Kern, A. Böttcher, and M. M. Kappes. *C_{58} on Au(111): A scanning tunneling microscopy study*. J. Chem. Phys. **138**, 104703 (2013). (cited on page 6)

[108] M. Walz, T. Zebrowski, J. Küchenmeister, and K. Busch. *B-spline modal method: A polynomial approach compared to the Fourier modal method*. Opt. Express **21**, 14683–14697 (2013). (cited on page 6)

[109] J. Wilhelm, M. Walz, and F. Evers. *Ab initio quantum transport through armchair graphene nanoribbons: Streamlines in the current density*. Phys. Rev. B **89**, 195406 (2014). (cited on pages 6, 39, 43)

[110] M. Walz, J. Wilhelm, and F. Evers. *Current Patterns and Orbital Magnetism in Mesoscopic dc Transport*. Phys. Rev. Lett. **113**, 136602 (2014). (cited on page 6)

[111] J. Wilhelm, M. Walz, and F. Evers. *Ab initio spin-flip conductance of hydrogenated graphene nanoribbons: Spin-orbit interaction and scattering with local impurity spins*. Phys. Rev. B **92**, 014405 (2015). (cited on pages 6, 17, 50, 94, 96)

[112] M. Walz, A. Bagrets, and F. Evers. *Local Current Density Calculations for Molecular Films from Ab Initio*. J. Chem. Theory Comput. **11**, 5161–5176 (2015). (cited on page 6)

[113] M. Walz, A. Bagrets, F. Evers, and I. Kondov. *Ab initio transport calculations for functionalized graphene flakes on a supercomputer*. In W. E. Nagel, D. H. Kröner, and M. M. Resch, eds., *High Performance Computing in Science and Engineering '15*. Springer, Berlin, Heidelberg (accepted, 2015). (cited on pages 6, 7)

[114] A. H. Castro Neto, F. Guinea, N. M. R. Peres, K. S. Novoselov, and A. K. Geim. *The electronic properties of graphene*. Rev. Mod. Phys. **81**, 109–162 (2009). (cited on pages 7, 113)

[115] N. M. R. Peres. *Colloquium: The transport properties of graphene: An introduction*. Rev. Mod. Phys. **82**, 2673–2700 (2010). (cited on pages 7, 90)

[116] S. Das Sarma, S. Adam, E. H. Hwang, and E. Rossi. *Electronic transport in two-dimensional graphene*. Rev. Mod. Phys. **83**, 407–470 (2011). (cited on page 7)

[117] A. K. Geim and I. V. Grigorieva. *Van der Waals heterostructures*. Nature **499**, 419–425 (2013). (cited on page 7)

[118] K. S. Novoselov, A. K. Geim, S. V. Morozov, D. Jiang, Y. Zhang, S. V. Dubonos, I. V. Grigorieva, and A. A. Firsov. *Electric Field Effect in Atomically Thin Carbon Films*. Science **306**, 666–669 (2004). (cited on page 7)

[119] N. D. Mermin and H. Wagner. *Absence of Ferromagnetism or Antiferromagnetism in One- or Two-Dimensional Isotropic Heisenberg Models*. Phys. Rev. Lett. **17**, 1133–1136 (1966). (cited on page 7)

[120] N. D. Mermin. *Crystalline Order in Two Dimensions*. Phys. Rev. **176**, 250–254 (1968). (cited on page 7)

[121] P. Tröster, P. Schmitteckert, and F. Evers. *Transport calculations based on density functional theory, Friedel's sum rule, and the Kondo effect*. Phys. Rev. B **85**, 115409 (2012). (cited on pages 7, 19)

[122] G. Stefanucci and S. Kurth. *Towards a Description of the Kondo Effect Using Time-Dependent Density-Functional Theory*. Phys. Rev. Lett. **107** (2011). (cited on pages 7, 19)

[123] J. P. Bergfield, Z.-F. Liu, K. Burke, and C. A. Stafford. *Bethe Ansatz Approach to the Kondo Effect within Density-Functional Theory*. Phys. Rev. Lett. **108** (2012). (cited on pages 7, 19)

[124] F. Evers and P. Schmitteckert. *Invariants of the single-impurity Anderson model and implications for conductance functionals*. EPL **103**, 47012 (2013). (cited on pages 7, 19)

[125] F. Evers and P. Schmitteckert. *Density functional theory with exact XC potentials: Lessons from DMRG studies and exactly solvable models*. Phys. Status Solidi B **250**, 2330–2341 (2013). (cited on pages 7, 19)

[126] B. Aradi, B. Hourahine, and T. Frauenheim. *DFTB+, a Sparse Matrix-Based Implementation of the DFTB Method*. J. Phys. Chem. A **111**, 5678–5684 (2007). (cited on page 9)

[127] J. M. Soler, E. Artacho, J. D. Gale, A. García, J. Junquera, P. Ordejón, and D. Sánchez-Portal. *The SIESTA method for ab initio order- N materials simulation. J. Phys.-Condens. Mat.* **14**, 2745 (2002). (cited on page 9)

[128] P. Giannozzi, S. Baroni, N. Bonini, M. Calandra, R. Car, C. Cavazzoni, D. Ceresoli, G. L. Chiarotti, M. Cococcioni, I. Dabo, A. D. Corso, S. de Gironcoli, S. Fabris, G. Fratesi, R. Gebauer, U. Gerstmann, C. Gougoussis, A. Kokalj, M. Lazzeri, L. Martin-Samos, N. Marzari, F. Mauri, R. Mazzarello, S. Paolini, A. Pasquarello, L. Paulatto, C. Sbraccia, S. Scandolo, G. Sclauzero, A. P. Seitsonen, A. Smogunov, P. Umari, and R. M. Wentzcovitch. *QUANTUM ESPRESSO: a modular and open-source software project for quantum simulations of materials. J. Phys.: Condens. Mat.* **21**, 395502 (2009). (cited on page 9)

[129] F. Evers and A. Arnold. *Molecular Conductance from Ab Initio Calculations: Self Energies and Adsorbing Boundary Conditions.* In C. Röthig, G. Schön, and M. Vojta, eds., *CFN Lectures on Functional Nanostructures - Volume 2: Nanoelectronics*, chap. 2. Springer Berlin Heidelberg (2011). (cited on pages 12, 16, 22)

[130] V. Blum, R. Gehrke, F. Hanke, P. Havu, V. Havu, X. Ren, K. Reuter, and M. Scheffler. *Ab initio molecular simulations with numeric atom-centered orbitals. Comput. Phys. Commun.* **180**, 2175 – 2196 (2009). (cited on pages 18, 33, 60, 113, 118)

[131] V. Havu, V. Blum, P. Havu, and M. Scheffler. *Efficient integration for all-electron electronic structure calculation using numeric basis functions. J. Comput. Phys.* **228**, 8367 – 8379 (2009). (cited on page 18)

[132] T. Auckenthaler, V. Blum, H. J. Bungartz, T. Huckle, R. Johanni, L. Krämer, B. Lang, H. Lederer, and P. R. Willems. *Parallel solution of partial symmetric eigenvalue problems from electronic structure calculations. Parallel Comput.* **37**, 783–794 (2011). (cited on page 18)

[133] A. Marek, V. Blum, R. Johanni, V. Havu, B. Lang, T. Auckenthaler, A. Heinecke, H.-J. Bungartz, and H. Lederer. *The ELPA library: scalable parallel eigenvalue solutions for electronic structure theory and computational science. J. Phys.: Condens. Mat.* **26**, 213201 (2014). (cited on pages 18, 33, 128)

[134] R. Ahlrichs, M. Bär, M. Häser, H. Horn, and C. Kölmel. *Electronic structure calculations on workstation computers: The program system turbomole. Chem. Phys. Lett.* **162**, 165 – 169 (1989). (cited on pages 18, 92, 98, 113, 118)

[135] P. Schmitteckert. *The dark side of DFT based transport calculations. Phys. Chem. Chem. Phys.* **15**, 15845 (2013). (cited on page 19)

[136] P.-O. Löwdin. *On the Non-Orthogonality Problem Connected with the Use of Atomic Wave Functions in the Theory of Molecules and Crystals. J. Chem. Phys.* **18**, 365–375 (1950). (cited on pages 19, 123)

[137] The HDF Group. *Hierarchical Data Format, vers. 5,* http://www.hdfgroup.org/HDF5/ (1997-2015). (cited on pages 33, 125)

[138] M. Fujita, K. Wakabayashi, K. Nakada, and K. Kusakabe. *Peculiar Localized State at Zigzag Graphite Edge. J. Phys. Soc. Jpn.* **65**, 1920–1923 (1996). (cited on pages 36, 37, 113)

[139] T. Pratchett. *The Colour of Magic (Discworld Novels).* Colin Smythe (1983). (cited on page 36)

[140] J. Wilhelm. *Quantum transport through graphene nanoribbons: Current patterns and spin-flip scattering.* Master's thesis, KIT, Karlsruhe (2014). (cited on pages 39, 40, 41, 49, 50, 92, 95, 96, 97, 136)

[141] Y.-W. Son, M. L. Cohen, and S. G. Louie. *Energy Gaps in Graphene Nanoribbons. Phys. Rev. Lett.* **97** (2006). (cited on page 39)

[142] M. Y. Han, B. Özyilmaz, Y. Zhang, and P. Kim. *Energy Band-Gap Engineering of Graphene Nanoribbons. Phys. Rev. Lett.* **98** (2007). (cited on page 39)

[143] A. Dasgupta, S. Bera, F. Evers, and M. J. van Setten. *Quantum size effects in the atomistic structure of armchair nanoribbons. Phys. Rev. B* **85**, 125433 (2012). (cited on pages 39, 41)

[144] R. Saito, G. Dresselhaus, and M. S. Dresselhaus. *Physical properties of carbon nanotubes.* Imperial College Press, London, repr. ed. (2005). (cited on page 41)

[145] J. Tersoff and D. R. Hamann. *Theory and Application for the Scanning Tunneling Microscope. Phys. Rev. Lett.* **50**, 1998–2001 (1983). (cited on page 43)

[146] J. Im, Y. Kim, C.-K. Lee, M. Kim, J. Ihm, and H. J. Choi. *Nanometer-Scale Loop Currents and Induced Magnetic Dipoles in Carbon Nanotubes with Defects. Nano Letters* **11**, 1418–1422 (2011). (cited on pages 49, 50, 54)

References

[147] G. Géranton, C. Seiler, A. Bagrets, L. Venkataraman, and F. Evers. *Transport properties of individual C60-molecules. J. Chem. Phys.* **139**, 234701 (2013). (cited on page 50)

[148] B. M. Schönauer. *Nonlinear quantum transport in nanoscopic interacting ring structures.* Master's thesis, KIT, Karlsruhe (2015). (cited on pages 56, 57, 58)

[149] S. R. White. *Density matrix formulation for quantum renormalization groups. Phys. Rev. Lett.* **69**, 2863–2866 (1992). (cited on page 56)

[150] S. R. White. *Density-matrix algorithms for quantum renormalization groups. Phys. Rev. B* **48**, 10345–10356 (1993). (cited on page 56)

[151] J. P. Perdew, K. Burke, and M. Ernzerhof. *Generalized Gradient Approximation Made Simple. Phys. Rev. Lett.* **77**, 3865–3868 (1996). (cited on pages 60, 114, 118)

[152] K. Efetov. *Supersymmetry in disorder and chaos.* Cambridge University Press, Cambridge, first ed. (1999). (cited on page 63)

[153] M. A. Topinka, B. J. LeRoy, S. E. J. Shaw, E. J. Heller, R. M. Westervelt, K. D. Maranowski, and A. C. Gossard. *Imaging Coherent Electron Flow from a Quantum Point Contact. Science* **289**, 2323–2326 (2000). (cited on page 67)

[154] M. A. Topinka, B. J. LeRoy, R. M. Westervelt, S. E. J. Shaw, R. Fleischmann, E. J. Heller, K. D. Maranowski, and A. C. Gossard. *Coherent branched flow in a two-dimensional electron gas. Nature* **410**, 183–186 (2001). (cited on page 67)

[155] R. A. Jalabert, W. Szewc, S. Tomsovic, and D. Weinmann. *What Is Measured in the Scanning Gate Microscopy of a Quantum Point Contact? Phys. Rev. Lett.* **105**, 166802 (2010). (cited on page 67)

[156] M. I. Dyakonov and V. I. Perel. *Spin relaxation of conduction electrons in noncentrosymmetric semiconductors. Sov. Phys. Solid State* **13**, 3023 (1971). (cited on page 67)

[157] R. C. Roundy and M. E. Raikh. *Spin relaxation of a diffusively moving carrier in a random hyperfine field. Phys. Rev. B* **90** (2014). (cited on page 68)

[158] A. H. C. Neto and F. Guinea. *Impurity-Induced Spin-Orbit Coupling in Graphene. Phys. Rev. Lett.* **103** (2009). (cited on pages 68, 93, 94)

[159] M. Gmitra, D. Kochan, and J. Fabian. *Spin-Orbit Coupling in Hydrogenated Graphene. Phys. Rev. Lett.* **110**, 246602 (2013). (cited on pages 68, 93, 94, 108)

[160] J. Balakrishnan, G. K. W. Koon, M. Jaiswal, A. H. C. Neto, and B. Özyilmaz. *Colossal enhancement of spin–orbit coupling in weakly hydrogenated graphene. Nat Phys* **9**, 284–287 (2013). (cited on pages 68, 93, 94)

[161] M. D. Graef. *2. Lorentz microscopy: Theoretical basis and image simulations.* In *Experimental Methods in the Physical Sciences*, 27–67. Elsevier BV (2001). (cited on page 68)

[162] M. D. Graef. *Recent Progress in Lorentz Transmission Electron Microscopy.* In *ESOMAT 2009 - 8th European Symposium on Martensitic Transformations.* EDP Sciences (2009). (cited on page 68)

[163] X. Feng, Y. Deng, and H. W. J. Blöte. *Percolation transitions in two dimensions. Physical Review E* **78** (2008). (cited on page 90)

[164] B. D. Hughes. *Random walks and random environments*, vol. 1: Random walks. Clarendon Press, Oxford (1995). (cited on page 90)

[165] E. W. Weisstein. *Random Walk–1-Dimensional.* From MathWorld–A Wolfram Web Resource (last visited on June 19th, 2015). `http://mathworld.wolfram.com/RandomWalk1-Dimensional.html`. (cited on page 90)

[166] N. M. R. Peres, F. Guinea, and A. H. Castro Neto. *Electronic properties of disordered two-dimensional carbon. Phys. Rev. B* **73**, 125411 (2006). (cited on page 90)

[167] A. Schuessler, P. M. Ostrovsky, I. V. Gornyi, and A. D. Mirlin. *Analytic theory of ballistic transport in disordered graphene. Phys. Rev. B* **79**, 075405 (2009). (cited on page 90)

[168] K. Capelle. *A bird's-eye view of density-functional theory* (2002). Available online: `http://arxiv.org/abs/cond-mat/0211443`. (cited on pages 92, 116)

[169] D. Peng, N. Middendorf, F. Weigend, and M. Reiher. *An efficient implementation of two-component relativistic exact-decoupling methods for large molecules. The Journal of Chemical Physics* **138**, 184105 (2013). (cited on pages 92, 94)

[170] F. Schwabl. *Quantenmechanik für Fortgeschrittene (QM II)*. Springer-Lehrbuch. Springer, Berlin, Heidelberg (2008). (cited on page 93)

[171] M. K. Armbruster, F. Weigend, C. van Wüllen, and W. Klopper. *Self-consistent treatment of spin–orbit interactions with efficient Hartree–Fock and density functional methods*. *Phys. Chem. Chem. Phys.* **10**, 1748 (2008). (cited on page 94)

[172] O. V. Yazyev and L. Helm. *Defect-induced magnetism in graphene*. *Phys. Rev. B* **75** (2007). (cited on page 100)

[173] Y. Ferro, D. Teillet-Billy, N. Rougeau, V. Sidis, S. Morisset, and A. Allouche. *Stability and magnetism of hydrogen dimers on graphene*. *Phys. Rev. B* **78** (2008). (cited on page 100)

[174] S. Casolo, O. M. Loøvvik, R. Martinazzo, and G. F. Tantardini. *Understanding adsorption of hydrogen atoms on graphene*. *The Journal of Chemical Physics* **130**, 054704 (2009). (cited on page 100)

[175] Ž. Šljivančanin, R. Balog, and L. Hornekær. *Magnetism in graphene induced by hydrogen adsorbates*. *Chemical Physics Letters* **541**, 70–74 (2012). (cited on page 100)

[176] M. V. Ulybyshev and M. I. Katsnelson. *Magnetism and Interaction-Induced Gap Opening in Graphene with Vacancies or Hydrogen Adatoms: Quantum Monte Carlo Study*. *Phys. Rev. Lett.* **114** (2015). (cited on page 100)

[177] K. Binder and A. P. Young. *Spin glasses: Experimental facts, theoretical concepts, and open questions*. *Rev. Mod. Phys.* **58**, 801–976 (1986). (cited on page 100)

[178] G. Vignale and M. Rasolt. *Density-functional theory in strong magnetic fields*. *Phys. Rev. Lett.* **59**, 2360–2363 (1987). (cited on pages 104, 114)

[179] G. Vignale and M. Rasolt. *Current- and spin-density-functional theory for inhomogeneous electronic systems in strong magnetic fields*. *Phys. Rev. B* **37**, 10685–10696 (1988). (cited on pages 104, 114)

[180] M. Gmitra, S. Konschuh, C. Ertler, C. Ambrosch-Draxl, and J. Fabian. *Band-structure topologies of graphene: Spin-orbit coupling effects from first principles*. *Phys. Rev. B* **80**, 235431 (2009). (cited on page 108)

[181] J. Meair, J. P. Bergfield, C. A. Stafford, and P. Jacquod. *Local temperature of out-of-equilibrium quantum electron systems*. *Phys. Rev. B* **90**, 035407 (2014). (cited on page 110)

[182] G. E. Moore. *Cramming More Components onto Integrated Circuits*. *Electronics* **38**, 114–117 (1965). (cited on pages 111, 112)

[183] A. D. Becke. *Density-functional exchange-energy approximation with correct asymptotic behavior*. *Phys. Rev. A* **38**, 3098–3100 (1988). (cited on pages 114, 118)

[184] J. P. Perdew. *Density-functional approximation for the correlation energy of the inhomogeneous electron gas*. *Phys. Rev. B* **33**, 8822–8824 (1986). (cited on pages 114, 118)

[185] S. Datta. *Quantum transport: atom to transistor*. Cambridge University Press, Cambridge (2005). (cited on page 115)

[186] H. Haug and A.-P. Jauho. *Quantum kinetics in transport and optics of semiconductors*. Springer series in solid state sciences. Springer, Berlin (1996). (cited on page 115)

[187] M. Born and R. Oppenheimer. *Zur Quantentheorie der Molekeln*. *Ann. Phys.* **389**, 457–484 (1927). (cited on page 116)

[188] P. Hohenberg and W. Kohn. *Inhomogeneous Electron Gas*. *Physical Review* **136**, B864–B871 (1964). (cited on page 116)

[189] M. Levy. *Universal variational functionals of electron densities, first-order density matrices, and natural spin-orbitals and solution of the v-representability problem*. *Proc. Natl. Acad. Sci. USA* **76**, 6062–6065 (1979). (cited on page 117)

[190] W. Kohn and L. J. Sham. *Self-Consistent Equations Including Exchange and Correlation Effects*. *Physical Review* **140**, A1133–A1138 (1965). (cited on page 117)

[191] J. F. Janak. *Proof that $\frac{\partial E}{\partial n_i} = \epsilon$ in density-functional theory*. *Phys. Rev. B* **18**, 7165–7168 (1978). (cited on page 118)

[192] J. P. Perdew, R. G. Parr, M. Levy, and J. L. Balduz. *Density-Functional Theory for Fractional Particle Number: Derivative Discontinuities of the Energy*. *Phys. Rev. Lett.* **49**, 1691–1694 (1982). (cited on page 118)

[193] J. P. Perdew and M. Levy. *Comment on "Significance of the highest occupied Kohn-Sham eigenvalue". Phys. Rev. B* **56**, 16021–16028 (1997). (cited on page 118)

[194] A. Schäfer, H. Horn, and R. Ahlrichs. *Fully optimized contracted Gaussian basis sets for atoms Li to Kr. J. Chem. Phys.* **97**, 2571–2577 (1992). (cited on page 118)

[195] F. Weigend and R. Ahlrichs. *Balanced basis sets of split valence, triple zeta valence and quadruple zeta valence quality for H to Rn: Design and assessment of accuracy. Phys. Chem. Chem. Phys.* **7**, 3297–3305 (2005). (cited on page 118)

[196] K. Eichkorn, O. Treutler, H. Öhm, M. Häser, and R. Ahlrichs. *Auxiliary basis sets to approximate Coulomb potentials (Chem. Phys. Letters 240 (1995) 283-290). Chemical Physics Letters* **242**, 652–660 (1995). (cited on page 118)

[197] K. Eichkorn, F. Weigend, O. Treutler, and R. Ahlrichs. *Auxiliary basis sets for main row atoms and transition metals and their use to approximate Coulomb potentials. Theoretical Chemistry Accounts: Theory, Computation, and Modeling (Theoretica Chimica Acta)* **97**, 119–124 (1997). (cited on page 118)

[198] M. Sierka, A. Hogekamp, and R. Ahlrichs. *Fast evaluation of the Coulomb potential for electron densities using multipole accelerated resolution of identity approximation. J. Chem. Phys.* **118**, 9136 (2003). (cited on page 118)

[199] L. Blackford, J. Choi, A. Cleary, E. D'Azevedo, J. Demmel, I. Dhillon, J. Dongarra, S. Hammarling, G. Henry, A. Petitet, K. Stanley, D. Walker, and R. Whaley. *ScaLAPACK User's Guide.* Society for Industrial and Applied Mathematics, Philadelphia, PA, USA (1997). (cited on pages 119, 128)

[200] B. C. Carlson and J. M. Keller. *Orthogonalization Procedures and the Localization of Wannier Functions. Phys. Rev.* **105**, 102–103 (1957). (cited on page 123)

[201] V. Strassen. *Gaussian elimination is not optimal. Numer. Math.* **13**, 354–356 (1969). (cited on page 127)

[202] *GNU scientific library: reference manual.* A GNU manual. Network Theory, third ed. (2009). (cited on page 170)